Modelling and simulation of the formation of single phase and compound fluid volumes

by

Jonathan Andrew Simmons

A thesis submitted to the
University of Birmingham
for the degree of
Doctor of Philosophy

School of Mathematics
University of Birmingham
August 2015

Abstract

In this thesis the formation of single phase and compound fluid volumes is investigated and simulated numerically. The continuum fluid mechanical models that describe the generation of a gas bubble from an orifice as well as the topologically inverse process of the formation of a single or compound liquid drop from a nozzle are complex, involving a time dependent flow domain and the non-linear dynamics of the fluid, so that to find a solution to the corresponding problem a numerical method is required. A computational framework based on the finite element method is therefore constructed to simulate these processes. In each study, the simulations are compared to available experimental results and the relevant parameter space is investigated in order to describe the influence that each parameter has on the process.

The work on bubble formation is split into two cases. In the first case, where the three phase solid-liquid-gas contact line remains pinned to the rim of the orifice, it is seen that the scaling laws that are used to describe the volume of a bubble are ineffectual over the range of flow rates considered. In the second and more complicated case, where the contact line is free to move along the solid surface, a model that allows the contact angle to behave dynamically and vary from its static value is required to accurately describe experiments. The work on liquid drops mainly focuses on the generation of a compound drop, which is extremely sensitive to changes in parameters, rather than a single drop, which is considered only as a test case.

Acknowledgements

I wish to thank my supervisors Prof. Yulii D. Shikhmurzaev and Dr James E. Sprittles for the time and effort they have invested in me over the past five years. It has been a privilege to work with such experts and I will be forever grateful for their guidance and patience during my studies. I would also like to thank Dr Grigori Sisoev for his help and support whenever it was needed. The financial support of the EPSRC and also the EPSRC Centre for Innovative Manufacturing in Additive Manufacturing at the University of Nottingham is also acknowledged.

I would also like to thank my respective internal and external examiners, Dr David Leppinen and Dr Mark Wilson, for the manner in which they conducted my oral examination and for their constructive comments which inspired many improvements to this thesis, and Dr Warren Smith for chairing my oral examination and assessing a much earlier version of this work which was submitted for an MRes(Qual) in 2012. Janette Lowe, Mike Finney and Dr Jamal Uddin also deserve my thanks.

The support of the many friends I have made during my time at the university must also be stated. Notable mentions go to those with whom I shared office 315 and also my Postgrad Mathletic teammates. My friend Dr Mark Esson deserves a special mention having lived together for the majority of our studies.

My final thanks go to my close friends outside the world of academia and, most importantly, to my family, Mum, Dad, Nick and Nan, to whom I dedicate this thesis.

Contents

Appendix:

List of Figures

Chapter 1

Introduction

The controlled production of small gas bubbles is of critical importance to many operations found in the chemical, petrochemical, nuclear, metallurgical and biomedical industries (Kumar & Kuloor, 1970; Clift *et al.*, 1978; Ponter & Surati, 1997; Kulkarni & Joshi, 2005; Yang *et al.*, 2007) whilst the generation of liquid drops is key to various procedures such as spray coating (Ruschak, 1985; Weinstein & Ruschak, 2004), ink-jet printing (Calvert, 2001; Basaran, 2002) and, more recently, additive manufacturing (Dimitrov *et al.*, 2006; Hopkinson *et al.*, 2006; Gibson *et al.*, 2010). Furthermore, the manufacture of compound drops is a process found in the pharmaceutical industry where the active ingredient is encapsulated within a second material (Nakano, 2000; Shah *et al.*, 2008). Understanding the formation of these single phase and compound fluid volumes is therefore essential.

There are various material, design and regime parameters that influence the generation of gas bubbles (see Figure 1.1a) and liquid drops (see Figure 1.1b). Therefore, it is vital to not only understand the role that these different effects have on each process, both individually and when coupled with together, but also to be able to consistently and confidently predict the outcome of such activities when given certain values of parameters.

The small temporal and spatial scales associated with this class of problems make an

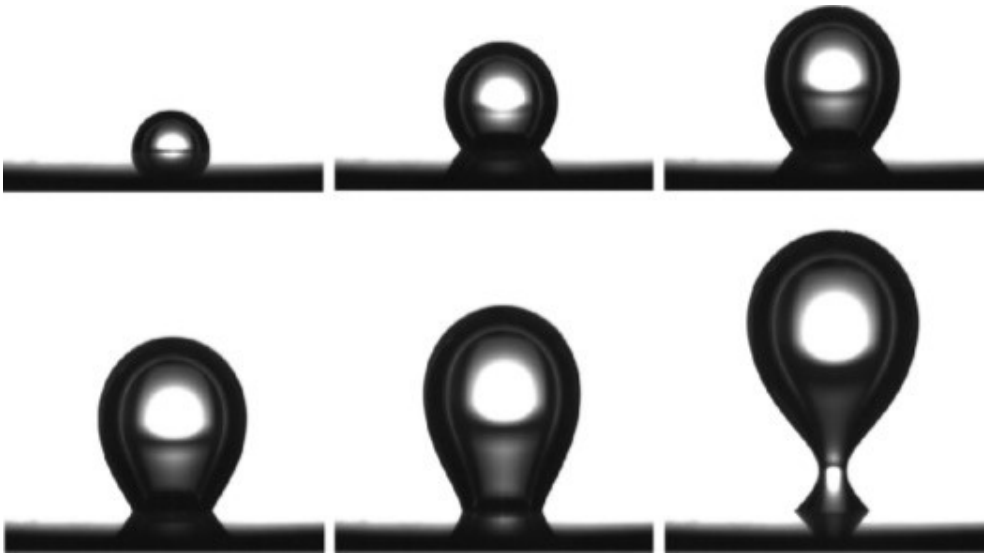

(a) Bubble formation from an orifice in a submerged solid surface (Albadawi *et al.*, 2013). The contact line remains pinned to the rim of the orifice whilst the picture on the bottom right shows the bubble with a 'neck'.

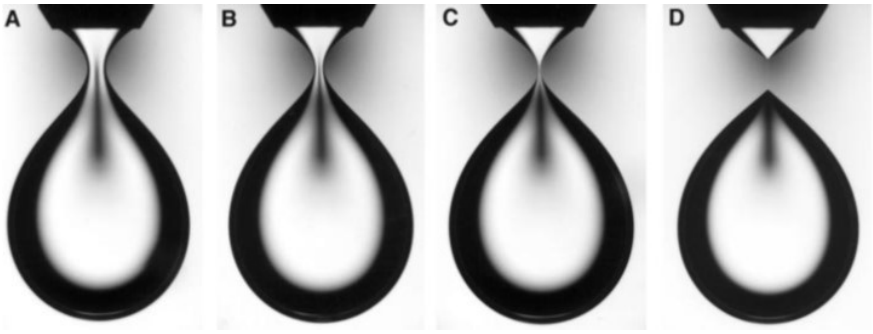

(b) Drop formation from a nozzle (Doshi *et al.*, 2003).

Figure 1.1: Experimental images of gas bubble and liquid drop formation.

experimental approach very challenging. Obtaining results that are reproducible is just one difficulty whilst accurately measuring certain features of the flow as well as observing the flow field and pressure distribution inside a liquid drop or adjacent to a bubble present additional challenges which are often extremely difficult to overcome. Consequently, a theoretical approach has numerous advantages over a purely experimental one.

By utilising the techniques of computational fluid dynamics, a framework can be produced that can capture all physical scales appearing in these flows. Reproducible results

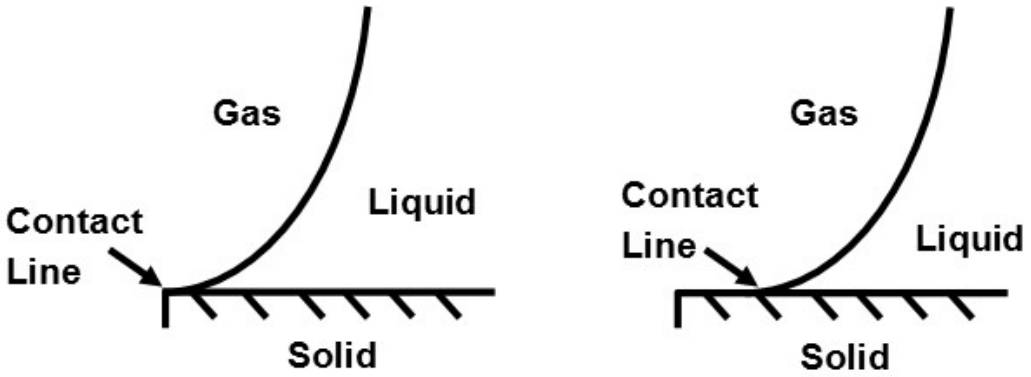

Figure 1.2: On the left, the three phase solid-liquid-gas contact line is pinned to the rim of the orifice, whilst on the right, the contact line has moved along the solid surface away from the rim of the orifice.

can be generated in a shorter time frame with well designed post-processing evaluating the dynamics of the problem. The development of such a numerical platform will result in a powerful tool for studying these fluid dynamical phenomena.

In this thesis, the first problem to be studied is the formation of a gas bubble from an orifice in a submerged solid surface where the three phase solid-liquid-gas contact line, the line in space at which the solid, liquid and gas phases all meet, will remain pinned to the rim of the orifice (see Figure 1.2). This restriction will then be relaxed as the more complex problem of bubble formation with a moving contact line is studied. By extending these developed numerical techniques, the focus of this work will then shift to the formation of liquid drops. The generation of a single drop from a nozzle is first studied before the more complicated case of a compound drop is considered.

The objective of this thesis is to develop and utilise a numerical platform to accurately simulate the formation of single phase and compound fluid volumes, namely gas bubbles and single and compound liquid droplets, and to investigate how various parameters influence (a) the 'global' dynamics of a process, such as the formation time or the volume of the bubble or drop formed, and (b) any 'small-scale' features, such as the thinning of a neck (see Figure 1.3) or the motion of the contact line. The structure of the thesis

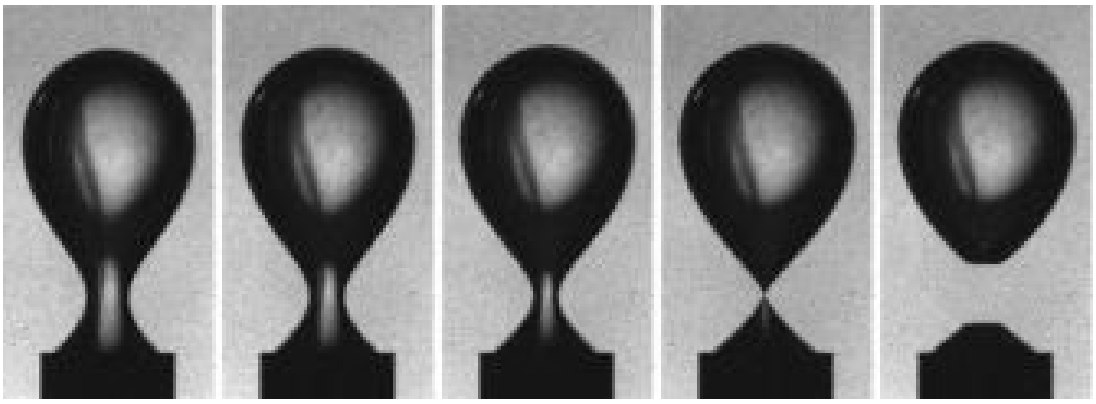

Figure 1.3: The thinning of the neck of a bubble, also known as the pinch-off, before the eventual break-up (far right) (Thoroddsen *et al.*, 2007).

pursuing these aims is now described.

1.1 Overview of the Thesis

The formation of a gas bubble from an orifice in a submerged solid surface is considered first. Chapter 2 contains a review of the related literature and Chapter 3 sets out the continuum model used to describe this process. The dimensional and dimensionless governing equations, boundary and initial conditions are described in detail. The problem is characterised in terms of three dimensionless parameters and the parameter regime of interest is then discussed.

The design and construction of the numerical platform used to solve the system of dimensionless equations formulated in Chapter 3 is given in Chapter 4. The possible numerical methods that could be used are appraised and the finite element method is chosen as the most appropriate to meet the aims of this thesis. The design of the computational mesh as well as the spatial and temporal discretisation of the system of equations are described in detail.

Having built the computational framework described in Chapter 4, the code is then

tested to check its accuracy in Chapter 5. The temporal evolution of a Rayleigh bubble is chosen as a test case that will validate many aspects of the code. With increasing spatial and temporal resolution, the results produced by the platform are seen to converge to the known solution which confirms that the code has been written correctly. Additional numerical details, such as the number of nodes and the time step required during a simulation of bubble formation to ensure the accuracy of the result, are then described.

The results for the formation of a bubble whose contact line is pinned to the rim of the orifice are then given in Chapter 6. A comparison with experiments available in the literature is presented before the influence of the regime of dimensionless parameters is explored. This focuses on the effect of these parameters on the global dynamics of the process, such as the volume of the bubbles formed and the formation times. These results are then used to validate a selection of scaling laws proposed in the published literature. Some local dynamics of the process such as the pinch-off of the bubble are also described. The work from Chapters 2–6 is soon to be published in a paper accepted for publication (Simmons *et al.*, 2015).

Chapter 7 describes the formation of a bubble whose contact line is free to move away from the orifice along the solid surface. First, a literature review covering the additional theoretical and computational issues involved in this extended problem is given. Then the supplementary dimensionless equations required for the model and the adaptations to the numerical platform are described in detail. The influence of the dimensionless parameters on the small-scale dynamics, such as the behaviour of the dynamic contact angle and the motion of the contact line, and the global dynamics of the problem, such as the volume of the bubble formed, are described. Results are also compared with experiments.

The computational framework developed for the formation of a bubble can also be used as a basis for the more complex phenomena such as the formation of a compound drop, which is described in Chapter 8. Once again an amended problem formulation is

followed by a brief description of any additional computational issues. Then simulations of a single drop are used as a starting point and compared with experiments. A 'base case' for the compound drop formation is established before the sensitivity of the formation process to the various dimensionless parameters is determined.

Finally, Chapter 9 gives a summary of the thesis before establishing potential areas of future research.

Chapter 2

The Formation of a Bubble from an Orifice with a Pinned Contact Line

The computational, experimental and theoretical literature on the formation of gas bubbles has focused on the case of generating a bubble by pumping gas through a single formation site, namely a submerged nozzle (Longuet-Higgins *et al.*, 1991; Oğuz & Prosperetti, 1993; Wong *et al.*, 1998; Thoroddsen *et al.*, 2007; Zhang *et al.*, 2014) or, as is the case in this work, an upward facing orifice in a submerged solid surface (Zhang & Shoji, 2001; Badam *et al.*, 2007; Gerlach *et al.*, 2007; Das *et al.*, 2011).

Some authors have considered the case of inflating a bubble under a constant gas pressure with the volumetric gas flow rate varying as the bubble inflates (Davidson & Schüler, 1960a,b; Satyanarayan *et al.*, 1969; La Nauze & Harris, 1972). Others have considered the case where the volumetric gas flow rate is determined by the difference between some ambient pressure away from the bubble and the gas pressure in a chamber that is connected to the formation site (Khurana & Kumar, 1969; Oğuz & Prosperetti, 1993). However, the most popular method, and the method employed here, is to apply a constant volumetric gas flow rate through the formation site and allow the gas pressure to

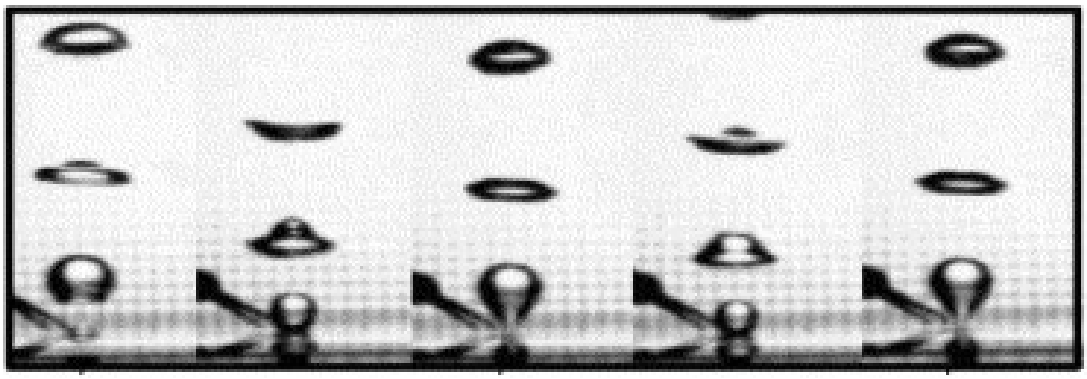

Figure 2.1: The formation of a continuous chain of bubbles (Zhang & Shoji, 2001).

vary in time (Wong *et al.*, 1998; Jamialahmadi *et al.*, 2001; Corchero *et al.*, 2006; Gerlach *et al.*, 2007).

2.1 Experimental Observations

The majority of experimental studies examine a chain of bubbles produced from the same site (Zhang & Shoji, 2001; Badam *et al.*, 2007; Das *et al.*, 2011). A bubble grows whilst attached to the formation site as gas is pumped through the site at a constant flow rate (see Figure 2.1), and as the volume of the bubble increases, the influence of buoyancy becomes more important, pulling the bubble upwards. The bubble seeks to minimise its surface area at a given volume and so a 'neck' develops in the bubble as the longitudinal curvature of the free surface changes sign at some point just above the three phase solid-liquid-gas contact line. The difference in pressure between the base and the apex of the bubble then drives the thinning of this neck as the free surface begins to pinch-off. This leads to the eventual break up of the bubble into two parts; a newly-formed bubble is released and rises away from the formation site under buoyancy, whilst the residual bubble, that is left attached to the formation site, begins to grow. This process repeats itself, thus producing a chain of bubbles.

The aim of many studies has been to find the global characteristics of the formation process, such as the frequency of formation and the volume of the bubbles that are formed, for a given set of material parameters (e.g. liquid density and viscosity), design parameters (e.g. orifice radius, wettability of substrate) and regime parameters (e.g. gas flow rate). These studies provide potentially useful material for comparing theoretical results with experiments. However, global characteristics of bubble formation in a chain accumulate several complex phenomena, and it is desirable to have a more detailed picture of each of them and of their interaction.

Theoretical and early computational studies focused on the behaviour of a single bubble which grows from some initial state up until the break up of the free surface is approached (Longuet-Higgins *et al.*, 1991; Wong *et al.*, 1998; Xiao & Tan, 2005). The mathematical difficulties of handling the topological change associated with the complete break up of the bubble prohibited any further progress and so, in this case, the formation time period and the volume of the bubble above the point of minimum neck radius are of interest and have been investigated. Here, the break up is assumed to be a local effect that does not affect the global dynamics of the formation process.

Experimental and theoretical studies identified three regimes for the formation of bubbles under a constant gas flow rate (McCann & Prince, 1971; Zhang & Shoji, 2001). For a given set of material and design parameters, the first of these regimes occurs at small gas flow rates and is known as the 'static' regime. In this regime, the volume of the bubbles formed is independent of flow rate, and therefore a decrease in the flow rate results in an increase in the formation time. Consequently, it is not possible to produce a bubble with a volume smaller than this limiting volume. Fritz (1935) suggested that this limiting final volume is proportional to the orifice radius. This, as well as other scaling laws are considered in Chapter 6.

At greater flow rates, bubble formation enters the 'dynamic' regime. It is now the

formation time that approaches a limiting value, resulting in an increase of bubble volume V_d with flow rate Q. In this regime, some authors used spherical bubble models to propose scaling laws for the bubble volume. Davidson & Schüler (1960b) and Oğuz & Prosperetti (1993) proposed that $V_d \propto Q^{\frac{6}{5}}$ for bubble formation in an inviscid liquid, whilst, Wong *et al.* (1998) suggested that $V_d \propto Q^{\frac{3}{4}}$ in the case of a highly viscous liquid.

Finally, under even greater flow rates, bubble formation enters the 'turbulent' regime. Here the motion is chaotic with successive bubbles coalescing with each other above the formation site. The transition between these three regimes is dependent on all of the material and design parameters involved.

2.2 Theoretical Progress

Under sufficiently small gas flow rates, the initial growth of a single bubble may be accurately modelled as a quasi-static process, an approach that has also been utilised for the description of the formation of liquid drops (Fordham, 1948; Thoroddsen *et al.*, 2005). By assuming that the fluid velocities are negligible, one can use the Young-Laplace equation, which balances the difference in the gas and hydrostatic pressures with the capillary pressure. This can be solved to find the free surface profile of a bubble at a particular volume. A series of successive profiles can be found (see Figure 2.2) which are in very good agreement with experiments that describe the initial evolution of a bubble (Marmur & Rubin, 1973; Longuet-Higgins *et al.*, 1991; Gerlach *et al.*, 2005; Lee & Tien, 2009; Vafaei & Wen, 2010; Vafaei *et al.*, 2010, 2011; Lee & Yang, 2012; Lesage & Marois, 2013; Lesage *et al.*, 2013).

However, once the neck forms and the pinch-off process begins, the liquid velocities adjacent to the point of minimum neck radius are no longer negligible. Due to the dynamics associated with the relatively large liquid velocities involved at this stage, the quasi-static

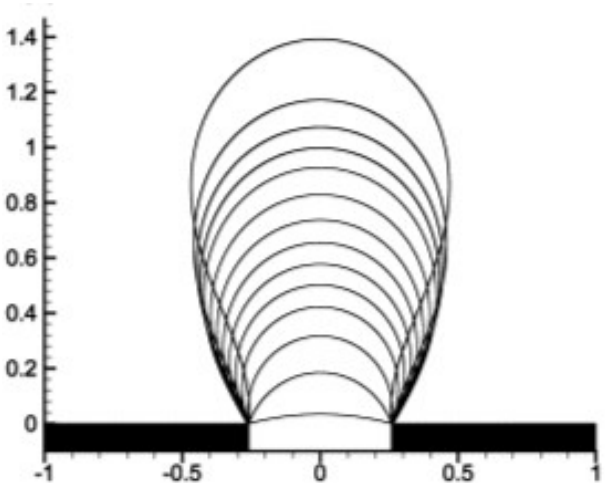

Figure 2.2: The theoretical quasi-static formation of a bubble (Gerlach *et al.*, 2005).

approach is no longer valid and thus, in general, one cannot expect to accurately predict the final volume of a newly formed bubble this way.

In an attempt to describe some aspects of the dynamic problem, early mathematical models of single bubble formation under a constant gas flow rate were based upon global force balances. The first 'one-stage' models for highly viscous (Davidson & Schüler, 1960a) and inviscid liquids (Davidson & Schüler, 1960b; McCann & Prince, 1969), which involved the bubble growing spherically, were developed into various ad-hoc 'two-stage' models for highly viscous (Ramakrishnan *et al.*, 1969; Gaddis & Vogelpohl, 1986) and inviscid liquids (Wraith, 1971; Buyevich & Webbon, 1996) by adding a detachment stage to the spherical expansion stage (see Figure 2.3). Once the spherical bubble had reached a certain volume, it translates away from the formation site but remains in contact with it via a cylindrical column of gas. The bubble is said to detach when certain criteria are met, such as the column reaches a certain height. Although these ad-hoc semi-empirical models are seen to give good agreement in certain regimes (Kulkarni & Joshi, 2005), to accurately describe the whole parameter space of interest, the use of more justifiable albeit complex computational techniques is needed.

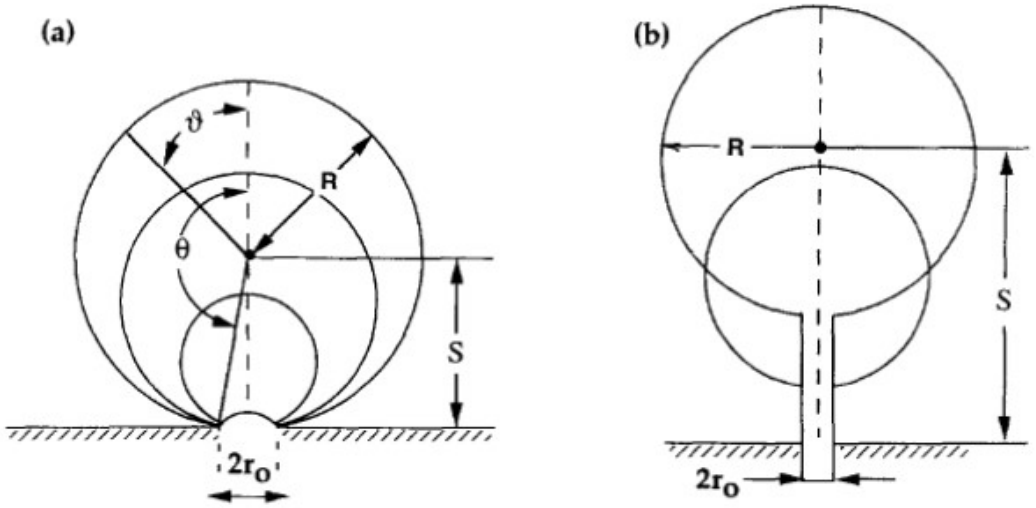

Figure 2.3: A diagram of a two-stage bubble formation model with the initial spherical growth, on the left, and the translation away from the orifice, on the right (Buyevich & Webbon, 1996).

2.3 Computational Approaches

To solve the unsteady free-boundary problem of bubble formation from an orifice or nozzle, subject to the forces of gravity, inertia, viscosity and capillarity, the development of computational fluid dynamics techniques is required. Much of the early work in this direction was concerned with the axisymmetric generation of a single bubble. The first methods to assume the bubble was non-spherical involved various finite difference schemes to solve equations imposed on the bubble surface (Marmur & Rubin, 1976; Pinczewski, 1981; Tan & Harris, 1986; Terasaka & Tsuge, 1990, 1993) before the boundary integral method, which can be used to reduce the problem's dimensionality to one, was used to study bubble formation in either the inviscid (Hooper, 1986; Oğuz & Prosperetti, 1993; Xiao & Tan, 2005) or highly viscous flow regime (Wong *et al.*, 1998).

Since then, the majority of work on bubble generation has focused on the influence of the material, design and regime parameters on the global characteristics of the flow using the volume-of-fluid method (Ma *et al.*, 2012), and its improved variants which utilise

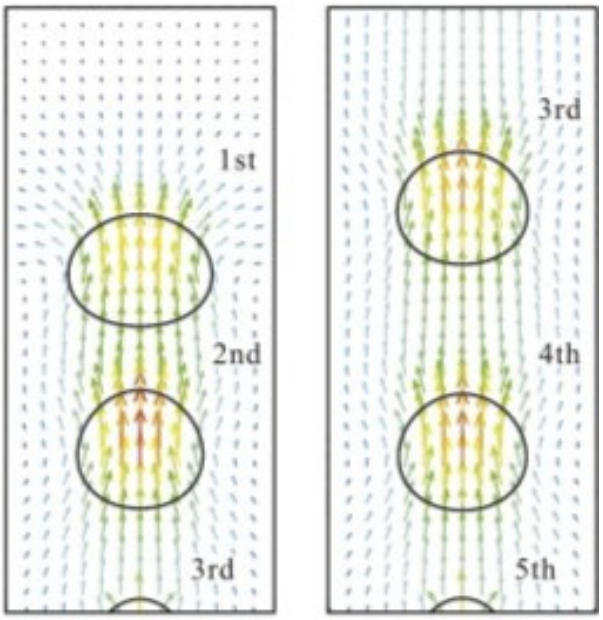

Figure 2.4: The coupled level set/volume-of-fluid method presented in Ohta *et al.* (2011) can describe the interaction between subsequent bubbles in a chain.

level-set methods (Buwa *et al.*, 2007; Gerlach *et al.*, 2007; Chakraborty *et al.*, 2009; Ohta *et al.*, 2011; Chakraborty *et al.*, 2011; Albadawi *et al.*, 2013). Due to the simple manner in which topological changes are 'automatically' handled, such techniques have proved successful at describing many features of the bubble formation phenomenon, including the wake effect of a preceding bubble on subsequent bubbles in a chain (see Figure 2.4), where the size of forming bubbles are relatively large and hence the details of how the topological transition (i.e. the break up of the bubble) takes place are assumed to be relatively unimportant.

Despite the advantages of volume-of-fluid based methods, as a relatively simple way of handling the global dynamics, it is well known that this class of numerical techniques are not well suited to resolving the multiscale physics which becomes critical in 'singular' flows, i.e. those in which liquid bodies coalesce (Hopper, 1990; Eggers *et al.*, 1999) or divide (Rayleigh, 1892; Eggers, 1997). For instance, for a millimetre-sized bubble, experiments

are able to resolve the minimum neck radius down to tens of microns (Burton *et al.*, 2005; Thoroddsen *et al.*, 2007; Bolaños Jiménez *et al.*, 2008, 2009), whilst numerical methods have, thus far, failed to capture these scales and often artificially truncate the simulation far above the scales which are still well within the realm of continuum mechanics, with the result that different commercial codes give different outputs for the same physical problem (Hysing *et al.*, 2009). Therefore this class of method cannot study the actual pinch-off of the bubble in order to validate several theories proposed in the literature for 'singular' flows (Burton *et al.*, 2005; Gordillo *et al.*, 2005; Gordillo & Pérez-Saborid, 2006; Thoroddsen *et al.*, 2007; Eggers *et al.*, 2007; Bolaños Jiménez *et al.*, 2008; Quan & Hua, 2008; Gordillo, 2008; Bolaños Jiménez *et al.*, 2009; Gekle *et al.*, 2009; Fontelos *et al.*, 2011).

The choice of the numerical method used in this work is clearly of great importance and is discussed in Chapter 4.

2.4 Summary

In this chapter, a review of the literature was presented for the formation of a bubble with a contact line pinned to the rim of an orifice or nozzle. The various experimental, theoretical and computational approaches used to investigate this problem were discussed. In the next chapter, the problem is formulated mathematically.

Chapter 3

Problem Formulation

In this chapter, the continuum model used to describe the formation of a single bubble from an orifice in a submerged solid surface is introduced. It is assumed that the wettability of the solid surface is sufficiently large so that the three phase solid-liquid-gas contact line remains pinned to the rim of the orifice. For that reason, there is no dynamic wetting and so the so-called 'classical' fluid mechanical boundary conditions are sufficient.

3.1 Dimensional Problem Formulation

Consider a smooth, horizontal, stationary, impermeable solid surface submerged in a quiescent, incompressible Newtonian liquid of constant density ρ and dynamic viscosity μ. The solid surface has a circular orifice of radius r_o through which an inviscid gas is pumped at a constant volumetric flow rate Q to form a single bubble (see Figure 3.1). The characteristic velocities in the gas and the size of the resulting bubble are assumed to be sufficiently small so that any spatial non-uniformity of the gas pressure in the bubble can be neglected and therefore the gas pressure can be regarded as a function of time.

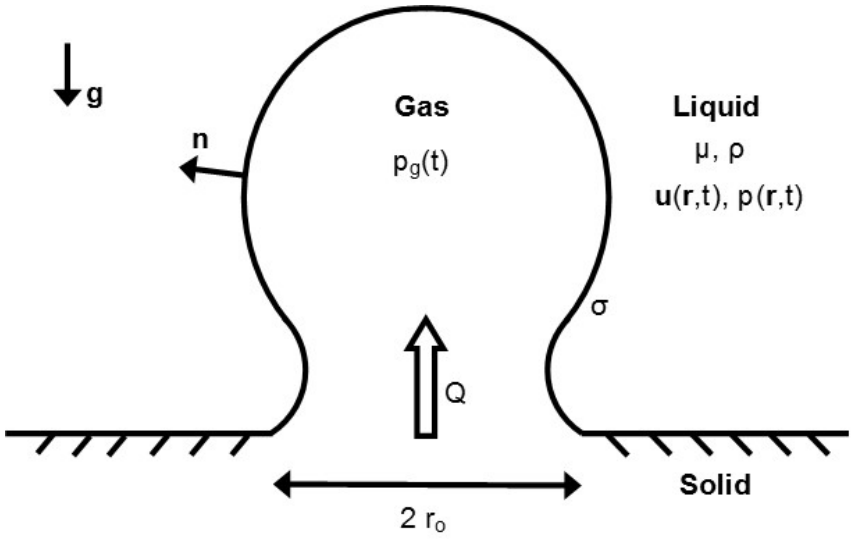

Figure 3.1: A sketch of the flow domain.

3.1.1 Bulk Equations

The incompressible flow of the bulk liquid phase is governed by the Navier-Stokes equations,

$$\nabla \cdot \mathbf{u} = 0, \tag{3.1a}$$

$$\rho \left(\frac{\partial \mathbf{u}}{\partial t} + \mathbf{u} \cdot \nabla \mathbf{u} \right) = \nabla \cdot \mathbf{P} + \rho \mathbf{g}, \tag{3.1b}$$

where $\mathbf{u}(\mathbf{r}, t)$ and $p(\mathbf{r}, t)$ are the liquid's velocity and pressure, t is time, $\mathbf{r}$ is the spatial coordinate vector and $\mathbf{g}$ is the gravity vector. The Newtonian stress tensor $\mathbf{P}$ is given by

$$\mathbf{P} = -p\mathbf{I} + 2\mu\mathbf{E}, \qquad \mathbf{E} = \frac{1}{2}\left[\nabla\mathbf{u} + (\nabla\mathbf{u})^T\right], \tag{3.2}$$

where $\mathbf{I}$ is the metric tensor and $\mathbf{E}$ is the rate-of-strain tensor.

3.1.2 Boundary Conditions

The combined no-slip and impermeability condition is applied on the solid-liquid interface,

$$\mathbf{u} = \mathbf{0}. \tag{3.3}$$

The kinematic boundary condition on the liquid-gas interface, that states the fluid particles that form the free surface remain there for all time, is given by

$$\frac{\partial f}{\partial t} + \mathbf{u} \cdot \nabla f = 0, \tag{3.4}$$

where $f(\mathbf{r}, t) = 0$ defines the a-priori unknown free surface. The balance of forces acting on an element of the free surface from the liquid and gas phases and neighbouring surface elements manifests itself through a dynamic boundary condition,

$$\mathbf{n} \cdot (\mathbf{P} - \mathbf{P}_g) - \sigma \mathbf{n} \nabla \cdot \mathbf{n} = \mathbf{0}, \tag{3.5}$$

where $\mathbf{P}_g = -p_g \mathbf{I}$ is the stress tensor for the gas phase and so

$$p_g \mathbf{n} + \mathbf{n} \cdot \mathbf{P} - \sigma \mathbf{n} \nabla \cdot \mathbf{n} = \mathbf{0}, \tag{3.6}$$

or in terms of $\mathbf{u}$,

$$(p_g - p)\,\mathbf{n} + \mu \mathbf{n} \cdot \left[\nabla \mathbf{u} + (\nabla \mathbf{u})^T\right] - \sigma \mathbf{n} \nabla \cdot \mathbf{n} = \mathbf{0}, \tag{3.7}$$

where $p_g = p_g(t)$ is the spatially uniform gas pressure, which is determined as part of the solution, σ is the surface tension of the liquid-gas interface and $\mathbf{n} = \nabla f / |\nabla f|$ is the unit normal to the free surface that points into the liquid phase (see Figure 3.1). The

components of (3.6) that are normal and tangential to the free surface are given by

$$p_g + \mathbf{n} \cdot \mathbf{P} \cdot \mathbf{n} = \sigma \nabla \cdot \mathbf{n}, \tag{3.8a}$$

$$\mathbf{n} \cdot \mathbf{P} \cdot (\mathbf{I} - \mathbf{nn}) = \mathbf{0}, \tag{3.8b}$$

respectively, so that in terms of $\mathbf{u}$,

$$p_g - p + \mu \mathbf{n} \cdot \left[\nabla \mathbf{u} + (\nabla \mathbf{u})^T \right] \cdot \mathbf{n} = \sigma \nabla \cdot \mathbf{n}, \tag{3.9a}$$

$$\mathbf{n} \cdot \left[\nabla \mathbf{u} + (\nabla \mathbf{u})^T \right] \cdot (\mathbf{I} - \mathbf{nn}) = \mathbf{0}. \tag{3.9b}$$

The scalar multiplication of a vector by the tensor $\mathbf{I} - \mathbf{nn}$ gives the tangential components of the vector along the surface of which $\mathbf{n}$ is the unit normal vector.

The normal stress boundary condition (3.9a) on the liquid-gas interface is itself a differential equation determining the free surface shape and as such requires its own boundary conditions. Since the three phase solid-liquid-gas contact line remains pinned to the rim of the orifice for all time,

$$f(\mathbf{r}_o, t) = 0, \qquad t \geqslant 0, \tag{3.10}$$

where $\mathbf{r}_o$ is the position of the rim of the orifice.

Finally, far from the bubble, the liquid is at rest,

$$\mathbf{u} \to 0, \quad \mathbf{r} \to \infty. \tag{3.11}$$

3.1.3 Constraint on the Bubble Volume

The constant volumetric gas flow rate Q implies that an equation is required that governs the volume of the bubble V. The volume of the bubble is therefore given by

$$V(t) = V_i + Q\,t, \qquad t \geqslant 0, \tag{3.12}$$

where V_i is the prescribed initial volume of the bubble.

3.1.4 Initial Conditions

To conclude the problem formulation, this initial-value problem requires the necessary initial conditions. The initial shape of the bubble and the initial velocity field must be prescribed. The initial shape of the free surface is assumed to be a spherical cap with a base radius of r_o and a volume of V_i, whilst the liquid is assumed to be initially at rest,

$$\mathbf{u}\,(\mathbf{r}, 0) = \mathbf{0}. \tag{3.13}$$

This set of dimensional equations (3.1)–(3.13) can now be rescaled to give the equations in dimensionless form.

3.2 Dimensionless Problem Formulation

The fluid flow is assumed to be axisymmetric about the vertical axis and therefore the problem is considered in the (r, z)-plane where r and z are the respective radial and vertical coordinates of a cylindrical coordinate system (see Figure 3.2). The velocity and pressure fields of the liquid can therefore be rewritten as $\mathbf{u}(r, z, t) = u(r, z, t)\mathbf{e}_r + w(r, z, t)\mathbf{e}_z$ and $p(r, z, t)$, respectively, where $\mathbf{e}_r$ and $\mathbf{e}_z$ are the respective unit coordinate vectors in the r

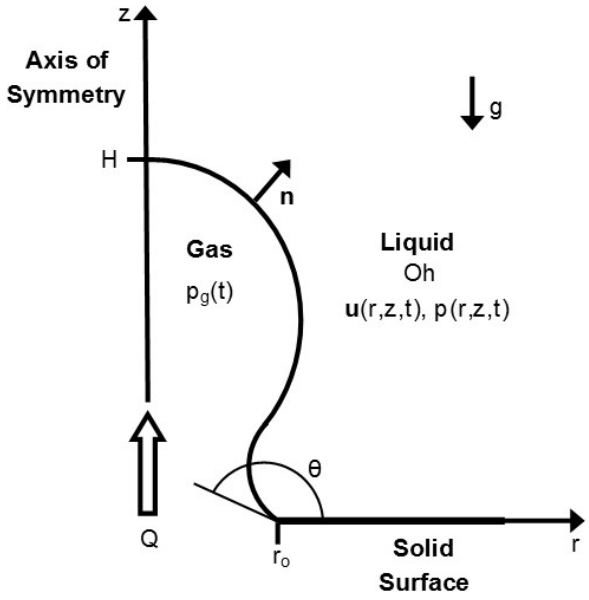

Figure 3.2: A sketch of the flow domain in the (r, z)-plane.

and z directions. The gravity vector in (3.1b) is then given by $\mathbf{g} = -g\mathbf{e}_z$, where g is the acceleration due to gravity.

The dimensional problem formulation (3.1)–(3.13) is rescaled using the following scales for length $L = \sqrt{\sigma/\rho g}$, velocity $U = \sigma/\mu$, pressure $\sigma/L = \sqrt{\rho\sigma g}$, time $L/U = \mu/\sqrt{\rho\sigma g}$ and flow rate $L^2U = \sigma^2/\mu\rho g$. In other words, the scales are based on a regime in which viscous, capillarity and buoyancy forces are of similar magnitude, so that the Bond number ($Bo = \rho g L^2/\sigma$) and capillary number ($Ca = \mu U/\sigma$) are unity.

From here on, all quantities are dimensionless unless stated and where dimensional quantities do appear, they are denoted with bars. Some equations of the following dimensionless problem formulation are also written in component form for future reference.

The stress tensor (3.2) is now given by $\mathbf{P} = -p\mathbf{I} + \nabla\mathbf{u} + (\nabla\mathbf{u})^T$ and so in physical component form, i.e. components with respect to the unit basis vectors, is

$$\mathbf{P} = P_{rr}\mathbf{e}_r\mathbf{e}_r + P_{rz}\mathbf{e}_r\mathbf{e}_z + P_{zr}\mathbf{e}_z\mathbf{e}_r + P_{zz}\mathbf{e}_z\mathbf{e}_z + P_{\varphi\varphi}\mathbf{e}_\varphi\mathbf{e}_\varphi, \tag{3.14}$$

where $P_{rr} = -p + 2\frac{\partial u}{\partial r}$, $P_{rz} = P_{zr} = \frac{\partial w}{\partial r} + \frac{\partial u}{\partial z}$, $P_{zz} = -p + 2\frac{\partial w}{\partial z}$ and $P_{\varphi\varphi} = -p + \frac{2u}{r}$, and $\mathbf{e}_\varphi$ is the azimuthal unit vector.

Therefore the Navier-Stokes equations (3.1) become,

$$\nabla \cdot \mathbf{u} = 0, \tag{3.15a}$$

$$\frac{\partial \mathbf{u}}{\partial t} + \mathbf{u} \cdot \nabla \mathbf{u} = Oh^2 \left(\nabla \cdot \mathbf{P} - \mathbf{e}_z \right), \tag{3.15b}$$

where the Ohnesorge number is $Oh = \mu / \sqrt{\rho \sigma L}$ which, by substituting the length scale, is

$$Oh = \frac{\mu g^{1/4}}{\rho^{1/4} \sigma^{3/4}}.$$

In component form (3.15) are

$$\frac{\partial u}{\partial r} + \frac{u}{r} + \frac{\partial w}{\partial z} = 0, \tag{3.16a}$$

$$\frac{\partial u}{\partial t} + u\frac{\partial u}{\partial r} + w\frac{\partial u}{\partial z} = Oh^2 \left(-\frac{\partial p}{\partial r} + \frac{\partial^2 u}{\partial r^2} + \frac{1}{r}\frac{\partial u}{\partial r} + \frac{\partial^2 u}{\partial z^2} - \frac{u}{r^2} \right), \tag{3.16b}$$

$$\frac{\partial w}{\partial t} + u\frac{\partial w}{\partial r} + w\frac{\partial w}{\partial z} = Oh^2 \left(-\frac{\partial p}{\partial z} + \frac{\partial^2 w}{\partial r^2} + \frac{1}{r}\frac{\partial w}{\partial r} + \frac{\partial^2 w}{\partial z^2} - 1 \right), \tag{3.16c}$$

where (3.16b) and (3.16c) are the components of (3.15b) in the respective r and z directions.

The combined no-slip and impermeability condition (3.3) on the liquid-solid interface remains as

$$\mathbf{u} = \mathbf{0}, \tag{3.17}$$

which can be written as

$$u = 0, \qquad w = 0, \tag{3.18}$$

and the kinematic equation (3.4) on the liquid-gas interface is

$$\frac{\partial f}{\partial t} + \mathbf{u} \cdot \nabla f = 0, \tag{3.19}$$

or

$$\left(\frac{\partial \mathbf{r}^{(1)}}{\partial t} - \mathbf{u} \right) \cdot \mathbf{n} = 0, \tag{3.20}$$

where $\mathbf{r}^{(1)}$ is a point on the free surface, which in component form is

$$n_r \left(\frac{\partial r^{(1)}}{\partial t} - u \right) + n_z \left(\frac{\partial z^{(1)}}{\partial t} - w \right) = 0, \tag{3.21}$$

where n_r and n_z are the r and z components of the unit normal to the free surface. The combined stress condition (3.6) on the liquid-gas interface is now

$$p_g \mathbf{n} + \mathbf{n} \cdot \mathbf{P} - \mathbf{n} \nabla \cdot \mathbf{n} = \mathbf{0}, \tag{3.22}$$

whilst the respective normal and tangential projections of (3.22) are

$$p_g + \mathbf{n} \cdot \mathbf{P} \cdot \mathbf{n} = \nabla \cdot \mathbf{n}, \tag{3.23a}$$

$$\mathbf{n} \cdot \mathbf{P} \cdot (\mathbf{I} - \mathbf{nn}) = \mathbf{0}, \tag{3.23b}$$

respectively, so that in terms of $\mathbf{u}$,

$$p_g - p + \mathbf{n} \cdot \left[\nabla \mathbf{u} + (\nabla \mathbf{u})^T \right] \cdot \mathbf{n} = \nabla \cdot \mathbf{n}, \tag{3.24a}$$

$$\mathbf{n} \cdot \left[\nabla \mathbf{u} + (\nabla \mathbf{u})^T \right] \cdot (\mathbf{I} - \mathbf{nn}) = \mathbf{0}. \tag{3.24b}$$

The boundary condition at the contact line (3.10) for the normal stress boundary

condition (3.24a) is now given by

$$f(r_o, 0, t) = 0, \tag{3.25}$$

where the contact angle $\theta = \theta(t)$ at the pinned contact line is then determined as a part of the solution (see Figure 3.2). Due to the axisymmetry of the problem another condition is required at the intersection of the free surface and the axis of symmetry. Therefore at the apex of the bubble ($r = 0$, $z = H$) the free surface should be smooth,

$$\nabla f \cdot \mathbf{e}_r = n_r = 0, \tag{3.26}$$

where $H = H(t)$ is the height of the bubble to also be determined as part of the solution.

On the axis of symmetry, there are the conditions of axial symmetry and smoothness of the velocity field,

$$u = 0, \qquad \frac{\partial w}{\partial r} = 0, \tag{3.27}$$

whilst far from the bubble,

$$u,\, w \to 0, \qquad r^2 + z^2 \to \infty. \tag{3.28}$$

The temporal evolution of the volume of the bubble (3.12) is given by

$$V(t) = V_i + Q\, t, \qquad t \geqslant 0, \tag{3.29}$$

and so if the free surface is described by the function $r = h(z, t)$, where $f(r, z, t) = h(z, t) - r$, then,

$$V(t) = \pi \int_{z=0}^{z=H} h^2(z, t)\, dz. \tag{3.30}$$

To conclude the problem formulation, the initial conditions for velocity (3.13) are,

$$u(r, z, 0) = 0, \qquad w(r, z, 0) = 0, \tag{3.31}$$

whilst the bubble is initially a spherical cap with volume V_i. The initial height of the bubble $H_i = H(t = 0)$ is the real solution of $\pi H_i \left(3r_o^2 + H_i^2\right) = 6V_i$ and the radius of the sphere is defined by $R_i = \left(H_i^2 + r_o^2\right)/2H_i$. The initial free surface shape is then given by

$$r^2 + \left(z + R_i - H_i\right)^2 = R_i^2, \qquad 0 \leqslant z \leqslant H_i. \tag{3.32}$$

In other words, by defining the radius of the orifice and the initial volume of the bubble, the initial shape is fully specified.

The set of equations (3.15)–(3.32) constitutes the complete dimensionless problem formulation for the formation of a bubble from an orifice in a submerged solid surface with the contact line pinned to the rim of the orifice. The problem is characterised by the three dimensionless parameters identified here; the orifice radius r_o, the Ohnesorge number Oh and the volumetric gas flow rate Q. The parameter regime of interest that will be investigated can now be described.

3.3 Parameter Regime of Interest

To estimate the parameter regime of interest, consider three typical technologically-relevant Newtonian liquids; water ($\mu = 1$ mPa s, $\rho = 998.2$ kg m^{-3}, $\sigma = 73$ mN m^{-1}), a silicone oil ($\mu = 0.01$ Pa s, $\rho = 800$ kg m^{-3}, $\sigma = 20$ mN m^{-1}) and glycerol ($\mu = 1.4$ Pa s, $\rho = 1200$ kg m^{-3}, $\sigma = 60$ mN m^{-1}). The respective length scales and Ohnesorge numbers for these three liquids are then $L = 2.73$ mm, 1.60 mm and 2.26 mm and $Oh = 2.24 \times 10^{-3}$, 6.26×10^{-2} and 3.49.

In order to investigate the full effects of these parameters, the system shall be examined using the orifice radii $r_o = 0.1$ and 1, since it is the generation of bubbles from orifice radii of the order of millimeters and below that are of interest; the Ohnesorge numbers $Oh = 2.24\times10^{-3}$, so that the case of water can be examined explicitly, and also $Oh = 10^{-2}$, 10^{-1}, 1 and 10, to cover the full range of liquid viscosity; and flow rates $10^{-6} \leqslant Q \leqslant 0.5$ for $r_o = 0.1$ and $10^{-5} \leqslant Q \leqslant 15$ for $r_o = 1$. Each simulation will be characterised by the notation (r_o, Oh, Q).

The initial volume of the bubble V_i is chosen to be sufficiently small so that, even though a smaller initial volume would slightly increase the formation time t_d, it would not alter the volume of the newly formed bubble V_d. It was seen for all simulations that an initial contact angle of $\theta(0) = 3\pi/4$ is suitable to fulfill this criterion and so the initial volumes for the cases of $r_o = 0.1$ and 1 are $V_i = 6.89 \times 10^{-4}$ and 6.89×10^{-1}, respectively.

The length and velocity scales used here could differ from those which the reader may have encountered in similar works where the Bond, Ohnesorge and Weber or capillary numbers are used. A guide on how to rescale the results presented in this thesis can be found in Appendix A.

3.4 Summary

In this chapter, the modelling of the formation of a bubble from an orifice in a submerged solid surface with the contact line pinned to the rim of the orifice was discussed. The complete dimensional problem formulation (3.1)–(3.13) was set out before the dimensionless problem formulation (3.15)–(3.32) with governing equations, boundary conditions and initial conditions was fully specified. The regime of parameters to be investigated was defined. In the next chapter, the construction of the numerical platform used to solve this system of equations (3.15)–(3.32) is described in detail.

Chapter 4

The Numerical Platform

In this chapter, the numerical platform used to simulate the formation of a bubble by solving the dimensionless system of equations (3.15)–(3.32), is described. A computational method is required to solve this system due to its mathematical complexity, with gravitational, viscous, inertial and capillarity forces all present in an unsteady free-boundary problem.

The platform has been designed so that it can be easily adapted to simulate more complex processes such as the formation of a bubble with a moving contact line (see Chapter 7) and the formation of a compound drop (see Chapter 8), which involves an additional liquid phase and a liquid-liquid interface.

The computational framework used here is based on a formulation described in detail in Sprittles & Shikhmurzaev (2012c, 2013), where a user-friendly step-by-step guide to its implementation can be found alongside numerous benchmark calculations. However the details are reproduced here for ease of future reference.

4.1 Choice of Numerical Method

In general, numerical methods solve a system of partial differential equations by discretizing these equations. Methods other than global spectral methods employ spatial discretisation over several points in the domain, commonly known as nodes. An approximate solution is then found at each node. The difference between the various numerical methods is how the equations are discretized and how the solution is approximated.

As stated in Section 2.3, various numerical methods have been used to simulate the formation of a bubble with a pinned contact line, namely, the finite difference method (Marmur & Rubin, 1976; Pinczewski, 1981; Tan & Harris, 1986; Terasaka & Tsuge, 1990, 1993), boundary integral method (Hooper, 1986; Oğuz & Prosperetti, 1993; Xiao & Tan, 2005; Wong *et al.*, 1998) and volume-of-fluid method (Buwa *et al.*, 2007; Gerlach *et al.*, 2007; Chakraborty *et al.*, 2009; Ohta *et al.*, 2011; Chakraborty *et al.*, 2011; Albadawi *et al.*, 2013; Ma *et al.*, 2012).

The numerical method chosen to solve the current problem, and also those described in Chapters 7 & 8, must satisfy the following criteria:

1. Solve the unsteady Navier-Stokes equations (3.15)

2. Capture the complex geometries encountered during the formation of a bubble and drop

3. Accurately resolve all scales of the problem so that global characteristics of the flow, such as the volume of the bubble formed, as well as small-scale characteristics, such as the pinch-off process, can be extracted

The boundary integral method has the advantage of decreasing the dimensionality of the problem by one and, therefore, reducing the complexity of the problem and lessening the computational burden. However the boundary integral method cannot be used to solve the Navier-Stokes equations and so fails to meet criterion (1).

The finite difference method is the simplest and oldest of these methods. However, the method's simplicity is off-set by the difficulties it faces when it is necessary to accurately track moving boundaries of the flow domain and especially when the resolution of small scales near the moving boundaries is required. Therefore it fails to satisfy criteria (2) and (3).

The volume-of-fluid method is more suitable in capturing complex geometries exhibited by the flow domain. It uses the finite difference or finite volume method to solve the Navier-Stokes equations and can handle the topological changes associated with the break up of the bubble in a simple manner. However, as noted in Eggers & Villermaux (2008), there is no guarantee that the physics associated with this transition, during the pinch-off and subsequent break-up of the bubble, has been properly accounted for as the volume-of-fluid method implements the topological change numerically rather than physically. This is a problem especially when the size of forming bubbles is small.

These deficiencies can be addressed by the finite element method which has previously been used to capture inherently multiscale flows in dynamic wetting (Wilson *et al.*, 2006; Sprittles & Shikhmurzaev, 2013) and in the coalescence of liquid drops (Sprittles & Shikhmurzaev, 2012a), amongst other free-boundary problems (Christodoulou & Scriven, 1992; Fukai *et al.*, 1993; Cairncross *et al.*, 2000; Sprittles & Shikhmurzaev, 2012b, 2014). Moreover, it can easily be applied to the bubble formation phenomenon so that the full Navier-Stokes equations are solved and the complex geometries encountered during the bubble formation process are handled with ease as all elements, over which the solution is constructed, are mapped to a master element. Where additional precision is required in areas of the flow domain where large gradients in the solution exist, smaller elements can be used to resolve the physics there.

Unlike the pinch-off of the bubble, simulating the actual break-up of the bubble into two parts is much more simple with the volume-of-fluid method than with the finite

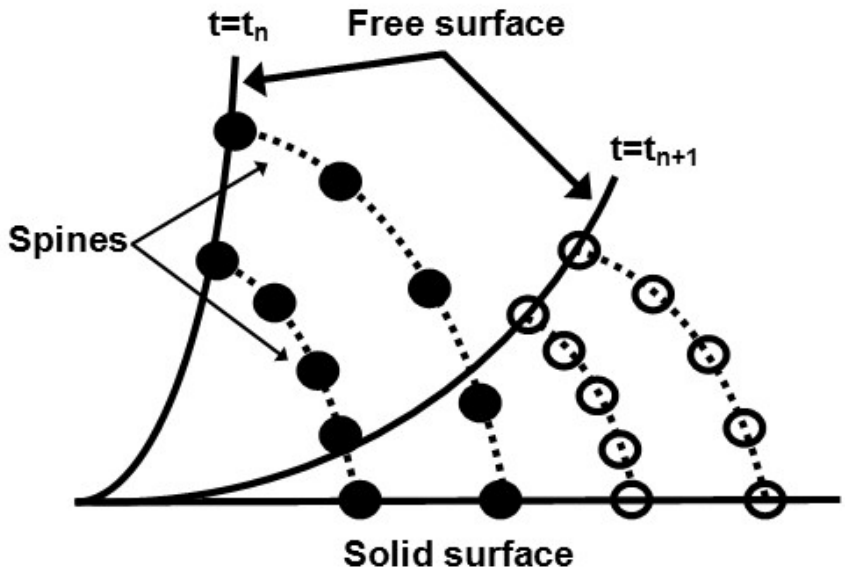

Figure 4.1: A sketch displaying how spines and nodes evolve as the free surface evolves in time.

element method. However, the break-up of the bubble is beyond the scope of this thesis and since the pinch-off process must be captured accurately, the numerical platform will be based on the finite element method.

4.2 Overview of The Finite Element Method

As is standard in the finite element method (Gresho & Sani, 1998), the system of equations is discretised over a set of nodes that are distributed throughout the finite computational flow domain. The method is based on the notion of tessellating a finite number of non-overlapping elements about these nodes to form a computational mesh. The global solution is constructed from the local solutions associated with each element and interpolation functions are used to find the solution at any point between the nodes. A historical review of the finite element method is given by Gupta & Meek (1996) and a detailed introduction can be found in Reddy (1993).

The design of the mesh is a key aspect of the finite element based computational framework. Two questions now arise. How are the nodes positioned in the computational domain? And how will the nodes evolve in time as the free surface evolves? The 'method of spines' (Kistler & Scriven, 1983) is an Arbitrary Lagrangian-Eulerian (ALE) method where nodes are distributed along the free surface to define it explicitly (see Figure 4.1). Meanwhile, each node in the bulk belongs to a so-called spine that runs from a free surface node to another boundary of the flow domain. As the free surface evolves in time from $t = t_n$ to $t = t_{n+1}$, the free surface nodes move along the free surface whilst the nodes in the bulk move in a prescribed manner. This structured meshing technique allows the movement of the nodes to be controlled so that the elements, tessellated about these nodes, remain non-degenerate.

In order to use the ALE approach, the Navier-Stokes equations (3.15b) are amended to include the mesh velocity $\frac{\partial \mathbf{r}}{\partial t}$ since the nodes evolve in time and carry information about the flow variables with them,

$$\frac{\partial \mathbf{u}}{\partial t} + \left(\mathbf{u} - \frac{\partial \mathbf{r}}{\partial t} \right) \cdot \nabla \mathbf{u} = Oh^2 \left(\nabla \cdot \mathbf{P} - \mathbf{e}_z \right), \tag{4.1}$$

where $\mathbf{u}$ is the velocity at the point $\mathbf{r}$ in the computational domain (Jimack & Wathen, 1991).

4.3 Far Field Boundary Conditions

The problem is formulated in an infinite domain ($r \geqslant 0$, $z \geqslant 0$) with boundary conditions (3.28) prescribed in the 'far-field'. In order to apply the finite element method, the flow domain must be truncated to a finite size. Therefore, a side boundary ($r = R$, $0 \leqslant z \leqslant Z$) and a top boundary ($0 \leqslant r \leqslant R$, $z = Z$) are constructed on which amended 'passive' boundary conditions are applied. To ensure these amended conditions are indeed passive,

R and Z are set large enough so that any increase in their values does not affect the growth of the bubble.

To find the appropriate passive boundary conditions, define the spherical coordinates $(\check{r}, \check{\theta}, \check{\varphi})$ and consider the far field-boundary as a hemisphere that encloses the bubble. The boundary conditions originate from viewing the bubble as a three-dimensional point source, the velocity field of which is spherically symmetric, i.e. there is no dependence on $\check{\theta}$ nor $\check{\varphi}$, and the radial component of velocity $u_{\check{r}}$ is proportional to $\frac{1}{\check{r}^2}$. Therefore, two conditions on the far field boundary in the $(\check{r}, \check{\theta})$-plane are

$$u_{\check{\theta}} = 0, \qquad \frac{\partial}{\partial \check{r}} \left(\check{r}^2 u_{\check{r}} \right) = 0. \tag{4.2}$$

Converting these conditions back to cylindrical polar coordinates, in which the problem is formulated, gives respectively,

$$rw - zu = 0, \tag{4.3a}$$

$$2\left(ru + zw\right) + r^2 \frac{\partial u}{\partial r} + rz\left(\frac{\partial u}{\partial z} + \frac{\partial w}{\partial r}\right) + z^2 \frac{\partial w}{\partial z} = 0, \tag{4.3b}$$

which will replace (3.28) in the dimensionless problem formulation.

In addition to this, as the bubble grows, the size of the flow domain decreases since the free surface is the only boundary of the flow domain that is not fixed in place. The application of the continuity equation (3.15a) in the finite element framework ensures incompressibility in the flow domain, however the 'level' of the pressure field could be arbitrarily large or small if it is not fixed at some point. Therefore a 'reference' pressure of the liquid must be prescribed at a particular point for the entire simulation. This arbitrary reference pressure should not affect the growth of the bubble and so the straightforward choice would be to base this pressure on the assumption that the pressure field along the side boundary should remain hydrostatic, $p(R, z, t) = -z$, for the entire simulation. When $p(R, 0, t) = 0$ is applied as the reference pressure, the point $(R, 0)$ behaves like a point

sink which affects the velocity field close to the bubble. As this is far from acceptable,

$$p(R, Z, t) = -Z, \tag{4.4}$$

is applied instead and this approach ensures the velocity field remains regular. With the values of R and Z set large enough (see Section 5.2), the pressure field along the side boundary remains hydrostatic for the entire solution.

4.4 Mesh Design

The design of the computational mesh is very important to successfully simulate the formation of a bubble. The mesh must handle the growth of the bubble as it expands whilst the size of the flow domain decreases. The mesh should be sufficiently refined near the bubble to adequately capture the physics there and yet the problem should remain computationally tractable with elements increasing in size away from the bubble where variables vary on a larger spatial scale. Additional refinement may also be required within the already refined region and so the design of the mesh should be flexible enough to cater for this.

The mesh must also be able to handle the full range of shapes that the bubble may take, from early deformation of the free surface near the contact line to the thinning of the neck during pinch-off. The mesh must evolve in such a way as to ensure that the elements do not become too stretched or deformed, as this lowers accuracy and can prevent the finite element method converging to a solution. Finally, the meshing strategy must be so well-defined as to not require remeshing at any stage of the simulation as this can have an adverse effect on accuracy.

Let the total number of nodes in the computational domain V be denoted by N and the number of nodes distributed along the free surface A_1, solid surface A_2, side boundary

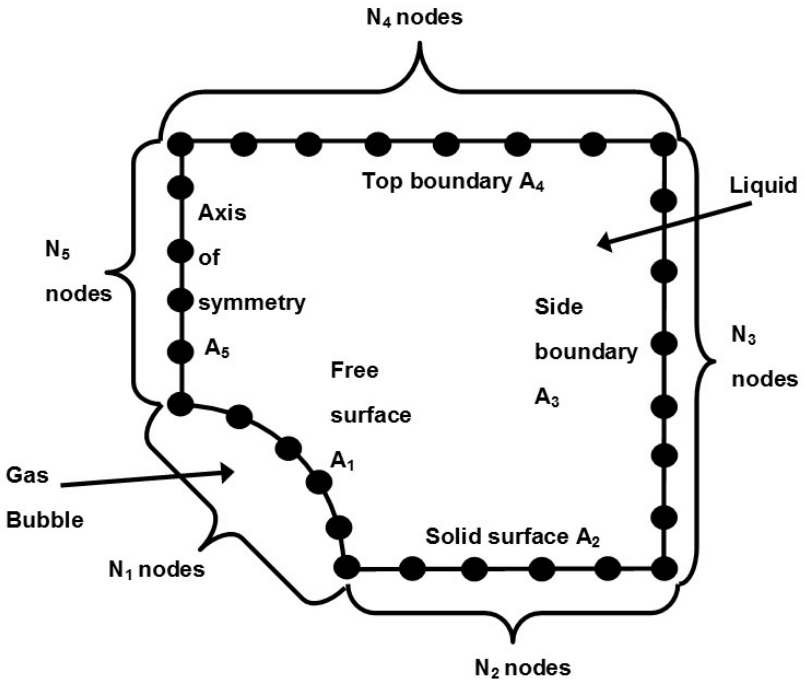

Figure 4.2: A sketch of the nodes distributed along the boundaries of the flow domain.

A_3, top boundary A_4 and axis of symmetry A_5 be N_1, N_2, N_3, N_4 and N_5, respectively (see Figure 4.2). One node can belong to two boundaries, for example the node at the contact line belongs to both the free surface and the solid surface. Each node in the domain is labelled with a global node number I, where $I = 1, ..., N$, and has the coordinates $\mathbf{x}_I = (r_I, z_I)$. The set X consists of all the global node numbers whilst X_1, X_2, X_3, X_4 and X_5 consist of all global node numbers for nodes on distributed along the free surface, solid surface, side boundary, top boundary and axis of symmetry, respectively. In addition, nodes distributed along the free surface also have the coordinates $\mathbf{x}_J^{(1)} = (r_J^{(1)}, z_J^{(1)})$ where $J = 1, ..., N_1$. The Jth node distributed along the free surface has the global number I denoted by the Jth entry in the vector $X^{(1)}$ and so $I = X_J^{(1)}$.

4.4.1 Structure of the Mesh

A specially-designed arrangement of spines is required adjacent to the neck of the bubble in order to accurately capture the shape of the thinning neck during pinch-off. In contrast, the shape of the detaching bubble above the neck is much simpler to handle. The mesh will therefore consist of two distinct regions; the pinch-off region and the detachment region (See Figure 4.3). Nodes in the detachment region will travel along straight spines which run from the free surface to the side and top domain boundaries, whilst spines in the pinch-off region run from the free surface to the solid surface and side boundary and are designed using a bipolar coordinate system with a focus at the contact line (see Appendix B). Therefore, near the contact line, the mesh is bipolar whilst further away it can match with the straight spines in the detachment region.

Each of the N_1 nodes positioned on the free surface, with coordinates $(r_J^{(1)}, z_J^{(1)})$, can be characterised by a pair of free surface unknowns (χ_J, ζ_J) for $J = 1, ..., N_1$. The first node on the free surface is located at the contact line. The coordinates in the (r, z)-plane in terms of the free surface unknowns are given by the simple transformation

$$r_1^{(1)} = \zeta_1 = r_c, \tag{4.5a}$$

$$z_1^{(1)} = \chi_1 = 0, \tag{4.5b}$$

where the r-coordinate of the node at the contact line is also denoted by r_c.

An important spine in the mesh is the horizontal spine that separates the pinch-off region from the detachment region. Let this be the Sth spine and so, including the contact line, there are $S - 1$ nodes distributed along the free surface in the pinch-off region, and $N_1 - S$ nodes distributed along the free surface in the detachment region. The position

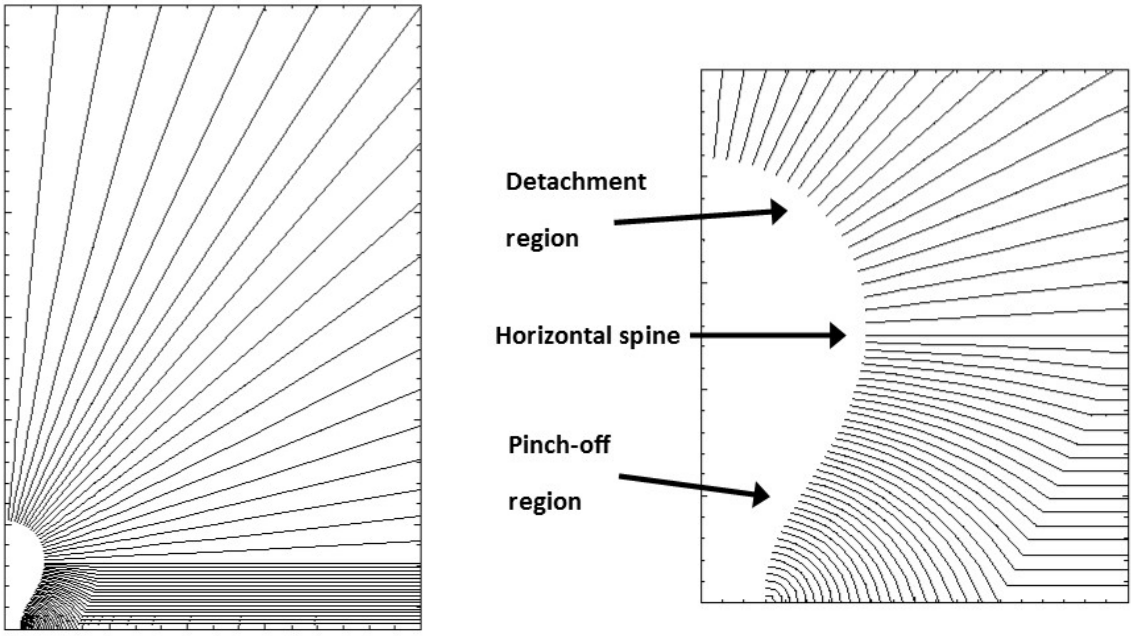

(a) The position of the spines for the entire mesh.

(b) A close up of the bubble.

Figure 4.3: The design of the spines in the detachment and pinch-off regions adjacent to the bubble.

of the free surface node on the Sth spine in terms of the free surface unknowns is

$$r_S^{(1)} = \zeta_S, \tag{4.6a}$$

$$z_S^{(1)} = \chi_S. \tag{4.6b}$$

The coordinates of the remaining $S-2$ nodes distributed along the free surface in the pinch-off region are related to the corresponding free surface unknowns by the transfor-

mations (see Appendix B),

$$r_J^{(1)} = \zeta_1 + \frac{\chi_S \sin\zeta_J}{\cosh\chi_J + \cos\zeta_J}, \tag{4.7a}$$

$$z_J^{(1)} = \chi_S + \frac{\chi_S \sinh\chi_J}{\cosh\chi_J + \cos\zeta_J}, \tag{4.7b}$$

and

$$\chi_J = \text{arctanh}\left(\frac{2(z_J^{(1)} - \chi_S)\chi_S}{\chi_S^2 + (z_J^{(1)} - \chi_S)^2 + (r_J^{(1)} - \zeta_1)^2}\right), \tag{4.8a}$$

$$\zeta_J = \arctan\left(\frac{2(r_J^{(1)} - \zeta_1)\chi_S}{\chi_S^2 - (z_J^{(1)} - \chi_S)^2 - (r_J^{(1)} - \zeta_1)^2}\right), \tag{4.8b}$$

where $J = 2, ..., S-1$.

The coordinates of the $N_1 - S$ nodes distributed along the free surface in the detachment region are related to the corresponding free surface unknowns by the transformations

$$r_J^{(1)} = \zeta_J \cos\chi_J, \tag{4.9a}$$

$$z_J^{(1)} = \chi_S + \zeta_J \sin\chi_J, \tag{4.9b}$$

and

$$\chi_J = \arctan\left(\frac{z_J^{(1)}}{r_J^{(1)}}\right), \tag{4.10a}$$

$$\zeta_J = \sqrt{\left(r_J^{(1)}\right)^2 + \left(z_J^{(1)} - \chi_S\right)^2}, \tag{4.10b}$$

where $J = S+1, ..., N_1 - 1$. Finally, the position of the node at the apex of the bubble is

given by,

$$r_{N_1}^{(1)} = \chi_{N_1} = 0, \tag{4.11a}$$

$$z_{N_1}^{(1)} = \chi_S + \zeta_{N_1}. \tag{4.11b}$$

All other nodes in the computational mesh lie on one and only one of the spines in either the pinch-off or detachment region. Consequently, the position of any node that lies on the same spine as the Jth free surface node, $J = 1, ..., N_1$, is dependent on the position of the Jth free surface node, $(r_J^{(1)}, z_J^{(1)})$, and therefore dependent on the free surface unknowns (χ_J, ζ_J). The free surface unknowns will be determined by the manner in which the nodes are distributed along the free surface which is discussed in Section 4.12. Once the positions of the nodes are known, a finite number of elements can be tessellated around these nodes to complete the computational mesh.

4.4.2 Elements

Let the number of elements tessellated about the nodes in the computational mesh be denoted by N_e. In two dimensions, elements are generally triangular or quadrilateral and also differ by the number of nodes they contain. During bubble formation, the contact line region can resemble a corner and so it seems sensible to use triangular elements here. For simplicity, triangular elements will be used throughout the mesh. The triangular elements are also required to have curved sides so that the free surface can be captured at least quadratically.

The choice of which type of element to tessellate around the nodes is very important as the Ladyzhenskaya-Babuška-Brezzi (LBB) stability condition (Aziz, 1972) must be satisfied to ensure the stability of the system of equations to be solved. To satisfy the LBB stability condition, the pressure field has to interpolated by a polynomial of one

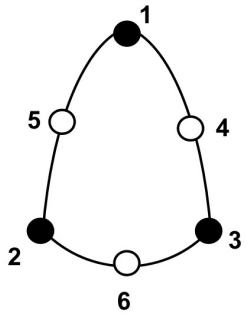

Figure 4.4: The Taylor-Hood V6P3 element with the local node numbers.

degree less than the velocity field.

The element used here will be the Taylor-Hood V6P3 element which has been used successfully in many similar studies (Sprittles & Shikhmurzaev, 2012c, 2013; Lukyanov & Shikhmurzaev, 2007). These triangular elements consist of six nodes, one at each vertex and one along each curved side (see Figure 4.4). These nodes at each vertex are locally numbered anticlockwise as $i = 1, 2, 3$ whilst the nodes on the curved sides of the element are numbered as $i = 4, 5, 6$. The pressure field is approximated bi-linearly by locally interpolating the pressure at the three vertex nodes, whilst the velocity field is approximated bi-quadratically by locally interpolating the velocity at all six nodes. The free surface is captured quadratically by the three nodes that make up one side of the element. Due to the isoparametric mapping to a master element (see Section 4.13), there are no additional difficulties in dealing with this curved-sided element rather than a straight-sided element.

Since the pressure field is found at fewer nodes than the velocity field, let the number of nodes at which the pressure field is approximated be denoted by N_p. The coordinates of these nodes can also be denoted by $\mathbf{x}_J^{(p)} = \left(r_J^{(p)}, z_J^{(p)}\right)$ where $J = 1, ..., N_p$. The Jth pressure node has the global number I denoted by the Jth entry in the vector X^p and so $I = X_J^p$.

Figure 4.5 shows how the elements are tessellated around the nodes with elements

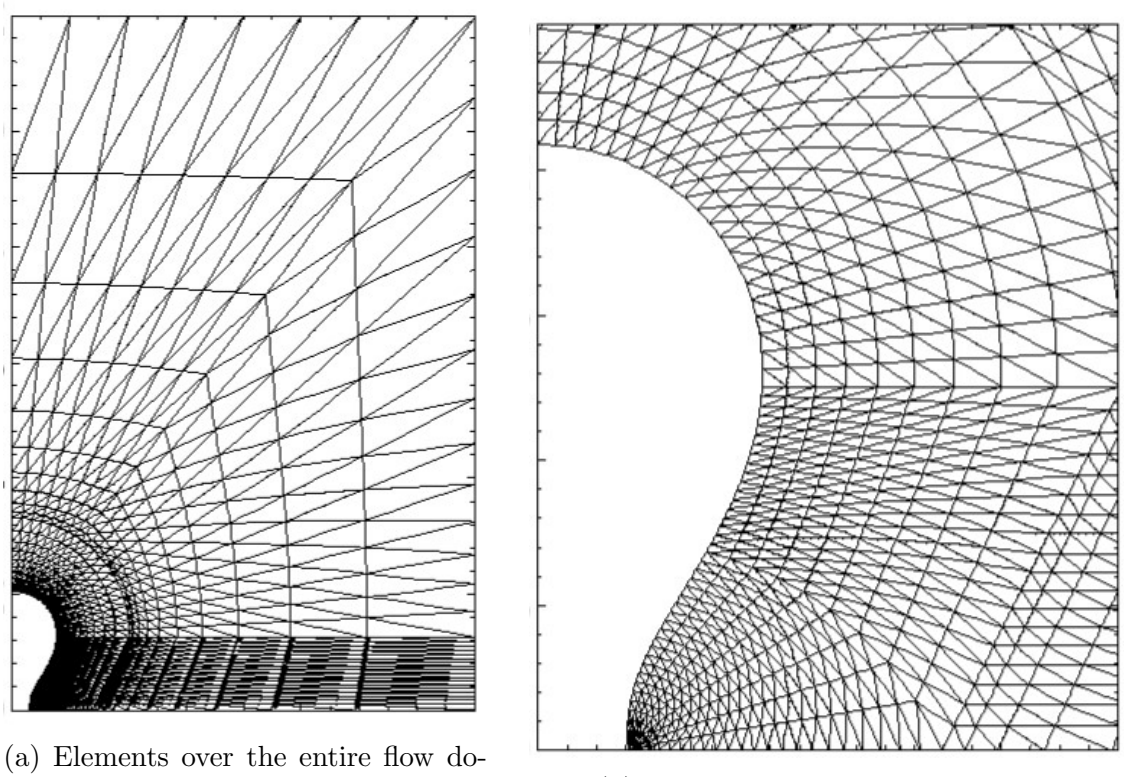

(a) Elements over the entire flow domain.

(b) Elements adjacent to the bubble.

Figure 4.5: The arrangement of V6P3 elements throughout the computational domain.

increasing in size away from the bubble. Neighbouring elements share nodes which ensures the continuity of the velocity and pressure fields from one element to another as the global solution is constructed from local contributions from each element. The next step is to find the weak form of the governing equations.

4.5 Weak Form of the Governing Equations

All of the unknowns that need to be found at every time step have now been identified. These are:

- Both components of velocity, $u_I(r_I, z_I, t)$ and $w_I(r_I, z_I, t)$, where $I = 1, ..., N$, at

every node in the flow domain

- The pressure field, $p_I(r_I^{(p)}, z_I^{(p)}, t)$, where $I = 1, ..., N_p$, at every pressure node in the flow domain
- The two free surface unknowns, χ_I and ζ_I where $I = 1, ..., N_1$, at every node distributed along the free surface
- The spatially uniform gas pressure, $p_g(t)$

Since there are $N_T = 2(N + N_1) + N_p + 1$ unknowns, then N_T equations are required to determine the unknowns.

Suppose the velocity components $u(r, z, t)$ and $w(r, z, t)$, pressure field $p(r, z, t)$, and free surface $r = h(z, t)$, where the function h is dependent on all the free surface unknowns, χ_I and ζ_I, for $I = 1, ..., N_1$, are approximated by the corresponding functions $u^*(r, z, t)$, $w^*(r, z, t)$, $p^*(r, z, t)$, and $h^*(z, t)$. Substituting these approximations into the Navier-Stokes equations (3.15) and kinematic condition (3.20) will result in the following residual errors,

$$\nabla \cdot \mathbf{u}^* = r^C, \tag{4.12a}$$

$$\mathbf{e}_\alpha \cdot \left[\frac{\partial \mathbf{u}^*}{\partial t} + \left(\mathbf{u}^* - \frac{\partial \mathbf{r}^*}{\partial t} \right) \cdot \nabla \mathbf{u}^* + Oh^2 \left(\mathbf{e}_z - \nabla \cdot \mathbf{P}^* \right) \right] = r^{M,\alpha}, \tag{4.12b}$$

$$\left(\frac{\partial \mathbf{r}^{(1)*}}{\partial t} - \mathbf{u}^* \right) \cdot \mathbf{n}^* = r^K, \tag{4.12c}$$

where $\mathbf{P}^* = -p^* + \nabla \mathbf{u}^* + (\nabla \mathbf{u}^*)^T$ and $\alpha = r$ or z to generate the r or z component of (4.12b).

The method of weighted residuals is used to minimize the residual errors (4.12) spatially over the domains on which they are defined. Each residual error is multiplied by an

arbitrary test function W and then integrated over the domain to which it applies,

$$R^C = \int_V W^C(r,z) r^C(r,z,t)\, dV, \tag{4.13a}$$

$$R^{M,\alpha} = \int_V W^M(r,z) r^{M,\alpha}(r,z,t)\, dV, \tag{4.13b}$$

$$R^K = \int_{A_1} W^K(r,z) r^K(r,z,t)\, dA_1. \tag{4.13c}$$

By the fundamental lemma of variational calculus, if the test functions are continuously differentiable over the domains on which they are applied then the weighted residuals (4.13) are zero and so the approximate solutions solve exactly the weak form of the governing equations given by

$$R^C = 0, \qquad R^{M,\alpha} = 0, \qquad R^K = 0. \tag{4.14}$$

This weak form of the governing equations can now be discretized.

4.6 The Galerkin Method

The Galerkin method is used to discretize the weak form of the governing equations (4.14) by replacing the arbitrary test function in each equation with a finite set of test functions. The velocity and pressure fields are approximated by the respective trial solutions,

$$\mathbf{u}(r,z,t) = \sum_{J=1}^{N} \mathbf{u}_J(t)\phi_J(r,z), \tag{4.15a}$$

$$p(r,z,t) = \sum_{J=1}^{N_p} p_J(t)\psi_J(r,z), \tag{4.15b}$$

which are linear combinations, over all the nodes at which the variable is to be found, of the two-dimensional global interpolation functions (ϕ_J, ψ_J) and the nodal values (p_J, $\mathbf{u}_J$) of the variables. To ensure that the Jth nodal value of a variable is indeed the value of the variable at the Jth node, the global interpolation functions take the value 1 at the node they are associated with and 0 at all other nodes so that,

$$\phi_J(\mathbf{x}_I) = \delta_{IJ}, \qquad I, J = 1, ..., N, \tag{4.16a}$$

$$\psi_J(\mathbf{x}_I^{(p)}) = \delta_{IJ}, \qquad I, J = 1, ..., N_p. \tag{4.16b}$$

The free surface shape is parameterised by the arc length s and is approximated by the trial solution,

$$\mathbf{r}^{(1)}(s) = \sum_{J=1}^{N_1} \mathbf{r}_J^{(1)} \phi_{1,J}(s), \tag{4.17}$$

where $\phi_{1,J}$ are the one-dimensional global interpolation functions such that,

$$\phi_{1,J}\left(s\left(r_I^{(1)}, z_I^{(1)}\right)\right) = \delta_{IJ}, \qquad I, J = 1, ..., N_1. \tag{4.18}$$

By replacing the arbitrary test functions in (4.13) with this finite set of interpolation functions, the weak form of the governing equations (4.14) can be discretised as follows,

$$R_I^C = \int_V \psi_I(r, z) r^C \, dV = 0, \qquad I = 1, ..., N_p, \tag{4.19a}$$

$$R_I^{M,\alpha} = \int_V \phi_I(r, z) r^{M,\alpha} \, dV = 0, \qquad I = 1, ..., N, \tag{4.19b}$$

$$R_I^K = \int_{A_1} \phi_{1,I}(s) r^K \, dA_1 = 0, \qquad I = 1, ..., N_1. \tag{4.19c}$$

These equations are referred to as the continuity residuals, the momentum residuals and the kinematic residuals, respectively, and can be written in full as

$$R_I^C = \int_V \psi_I(r,z)\left(\nabla \cdot \mathbf{u}\right) dV, \qquad I = 1, ..., N_p, \tag{4.20a}$$

$$R_I^{M,\alpha} = \int_V \phi_I(r,z)\mathbf{e}_\alpha \cdot \left[\frac{\partial \mathbf{u}}{\partial t} + \left(\mathbf{u} - \frac{\partial \mathbf{r}}{\partial t}\right) \cdot \nabla \mathbf{u} + Oh^2\left(\mathbf{e}_z - \nabla \cdot \mathbf{P}\right)\right] dV, \qquad I = 1, ..., N, \tag{4.20b}$$

$$R_I^K = \int_{A_1} \phi_{1,I}(s)\left(\frac{\partial \mathbf{r}^{(1)}}{\partial t} - \mathbf{u}\right) \cdot \mathbf{n}\, dA_1, \qquad I = 1, ..., N_1, \tag{4.20c}$$

where the velocity field, pressure field and free surface shape are approximated by (4.15a), (4.15b) and (4.17), respectively.

The next step is to incorporate the boundary conditions into these governing residuals to obtain the complete discrete problem formulation.

4.7 Implementation of the Boundary Conditions

Having derived the discretized weak form of the governing equations (4.20) using the method of weighted residuals and then the Galerkin method, the remaining boundary conditions are applied to obtain the complete discrete formulation. Boundary conditions fall into two categories, natural or essential.

Natural boundary conditions are incorporated into the discrete formulation by manipulating the governing residuals (4.20) into a form in which the boundary condition can be substituted and therefore applied 'naturally'. When it is not possible to incorporate a

boundary condition naturally then it must be applied as an essential condition. In this case, the contribution at a particular node from the governing residual is removed and the boundary condition is applied instead.

Consider the combined stress boundary condition (3.22) on the free surface. With the following identity for the stress tensor,

$$\nabla\left(\phi_I \mathbf{e}_\alpha\right) : \mathbf{P} = \nabla \cdot \left(\phi_I \mathbf{e}_\alpha \cdot \mathbf{P}\right) - \phi_I \mathbf{e}_\alpha \cdot \nabla \cdot \mathbf{P}, \tag{4.21}$$

then by the divergence theorem,

$$\begin{aligned} -\int_V \phi_I \mathbf{e}_\alpha \cdot \nabla \cdot \mathbf{P}\, dV &= \int_V \nabla\left(\phi_I \mathbf{e}_\alpha\right) : \mathbf{P}\, dV - \int_V \nabla \cdot \left(\phi_I \mathbf{e}_\alpha \cdot \mathbf{P}\right)\, dV \\ &= \int_V \nabla\left(\phi_I \mathbf{e}_\alpha\right) : \mathbf{P}\, dV + \int_A \phi_{1,I} \mathbf{e}_\alpha \cdot \mathbf{P} \cdot \mathbf{n}\, dA, \end{aligned} \tag{4.22}$$

where A represents all boundaries that enclose V. The momentum residual (4.20b) is rewritten as,

$$R_I^{M,\alpha} = \left(R_I^{M,\alpha}\right)_V + \left(R_I^{M,\alpha}\right)_A, \qquad I = 1, ..., N, \tag{4.23}$$

where,

$$\left(R_I^{M,\alpha}\right)_V = \int_V \left\{ \phi_I \mathbf{e}_\alpha \cdot \left[\frac{\partial \mathbf{u}}{\partial t} + \left(\mathbf{u} - \frac{\partial \mathbf{r}}{\partial t} \right) \cdot \nabla \mathbf{u} + Oh^2 \mathbf{e}_z \right] + Oh^2 \nabla\left(\phi_I \mathbf{e}_\alpha\right) : \mathbf{P} \right\} dV, \tag{4.24a}$$

$$\left(R_I^{M,\alpha}\right)_A = Oh^2 \int_A \phi_{1,I} \mathbf{e}_\alpha \cdot \mathbf{P} \cdot \mathbf{n}\, dA, \tag{4.24b}$$

are the respective volume and surface contributions to the momentum residual. The surface contribution (4.24b) is clearly of stress type and so by considering the free surface

contribution to this integral and substituting (3.22),

$$\begin{aligned}\left(R_I^{M,\alpha}\right)_{A_1} &= Oh^2 \int_{A_1} \phi_{1,I}\mathbf{e}_\alpha \cdot \mathbf{P} \cdot \mathbf{n}\, dA_1 \\ &= Oh^2 \int_{A_1} \phi_{1,I}\mathbf{e}_\alpha \cdot (\mathbf{n}\nabla \cdot \mathbf{n} - p_g\mathbf{n})\; dA_1. \end{aligned} \tag{4.25}$$

By the following identity,

$$\begin{aligned}\phi_{1,I}\mathbf{e}_\alpha \cdot (\mathbf{n}\nabla \cdot \mathbf{n}) &= -\phi_{1,I}\mathbf{e}_\alpha \cdot \nabla^s \cdot (\mathbf{I} - \mathbf{nn}) \\ &= \nabla^s \cdot (\phi_{1,I}\mathbf{e}_\alpha) - \nabla^s \cdot [\phi_{1,I}\mathbf{e}_\alpha \cdot (\mathbf{I} - \mathbf{nn})]\,, \end{aligned} \tag{4.26}$$

where $\nabla^s = (\mathbf{I} - \mathbf{nn}) \cdot \nabla$ is the surface gradient operator, and the surface divergence theorem (Aris, 2012), then

$$\begin{aligned}\int_{A_1} \phi_{1,I}\mathbf{e}_\alpha \cdot (\mathbf{n}\nabla \cdot \mathbf{n})\; dA_1 &= \int_{A_1} \{\nabla^s \cdot (\phi_{1,I}\mathbf{e}_\alpha) - \nabla^s \cdot [\phi_{1,I}\mathbf{e}_\alpha \cdot (\mathbf{I} - \mathbf{nn})]\}\; dA_1 \\ &= \int_{A_1} \nabla^s \cdot (\phi_{1,I}\mathbf{e}_\alpha)\; dA_1 + \int_{L_c} \phi_{1,I}\mathbf{e}_\alpha \cdot \mathbf{m}_1\, dL_c, \end{aligned} \tag{4.27}$$

where integration over L_c is along the contact line and the vector $\mathbf{m}_1 = \cos\theta\mathbf{e}_r + \sin\theta\mathbf{e}_z$ is the vector inwardly tangent to A_1 and normal to the contact line (see Figure 4.6). This is equivalent to the tangent vector to the free surface at the contact line.

The momentum residual (4.23) now has the volume, free surface and contact line contributions,

$$R_I^{M,\alpha} = \left(R_I^{M,\alpha}\right)_V + \left(R_I^{M,\alpha}\right)_{A_1} + \left(R_I^{M,\alpha}\right)_L, \qquad I = 1, ..., N, \tag{4.28}$$

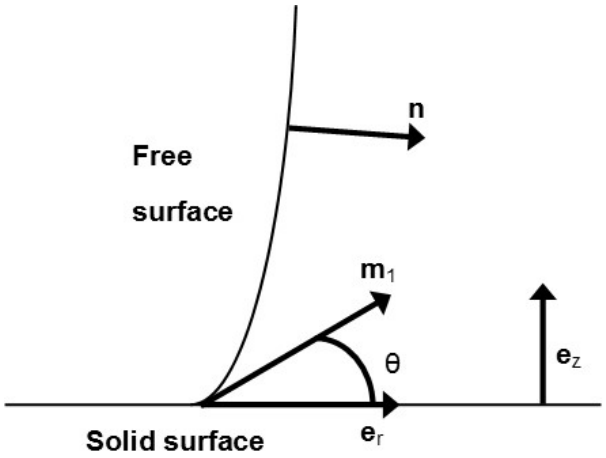

Figure 4.6: A sketch of the contact line region.

given by,

$$\left(R_I^{M,\alpha}\right)_V = \int_V \left\{\phi_I \mathbf{e}_\alpha \cdot \left[\frac{\partial \mathbf{u}}{\partial t} + \left(\mathbf{u} - \frac{\partial \mathbf{r}}{\partial t}\right) \cdot \nabla \mathbf{u} + Oh^2 \mathbf{e}_z\right] + Oh^2 \nabla \left(\phi_I \mathbf{e}_\alpha\right) : \mathbf{P}\right\} dV, \tag{4.29a}$$

$$\left(R_I^{M,\alpha}\right)_{A_1} = Oh^2 \int_{A_1} \left[\nabla^s \cdot \left(\phi_{1,I} \mathbf{e}_\alpha\right) - p_g \left(\phi_{1,I} \mathbf{e}_\alpha \cdot \mathbf{n}\right)\right] dA_1, \tag{4.29b}$$

$$\left(R_I^{M,\alpha}\right)_L = Oh^2 \int_{L_c} \phi_{1,1} \mathbf{e}_\alpha \cdot \left(\cos\theta \mathbf{e}_r + \sin\theta \mathbf{e}_z\right) dL_c. \tag{4.29c}$$

On the axis of symmetry there are the conditions of axial symmetry and smoothness of the velocity field (3.27). The second of these makes no additional contribution to the momentum residual (4.28) whilst the first must be applied as an essential condition. Since this condition is of Dirichlet type, it is applied in a pointwise manner. The r-component of the momentum residual is replaced at every node along the axis of symmetry, including the node at the apex of the bubble, with

$$R_I^{M,r} = u_I, \qquad I \in X_5. \tag{4.30}$$

On the solid surface, there are the no-slip and impermeability conditions (3.18). Once again this condition is of Dirichlet type and so at every node on the solid surface, the r-component of the momentum residual is replaced by

$$R_I^{M,r} = u_I, \qquad I \in X_2, \tag{4.31}$$

and the z-component of the momentum residual is replaced by

$$R_I^{M,z} = w_I, \qquad I \in X_2. \tag{4.32}$$

The contribution from the contact line (4.29c) is therefore discounted since neither the r nor z component of (4.28) is applied there.

The boundary conditions on the side and top boundaries (4.3) are not of Dirichlet type and therefore must be incorporated into the framework of the method of weighted residuals and then discretised using the Galerkin method. On the side boundary, the r and z components of the momentum residual (4.28) are replaced by,

$$\left(R_I^{M,r}\right)_{A_3} = \int_{A_3} \phi_{1,I}(z)\,(Rw - zu)\; dA_3, \tag{4.33a}$$

$$\left(R_I^{M,z}\right)_{A_3} = \int_{A_3} \phi_{1,I}(z) \left[2\,(Ru + zw) + R^2\frac{\partial u}{\partial r} + Rz\left(\frac{\partial u}{\partial z} + \frac{\partial w}{\partial r}\right) + z^2\frac{\partial w}{\partial z}\right] dA_3, \tag{4.33b}$$

whilst on the top boundary, the r and z components of the momentum residual are replaced by,

$$\left(R_I^{M,r}\right)_{A_4} = \int_{A_4} \phi_{1,I}(r)\,(rw - Zu)\; dA_4, \tag{4.34a}$$

$$\left(R_I^{M,z}\right)_{A_4} = \int_{A_4} \phi_{1,I}(r) \left[2\,(ru + Zw) + r^2\frac{\partial u}{\partial r} + rZ\left(\frac{\partial u}{\partial z} + \frac{\partial w}{\partial r}\right) + Z^2\frac{\partial w}{\partial z}\right] dA_4. \tag{4.34b}$$

At the nodes that belong to two domain boundaries, a choice must be made of which boundary condition to apply there. Where the side boundary meets the solid surface, the boundary conditions on the solid surface will be applied and at the node where the top boundary meets the axis of symmetry, the boundary conditions on the axis of symmetry will be applied. Consequently, the respective r and z components of the momentum residual can be summarized as follows,

$$R_I^{M,r} = \begin{cases} u_I & \text{for } I \in X_2 \cup X_5 \\ \left(R_I^{M,r}\right)_{A_3} & \text{for } I \in X_3 \backslash (X_2 \cup X_4) \\ \left(R_I^{M,r}\right)_{A_4} & \text{for } I \in X_4 \backslash X_5 \\ \left(R_I^{M,r}\right)_{V} & \text{for } I \in X \backslash (X_1 \cup X_2 \cup X_3 \cup X_4 \cup X_5) \\ \left(R_I^{M,r}\right)_{V} + \left(R_I^{M,r}\right)_{A_1} & \text{for } I \in X_1 \backslash (X_2 \cup X_5), \end{cases} \tag{4.35a}$$

$$R_I^{M,z} = \begin{cases} w_I & \text{for } I \in X_2 \\ \left(R_I^{M,z}\right)_{A_3} & \text{for } I \in X_3 \backslash (X_2 \cup X_4) \\ \left(R_I^{M,z}\right)_{A_4} & \text{for } I \in X_4 \backslash X_5 \\ \left(R_I^{M,z}\right)_{V} & \text{for } I \in X \backslash (X_1 \cup X_2 \cup X_3 \cup (X_4 \backslash X_5)) \\ \left(R_I^{M,z}\right)_{V} + \left(R_I^{M,z}\right)_{A_1} & \text{for } I \in X_1 \backslash X_2. \end{cases} \tag{4.35b}$$

The boundary condition at the contact line (3.25) for the normal stress boundary condition must also be accounted for in this discrete formulation. Since the contact line remains pinned to the rim of the orifice, the free surface unknown that determines the r-coordinate of the node at the contact line (4.5) must be fixed as $\zeta_1 = r_o$. Therefore, at the contact line node, the contribution from the kinematic residual (4.20c) is replaced

with this essential condition. The kinematic residual is rewritten as,

$$R_I^K = \begin{cases} \zeta_1 - r_o & \text{for } I = 1 \\ \left(R_I^K\right)_{A_1} & \text{for } I = 2, ..., N_1, \end{cases} \tag{4.36}$$

where,

$$\left(R_I^K\right)_{A_1} = \int_{A_1} \phi_{1,I} \left(\frac{\partial \mathbf{r}^{(1)}}{\partial t} - \mathbf{u} \right) \cdot \mathbf{n} \, dA_1, \tag{4.37}$$

is the free surface contribution to the kinematic residual.

Finally, the condition for the pressure field (4.4) must also be accounted for. Let the mth pressure node be the node at (R, Z). The contribution from the continuity residual is replaced at the mth pressure node with the essential condition $p_m = -Z$. Therefore the continuity residual (4.20a) becomes,

$$R_I^C = \begin{cases} \left(R_I^C\right)_V & \text{for } I = 1, ..., N_p;\ I \neq m \\ p_m + Z & \text{for } I = m, \end{cases} \tag{4.38}$$

where,

$$\left(R_I^C\right)_V = \int_V \psi_I \left(\nabla \cdot \mathbf{u}\right) \, dV, \tag{4.39}$$

is the volume contribution to the continuity residual.

To summarise, the discrete formulation is given by the system of algebraic equations described by the continuity residual (4.38), the r and z components of the momentum residual (4.35) and the kinematic residual (4.36).

4.8 Residuals in Component Form

It is useful to write down the residuals (4.38, 4.35 & 4.36) in component form. Due to the axisymmetry of the problem, the integral of a function f over the volume V corresponds to the integration of f over a proportion of the (r, z)-plane and so,

$$\int_V f \, dV = 2\pi \int_z \int_r f \, r \, dr \, dz. \tag{4.40}$$

Integrals over the free surface A_1 in the (r, z)-plane are parametrized by the arc length s along the free surface and so,

$$\int_{A_1} f \, dA_1 = 2\pi \int_s f \, r \, ds. \tag{4.41}$$

Similarly, integrals over the side boundary and top boundary are parameterised by z and r, respectively, and so

$$\int_{A_3} f \, dA_3 = 2\pi \int_z f \, R \, dz, \tag{4.42a}$$

$$\int_{A_4} f \, dA_4 = 2\pi \int_r f \, r \, dr, \tag{4.42b}$$

For future reference, integrals over the contact line are given by,

$$\int_{L_c} f \, dL_c = 2\pi r_c f, \tag{4.43}$$

where r_c is the r coordinate of the contact line.

When it comes to solving the residuals, the factor of 2π in front of each residual will cancel out and so henceforth this prefactor is dropped.

The volume integrals required in component form are the volume contribution to the continuity residual (4.39) and the r and z components of the volume contribution to the momentum residual (4.29a). In component form, (4.39) is given by,

$$\left(R_I^C\right)_V = \int_z \int_r \psi_I \left(\frac{\partial u}{\partial r} + \frac{u}{r} + \frac{\partial w}{\partial z}\right) r\, dr\, dz. \tag{4.44}$$

Before specifying (4.29a) in component form, it should be stated that the r and z components of the term $\nabla\left(\phi_I \mathbf{e}_\alpha\right) : \mathbf{P}$ are given by

$$\begin{aligned}\nabla\left(\phi_I \mathbf{e}_r\right) : \mathbf{P} &= \frac{\partial \phi_I}{\partial r} P_{rr} + \frac{\partial \phi_I}{\partial z} P_{rz} + \frac{\phi_I}{r} P_{\varphi\varphi} \\ &= \frac{\partial \phi_I}{\partial r}\left(-p + 2\frac{\partial u}{\partial r}\right) + \frac{\partial \phi_I}{\partial z}\left(\frac{\partial w}{\partial r} + \frac{\partial u}{\partial z}\right) + \frac{\phi_I}{r}\left(-p + \frac{2u}{r}\right),\end{aligned} \tag{4.45a}$$

$$\begin{aligned}\nabla\left(\phi_I \mathbf{e}_z\right) : \mathbf{P} &= \frac{\partial \phi_I}{\partial r} P_{zr} + \frac{\partial \phi_I}{\partial z} P_{zz} \\ &= \frac{\partial \phi_I}{\partial r}\left(\frac{\partial w}{\partial r} + \frac{\partial u}{\partial z}\right) + \frac{\partial \phi_I}{\partial z}\left(-p + 2\frac{\partial w}{\partial z}\right),\end{aligned} \tag{4.45b}$$

where P_{rr}, P_{rz}, $P_{\varphi\varphi}$, $P_{z,r}$ and P_{zz} are components of the stress tensor (3.14). Therefore, the respective r and z components of (4.29a) are

$$\begin{aligned}\left(R_I^{M,r}\right)_V = \int_z \int_r \Bigg\{ &\phi_I \left[\frac{\partial u}{\partial t} + \left(u - \frac{\partial r}{\partial t}\right)\frac{\partial u}{\partial r} + \left(w - \frac{\partial z}{\partial t}\right)\frac{\partial u}{\partial z}\right] \\ &+ Oh^2 \left[\frac{\partial \phi_I}{\partial r}\left(-p + 2\frac{\partial u}{\partial r}\right) + \frac{\partial \phi_I}{\partial z}\left(\frac{\partial w}{\partial r} + \frac{\partial u}{\partial z}\right) + \frac{\phi_I}{r}\left(-p + \frac{2u}{r}\right)\right]\Bigg\}\, r\, dr\, dz,\end{aligned} \tag{4.46a}$$

$$\begin{aligned}\left(R_I^{M,z}\right)_V = \int_z \int_r \Bigg\{ &\phi_I \left[\frac{\partial w}{\partial t} + \left(u - \frac{\partial r}{\partial t}\right)\frac{\partial w}{\partial r} + \left(w - \frac{\partial z}{\partial t}\right)\frac{\partial w}{\partial z}\right] \\ &+ Oh^2 \left[\frac{\partial \phi_I}{\partial r}\left(\frac{\partial w}{\partial r} + \frac{\partial u}{\partial z}\right) + \frac{\partial \phi_I}{\partial z}\left(-p + 2\frac{\partial w}{\partial z}\right) + \phi_I\right]\Bigg\}\, r\, dr\, dz.\end{aligned} \tag{4.46b}$$

The integrals over the free surface that are required in component form are the r and z components of the free surface contribution to the momentum residual (4.29b) and the free surface contribution to the kinematic residual (4.37). In component form, (4.37) is given by,

$$\left(R_I^K\right)_{A_1} = \int_s \phi_{1,I} \left[\left(u - \frac{\partial r}{\partial t} \right) n_r + \left(w - \frac{\partial z}{\partial t} \right) n_z \right] r \, ds. \tag{4.47}$$

Before specifying (4.29b) in component form, the r and z components of the term $\nabla^s \cdot (\phi_{1,I} \mathbf{e}_\alpha)$ must be found. On the free surface,

$$\begin{aligned} \nabla^s &= (\mathbf{I} - \mathbf{nn}) \cdot \nabla \\ &= (\mathbf{tt} + \mathbf{e}_\varphi \mathbf{e}_\varphi) \cdot \nabla \\ &= \mathbf{t} \left(\mathbf{t} \cdot \nabla \right) + \mathbf{e}_\varphi \left(\mathbf{e}_\varphi \cdot \nabla \right) \\ &= \mathbf{t} \left(\mathbf{t} \cdot \nabla \right) + \frac{\mathbf{e}_\varphi}{r} \frac{\partial}{\partial \varphi}, \end{aligned} \tag{4.48}$$

where $\mathbf{t}$ is the unit tangent to the free surface, and since, $\mathbf{t} \cdot \nabla = \frac{\partial}{\partial s}$, then

$$\begin{aligned} \nabla^s \cdot (\phi_{1,I} \mathbf{e}_r) &= (\mathbf{t} \cdot \mathbf{e}_r) \frac{d\phi_{1,I}}{ds} + \phi_{1,I} \mathbf{t} \cdot \frac{\partial \mathbf{e}_r}{\partial s} + \frac{\mathbf{e}_r \cdot \mathbf{e}_\varphi}{r} \frac{\partial \phi_{1,I}}{\partial \varphi} + \frac{\phi_{1,I}}{r} \mathbf{e}_\varphi \cdot \frac{\partial \mathbf{e}_r}{\partial \varphi} \\ &= -\frac{d\phi_{1,I}}{ds} n_z + \frac{\phi_{1,I}}{r}, \end{aligned} \tag{4.49a}$$

$$\begin{aligned} \nabla^s \cdot (\phi_{1,I} \mathbf{e}_z) &= (\mathbf{t} \cdot \mathbf{e}_z) \frac{d\phi_{1,I}}{ds} + \phi_{1,I} \mathbf{t} \cdot \frac{\partial \mathbf{e}_z}{\partial s} + \frac{\mathbf{e}_\varphi \cdot \mathbf{e}_z}{r} \frac{\partial \phi_{1,I}}{\partial \varphi} + \frac{\phi_{1,I}}{r} \mathbf{e}_\varphi \cdot \frac{\partial \mathbf{e}_z}{\partial \varphi} \\ &= \frac{d\phi_{1,I}}{ds} n_r, \end{aligned} \tag{4.49b}$$

since $\frac{\partial \mathbf{e}_r}{\partial s} = \frac{\partial \mathbf{e}_z}{\partial s} = \mathbf{0}$, $\mathbf{e}_r \cdot \mathbf{e}_\varphi = \mathbf{e}_\varphi \cdot \mathbf{e}_z = 0$, $\frac{\partial \mathbf{e}_r}{\partial \varphi} = \mathbf{e}_\varphi$ and $\frac{\partial \mathbf{e}_z}{\partial \varphi} = \mathbf{0}$. Therefore the respective r and z components of the free surface contribution to the momentum residual (4.29b)

are

$$\left(R_I^{M,r}\right)_{A_1} = Oh^2 \int_s \left(\frac{\phi_{1,I}}{r} - \frac{d\phi_{1,I}}{ds} n_z - p_g \phi_{1,I} n_r \right) r \, ds, \tag{4.50a}$$

$$\left(R_I^{M,z}\right)_{A_1} = Oh^2 \int_s \left(\frac{d\phi_{1,I}}{ds} n_r - p_g \phi_{1,I} n_z \right) r \, ds, \tag{4.50b}$$

and the unit tangent vector on the free surface in the (r, z)-plane pointing away from the contact line is given by

$$\mathbf{t} = (-n_z, n_r) = \frac{\left(\frac{\partial r}{\partial s}, \frac{\partial z}{\partial s}\right)}{\sqrt{\left(\frac{\partial r}{\partial s}\right)^2 + \left(\frac{\partial z}{\partial s}\right)^2}}, \tag{4.51}$$

and so the inwardly facing unit normal vector to the free surface pointing into the liquid phase is

$$\mathbf{n} = (n_r, n_z) = \frac{\left(\frac{\partial z}{\partial s}, -\frac{\partial r}{\partial s}\right)}{\sqrt{\left(\frac{\partial r}{\partial s}\right)^2 + \left(\frac{\partial z}{\partial s}\right)^2}}. \tag{4.52}$$

4.9 Interpolation Functions and Element Contributions to the Residuals

As stated in section 4.4.2, the Taylor-Hood V6P3 elements are triangular and consist of six nodes. The nodes at each vertex are numbered anticlockwise as $i = 1, 2, 3$ whilst the nodes on the curved sides of the element are numbered as $i = 4, 5, 6$ (see Figure 4.4). Note that the lower case i is used to identify a particular node locally, i.e. within a particular element, in contrast to its label I which identifies the node globally, i.e. within the whole computational mesh.

Each element is also given an element number $e = 1, ..., N_e$. The entry in the eth row and ith column of the matrix F gives the global node number of the ith local node of the eth element, i.e. $I = F_{ei}$, and since no remeshing takes place, F remains unchanged throughout an entire simulation. The coordinates of a node in a given element

can therefore also be denoted locally by (r_i, z_i), $i = 1, ..., 6$.

Since the pressure field is approximated bi-linearly and the velocity field is approximated bi-quadratically, the r and z components of velocity and the pressure field in the eth element are given by

$$u^e = \sum_{j=1}^{6} u_j(t)\phi_j(r,z), \qquad w^e = \sum_{j=1}^{6} w_j(t)\phi_j(r,z), \qquad p^e = \sum_{j=1}^{3} p_j(t)\psi_j(r,z), \tag{4.53}$$

where ψ_j, $j = 1, 2, 3$, and ϕ_j, $j = 1, ..., 6$, are the bi-linear and bi-quadratic local interpolation functions which in any given element satisfy the criteria,

$$\psi_i(r_j, z_j) = \delta_{ij}, \qquad i, j = 1, 2, 3, \tag{4.54a}$$

$$\phi_i(r_j, z_j) = \delta_{ij}, \qquad i, j = 1, ..., 6. \tag{4.54b}$$

At this point, it is also worth defining,

$$r^e = \sum_{j=1}^{6} r_j(t)\phi_j(r,z), \qquad z^e = \sum_{j=1}^{6} z_j(t)\phi_j(r,z). \tag{4.55}$$

The global interpolation functions, ψ_I $(I = 1, ..., N_p)$ and ϕ_I $(I = 1, ..., N)$ are constructed by stitching together the local interpolation functions from each element in the following manner,

$$\psi_I(r,z) = \begin{cases} \psi_i(r,z) & \text{where } I = 1, ..., N_p,\ X_I^p = F_{ei} \\ 0 & \text{otherwise,} \end{cases} \tag{4.56a}$$

$$\phi_I(r,z) = \begin{cases} \phi_i(r,z) & \text{where } I = 1, ..., N,\ I = F_{ei} \\ 0 & \text{otherwise.} \end{cases} \tag{4.56b}$$

In other words, the global interpolation function ϕ_I, $I = 1, ..., N$, is zero in all elements that do not contain the Ith node. When an element e does contain the Ith node, the Ith global interpolation function takes the value of the ith local interpolation function where $I = F_{ei}$. Similarly, the global interpolation function ψ_I, $I = 1, ..., N_p$ is zero in all elements the do not contain the I pressure node. Where an element does contain the Ith pressure node, the Ith interpolation function takes the value of the ith local interpolation function where $X_I^p = F_{ei}$.

The volume contributions to the r and z components of the momentum residual (4.46) and the continuity residual (4.44) can now be written in terms of the contributions from each element. The volume contribution to the continuity residual (4.44) becomes,

$$\left(R_I^C\right)_V = \sum_{\substack{e=1 \\ X_I^p = F_{ei}}}^{N_e} \sum_{i=1}^{3} \int_{V_e} \psi_i \left(\frac{\partial u^e}{\partial r} + \frac{u^e}{r^e} + \frac{\partial w^e}{\partial z} \right) r^e \, dV_e, \tag{4.57}$$

where integration over V_e represents integration over the volume of element e. The r and

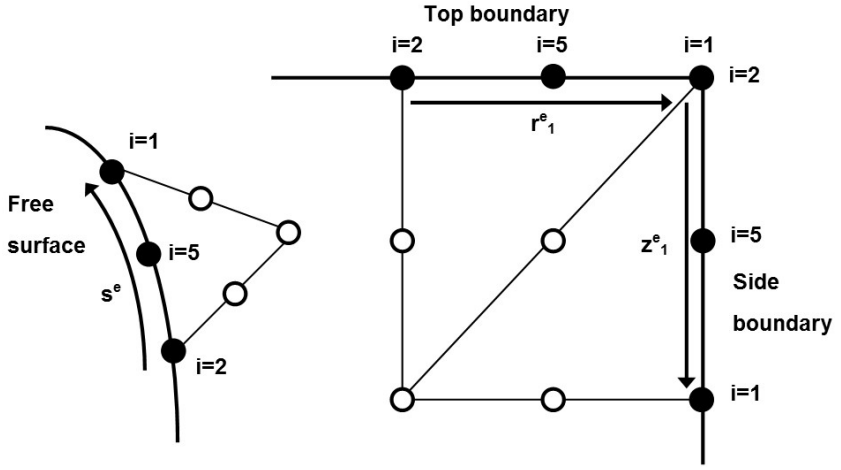

Figure 4.7: Elements which have a boundary that coincides with the free surface, side and top boundaries.

z components of the momentum residual (4.46) are

$$\left(R_I^{M,r}\right)_V = \sum_{\substack{e=1 \\ I=F_{ei}}}^{N_e} \sum_{i=1}^{6} \int_{V_e} \left\{ \phi_i \left[\frac{\partial u^e}{\partial t} + \left(u^e - \frac{\partial r^e}{\partial t} \right) \frac{\partial u^e}{\partial r} + \left(w^e - \frac{\partial z^e}{\partial t} \right) \frac{\partial u^e}{\partial z} \right] \right.$$
$$+ Oh^2 \left[\frac{\partial \phi_i}{\partial r} \left(-p^e + 2\frac{\partial u^e}{\partial r} \right) + \frac{\partial \phi_i}{\partial z} \left(\frac{\partial w^e}{\partial r} + \frac{\partial u^e}{\partial z} \right) \right.$$
$$\left. \left. + \frac{\phi_i}{r^e} \left(-p^e + \frac{2u^e}{r^e} \right) \right] \right\} r^e \, dV_e, \tag{4.58a}$$

$$\left(R_I^{M,z}\right)_V = \sum_{\substack{e=1 \\ I=F_{ei}}}^{N_e} \sum_{i=1}^{6} \int_{V_e} \left\{ \phi_i \left[\frac{\partial w^e}{\partial t} + \left(u^e - \frac{\partial r^e}{\partial t} \right) \frac{\partial w^e}{\partial r} + \left(w^e - \frac{\partial z^e}{\partial t} \right) \frac{\partial w^e}{\partial z} \right] \right.$$
$$\left. + Oh^2 \left[\frac{\partial \phi_i}{\partial r} \left(\frac{\partial w^e}{\partial r} + \frac{\partial u^e}{\partial z} \right) + \frac{\partial \phi_i}{\partial z} \left(-p^e + 2\frac{\partial w^e}{\partial z} \right) + \phi_i \right] \right\} r^e \, dV_e. \tag{4.58b}$$

Some of the sides of elements in the domain also coincide with the boundaries of the domain. The nodes that make up these so-called one-dimensional elements are numbered $i = 1, 5, 2$ on the free surface, side boundary and top boundary (see Figure 4.7). The sets

of element numbers that coincide with the free surface, side boundary and top boundary are given by E_1, E_3 and E_4, respectively. The arc lengths of a one-dimensional free surface element, side boundary element and top boundary element are given by s^e, z_1^e and r_1^e.

The components of the velocity field along these one-dimensional elements can be defined as

$$u_1^e = \begin{cases} \sum\limits_{j=1,5,2} u_j \phi_{1,j}(s) & \text{where } e \in E_1 \\ \sum\limits_{j=1,5,2} u_j \phi_{1,j}(z) & \text{where } e \in E_3 \\ \sum\limits_{j=1,5,2} u_j \phi_{1,j}(r) & \text{where } e \in E_4, \end{cases} \tag{4.59a}$$

$$w_1^e = \begin{cases} \sum\limits_{j=1,5,2} w_j \phi_{1,j}(s) & \text{where } e \in E_1 \\ \sum\limits_{j=1,5,2} w_j \phi_{1,j}(z) & \text{where } e \in E_3 \\ \sum\limits_{j=1,5,2} w_j \phi_{1,j}(r) & \text{where } e \in E_4, \end{cases} \tag{4.59b}$$

and also

$$r_1^e = \begin{cases} \sum\limits_{j=1,5,2} r_j \phi_{1,j}(s) & \text{where } e \in E_1 \\ \sum\limits_{j=1,5,2} r_j \phi_{1,j}(r) & \text{where } e \in E_4, \end{cases} \tag{4.60a}$$

$$z_1^e = \begin{cases} \sum\limits_{j=1,5,2} z_j \phi_{1,j}(s) & \text{where } e \in E_1 \\ \sum\limits_{j=1,5,2} z_j \phi_{1,j}(z) & \text{where } e \in E_3, \end{cases} \tag{4.60b}$$

where $\phi_{1,j}$, $j = 1, 5, 2$, are the quadratic local interpolation functions which in any given

element, $e \in E_1 \cup E_3 \cup E_4$, satisfy the criterion,

$$\phi_{1,i}(s(r_j^{(1)}, z_j^{(1)})) = \delta_{ij}, \qquad i,j = 1,5,2, \qquad e \in E_1, \tag{4.61a}$$

$$\phi_{1,i}(z_j) = \delta_{ij}, \qquad i,j = 1,5,2, \qquad e \in E_3, \tag{4.61b}$$

$$\phi_{1,i}(r_j) = \delta_{ij}, \qquad i,j = 1,5,2, \qquad e \in E_4. \tag{4.61c}$$

The global one-dimensional interpolation functions are constructed from by stitching together these local interpolation functions but can also formed from the corresponding two-dimensional interpolation functions in the following manner,

$$\phi_{1,I} = \begin{cases} \phi_{1,i}(s) = \phi_i(r,z) & \text{where } I \in X_1,\ I = F_{ei},\ e \in E_1, \\ \phi_{1,i}(z) = \phi_i(R,z) & \text{where } I \in X_3,\ I = F_{ei},\ e \in E_3, \\ \phi_{1,i}(r) = \phi_i(r,Z) & \text{where } I \in X_4,\ I = F_{ei},\ e \in E_4, \\ 0 & \text{otherwise.} \end{cases} \tag{4.62}$$

The free surface, side boundary and top boundary contributions to the r and z components of the momentum residual (4.50, 4.33 & 4.34) and the free surface contribution to the kinematic residual (4.47) can now be written in terms of local contributions from element along those domain boundaries. The free surface contribution to the momentum residual (4.50) can now be written as

$$\left(R_I^{M,r}\right)_{A_1} = \sum_{e=1}^{N_e} \sum_{\substack{i=1,5,2 \\ e \in E_1 \\ I = F_{ei}}} Oh^2 \left(F_i^{(11)} + p_g F_i^{(12)}\right), \tag{4.63a}$$

$$\left(R_I^{M,z}\right)_{A_1} = \sum_{e=1}^{N_e} \sum_{\substack{i=1,5,2 \\ e \in E_1 \\ I = F_{ei}}} Oh^2 \left(F_i^{(21)} + p_g F_i^{(22)}\right), \tag{4.63b}$$

where the free surface stress vectors are defined as,

$$\begin{aligned} F_i^{(11)} &= \int_{s^e} \left(\frac{\phi_{1,i}}{r_1^e} - \frac{d\phi_{1,i}}{ds} n_z \right) r_1^e ds^e, \quad F_i^{(12)} = -\int_{s^e} \phi_{1,i} n_r r_1^e ds^e, \\ F_i^{(21)} &= \int_{s^e} \frac{d\phi_{1,i}}{ds} n_r r_1^e ds^e, \qquad\qquad F_i^{(22)} = -\int_{s^e} \phi_{1,i} n_z r_1^e ds^e. \end{aligned} \tag{4.64}$$

The contributions of the side boundary to the momentum residual (4.33) are

$$\left(R_I^{M,r}\right)_{A_3} = \sum_{\substack{e=1 \\ e\in E_3 \\ I=F_{ei}}}^{N_e} \sum_{i=1,5,2} \int_{z_1^e} \phi_{1,i} \left(R w_1^e - z_1^e u_1^e\right) R dz_1^e, \tag{4.65a}$$

$$\begin{aligned} \left(R_I^{M,z}\right)_{A_3} = \sum_{\substack{e=1 \\ e\in E_3 \\ I=Fei}}^{N_e} \sum_{i=1,5,2} \int_{z_1^e} \phi_{1,i} \Bigg[& 2\left(R u_1^e + z_1^e w_1^e\right) + R^2 \frac{\partial u^e}{\partial r} + R z_1^e \left(\frac{\partial w^e}{\partial r} + \frac{\partial u_1^e}{\partial z} \right) \\ & + \left(z_1^e\right)^2 \frac{\partial w_1^e}{\partial z} \Bigg] R dz_1^e, \end{aligned} \tag{4.65b}$$

whist the contributions of the top boundary (4.34) are

$$\left(R_I^{M,r}\right)_{A_4} = \sum_{\substack{e=1 \\ e\in E_4 \\ I=F_{ei}}}^{N_e} \sum_{i=1,5,2} \int_{r_1^e} \phi_{1,i} \left(r_1^e w_1^e - Z u_1^e\right) r_1^e dr_1^e, \tag{4.66a}$$

$$\begin{aligned} \left(R_I^{M,z}\right)_{A_4} = \sum_{\substack{e=1 \\ e\in E_4 \\ I=F_{ei}}}^{N_e} \sum_{i=1,5,2} \int_{r_1^e} \phi_{1,i} \Bigg[& 2\left(r_1^e u_1^e + Z w_1^e\right) + {r_1^e}^2 \frac{\partial u_1^e}{\partial r} + r_1^e Z \left(\frac{\partial w_1^e}{\partial r} + \frac{\partial u^e}{\partial z} \right) \\ & + Z^2 \frac{\partial w^e}{\partial z} \Bigg] r_1^e dr_1^e. \end{aligned} \tag{4.66b}$$

Finally, the free surface contribution to the kinematic residual (4.47) is given by,

$$\left(R_I^K\right)_{A_1} = \sum_{\substack{e=1 \\ e\in E_1 \\ X_I^1=F_{ei}}}^{N_e} \sum_{i=1,5,2} \int_{s^e} \phi_{1,i} \left[\left(u_1^e - \frac{dr_1^e}{dt} \right) n_r + \left(w_1^e - \frac{dz_1^e}{dt} \right) n_z \right] r_1^e ds^e. \tag{4.67}$$

The volume, free surface and far field contributions to the residuals have now been expressed in terms of local quantities associated with each element. These contributions can now be spatially discretized over each element.

4.10 Spatial Discretisation

The element level contributions are spatially discretised by substituting the expressions for local velocity, pressure and position (4.53, 4.55, 4.59 & 4.60).

The volume contribution to the continuity residual (4.57) becomes,

$$\left(R_I^C\right)_V = \sum_{e=1}^{N_e} \sum_{\substack{i=1 \\ X_I^p = F_{ei}}}^{3} \sum_{\substack{j=1 \\ J = F_{ej}}}^{6} \left(u_j C_{ij}^{(1)} + w_j C_{ij}^{(2)} \right), \tag{4.68}$$

where the continuity matrices are

$$C_{ij}^{(1)} = \int_{V_e} \psi_i \left(\frac{\partial \phi_j}{\partial r} + \frac{\phi_j}{r^e} \right) r^e \, dV_e, \qquad C_{ij}^{(2)} = \int_{V_e} \psi_i \frac{\partial \phi_j}{\partial z} \, r^e \, dV_e, \qquad i = 1, 2, 3, \;\; j = 1, ..., 6. \tag{4.69}$$

The volume contributions to the r and z components of the momentum residual (4.58)

are

$$\left(R_I^{M,r}\right)_V = \sum_{\substack{e=1 \\ I=F_{ei}}}^{N_e} \sum_{i=1}^{6} \left\{ \sum_{\substack{j=1 \\ J=F_{ej}}}^{6} \left[\frac{du_j}{dt} M_{ij} + u_j \left(A_{ij} + Oh^2 V_{ij}^{(11)} \right) + Oh^2 w_j V_{ij}^{(12)} \right] \right.$$
$$\left. -Oh^2 \sum_{\substack{j=1 \\ X_J^P=F_{ej}}}^{3} p_j C_{ji}^{(1)} \right\}, \tag{4.70a}$$

$$\left(R_I^{M,z}\right)_V = \sum_{\substack{e=1 \\ I=F_{ei}}}^{N_e} \sum_{i=1}^{6} \left(\left\{ \sum_{\substack{j=1 \\ J=F_{ej}}}^{6} \left[\frac{dw_j}{dt} M_{ij} + Oh^2 u_j V_{ji}^{(12)} + w_j \left(A_{ij} + Oh^2 V_{ij}^{(22)} \right) \right] \right. \right.$$
$$\left. \left. -Oh^2 \sum_{\substack{j=1 \\ X_J^p=F_{ej}}}^{3} p_j C_{ji}^{(2)} \right\} + Oh^2 G_i \right), \tag{4.70b}$$

where the mass matrix is

$$M_{ij} = \int_{V_e} \phi_i \phi_j r^e \, dV_e, \qquad i,j = 1, ..., 6, \tag{4.71}$$

the body force vector is

$$G_i = \int_{V_e} \phi_i r^e \, dV_e, \qquad i = 1, ..., 6, \tag{4.72}$$

the inertial terms are

$$A_{ij} = \sum_{\substack{k=1 \\ K=Fek}}^{6} \left[\left(u_k - \frac{dr_k}{dt} \right) a_{ijk}^{(1)} + \left(w_k - \frac{dz_k}{dt} \right) a_{ijk}^{(2)} \right], \tag{4.73a}$$

$$a_{ijk}^{(1)} = \int_{V_e} \phi_i \frac{\partial \phi_j}{\partial r} \phi_k r^e \, dV_e, \qquad i,j = 1,...,6, \tag{4.73b}$$

$$a_{ijk}^{(2)} = \int_{V_e} \phi_i \frac{\partial \phi_j}{\partial z} \phi_k r^e \, dV_e, \qquad i,j = 1,...,6, \tag{4.73c}$$

and the viscous terms are

$$V_{ij}^{(11)} = \int_{V_e} \left(2 \frac{\partial \phi_i}{\partial r} \frac{\partial \phi_j}{\partial r} + \frac{\partial \phi_i}{\partial z} \frac{\partial \phi_j}{\partial z} + \frac{2}{r^{e^2}} \phi_i \phi_j \right) r^e \, dV_e, \qquad i,j = 1,...,6, \tag{4.74a}$$

$$V_{ij}^{(12)} = \int_{V_e} \frac{\partial \phi_i}{\partial z} \frac{\partial \phi_j}{\partial r} \, r^e \, dV_e, \qquad i,j = 1,...,6, \tag{4.74b}$$

$$V_{ij}^{(22)} = \int_{V_e} \left(\frac{\partial \phi_i}{\partial r} \frac{\partial \phi_j}{\partial r} + 2 \frac{\partial \phi_i}{\partial z} \frac{\partial \phi_j}{\partial z} \right) r^e \, dV_e, \qquad i,j = 1,...,6. \tag{4.74c}$$

The r and z components of the free surface contribution to the momentum residual (4.63) do not require spatial discretization since the gas pressure p_g is spatially uniform. The free surface contribution to the kinematic residual (4.67) is

$$\left(R_I^K \right)_{A_1} = \sum_{e=1}^{N_e} \sum_{\substack{i=1,5,2 \\ e \in E_1 \\ X_I^1 = F_{ei}}} \sum_{\substack{j=1,5,2 \\ J = F_{ej}}} \left[\left(u_j - \frac{dr_j}{dt} \right) K_{ij}^{(1)} + \left(w_j - \frac{dz_j}{dt} \right) K_{ij}^{(2)} \right], \tag{4.75}$$

where the kinematic matrices are,

$$K_{ij}^{(1)} = \int_{s^e} \phi_{1,i} \phi_{1,j} n_r r_1^e ds^e, \qquad K_{ij}^{(2)} = \int_{s^e} \phi_{1,i} \phi_{1,j} n_z r_1^e ds^e, \qquad i,j = 1,5,2. \tag{4.76}$$

The r and z components of the side boundary contribution to the momentum residual (4.65) are

$$\left(R_I^{M,r}\right)_{A_3} = \sum_{e=1}^{N_e} \sum_{\substack{i=1,5,2 \\ e\in E_3 \\ I=F_{ei}}} \sum_{j=1,5,2} \left(u_j B_{ij}^{(11)} + w_j B_{ij}^{(12)}\right), \tag{4.77a}$$

$$\left(R_I^{M,z}\right)_{A_3} = \sum_{e=1}^{N_e} \sum_{\substack{i=1,5,2 \\ e\in E_3 \\ I=F_{ei}}} \left[\sum_{\substack{j=1,5,2 \\ J=F_{ej}}} \left(u_j B_{ij}^{(111)} + w_j B_{ij}^{(112)}\right) + \sum_{\substack{j=1 \\ J=F_{ej}}}^{6} \left(u_j B_{ij}^{(121)} + w_j B_{ij}^{(122)}\right) \right], \tag{4.77b}$$

where the side boundary matrices are

$$B_{ij}^{(11)} = -\int_{z_1^e} \phi_{1,i}\phi_{1,j} R z_1^e dz_1^e, \qquad i,j = 1,5,2, \tag{4.78a}$$

$$B_{ij}^{(12)} = \int_{z_1^e} \phi_{1,i}\phi_{1,j} R^2 dz_1^e, \qquad i,j = 1,5,2, \tag{4.78b}$$

$$B_{ij}^{(111)} = \int_{z_1^e} \phi_{1,i}\left(2\phi_{1,j} + z_1^e \frac{\partial \phi_{1,j}}{\partial z}\right) R^2 dz_1^e, \qquad i,j = 1,5,2, \tag{4.78c}$$

$$B_{ij}^{(112)} = \int_{z_1^e} \phi_{1,i}\left(2\phi_{1,j} + z_1^e \frac{\partial \phi_{1,j}}{\partial z}\right) R z_1^e dz_1^e, \qquad i,j = 1,5,2, \tag{4.78d}$$

$$B_{ij}^{(121)} = \int_{z_1^e} \phi_{1,i} \frac{\partial \phi_j}{\partial r} R^3 dz_1^e, \qquad i = 1,5,2,\ j = 1,...,6, \tag{4.78e}$$

$$B_{ij}^{(122)} = \int_{z_1^e} \phi_{1,i} \frac{\partial \phi_j}{\partial r} R^2 z_1^e dz_1^e, \qquad i = 1,5,2,\ j = 1,...,6. \tag{4.78f}$$

Finally the r and z components of the top boundary contribution to the momentum

residual (4.66) are

$$\left(R_I^{M,r}\right)_{A_4} = \sum_{e=1}^{N_e} \sum_{\substack{i=1,5,2 \\ e\in E_4 \\ I=F_{ei}}} \sum_{\substack{j=1,5,2 \\ J=F_{ej}}} \left(u_j B_{ij}^{(21)} + w_j B_{ij}^{(22)}\right), \tag{4.79a}$$

$$\left(R_I^{M,z}\right)_{A_4} = \sum_{e=1}^{N_e} \sum_{\substack{i=1,5,2 \\ e\in E_4 \\ I=F_{ei}}} \left[\sum_{\substack{j=1,5,2 \\ J=F_{ej}}} \left(u_j B_{ij}^{(211)} + w_j B_{ij}^{(212)}\right) + \sum_{\substack{j=1 \\ J=F_{ej}}}^{6} \left(u_j B_{ij}^{(221)} + w_j B_{ij}^{(222)}\right) \right], \tag{4.79b}$$

where the top boundary matrices are

$$B_{ij}^{(21)} = -\int_{r_1^e} \phi_{1,i}\phi_{1,j} r_1^e Z dr_1^e, \qquad i,j = 1,5,2, \tag{4.80a}$$

$$B_{ij}^{(22)} = \int_{r_1^e} \phi_{1,i}\phi_{1,j} \left(r_1^e\right)^2 dr_1^e, \qquad i,j = 1,5,2, \tag{4.80b}$$

$$B_{ij}^{(211)} = \int_{r_1^e} \phi_{1,i} \left(2\phi_{1,j} + r_1^e \frac{\partial \phi_{1,j}}{\partial r}\right) \left(r_1^e\right)^2 dr_1^e, \qquad i,j = 1,5,2, \tag{4.80c}$$

$$B_{ij}^{(212)} = \int_{r_1^e} \phi_{1,i} \left(2\phi_{1,j} + r_1^e \frac{\partial \phi_{1,j}}{\partial r}\right) r_1^e Z dr_1^e, \qquad i,j = 1,5,2, \tag{4.80d}$$

$$B_{ij}^{(221)} = \int_{r_1^e} \phi_{1,i} \frac{\partial \phi_j}{\partial z} \left(r_1^e\right)^2 Z dr_1^e, \qquad i = 1,5,2,\ j = 1,...,6, \tag{4.80e}$$

$$B_{ij}^{(222)} = \int_{r_1^e} \phi_{1,i} \frac{\partial \phi_j}{\partial z} r_1^e Z^2 dr_1^e, \qquad i = 1,5,2,\ j = 1,...,6. \tag{4.80f}$$

The r and z components of the momentum resdiuals (4.35), the continuity residual (4.38) and the kinematic residual (4.36) have now been fully discretised in space. The next step is to, where necessary, discretise these equations in time.

4.11 Temporal Discretisation

A constant time step is used for the initial growth of the bubble until the pinch-off process begins. The time step then decreases, in a manner described in Section 5.2, in order for the numerical platform to resolve the small time scales involved in the pinch-off process. Therefore the temporal discretisation of the equations must allow for a variable time step.

A second-order backward differentiation formula for variable time steps is used to calculate all derivatives with respect to time after the first time step (Gresho & Sani, 1998). Suppose the value of an unknown at the current time $t = t_i$ is $\alpha^{(i)} = \alpha(t_i)$, and at the previous times of $t = t_{i-1}$ and $t = t_{i-2}$, it was $\alpha^{(i-1)} = \alpha(t_{i-1})$ and $\alpha^{(i-2)} = \alpha(t_{i-2})$, respectively, where $\Delta t_i = t_i - t_{i-1}$ and $\Delta t_{i-1} = t_{i-1} - t_{i-2}$ are the current and previous time steps. The time derivative is given by

$$\frac{d\alpha^{(i)}}{dt} = \frac{2\Delta t_i + \Delta t_{i-1}}{\Delta t_i (\Delta t_i + \Delta t_{i-1})}\alpha^i + \frac{\Delta t_i}{\Delta t_{i-1}(\Delta t_i + \Delta t_{i-1})}\alpha^{(i-2)} - \frac{\Delta t_i + \Delta t_{i-1}}{\Delta t_i \Delta t_{i-1}}\alpha^{(i-1)}. \quad (4.81)$$

At the first time step a simple first-order backward differentiation formula is used,

$$\frac{d\alpha^{(1)}}{dt} = \frac{\alpha^{(1)} - \alpha^{(0)}}{\Delta t_1}. \quad (4.82)$$

4.12 Additional Equations

The r and z components of the momentum residuals (4.35), the continuity residual (4.38) and the kinematic residual (4.36) provide $2N + N_p + N_1$ equations. However, as stated in Section 4.5 there are $2(N + N_1) + N_p + 1$ unknowns in the system of equations and so another $N_1 + 1$ equations are required. All equations in the dimensionless problem formulation have been accounted for apart from the volume constraint (3.29) and as stated in Section 4.4.1 the distribution of the nodes on the free surface must be prescribed.

4.12.1 The Volume Constraint

The volume constraint (3.29) provides one extra equation for the system. Let the volume residual be denoted by

$$R^V = V(t) - V_i - Qt, \tag{4.83}$$

where the volume at a given time is given by (3.30). Written in terms of local contributions from the free surface elements, (4.83) can be spatially discretised as

$$R^V = \pi \left(\sum_{\substack{e=1 \\ e \in E_1}}^{N_e} \int_{z_2}^{z_1} h_e^2 dz \right) - V_i - Qt, \tag{4.84}$$

where $h_e = h_e(z,t)$ is the quadratic equation that approximates the part of the free surface which coincides with element e, and can be found simply from the nodal values of r_i and z_i, $i = 1, 5, 2$. Only N_1 more equations are required to complete the system.

4.12.2 Distribution of Nodes along the Free Surface

As stated in Section 4.4.1, the mesh consists of two regions, the pinch-off region and the detachment region. These regions are separated by a horizontal spine which runs from the Sth free surface node to the side boundary. In order to ensure the pinch-off region of the mesh captures the thinning of the neck, the height of this horizontal spine, given by the free surface unknown χ_S, must be prescribed. Therefore, χ_S is considered to be a function of the bubble's height H and so the Sth component of the mesh residual R^n is described,

$$R_S^n = \begin{cases} \chi_S - k_S H & \text{for } H < k_H \\ \chi_S - k_S k_H & \text{for } H \geqslant k_H, \end{cases} \tag{4.85}$$

where $0 < k_S < 1$ is a ratio of how high the Sth spine should be relative to the height of the bubble until the height of the bubble reaches k_H, in which case the Sth spine will stay at the height $k_S k_H$.

From Section 4.4.1, it is also known that $\chi_1 = 0$ and $\chi_{N_1} = 0$, and so

$$R_I^n = \chi_I, \qquad I = 1, N_1. \tag{4.86}$$

The distribution of the remaining $S - 2$ nodes along the free surface in the pinch-off region and the remaining $N_1 - S - 1$ nodes along the free surface in the detachment region must also be prescribed. By describing the arc length of a given free surface element relative to the arc length of another free surface element, additional refinement can be added to parts of the mesh where it is required. In the pinch-off region this results in another $(S - 3)/2$ equations where

$$R_I^n = s^e - k_e s^{e+1}, \qquad e = 1, ..., (S-3)/2, \qquad I = 2e + 1, \tag{4.87}$$

and k_e is the ratio of the arc lengths for two neighbouring free surface elements. In the detachment region this leads to another $(N - S - 2)/2$ equations where

$$R_I^n = s^e - k_e s^{e+1}, \qquad e = (S+1)/2, ..., (N_1 - 5)/2, \qquad I = 2e + 1. \tag{4.88}$$

Therefore, only $(N_1 - 1)/2$ equations are now required. The position of each local node at the end of a free surface element has been prescribed but the position of the nodes between these end points still needs to be given. The local node $i = 5$ sits between the local nodes $i = 1$ and $i = 2$, and in order to keep the mesh regular, its position can be

described in terms of these two end nodes as follows, for $I = 2j$ where $j = 1, ..., (N_1-1)/2$,

$$R_I^n = \begin{cases} r_5 - \frac{1}{2}(r_1 + r_2) & \text{for } |(z_1 - z_2)/(r_1 - r_2)| < 1 \\ z_5 - \frac{1}{2}(z_1 + z_2) & \text{for } |(z_1 - z_2)/(r_1 - r_2)| \geqslant 1, \end{cases} \tag{4.89}$$

The number of equations and unknowns is now equal. At each time step, the N_T unknowns of the system, the r and z components of the velocity field, u_I and w_I for $I = 1, ..., N$, the pressure p_I for $I = 1, ..., N_p$, the free surface unknowns χ_I and ζ_I for $I = 1, ..., N$ and the gas pressure p_g will be determined by the N r-component of momentum equations (4.35a), the N z-component of momentum equations (4.35b), the N_p continuity equations (4.38), the N_1 kinematic equations (4.36), the N_1 mesh equations and the volume constraint (4.84).

However, before this algebraic system can be solved, the matrices identified previously that represent the coefficients of this system must be evaluated.

4.13 Mapping to the Master Element

The coefficients of the system of algebraic equations given by the residuals consist of the mass matrix (4.71), the body force terms (4.72), the inertial terms (4.73), the viscous terms (4.74), the continuity terms (4.69), the free surface stress terms (4.64), the kinematic terms (4.76), the side boundary terms (4.78) and the top boundary terms (4.80). Rather than evaluating these integrals on an element by element basis, they can be mapped from their elements in the computational domain in the (r, z)-plane to a master element in the (ξ, η)-plane where numerical integration techniques can be routinely implemented (see Figure 4.8). Similar to the elements in the computational domain, the local nodes at the vertices of the master element are labelled $i = 1, 2, 3$ in an anticlockwise manner and the nodes between the pairs of vertices are labelled anticlockwise as $i = 4, 5, 6$.

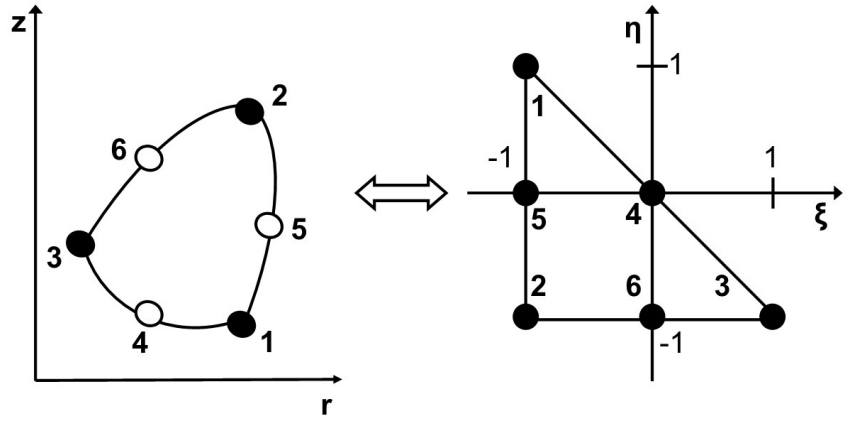

Figure 4.8: The V6P3 Taylor-Hood master element in the (ξ, η)-plane.

The local bilinear interpolation functions on the master element are given by,

$$\psi_1 = \frac{1+\eta}{2}, \qquad \psi_2 = -\frac{\xi+\eta}{2}, \qquad \psi_3 = \frac{1+\xi}{2}, \tag{4.90}$$

from which the local bi-quadratic interpolating functions can be constructed,

$$\begin{aligned} &\phi_1 = \psi_1\left(2\psi_1 - 1\right), \quad \phi_2 = \psi_2\left(2\psi_2 - 1\right), \quad \phi_3 = \psi_3\left(2\psi_3 - 1\right), \\ &\phi_4 = 4\psi_1\psi_3, \qquad\qquad \phi_5 = 4\psi_1\psi_2, \qquad\qquad \phi_6 = 4\psi_2\psi_3. \end{aligned} \tag{4.91}$$

The coordinates of a point in the eth element in the (r, z)-plane are transformed to the master element in the (ξ, ζ)-plane by the following isoparametric mapping,

$$r^e = \sum_{j=1}^{6} r_j \phi_j\left(\xi, \eta\right), \qquad z^e = \sum_{j=1}^{6} z_j \phi_j\left(\xi, \eta\right). \tag{4.92}$$

Local volume integrals are transformed to the master element by,

$$\int_{V_e} f(r, z)\, dV_e = \int_{\xi=-1}^{\xi=1} \int_{\eta=-1}^{\eta=-\xi} f(\xi, \eta) \det J_e \, d\eta d\xi, \tag{4.93}$$

where J_e is the Jacobian matrix of the isoparametric mapping (4.92),

$$J_e = \begin{pmatrix} \frac{\partial r^e}{\partial \xi} & \frac{\partial r^e}{\partial \eta} \\ \frac{\partial z^e}{\partial \xi} & \frac{\partial z^e}{\partial \eta} \end{pmatrix}, \tag{4.94}$$

and so,

$$\det J_e = \frac{\partial r^e}{\partial \xi}\frac{\partial z^e}{\partial \eta} - \frac{\partial r^e}{\partial \eta}\frac{\partial z^e}{\partial \xi}. \tag{4.95}$$

By numbering the local nodes on the master element in the same way as the local nodes on the elements in the computational domain, then $\det J_e > 0$. From (4.92),

$$\frac{\partial r^e}{\partial \xi} = \sum_{i=1}^{6} r_j \frac{\partial \phi_j}{\partial \xi}, \qquad \frac{\partial r^e}{\partial \eta} = \sum_{i=1}^{6} r_j \frac{\partial \phi_j}{\partial \eta}, \tag{4.96a}$$

$$\frac{\partial z^e}{\partial \xi} = \sum_{j=1}^{6} z_j \frac{\partial \phi_j}{\partial \xi}, \qquad \frac{\partial z^e}{\partial \eta} = \sum_{j=1}^{6} z_j \frac{\partial \phi_j}{\partial \eta}, \tag{4.96b}$$

and by substituting these expressions into (4.95),

$$\det J_e = \sum_{i=1}^{6}\sum_{j=1}^{6} \widehat{T}_{ij} r_i z_j, \tag{4.97}$$

where a useful tensor is given by,

$$\widehat{T}_{ij} = \frac{\partial \phi_i}{\partial \xi}\frac{\partial \phi_j}{\partial \eta} - \frac{\partial \phi_i}{\partial \eta}\frac{\partial \phi_j}{\partial \xi}. \tag{4.98}$$

Derivatives required for the volume integrals can be written using the chain rule as

$$\frac{\partial \phi_i}{\partial r} = \frac{\partial \phi_i}{\partial \xi}\frac{\partial \xi}{\partial r^e} + \frac{\partial \phi_i}{\partial \eta}\frac{\partial \eta}{\partial r^e}, \qquad \frac{\partial \phi_i}{\partial z} = \frac{\partial \phi_i}{\partial \xi}\frac{\partial \xi}{\partial z^e} + \frac{\partial \phi_i}{\partial \eta}\frac{\partial \eta}{\partial z^e}. \tag{4.99}$$

By taking the inverse of the Jacobian matrix (4.94),

$$J_e^{-1} = \begin{pmatrix} \frac{\partial \xi}{\partial r^e} & \frac{\partial \xi}{\partial z^e} \\ \frac{\partial \eta}{\partial r^e} & \frac{\partial \eta}{\partial z^e} \end{pmatrix} = \frac{1}{\det J_e} \begin{pmatrix} \frac{\partial z^e}{\partial \eta} & -\frac{\partial r^e}{\partial \eta} \\ -\frac{\partial z^e}{\partial \xi} & \frac{\partial r^e}{\partial \xi} \end{pmatrix}, \tag{4.100}$$

and substituting the expressions required back into (4.99), then,

$$\frac{\partial \phi_i}{\partial r} = \frac{1}{\det J_e} \left(\frac{\partial \phi_i}{\partial \xi} \frac{\partial z^e}{\partial \eta} - \frac{\partial \phi_i}{\partial \eta} \frac{\partial z^e}{\partial \xi} \right) = \frac{T_i^{(1)}}{\det J_e}, \tag{4.101a}$$

$$\frac{\partial \phi_i}{\partial z} = -\frac{1}{\det J_e} \left(\frac{\partial \phi_i}{\partial \xi} \frac{\partial r^e}{\partial \eta} - \frac{\partial \phi_i}{\partial \eta} \frac{\partial r^e}{\partial \xi} \right) = -\frac{T_i^{(2)}}{\det J_e}, \tag{4.101b}$$

where,

$$T_i^{(1)} = \sum_{j=1}^{6} \widehat{T}_{ij} z_j, \qquad T_i^{(2)} = \sum_{j=1}^{6} \widehat{T}_{ij} r_j. \tag{4.102}$$

The local quadratic interpolation functions $\phi_{1,i}$ are defined on the side of the master element where $\xi = -1$, $\eta = [-1, 1]$ with local nodes $i = 1, 5, 2$. This is the one-dimensional master element. The local linear interpolation functions are defined as,

$$\psi_{1,1} = \psi_1 (\xi = -1, \eta) = \frac{1 + \eta}{2}, \qquad \psi_{1,2} = \psi_2 (\xi = -1, \eta) = \frac{1 - \eta}{2}, \tag{4.103}$$

from which the non-zero local quadratic interpolation functions are constructed as follows,

$$\phi_{1,1} = \psi_{1,1} (2\psi_{1,1} - 1), \quad \phi_{1,2} = \psi_{1,2} (2\psi_{1,2} - 1), \quad \phi_{1,5} = 4\psi_{1,1}\psi_{1,2}. \tag{4.104}$$

Using these local quadratic interpolation functions, the following mapping can be defined which transforms a point on the one dimensional master element to a point on the bound-

ary of an element that coincides with the free surface, side boundary or top boundary,

$$r_1^e = \sum_{j=1,5,2} r_j \phi_{1,j}(\eta), \qquad z_1^e = \sum_{j=1,5,2} z_j \phi_{1,j}(\eta). \tag{4.105}$$

Local free surface, side boundary and top boundary integrals are transformed by,

$$\int_{s^e} f(s)\, ds^e = \int_{\eta=-1}^{\eta=1} f(\eta) \left| \frac{ds^e}{d\eta} \right| d\eta, \tag{4.106a}$$

$$\int_{z_1^e} f(z)\, dz_1^e = -\int_{\eta=-1}^{\eta=1} f(\eta) \left| \frac{dz_1^e}{d\eta} \right| d\eta, \tag{4.106b}$$

$$\int_{r_1^e} f(r)\, dr_1^e = \int_{\eta=-1}^{\eta=1} f(\eta) \left| \frac{dr_1^e}{d\eta} \right| d\eta, \tag{4.106c}$$

respectively, where,

$$\left| \frac{ds^e}{d\eta} \right| = \sqrt{\left(\frac{dr_1^e}{d\eta} \right)^2 + \left(\frac{dz_1^e}{d\eta} \right)^2}, \tag{4.107}$$

and

$$\frac{dr_1^e}{d\eta} = \sum_{i=1,5,2} r_i \frac{d\phi_{1,i}}{d\eta}, \qquad \frac{dz_1^e}{d\eta} = \sum_{i=1,5,2} z_i \frac{d\phi_{1,i}}{d\eta}. \tag{4.108}$$

Therefore,

$$\frac{d\phi_{1,i}}{ds} = \frac{d\phi_{1,i}}{d\eta} \frac{d\eta}{ds^e} = \frac{1}{\sqrt{\left(\frac{dr_1^e}{d\eta} \right)^2 + \left(\frac{dz_1^e}{d\eta} \right)^2}} \frac{d\phi_{1,i}}{d\eta}, \tag{4.109}$$

and so the normal vector on the free surface is given by,

$$\mathbf{n} = (n_r, n_z) = \frac{\left(\frac{dz_1^e}{d\eta}, -\frac{dr_1^e}{d\eta} \right)}{\sqrt{\left(\frac{dr_1^e}{d\eta} \right)^2 + \left(\frac{dz_1^e}{d\eta} \right)^2}}. \tag{4.110}$$

All of the required expressions to map the coefficients of the system of algebraic equations

in the (r, z)-plane to the master element in the (ξ, η)-plane have been found. Appendix C lists the coefficients in terms of (ξ, η). Routine numerical techniques can now be implemented to evaluate these integrals.

4.14 Numerical Integration

Now that the necessary coefficients of the algebraic system can be mapped to the master element, numerical integration is used to evaluate the various volume and surface integrals involved. Since the integrands are polynomials, Gaussian quadrature is ideally suited to this task(Cowper, 1973). For the one dimensional master element, N_1 Gauss points will integrate a polynomial of degree $2N_1 - 1$ exactly. Four Gauss points has been seen to be sufficient in the computations and so,

$$\int_{\eta=-1}^{\eta=1} f(\eta)\, d\eta = \sum_{i=1}^{4} W_i f(\eta_i), \tag{4.111}$$

where the Gauss points η_i and weights W_i are given by,

$$\begin{aligned} &\eta_1 = -\eta_2 = -0.861136311594052 \quad \eta_3 = -\eta_4 = -0.339981043584856 \\ &W_1 = W_2 = 0.347854845137453 \qquad W_3 = W_4 = 0.652145154862546. \end{aligned} \tag{4.112}$$

For the two-dimensional master element, N_1^2 Gauss points will integrate a polynomial of degree $2N_1 - 1$ exactly. Nine Gauss points has been seen to be sufficient in the computations and so,

$$\int_{\xi=-1}^{\xi=1} \int_{\eta=-1}^{\eta=-\xi} f(r(\xi,\eta), z(\xi,\eta))\, d\eta d\xi = \sum_{i=1}^{9} W_i f(\xi_i, \eta_i), \tag{4.113}$$

where the Gauss points (ξ_i, η_i) and weights W_i are given by,

$$\begin{aligned}
&\xi_1 = 0.000000000000000 && \xi_2 = 0.000000000000000 && \xi_3 = 0.000000000000000 \\
&\xi_4 = 0.774596669241483 && \xi_5 = 0.774596669241483 && \xi_6 = 0.774596669241483 \\
&\xi_7 = -0.774596669241483 && \xi_8 = -0.774596669241483 && \xi_9 = -0.774596669241483 \\
&\eta_1 = -0.887298334620741 && \eta_2 = -0.500000000000000 && \eta_3 = -0.112701665379258 \\
&\eta_4 = -0.974596669241483 && \eta_5 = -0.887298334620741 && \eta_6 = -0.800000000000000 \\
&\eta_7 = -0.800000000000000 && \eta_8 = -0.112701665379258 && \eta_9 = 0.574596669241483 \\
&W_1 = 0.246913580246913 && W_2 = 0.395061728395061 && W_3 = 0.246913580246913 \\
&W_4 = 0.034784464623227 && W_5 = 0.055655143397164 && W_6 = 0.034784464623227 \\
&W_7 = 0.273857510685414 && W_8 = 0.438172017096662 && W_9 = 0.273857510685414.
\end{aligned} \tag{4.114}$$

The coefficients of the system of algebraic equations given by the residuals can now be evaluated. However, a method is required to solve this system of non-linear algebraic equations.

4.15 Solution to the System of Equations

The system of algebraic equations, given by the continuity residual (4.38), the r and z components of the momentum residual (4.35a & 4.35b), the kinematic residual (4.36), mesh residual (see Section 4.12.2) and volume constraint (4.84), is represented by,

$$\begin{aligned}
\mathbf{R}(\boldsymbol{\alpha}) = \Big[& R_1^{M,r}(\boldsymbol{\alpha}), ..., R_N^{M,r}(\boldsymbol{\alpha}), R_1^{M,z}(\boldsymbol{\alpha}), ..., R_N^{M,z}(\boldsymbol{\alpha}), R_1^{C}(\boldsymbol{\alpha}), ..., R_{N_p}^{C}(\boldsymbol{\alpha}), \\
& R_1^{K}(\boldsymbol{\alpha}), ..., R_{N_1}^{K}(\boldsymbol{\alpha}), R_1^{n}(\boldsymbol{\alpha}), ..., R_{N_1}^{n}(\boldsymbol{\alpha}), R^{V}(\boldsymbol{\alpha}) \Big]
\end{aligned} \tag{4.115}$$

where,

$$\boldsymbol{\alpha} = \left(u_1, ..., u_N, w_1, ..., w_N, p_1, ..., p_{N_p}, \chi_1, ..., \chi_{N_1}, \zeta_1, ..., \zeta_{N_1}, p_g\right), \tag{4.116}$$

is the solution vector. A Newton-Raphson solution method,

$$\mathbf{J}\left[\boldsymbol{\alpha}_{(m+1)} - \boldsymbol{\alpha}_{(m)}\right] = -\mathbf{R}\left(\boldsymbol{\alpha}_{(m)}\right), \tag{4.117}$$

where an updated solution vector $\boldsymbol{\alpha}_{(m+1)}$ is computed from the existing solution vector $\boldsymbol{\alpha}_{(m)}$ using the Jacobian matrix $\mathbf{J}$ and the residuals $\mathbf{R}$ evaluated using the existing solution vector. The Jacobian matrix is defined as

$$J_{ik} = \frac{\partial R_i(\boldsymbol{\alpha}_{(m)})}{\partial \alpha_{(m),K}}, \qquad i, k = 1, ..., N_T. \tag{4.118}$$

The entries of the Jacobian matrix are calculated analytically apart from the dependences on the free surface unknowns. The dependency of each node position on the free surface unknowns are calculated numerically.

For the first time step, the initial solution vector $\boldsymbol{\alpha}^0$ contains the initial conditions. The residuals and the Jacobian matrix are then computed using this solution and are then updated after every iteration. When $|\boldsymbol{\alpha}_{m+1} - \boldsymbol{\alpha}_m| / |\boldsymbol{\alpha}_m|$ is within a certain tolerance, then $\boldsymbol{\alpha}^{(1)} = \boldsymbol{\alpha}_{m+1}$ is the solution at the first time step. For the second time step, $\boldsymbol{\alpha}_{m+1}$ becomes $\boldsymbol{\alpha}^0$ and the process continues.

This system (4.117) is solved using the MA41 solver, for a sparse, unsymmetrical linear system of equations, from the Harwell Subroutine Library.

4.16 Summary

In this chapter, the construction of a finite element method based computational framework, to solve the system of equations identified in Chapter 3, was described. In the next chapter, the accuracy of the numerical platform is validated using a test case.

Chapter 5

Validation of the Numerical Platform

To ensure that the numerical platform described in Chapter 4 will produce accurate results, the code should be benchmarked against selected test cases with known analytical results. The test case discussed here is the evolution of a Rayleigh bubble where the temporal evolution of the radius of the bubble is described by the Rayleigh-Plesset equation (Plesset & Prosperetti, 1977). As the temporal and spatial resolution is increased, the solution produced by the numerical platform should converge towards the solution given by the equation.

Once the numerical platform has been seen to produce accurate results for the simulation of a Rayleigh bubble, additional numerical details, such as the number of spines or the time step, required for an accurate simulation of the formation of a bubble are given.

In order to validate the viscous terms in the numerical platform, a simple test case of Poiseuille flow in a pipe was considered but not described here. As spatial resolution was increased, the solution computed by the code converged to the exact solution. The test case of the Rayleigh bubble will validate the inertial, capillarity and kinematic terms in the code.

5.1 The Rayleigh Bubble

The dimensional radius $R(t)$ of a spherical bubble of gas that oscillates in a viscous, incompressible liquid in an infinite medium, in the absence of body forces, is described by the Rayleigh-Plesset equation,

$$R\frac{d^2R}{dt^2} + \frac{3}{2}\left(\frac{dR}{dt}\right)^2 = \frac{1}{\rho}\left(p_g - p_\infty - \frac{2\sigma}{R} - \frac{4\mu}{R}\frac{dR}{dt}\right), \tag{5.1}$$

with the initial conditions,

$$R = R_0, \qquad \frac{dR}{dt} = 0, \tag{5.2}$$

where p_∞ is the pressure at infinity (Plesset and Prosperetti 1977). The gas is assumed to be adiabatic and so,

$$p_g = p_v + p_i\left(\frac{R_0}{R}\right)^{3\kappa}, \tag{5.3}$$

where p_v is the vapor pressure, p_i is the initial pressure of the gas and κ is the adiabatic gas constant.

Rescaling (5.1) with the following scales for length R_0, velocity $U = \sigma/\mu$, time $T = R_0\mu/\sigma$ and pressure σ/R_0 gives,

$$R\frac{d^2R}{dt^2} + \frac{3}{2}\left(\frac{dR}{dt}\right)^2 = Oh^2\left[p_v + p_i\left(\frac{1}{R}\right)^{3\kappa} - \frac{2}{R} - p_\infty - \frac{4}{R}\frac{dR}{dt}\right], \tag{5.4}$$

with the initial conditions,

$$R = 1, \qquad \frac{dR}{dt} = 0, \tag{5.5}$$

where the Ohnesorge number is $Oh = \mu/\sqrt{\rho\sigma R_0}$.

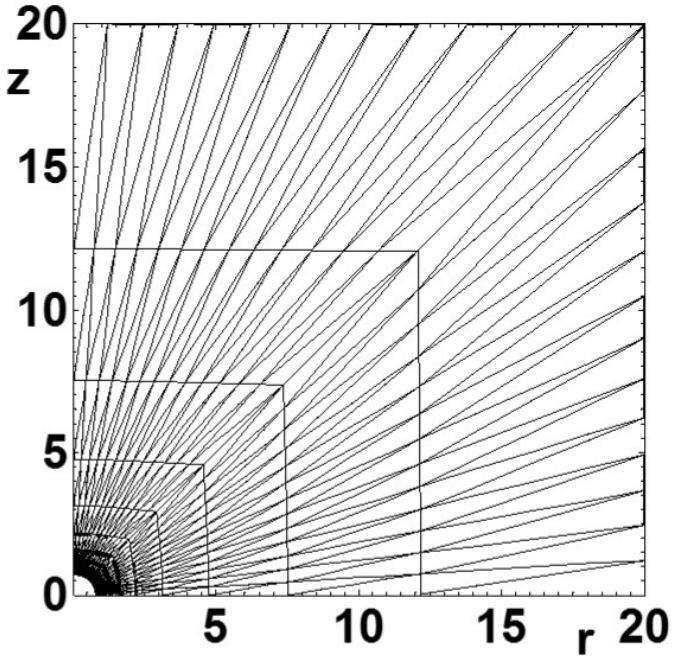

Figure 5.1: The computational mesh used for the simulation of a Rayleigh bubble.

5.1.1 Numerical Details

In order to simulate the evolution of a Rayleigh bubble some small changes were made to the framework described in Chapter 4. First of all, a much simpler computational mesh is used. Due to the spherical symmetry of the problem, which is not explicitly assumed in the computational solution, the spines are fixed in position and travel radially from the free surface to the side and top boundaries of the flow domain (see Figure 5.1) whilst the nodes distributed along the free surface remain equally spaced.

The position of each free surface node can then be described using only one unknown, rather than two, since the angle each spine makes with the axis of symmetry remains fixed. The free surface unknown for each free surface node is simply the distance from the node to the origin. Consequently, the mesh residuals are not required here. The evolution of the bubble volume is also not prescribed so the volume constraint is not required either.

The solid surface described in Chapter 4 is now a plane of symmetry and therefore the corresponding symmetry conditions must be applied to this domain boundary. The z component of the momentum residual (4.35b) remains unchanged whilst the r component of the momentum residual (4.35a) for nodes along this new axis of symmetry is given by the r component of the velocity contribution (4.29a). At the first free surface node, the r components of both the volume and free surface contributions must be applied. Therefore (4.35a) is amended as follows,

$$R_I^{M,r} = \begin{cases} u_I & \text{for } I \in X_5 \\ \left(R_I^{M,r}\right)_{A_3} & \text{for } I \in X_3 \backslash (X_2 \cup X_4) \\ \left(R_I^{M,r}\right)_{A_4} & \text{for } I \in X_4 \backslash X_5 \\ \left(R_I^{M,r}\right)_{V} & \text{for } I \in X \backslash (X_1 \cup (X_3 \backslash X_2) \cup X_4 \cup X_5) \\ \left(R_I^{M,r}\right)_{V} + \left(R_I^{M,r}\right)_{A_1} & \text{for } I \in X_1 \backslash X_5. \end{cases} \tag{5.6}$$

The continuity residual (4.38) is slightly amended with $p_m = p_\infty$, whilst the kinematic residual (4.36) is given by

$$R_I^K = \left(R_I^K\right)_{A_1} \qquad I = 1, ..., N_1, \tag{5.7}$$

since no free surface node remains pinned.

5.1.2 Results

The numerical platform is now set up to simulate the evolution of a Rayleigh bubble. Two sets of parameters are considered,

(a) $Oh = 10^{-1}$, $p_i = 1$ and $p_\infty = 0$.

(b) $Oh = 1$, $p_i = 20$ and $p_\infty = 5$.

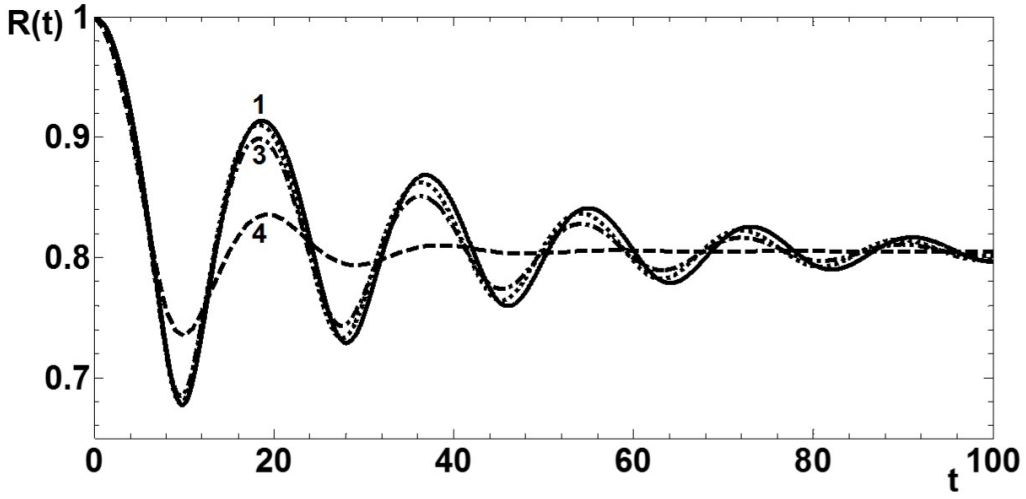

Figure 5.2: The evolution of the bubble radius with time for parameter set (a) for various time steps Δt. The Rayleigh-Plesset solution is given by line 1, $\Delta t = 10^{-2}$ (2), $\Delta t = 10^{-1}$ (3) and $\Delta t = 1$ (4) where $N_1 = 101$.

The remaining parameters are the same for both sets, $p_v = 0$ and $\kappa = 1.4$. The solution to the Rayleigh-Pleset equation is generated using the ode45 solver in MATLAB.

For parameter set (a), the influence of the time step Δt on the accuracy of the solution computed by the numerical platform is shown by Figure 5.2. As Δt decreases, the solution computed by the numerical platform converges to the solution described by the Rayleigh-Plesset equation. The influence of the number of spines N_1 on the temporal evolution of the bubble radius is negligible and so curves representing the evolution of bubble radius against time are nearly indistinguishable and so are not given here.

For parameter set (b), the influence of the time step Δt on the accuracy of the solution computed by the numerical platform is shown by Figure 5.3a. As Δt decreases, the solution computed by the numerical platform converges to the solution described by the Rayleigh-Plesset equation.

The influence of the number of spines N_1, on the accuracy of the solution is shown by Figure 5.3b. As N_1 increases, the solution computed by the numerical platform converges to the solution described by the Rayleigh-Plesset equation.

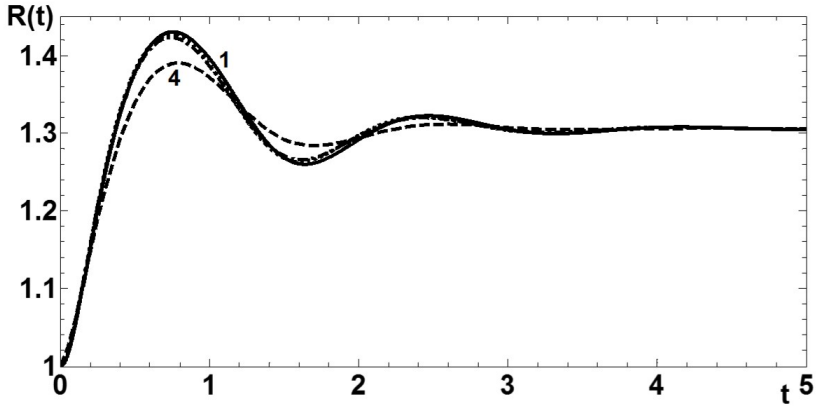

(a) For $N_1 = 101$, the Rayleigh-Plesset solution is given by line 1, $\Delta t = 5 \times 10^{-4}$ (2), $\Delta t = 5 \times 10^{-3}$ (3) and $\Delta t = 5 \times 10^{-2}$ (4).

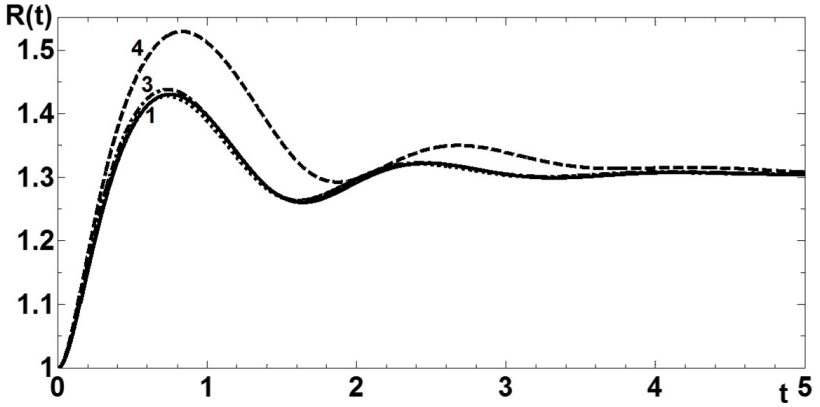

(b) For $\Delta t = 5 \times 10^{-4}$, the Rayleigh-Plesset solution is given by line 1, $N_1 = 101$ (2), $N_1 = 53$ (3) and $N_1 = 17$ (4).

Figure 5.3: The evolution of the bubble radius with time for parameter set (b) for various time steps Δt and number of spines N_1.

For both parameter sets, (a) and (b), as the number of spines is increased and the time step is decreased, the solution computed by the numerical platform converges to the solution given by the Rayleigh-Plesset equation. Therefore, as required, the accuracy of the solution computed by the numerical platform improves for increased temporal and spatial resolution.

5.2 Additional Numerical Details for Bubble Formation

As discussed in Section 4.3, the values of R and Z need to be sufficiently large so that the boundary conditions imposed on the side and top boundaries do not influence the growth of the bubble and also the pressure field remains hydrostatic along the side boundary. For all computations, R was at least five times the maximum width of the bubble and Z was at least four times the maximum height of the bubble. Increasing these values had a negligible effect on the formation process.

At least 125 nodes were distributed along the free surface. The majority of which, 81 nodes, were required in the pinch-off region of the mesh so that the pinch-off of the bubble could be captured accurately. In some cases of very large flow rates, simulations used up to 153 free surface nodes as additional precision was needed adjacent to the contact line to capture the initial deformation of the free surface. Further increases in the number of nodes was seen to have a negligible impact on the global characteristics of the flow.

In each simulation, at least 100 time steps were used before the bubble formed a neck. Once the pinch-off process began, it was necessary to reduce the time step in order to accurately capture the dynamics involved in this process. A time step that decreased logarithmically with the minimum neck radius was chosen and so around 500–700 time steps captured the pinch-off process. The final time step for a simulation was $\mathcal{O}\left(10^{-5}\right)$–$\mathcal{O}\left(10^{-4}\right)$.

5.3 Summary

In this chapter, the numerical platform described in Chapter 4 was benchmarked against a test case of the evolution of the Rayleigh bubble. The results produced by the code

were seen to converge with increasing spatial and temporal resolution to the solution given by the Rayleigh-Plesset equation. Additional numerical details required for the accurate simulation of the formation of a bubble were also given.

In the next chapter, the formation of a bubble from an orifice in a submerged solid surface with the contact line pinned to the rim of the orifice is investigated.

Chapter 6

Bubble Formation from an Orifice

In this chapter, the influence of the three dimensionless parameters identified in Chapter 3, the orifice radius r_o, the Ohnesorge number Oh and the gas flow rate Q, on the global characteristics of bubble formation, in particular on the dimensionless formation time t_d and volume V_d, can now be investigated.

A simulation runs until the minimum neck radius $r_{min} = r_{tol}$, where the tolerance $r_{tol} = 5 \times 10^{-2}\ r_o$. The formation time t_d is taken to be the time of the final solution, as $r_{min} = r_{tol}$, whilst the volume V_d of the bubble that is formed is the volume of the bubble above the point on the free surface which represents the minimum neck radius at the formation time.

6.1 A Typical Case of Bubble Formation

Figure 6.1 shows a typical case of bubble formation. Figures (6.1a)–(6.1d) comprise of experimental images, reproduced from a recent paper of Di Bari & Robinson (2013), with the corresponding free surface profile, computed by the numerical platform, superimposed on top. The solid surface is shown as a horizontal black line at $r \geqslant r_o$, $z = 0$. Since Figure 6.1 shows the entire cross-section of the bubble, the dimensional abscissa is given

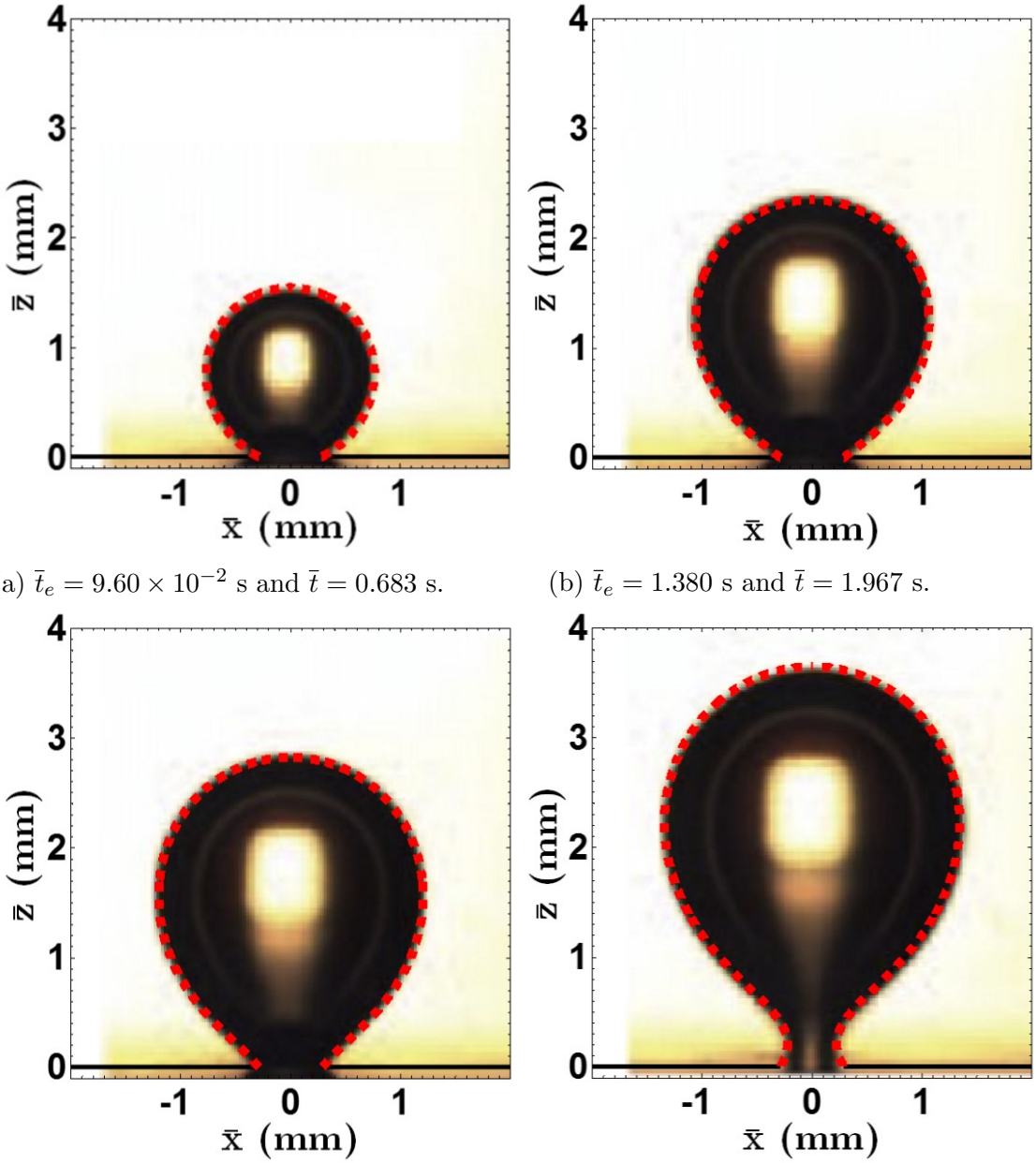

(a) $\bar{t}_e = 9.60 \times 10^{-2}$ s and $\bar{t} = 0.683$ s.

(b) $\bar{t}_e = 1.380$ s and $\bar{t} = 1.967$ s.

(c) $\bar{t}_e = 2.340$ s and $\bar{t} = 2.927$ s.

(d) $\bar{t}_e = 3.550$ s and $\bar{t} = 4.137$ s.

Figure 6.1: The superposition of computational free surface profiles and experimental images for the case $(r_o, Oh, Q) = (0.106, 2.24 \times 10^{-3}, 5.11 \times 10^{-6})$. The experimental images are reproduced from Di Bari & Robinson (2013). The dimensional experimental $\bar{t}_e$ and simulation $\bar{t}$ times are given with each subfigure.

by $\overline{x}$ rather than $\overline{r}$. The experimental images show the formation of an air bubble in water ($\rho = 998.2$ kg m^{-3}, $\mu = 10^{-3}$ Pa s, $\sigma = 73$ mN m^{-1}) by applying a dimensional volumetric

gas flow rate of $\overline{Q} = 2.78$ mm^3 s^{-1} through an orifice of dimensional radius $\overline{r}_c = 0.29$ mm in a submerged solid surface. There is very good agreement between the simulation and the experiment.

With $g = 9.81$ m s^{-2} and using the scales identified in the problem formulation, the material parameters of the liquid give rise to the length scale $L = 2.73$ mm, velocity scale $U = 73$ m s^{-1}, pressure scale $\sigma/L = 26.7$ Pa, time scale $L/U = 3.74 \times 10^{-5}$ s and flow rate scale $L^2U = 5.44 \times 10^{-4}$ m^3 s^{-1}. The experiment is then classified as the dimensionless case of $(r_o, Oh, Q) = (0.106, 2.24 \times 10^{-3}, 5.11 \times 10^{-6})$.

The dimensional experimental times $\overline{t}_e$ that accompany each image are 9.60×10^{-2} s, 1.380 s, 2.340 s and 3.550 s, respectively. However, the initial configuration at $\overline{t}_e = 0$ s is unclear as that result was not published and so, in order to compare the simulation to the experiment, the simulated free surface profile that best matched the fourth experimental image (see Figure 6.1d) was selected. This profile occurred at the dimensional simulation time $\overline{t} = 4.137$ s, and so the criterion $\overline{t} = \overline{t}_e + 0.587$ was used to find the corresponding simulation time of the first three experimental images. The dimensional simulation times of the four computed solutions are therefore $\overline{t} = 0.683$ s, 1.967 s, 2.927 s and 4.137 s.

At $\overline{t} = 0$ s, the simulated bubble starts as a spherical cap of volume 1.677×10^{-2} mm^3. Initially, the bubble grows spherically as the force of capillarity controls the early growth (see Figure 6.1a and 6.1b). The volume of the bubble at $\overline{t} = 0.683$ s and 1.967 s is 1.937 mm^3 and 5.473 mm^3, respectively. By $\overline{t} = 2.927$ s, the force of buoyancy becomes important on the bubble of volume 8.176 mm^3. The bubble translates upwards and begins to lose sphericity above the contact line (see Figure 6.1c).

As the bubble seeks to minimise its surface area at a given volume and due to the fact that the hydrostatic pressure varies linearly along the bubble, a neck begins to form in the free surface. This can be seen at $\overline{t} = 4.137$ s (see Figure 6.1d) where the volume of the bubble is now 11.518 mm^3. Once the neck has formed, as there is a change in the sign

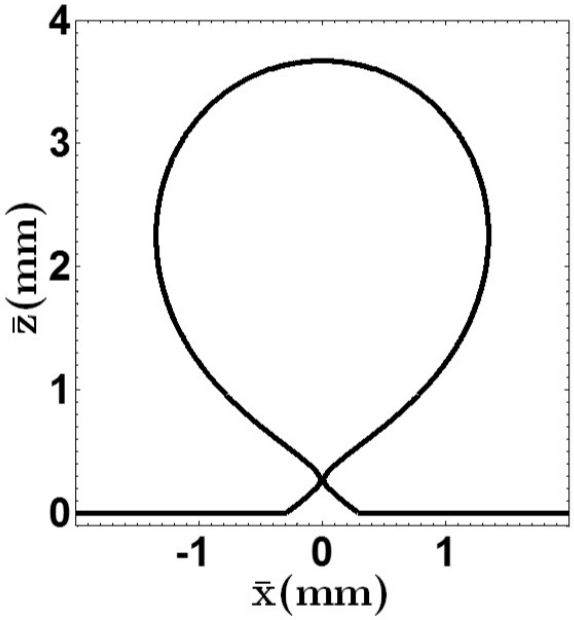

Figure 6.2: The final computed solution of the case $(r_o, Oh, Q) = (0.106, 2.24\times10^{-3}, 5.11\times10^{-6})$, as $r_{min} = r_{tol}$, where $\bar{t} = 4.139$ s and so $t_d = 1.107 \times 10^5$.

of the longitudinal curvature at some point on the free surface, the pinch-off process can begin. The increasing difference in hydrostatic pressure between the apex and the base of the bubble results in an increase of capillary pressure at the neck which then drives the shrinking of the neck still further.

Figure 6.2 shows the final computed solution, as $r_{min} = r_{tol}$, at $\bar{t} = 4.139$ s. Here, the total volume of the bubble is 11.523 mm^3, whilst the volume of the newly formed bubble, measured above the point of minimum neck radius is 11.502 mm^3. Therefore, this final solution corresponds to a dimensionless formation time of $t_d = 1.107 \times 10^5$ and a dimensionless bubble volume of $V_d = 0.5651$.

Compared to the overall generation of the bubble, which took 4.139 s, the pinch-off process, occurring between Figure 6.1d and Figure 6.2, takes place much faster in just 1.68×10^{-2} s. Notably, while the experiments appear unable to capture the very small time scales in the final stages of pinch-off, this is no barrier for the computations.

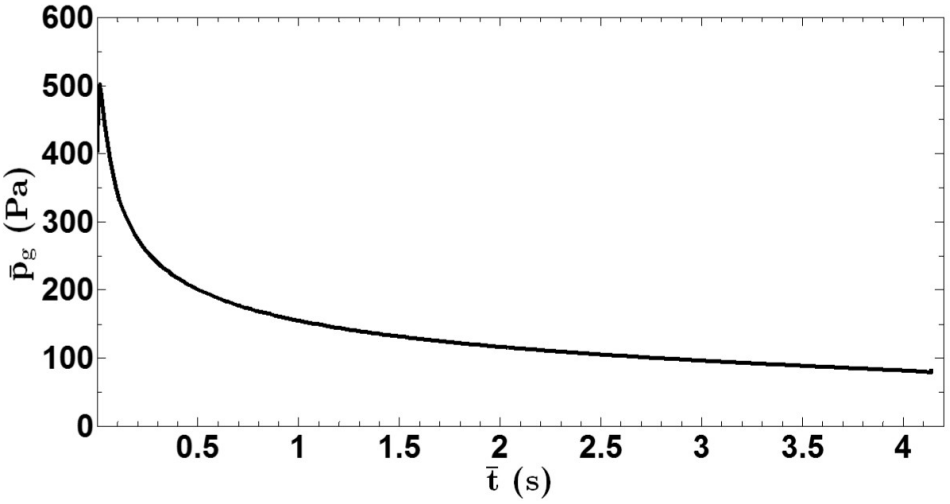

Figure 6.3: The variation of the dimensional gas pressure $\overline{p}_g$ from its reference value with dimensional simulation time $\bar{t}$ for the case of $(r_o, Oh, Q) = (0.106, 2.24\times10^{-3}, 5.11\times10^{-6})$.

The evolution of the dimensional gas pressure during the simulation is shown by Figure 6.3. Recalling that the pressure field along the side boundary of the domain remains hydrostatic with $p(R, 0, t) = 0$, the gas pressure reaches its greatest value near the start of the simulation as the bubble resembles a hemisphere. The gas pressure then decreases by almost 80% until there is a very slight increase as $r_{min} \to r_{tol}$, which can only be seen under the appropriate magnification.

6.2 Influence of Parameters

Figure 6.4 shows how the global characteristics of bubble formation, the dimensionless formation time t_d (see Figure 6.4a) and the dimensionless bubble volume V_d (see Figure 6.4b), depend upon the gas flow rate Q and the Ohnesorge number Oh for the dimensionless orifice radii of $r_o = 0.1$ and 1. These benchmark calculations fall into two regimes, the regimes of low gas flow rates and high gas flow rates, otherwise known as the 'static' and 'dynamic' regimes, respectively. These regimes are now considered separately.

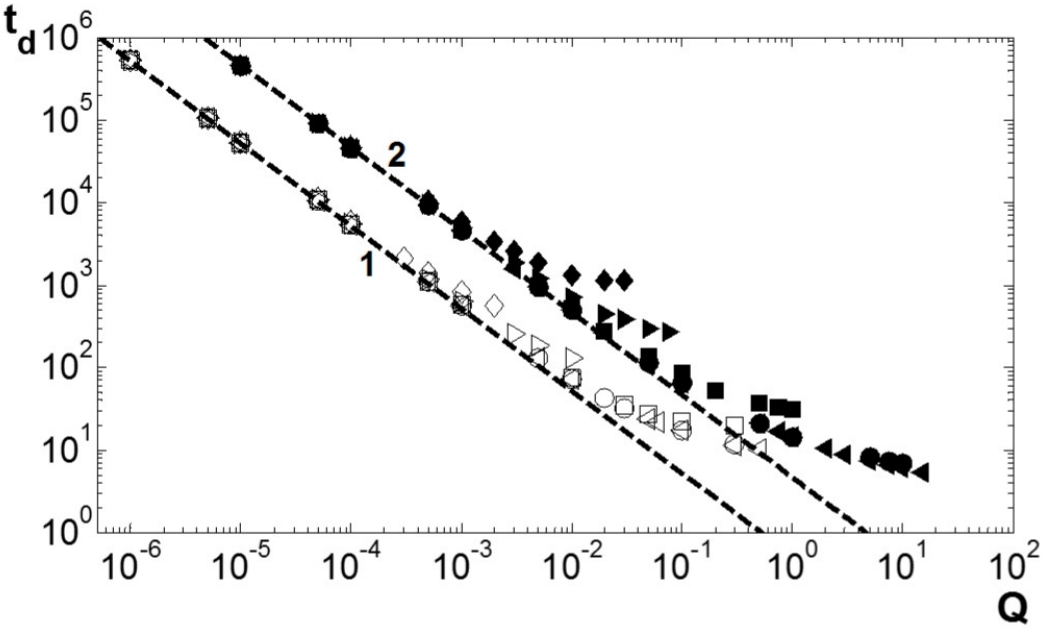

(a) A log-log plot of the dimensionless formation time t_d of the bubble versus the dimensionless flow rate Q for a variety of Ohnesorge numbers Oh. Line 1 is $t_d = 0.53/Q$ and line 2 is $t_d = 4.7/Q$.

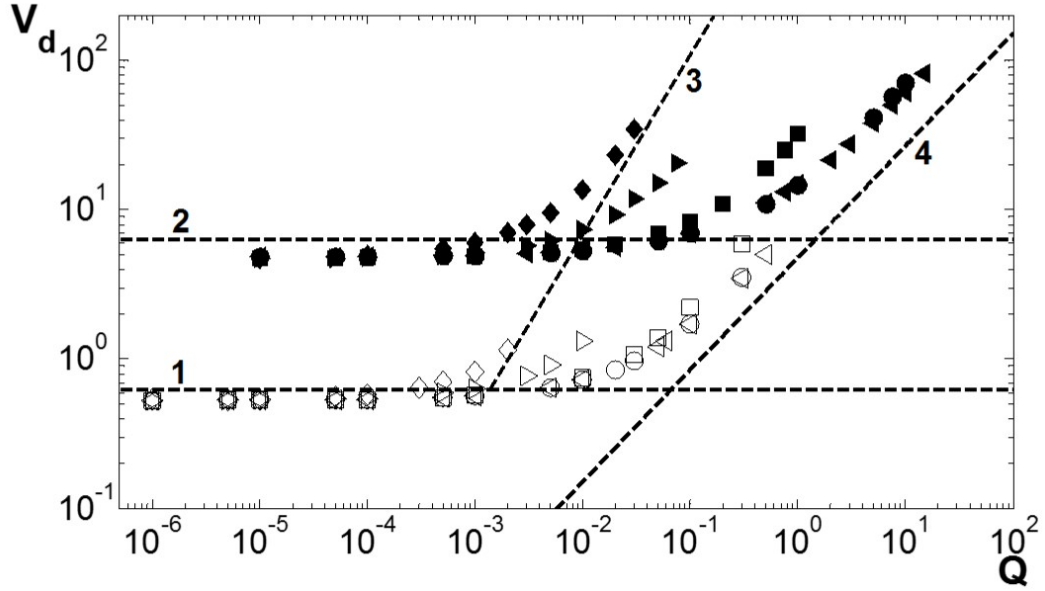

(b) A log-log plot of the dimensionless bubble volume V_d versus the dimensionless flow rate Q for a variety of Ohnesorge numbers Oh. Line 1 is $V_F = 6.28 \times 10^{-1}$, line 2 is $V_F = 6.28$, line 3 is equation (6.4) with $Oh = 2.24 \times 10^{-3}$ and line 4 is equation (6.5).

Figure 6.4: A map of the parameter space where open symbols correspond to $r_o = 0.1$ and filled symbols correspond to $r_o = 1$. The various Ohnesorge numbers are represented by ($\diamond$) $Oh = 2.24 \times 10^{-3}$, ($\triangleright$) $Oh = 10^{-2}$, ($\square$) $Oh = 10^{-1}$, ($\circ$) $Oh = 1$ and ($\triangleleft$) $Oh = 10$.

6.2.1 Regime of Low Gas Flow Rates

For a relatively small gas flow rate, a variation in the Ohnesorge number has little influence on the formation time (see Figure 6.4a) and, consequently, very little effect on the bubble volume (see Figure 6.4b). Therefore, for a given orifice radius, as $Q \to 0$, then $V_d \to V_c$, where V_c is the limiting bubble volume. Specifically, $V_c = 0.53$ and 4.7 for $r_o = 0.1$ and 1.0, respectively. In other words, for a given orifice radius, simply decreasing the flow rate does not lead to smaller bubble volumes in this regime. The force of buoyancy is simply not large enough to detach the bubble from the formation site until the bubble volume approaches V_c.

By assuming that the bubble remains spherical and balancing the forces of buoyancy and capillarity, Fritz (1935) (see Kumar & Kuloor (1970)) derived an expression for this limiting bubble volume which, when rescaled using the scales found in the problem formulation, is given by

$$V_F = 2\pi r_o. \tag{6.1}$$

Therefore $V_F = 6.28 \times 10^{-1}$ and 6.28 for $r_o = 0.1$ and 1, respectively (see lines 1 and 2 respectively on Figure 6.4b). This gives way to large relative errors of 18.5% and 33.6% for $r_o = 0.1$ and 1, respectively, when compared to the simulated limiting volume V_c.

Since the volume of the newly formed bubble is much greater than the volume of the residual bubble then $t_d \approx V_c/Q$ in this regime. Therefore, for $r_o = 0.1$ and 1, the respective formation times can be expressed as $t_d = 0.53/Q$ and $t_d = 4.7/Q$ when $Q < 10^{-4}$ (see lines 1 and 2 respectively in Figure 6.4a).

As expected, the limiting bubble volume V_c increases with orifice radius. These conclusions are in agreement with the literature where the regime of low gas flow rates is also known as the 'static' regime. As will now be shown below, much of the growth of the bubble can be described by a quasi-static approach that involves the Young-Laplace

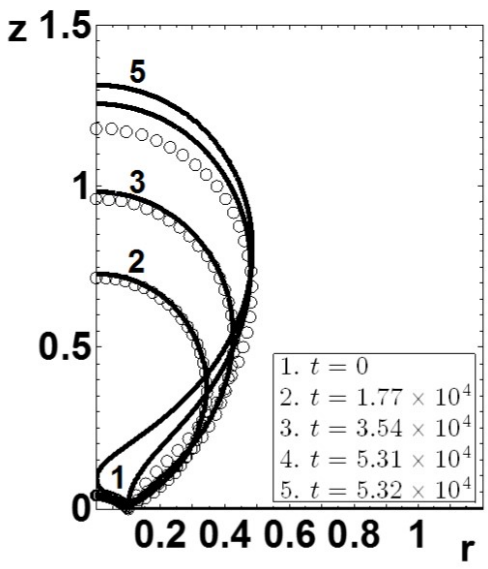

(a) The case of $(r_o, Oh, Q) = (0.1, 1, 10^{-5})$.

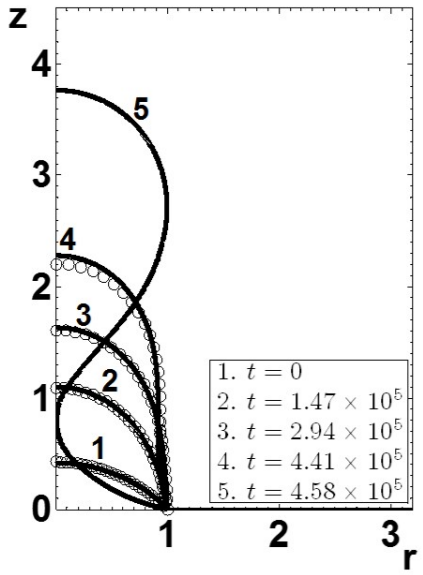

(b) The case of $(r_o, Oh, Q) = (1, 1, 10^{-5})$.

Figure 6.5: The formation of bubbles in the regime of low gas flow rates. The dynamic finite element simulations are given by the black lines whilst the circular symbols represent the finite difference Young-Laplace solutions for quasi-static growth.

equation.

Figure 6.5 shows the simulated temporal evolution of a bubble (continuous black lines) for two cases in the regime of low gas flow rates, $(r_o, Oh, Q) = (0.1, 1, 10^{-5})$ and $(1, 1, 10^{-5})$, respectively. In both cases, curve 1 is the initial solution and curve 4 shows the free surface when the neck first begins to develop. Curves 2 and 3 are equally spaced in time between curves 1 and 4, where it can be seen that, once again, the capillarity force dominates the early stages of bubble growth. This is particularly evident in the case of $r_o = 0.1$ (see Figure 6.5a) where the bubble grows spherically for almost the entire formation time due to its smaller size than the case of $r_o = 1.0$ (see Figure 6.5b). As the pinch-off process continues, the bubble approaches break up and the final solution is given by curve 5 where a bubble of volume $V_d = 0.532$ or 4.90 are formed for $r_o = 0.1$ or 1, respectively.

Due to the relatively small liquid velocities associated with the initial bubble growth

in these cases, the initial growth can be accurately described by a series of quasi-static profiles that are found by solving the Young-Laplace equation and stipulating a small increase in volume from one solution to the next.

Assuming that liquid velocities are negligible and rescaling, the dimensionless Young-Laplace equation is

$$p_g + z = \kappa_1 + \kappa_2, \tag{6.2}$$

where κ_1 and κ_2 are the dimensionless longitudinal and cross-sectional curvatures at each point on the free surface and the liquid pressure is assumed to be hydrostatic, $p(r, z, t) = -z$.

Fordham (1948) and Thoroddsen *et al.* (2005) described a scheme that can be used to solve (6.2), which involves a system of first-order ordinary differential equations. The finite difference method can be used to solve this system and so for a given finite element profile, the corresponding quasi-static solution, with the same bubble volume as the simulation, can then be found. The uniform gas pressure in (6.2) is found as part of each quasi-static solution.

These series of quasi-static profiles are also shown in Figure 6.5 with the circular symbols. There is very good agreement between the first three quasi-static and finite element solutions. However, as the bubble continues to grow, the quasi-static solutions become less accurate, as seen by the fourth solutions. Any further quasi-static solutions are wildly inaccurate.

In summary, in the regime of low gas flow rates, the initial growth of the bubble is a quasi-static process that is governed by the gas, hydrostatic and capillary pressures. As the neck forms and pinch-off begins, bubble growth is an essentially dynamic process, and unsurprisingly, the quasi-static approach using the Young-Laplace equation (6.2) is inadequate in describing the effects of the large velocities associated with the thinning of the neck together with the importance of inertia and viscosity in the liquid.

6.2.2 Regime of High Gas Flow Rates

Greater gas flow rates than those associated with the previous regime are now considered. For a given Ohnesorge number, as the flow rate is increased, it is now the formation time that tends to a limiting value t_c (see Figure 6.4a). In other words, when the flow rate is sufficiently large, a bubble can not form quicker than this limiting time. This effect is most clear in the case of $r_o = 1$. As Q increases, the difference between the formation time of the simulations and the formation time associated with the regime of low gas flow rates ($t_d = 0.53/Q$ and $4.7/Q$ for $r_o = 0.1$ and 1, respectively) increases. In agreement with the literature, this results in an increase in bubble volume V_d with flow rate (see Figure 6.4b).

For a given gas flow rate, the formation time increases with decreasing Ohnesorge number and therefore, due to the bubble inflating at a constant volumetric flow rate, the bubble volume increases with decreasing Ohnesorge number. This is once again more obvious in the case of $r_o = 1.0$ as the formation times tend to a limiting value. As the Ohnesorge number increases, the limiting formation time decreases. For $r_o = 1$, $t_c \approx 1130$, 260, 30, 7 and 5 for $Oh = 2.24 \times 10^{-3}$, 10^{-2}, 10^{-1}, 1 and 10, respectively (see Figure 6.4a). The reason for this is the increased inertia in the liquid opposes the pinching of the neck which leads to a prolonging of the formation time. There is very little difference in the results between an Ohnesorge number of 1 and 10 for all but the very largest of flow rates considered, suggesting that inertial effects become negligible for $Oh > 1$ for the majority of flow rates. Once again, it is worth reiterating that the bubbles formed at a given flow rate from a larger orifice have a larger formation time and therefore a greater volume.

Oğuz & Prosperetti (1993) used a two-stage model which includes the forces of inertia, capillarity and buoyancy to derive a critical flow rate at which, in the case of an inviscid liquid, bubble formation transitions from the low flow rate regime to the high flow rate regime. By rescaling this critical flow rate, using scales described in Chapter 3, it is given

by

$$Q_{cr} = (16/3)^{1/6}\,\pi\; Oh\; r_o^{5/6}. \tag{6.3}$$

For a flow rate $Q \leqslant Q_{cr}$, $V_d = V_F$, whilst for $Q > Q_{cr}$, it was found that

$$V_0 = A_1 \left(\frac{Q}{Oh}\right)^{6/5}, \quad A_1 = \frac{4\pi}{3}\left(\frac{9}{8\pi^2}\right)^{3/5}, \tag{6.4}$$

where A_1 is a constant and the subscript 0 represents the inviscid regime, $Oh \to 0$.

To compare (6.4) with the results presented here, line 3 in Figure 6.4b is (6.4) with $Oh = 2.24 \times 10^{-3}$, the smallest Ohnesorge number simulated. The simulated bubble volumes for $Oh = 2.24 \times 10^{-3}$ and $r_o = 1.0$ approach those values predicted by (6.4) as the flow rate increases. It is unclear whether the scaling law is valid for $r_o = 0.1$ because the greater flow rates required could not be computed by the numerical platform.

Once again, the case of $Oh = 2.24 \times 10^{-3}$ is used to examine the critical flow rate given by (6.3), where $Q_{cr} = 1.37 \times 10^{-3}$ and 9.3×10^{-3} for $r_o = 0.1$ and 1, respectively. These flow rates are also given by the points of intersection of line 3 by line 1 for $r_o = 0.1$ and line 2 for $r_o = 1$ in Figure 6.4b. It can be seen from the simulations that (6.3) overestimates the flow rate at which inviscid bubble formation transitions from the regime of low flow rates to the regime of high flow rates.

In the case of a highly viscous liquid, Wong *et al.* (1998) used a spherical model and balanced the viscous and capillarity forces to derive an expression for the bubble volume where $r_o \to 0$. When rescaled,

$$V_\infty = A_2 Q^{3/4}, \quad A_2 = (500\pi/3)^{1/4}, \tag{6.5}$$

where the subscript ∞ represents the highly viscous regime of $Oh \to \infty$. The volumes predicted by (6.5) underestimate those given by the simulations for the most viscous case

of $Oh = 10$ for both $r_o = 0.1$ and 1 (see line 4 on Figure 6.4b).

It is possible to interpolate between the scaling laws (6.4) and (6.5), for the respective limiting cases of $Oh \to 0$ and $Oh \to \infty$, in an attempt to fit a scaling law to the results for intermediate Ohnesorge numbers shown in Figure 6.4b. Appendix D shows that whilst scaling laws may give a valid approximation of the global characteristics of bubble formation in certain regimes, simulations are required to obtain a more accurate representation of the entire parameter space.

Figures 6.6 and 6.7 show the evolution of the bubble for a cross-section of the parameter space in the regime of high gas flow rates for $r_o = 0.1$ and 1.0, respectively. The cases of $Oh = 1$ and $Oh = 10$ are very similar for this range of flow rates and so the case of $Oh = 10$ is not given in Figures 6.6 and 6.7.

The plots in Figure 6.6 each show six curves. Curve 1 is the initial solution, curve 5 is where the bubble first obtains a neck and curve 6 is the final solution as $r_{min} = r_{tol}$. Curves 2, 3 and 4 are equally spaced in time between curves 1 and 5. The plots in Figure 6.7 have an extra curve. Here, curve 4 is where the neck begins to develop and curve 7 is the final solution, curves 2 and 3 are equally spaced in time between curves 1 and 4, and curves 5 and 6 show the bubble when $r_{min} = 2/3\ r_o$ and $r_{min} = 1/3\ r_o$, respectively.

Due to the greater velocity imparted in the liquid from the larger flow rates and because inertia cannot be ignored at these flow rates, the aforementioned quasi-static approach, using the Young-Laplace equation (6.2), to compute free surface profiles, is valid for a much smaller proportion of the overall formation process than was seen in Figure 6.5 for bubble formation under low gas flow rates. For greater flow rates, the bubble formation process is almost entirely dynamic and therefore this regime of high gas flow rates is also known as the 'dynamic' regime.

A major difference between bubbles forming from orifices of different radii is the increased sphericity of those bubbles for $r_o = 0.1$ due to the larger surface-to-volume ratio

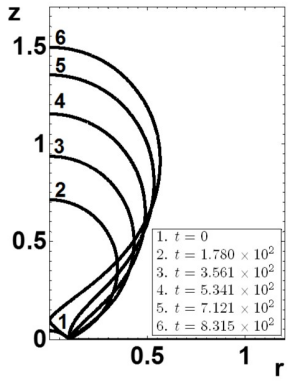

(a) $Oh = 2.24 \times 10^{-3}$, $Q = 10^{-3}$.

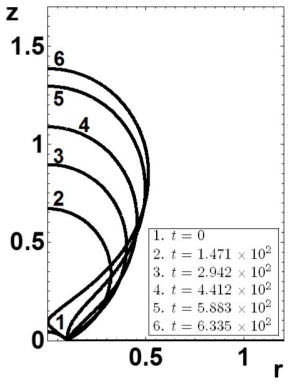

(b) $Oh = 10^{-2}$, $Q = 10^{-3}$.

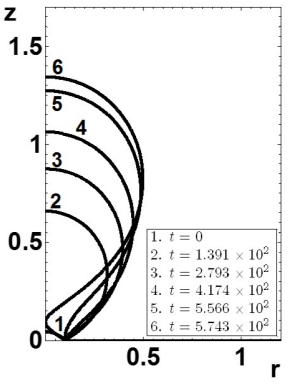

(c) $Oh = 10^{-1}$, $Q = 10^{-3}$.

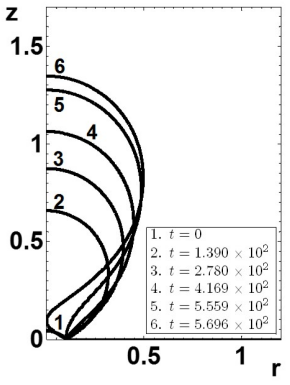

(d) $Oh = 1$, $Q = 10^{-3}$.

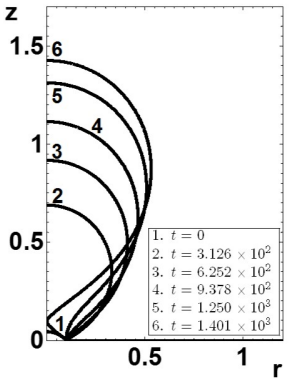

(e) $Oh = 2.24 \times 10^{-3}$, $Q = 5 \times 10^{-4}$.

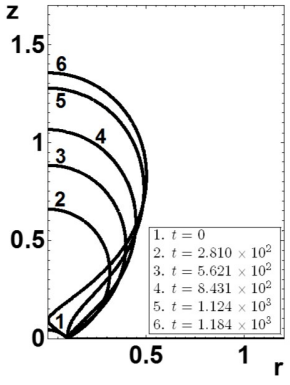

(f) $Oh = 10^{-2}$, $Q = 5 \times 10^{-4}$.

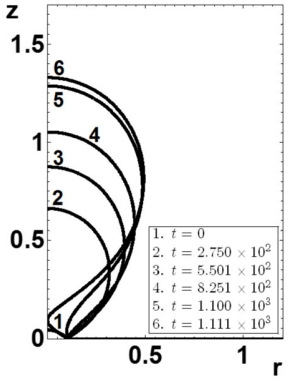

(g) $Oh = 10^{-1}$, $Q = 5 \times 10^{-4}$.

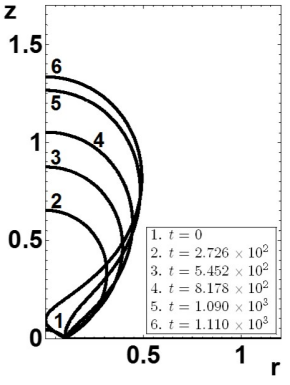

(h) $Oh = 1$, $Q = 5 \times 10^{-4}$.

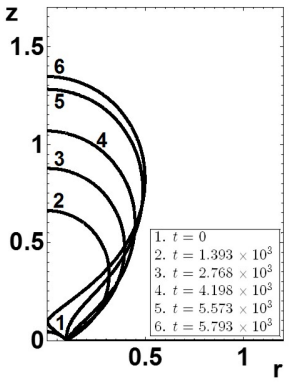

(i) $Oh = 2.24 \times 10^{-3}$, $Q = 10^{-4}$.

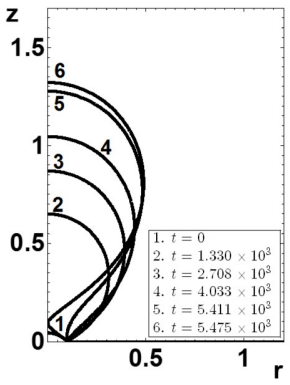

(j) $Oh = 10^{-2}$, $Q = 10^{-4}$.

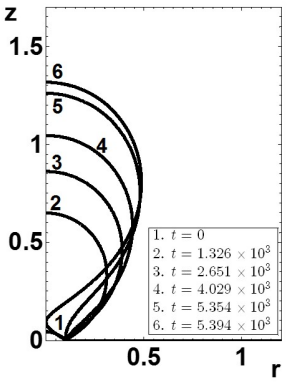

(k) $Oh = 10^{-1}$, $Q = 10^{-4}$.

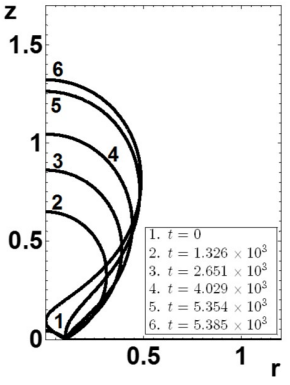

(l) $Oh = 1$, $Q = 10^{-4}$.

Figure 6.6: Temporal evolution of the free surface for various Ohnesorge numbers Oh and flow rates Q for an orifice of radius $r_o = 0.1$.

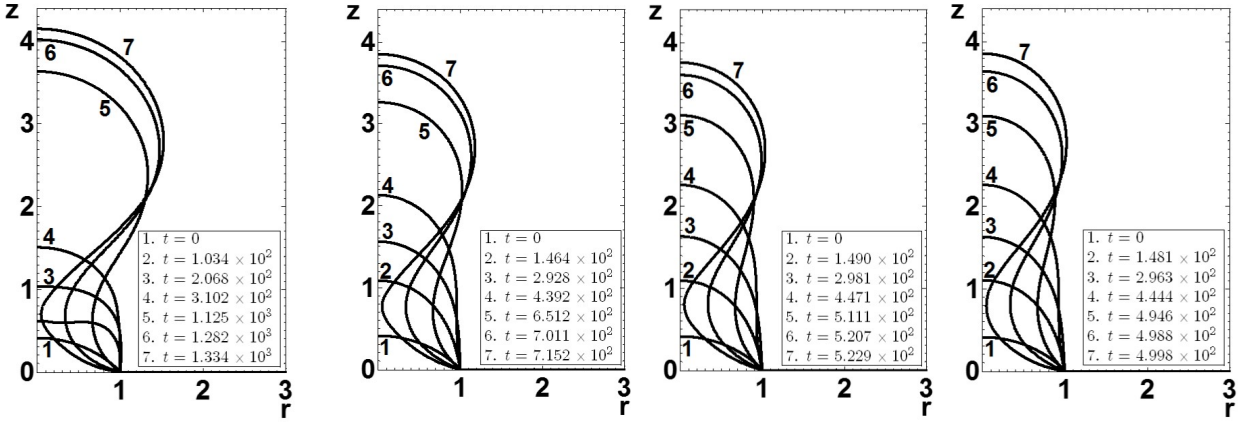

(a) $Oh = 2.24 \times 10^{-3}$, $Q = 10^{-2}$.

(b) $Oh = 10^{-2}$, $Q = 10^{-2}$.

(c) $Oh = 10^{-1}$, $Q = 10^{-2}$.

(d) $Oh = 1$, $Q = 10^{-2}$.

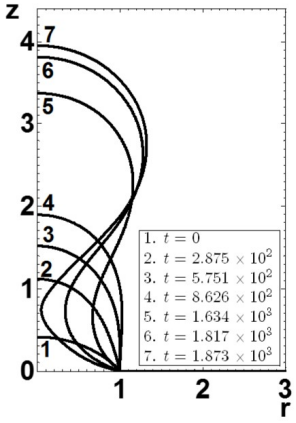

(e) $Oh = 2.24 \times 10^{-3}$, $Q = 5 \times 10^{-3}$.

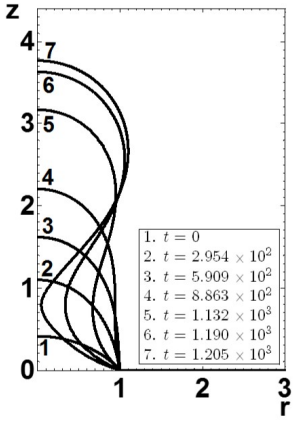

(f) $Oh = 10^{-2}$, $Q = 5 \times 10^{-3}$.

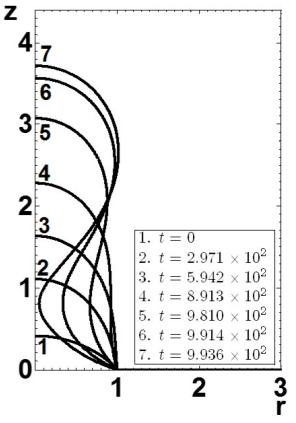

(g) $Oh = 10^{-1}$, $Q = 5 \times 10^{-3}$.

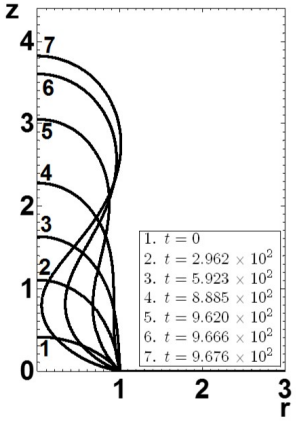

(h) $Oh = 1$, $Q = 5 \times 10^{-3}$.

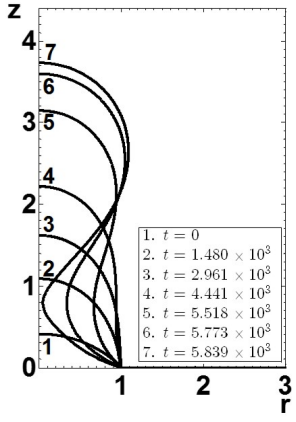

(i) $Oh = 2.24 \times 10^{-3}$, $Q = 10^{-3}$.

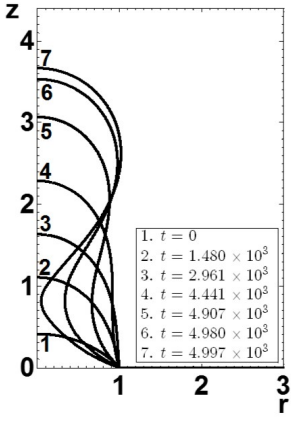

(j) $Oh = 10^{-2}$, $Q = 10^{-3}$.

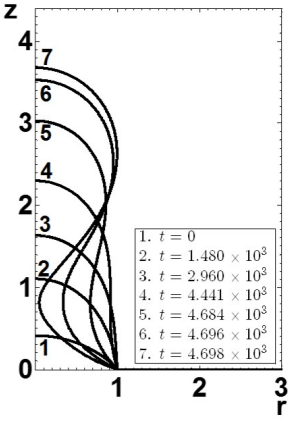

(k) $Oh = 10^{-1}$, $Q = 10^{-3}$.

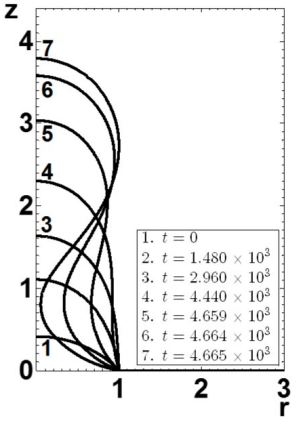

(l) $Oh = 1$, $Q = 10^{-3}$.

Figure 6.7: Temporal evolution of the free surface for various Ohnesorge numbers Oh and flow rates Q for an orifice of radius $r_o = 1.0$.

where surface effects are more important for smaller systems. Also the bubbles generated in the case of $r_o = 0.1$ are much larger relative to the orifice radius than those in the case of $r_o = 1$, which is to be expected since $r_o = 1$ corresponds to the dimensional case where the orifice radius is equal to the length scale.

Once a neck forms, as the longitudinal curvature of the free surface changes sign at a point, let t_n be the time it takes for the bubble to then approach pinch-off as $r_{min} = r_{tol}$. For a given flow rate, the ratio t_n/t_d increases with decreasing Ohnesorge number. The influence of inertia in prolonging the formation time by opposing the thinning of the neck of the bubble is illustrated by Figures 6.6l and 6.6k for $r_o = 0.1$, and by Figures 6.7l and 6.7i for $r_o = 1$, where the times taken for the necks to form are almost equal, yet t_d increases with decreasing Ohnesorge number. This is further highlighted by the rapid vertical displacement of the apex of the bubble seen in Figure 6.7d, where, the apex must rise quickly to make up the volume lost due to this rapid pinch-off, in order to keep the flow rate constant at $Q = 10^{-2}$.

For a given Ohnesorge number, as the flow rate increases, the majority of the increase in volume is accounted for by the increased width of the bubbles, see, for example, Figures 6.6i and 6.6a for $r_o = 0.1$ or Figures 6.7i and 6.7a for $r_o = 1$. The ratio t_n/t_d initially increases with increasing flow rate, as seen in Figure 6.6 and 6.7, before reaching a maximum and then decreasing with increasing flow rate.

Figure 6.8 shows the influence of the Ohnesorge number on the pinch-off process. The outermost and innermost curves on each plot show the free surface as $r_{min} = r_o/2$ and $r_{min} = r_{tol}$, respectively. The eight curves in between these are equally spaced in time with time step $\Delta t = 17.6$, 0.67 and 0.25 for $Oh = 2.24 \times 10^{-3}$, 10^{-1} and 10, respectively.

The spacing of the curves show that the pinch-off of the bubble accelerates as $r_{min} \to 0$, whilst the longitudinal radius of curvature at the point on the free surface which represents the minimum neck radius increases with increasing Ohnesorge number.

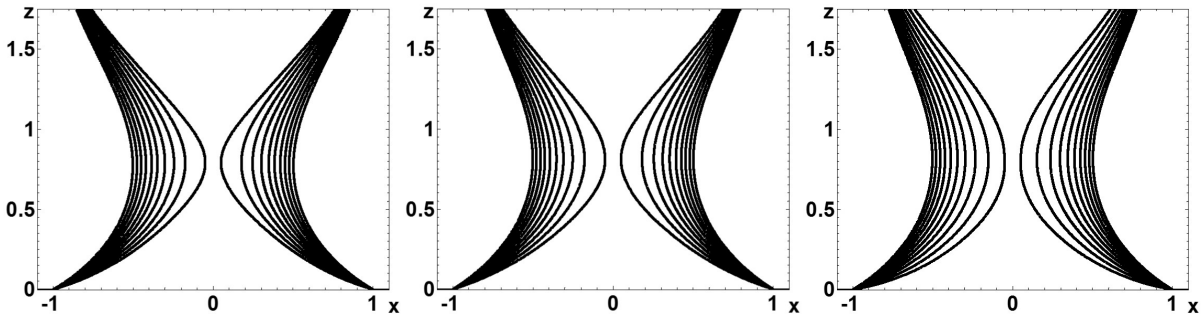

(a) $Oh = 2.24 \times 10^{-3}$ and $\Delta t = 17.6$.

(b) $Oh = 10^{-1}$ and $\Delta t = 0.67$.

(c) $Oh = 10$ and $\Delta t = 0.25$.

Figure 6.8: The influence of Ohnesorge number on the temporal evolution of the neck of the bubble during the pinch-off process for the case $r_o = 1$ and $Q = 10^{-3}$. The outermost and innermost curves represent the respective cases of $r_{min} = r_o/2$ and $r_{min} = r_{tol}$. The intermediate curves are equally spaced in time, with time step Δt.

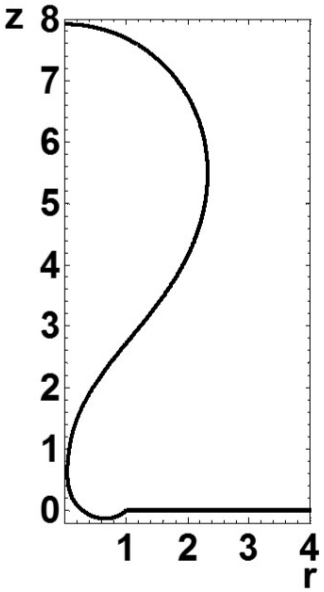

Figure 6.9: Evidence of the liquid phase entering the mouth of the orifice as $r_{min} = r_{tol}$ for the case $(r_o, Oh, Q) = (1, 10, 7.5)$ where $t_d = 6.596$ and $V_d = 50.12$.

Finally, for larger Ohnesorge numbers at sufficiently high flow rates when $r_o = 1$, the liquid phase enters the mouth of the orifice towards the end of the formation process (see Figure 6.9). The gas phase with spatially uniform pressure p_g is present not just above the orifice but below it too. Therefore there is no restriction on the free surface entering

the mouth of the orifice if the normal stress boundary condition dictates this.

6.3 Summary

In this chapter, the formation of a bubble from an orifice in a submerged solid surface whose contact line is pinned to the rim of the orifice was investigated.

In the next chapter, the more complex case of bubble formation with a moving contact line is investigated.

Chapter 7

The Formation of a Bubble with a Moving Contact Line

In this chapter, the influence of wettability on the formation of a bubble is considered. The wettability of the substrate is no longer required to be sufficiently large to pin the contact line to the rim of the orifice and so it is free to move along the solid surface. As will be shown, incorporating a moving contact line into the computational framework involves additional theoretical and numerical complexities.

7.1 Review of the Literature

The generation of a gas bubble, when the contact line is free to move, is critical for the successful operation of numerous technologies, ranging from traditional applications of chemical engineering, such as boiling (Rohsenow, 1971), through to emerging microfluidic ones, including lab-on-a-chip devices (Stone *et al.*, 2004). Establishing how the local dynamics, such as the motion of the contact line, and the global dynamics, such as the formation time and volume of the detaching bubble, behave under certain regimes of parameters is key to understanding and optimising these processes.

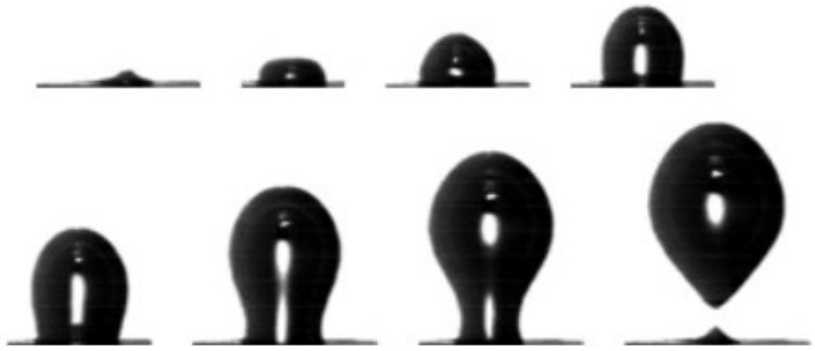

Figure 7.1: The formation of air bubbles in water from an orifice with a moving contact line (Chen *et al.*, 2009).

In the case of boiling, a vapour bubble is formed at a nucleation site which is created through irregularities in the surface. The bubble then grows, breaks away from the nucleation site and then another bubble can form in its place. In order to better understand certain aspects of this problem, some experiments generate a bubble by pumping gas through an orifice in a submerged solid surface. Therefore, there are two cases of bubble formation with a moving contact line to consider, (a) the formation from an orifice of finite size and (b) the formation from an impermeable wall, which is considered here as formation from an infinitesimally small orifice.

Experiments have shown that the formation of a bubble, when the contact line is free to move, undergoes the following stages (see Figure 7.1). First, as the bubble begins to grow, it displaces the ambient liquid from the solid, so that, if viewed through the liquid, the contact line recedes and the solid is 'de-wet'. As the volume of the bubble increases, the process begins to be dominated by buoyancy which pulls the growing bubble upwards and acts to oppose the motion of the receding contact line by slowing its progress. As this de-wetting of the solid comes to an end, the contact line may then start to advance, as the liquid phase now displaces the gas from the solid, in a process of 'dynamic wetting'. The bubble then detaches as a result of the break-up of the neck connecting the departing

bubble with the one remaining on the solid (as shown in Figure 7.1) or, possibly, in the case of a bubble formation from a wall, the complete disappearance of its base.

In terms of the physics involved, the formation of a bubble with a moving contact line brings into play several additional factors compared to the case where the contact line is pinned, namely the wettability of the solid surface and, most importantly, its characteristics with regard to the wetting/de-wetting dynamics. As is known from experiments, in certain regimes these factors dramatically alter the process of bubble formation and its global characteristics (Lin *et al.*, 1994).

The wettability of an ideal solid surface, free from roughness and chemical inhomogeneity, is characterised by a unique static contact angle determined by the balance of forces acting on the contact line and defined by Young's equation (Young, 1805). The contact line will recede when the contact angle is smaller than the static contact angle and then advance when the contact angle becomes larger than the static contact angle. The static contact angle is locally unique at every point of the contact line on a heterogeneous surface.

An additional physical mechanism is contact angle hysteresis, i.e. the existence of an entire interval of contact angles, between the 'static receding' contact angle θ_r and the 'static advancing' one θ_a. The contact line recedes when the contact angle is smaller than the static receding angle and will advance when the contact angle is larger than the static advancing angle. In the interval of contact angles between the static receding and static advancing contact angles, the contact line is pinned (Eral & Oh, 2013). This phenomenon is a collective effect caused by roughness and/or chemical inhomogeneity of the solid substrate.

Experiments in bubble formation show that the contact line of a bubble forming from a finite-size orifice in a hydrophilic surface (small static contact angle) will not recede very far from the orifice before advancing and becoming pinned again, it may even remain

pinned to the rim of the orifice for the duration of bubble formation (Lin *et al.*, 1994; Gnyloskurenko *et al.*, 2003; Byakova *et al.*, 2003). Therefore the volume of the bubble increases as the size of the orifice increases. On the other hand, the contact line of a bubble forming from an orifice in a hydrophobic surface will recede much further, even at low gas flow rates, thus increasing the formation time and therefore increasing the volume of the bubble formed. In some cases, the volume of a bubble formed on a hydrophobic surface may be independent of the orifice size as the bubble pinches off, at a point above the substrate, before the contact line has advanced back to the rim of the orifice.

Two formation regimes are known to exist (Chen *et al.*, 2013b; Corchero *et al.*, 2006). At sufficiently small gas flow rates for a given wettability, the volume of the bubble is independent of the gas flow rate with the formation time simply increasing with decreasing flow rate. However at greater gas flow rates, the volume of the bubble increases with increasing flow rate, and is independent of the orifice size and, at sufficiently high flow rates, wettability.

From a theoretical perspective, the motion of the contact line opens up a number of challenging issues associated with the mathematical modelling of dynamic wetting/de-wetting processes first identified in Huh & Scriven (1971). Furthermore, as will be seen below, the models developed to address the 'moving contact-line problem' invariably introduce small length scales associated with the specific physics of wetting into the mathematical formulation, thus making the resulting problem inherently multiscale and calling for tailor-made computational schemes to be developed. In other words, adding contact line motion to the bubble formation and detachment process leads to a considerable increase in the complexity of the problem.

Dynamic wetting/de-wetting phenomena have been the focus of intense research effort, due to their widespread industrial importance in, for example, optimizing coating flows (Weinstein & Ruschak, 2004), where the aim is to 'coat' a solid substrate with a liquid in a

fast and controllable way. This and other applications motivated numerous experimental and theoretical works analyzed in a number of review articles (Dussan V, 1979; De Gennes, 1985; Kistler, 1993; Blake, 2006) and books (De Gennes *et al.*, 2004; Starov *et al.*, 2007; Shikhmurzaev, 2007) as well as recent discussion papers (Velarde, 2011). Surprisingly, the theoretical advances made in the study of coating and related flows have not been transferred and applied to the bubble formation processes.

Some authors modelled the initial growth of the bubble as a quasi-static process with the contact angle kept equal to the static contact angle (Lee & Tien, 2009; Gerlach *et al.*, 2005), whilst the boundary element method has been used to investigate bubble formation in an inviscid liquid (Higuera & Medina, 2006) and a highly viscous liquid (Higuera, 2005), also with the contact angle remaining at its static value. A level-set method has been proposed that allows the contact angle to vary from its static value, however there was no explicit relationship between the contact angle and the contact line speed (Chen *et al.*, 2009). Therefore non-equilibrium effects, such as the dynamics of the contact angle or the role of the physical mechanisms whose presence in the model allows the contact line to move across the solid in the wetting/de-wetting phenomena, have, until now, remained unexplored.

The essence of the moving contact-line problem central to the modelling of wetting/de-wetting phenomena is that:

(a) The Navier-Stokes equations subject to the no-slip condition on the solid boundary (3.17) and the standard kinematic (3.19) and dynamic boundary conditions (3.22) on the free surface do not have a solution when the contact line is moving with respect to the solid (Shikhmurzaev, 2006, 2007). In a simplified formulation, where the free-surface shape is prescribed and the normal-stress boundary condition on the free-surface dropped, the problem manifests itself in the form of a non-integrable singular shear stress acting on the solid from the liquid (Huh & Scriven, 1971).

(b) The dynamic contact angle θ has to be specified. Experiments show that this angle depends on the speed of the contact line (Hoffman, 1975) and, if the flow field near the contact line is affected by other closely located boundaries, also on the flow field (Blake *et al.*, 1999; Wilson *et al.*, 2006), the effect which came to be known as 'hydrodynamic assist of dynamic wetting' (Blake *et al.*, 1994).

In the absence of hydrodynamic assist of dynamic wetting, which in the bubble formation process is almost invariably the case, several models proposed in the literature to address the moving contact-line problem perform in an equally satisfactory way (Seveno *et al.*, 2009), so that the choice of a particular model largely depends on the convenience of its implementation in a numerical algorithm. Importantly, all the models addressing the moving contact-line problem involve a small length scale associated with the specific physics of wetting/de-wetting to remove the singularity at the contact line, in the form of 'slip' (Dussan V, 1976; Lauga *et al.*, 2007), and this length scale, which is $\ell = 1 - 100$ nm, known as the slip length, has to be fully resolved to avoid mixing numerical artifacts and physical effects (Sprittles & Shikhmurzaev, 2012c).

Dynamic wetting belongs to a more general class of fluid flows, including the coalescence of liquid drops and the break up of liquid jets, where an interface is formed or destroyed. A variety of models have been used to explain each of these processes in turn, but only the interface formation model has been successful in describing them all as a particular case of this more general problem (Shikhmurzaev, 2007). This model, derived using concepts from irreversible thermodynamics, is more complicated than the formulation described in Chapter 3 as a dynamic surface tension is introduced as well as a surface tension relaxation time which is the time it takes for a material element of the free surface to advect from the liquid-gas interface to the solid-liquid interface and hence form a new interface. Since the priority here is to investigate the influence of the contact line motion on the formation of a bubble rather than the local dynamics at the

contact line, an asymptotic result derived from the full model will be used to describe the behaviour of the dynamic contact angle (Shikhmurzaev, 1993).

To remove the singularity at the contact line, it is convenient to use the simplest approach and replace the no-slip boundary condition (3.17) on the solid surface with a Navier-slip condition (Navier, 1823) thus resolving part (a) above. To address part (b), the dynamic contact angle is specified using the asymptotic result derived from the interface formation model which also involves the contact line speed and the static contact angle. A similar approach to modelling one of the coating flows has been successfully implemented by Wilson and co-workers (Wilson *et al.*, 2001).

The issue of the contact-angle hysteresis can be efficiently addressed by splitting the static contact angle into the static receding contact angle θ_r and the static advancing contact angle θ_a and using these values, as the static contact angle, in the velocity-dependence of the dynamic contact angle obtained for an ideal substrate depending on whether the contact line is receding or advancing, with the contact line remaining stationary if the contact angle is between these values (Hocking, 1990).

7.2 Amendments to the Problem Formulation

As described in the previous section, the combined no-slip and impermeability boundary condition (3.17) on the solid surface is replaced with the impermeability and Navier-slip boundary conditions,

$$\mathbf{u} \cdot \mathbf{e}_z = 0, \tag{7.1a}$$

$$\mathbf{e}_z \cdot \mathbf{P} \cdot (\mathbf{I} - \mathbf{e}_z\mathbf{e}_z) = \beta \mathbf{u} \cdot (\mathbf{I} - \mathbf{e}_z\mathbf{e}_z)\,, \tag{7.1b}$$

respectively, where $\beta = L/\ell$ is the dimensionless slip coefficient and ℓ is the slip length. Since the contact line is no longer pinned to the rim of the orifice, the boundary condition

at the contact line (3.25) for the normal stress condition is replaced by the asymptotic result from Shikhmurzaev (2007) that relates the dynamic contact angle with the speed of the contact line,

$$\frac{u}{U_c} = \begin{cases} (\cos\theta - \cos\theta_r)\,\lambda(\theta,\theta_r)\,, & \theta < \theta_r \\ 0, & \theta_r \leqslant \theta \leqslant \theta_a \\ (\cos\theta - \cos\theta_a)\,\lambda(\theta,\theta_a)\,, & \theta > \theta_a, \end{cases} \tag{7.2}$$

where

$$\lambda(\theta,\varphi) = \sqrt{\frac{1+\cos\varphi\,(1-\rho_G^s)}{4\left(\cos\varphi + \frac{1+\rho_G^s u_m(\theta)}{1-\rho_G^s}\right)\left(\cos\theta + \frac{1+\rho_G^s u_m(\theta)}{1-\rho_G^s}\right)}}$$

and

$$u_m(\theta) = \frac{\sin\theta - \theta\cos\theta}{\sin\theta\cos\theta - \theta}$$

is a solution found in Moffatt (1964). The respective static receding and static advancing contact angles are given by θ_r and θ_a, and $0 < \rho_G^s < 1$ is a parameter, found in the interface formation model (Shikhmurzaev, 2007), which is known as the equilibrium surface density for liquid-gas interface. It is related to the dynamic surface tension through a surface equation of state but for all simulations presented here $\rho_G^s = 1/2$. The characteristic contact line speed $U_c > 0$ is also a parameter from the interface formation model and, in theory, is determined by a combination of dimensional quantities that appear in the model. However, to simplify things, it will appear here as a free parameter.

The initial condition for the free surface (3.32) is also slightly amended. The bubble is initially a spherical cap with initial contact angle θ_i and base radius r_i, where in the case of an orifice of finite size, $r_i = r_o$. The radius of the sphere is now defined by $R_i = r_i/\sin\theta_i$ and the initial height of the bubble is then $H_i = R_i\,[1+\cos\theta_i]$. Therefore, the initial free

surface shape is given by

$$r^2 + (z + R_i - H_i)^2 = R_i^2, \qquad 0 \leqslant z \leqslant H_i, \tag{7.3}$$

where the initial shape is fully specified by defining the initial contact angle and initial base radius of the bubble.

Finally, in the case of bubble formation from an orifice of finite size, the contact line may become pinned to the rim of the orifice. If this occurs, then (7.2) must be replaced with the original equation for a pinned contact line at the rim of the orifice (3.25) and the Navier-slip condition (7.1) is replaced by the no-slip condition (3.17) at the contact line only.

7.3 Contact Line Motion

The relationship between the dynamic contact angle and the contact line speed (7.2) depends on two parameters, the characteristic contact line speed U_c and the static receding contact angle θ_r, when the contact line recedes, or the static advancing contact angle θ_a, when the contact line advances.

Figure 7.2 shows how the characteristic contact line speed U_c and the static contact angles, θ_r or θ_a, influence the relationship between the dynamic contact angle and the contact line speed (7.2). As is known from experiments (Shikhmurzaev, 2007), for an advancing contact line, the contact line speed increases with the dynamic contact angle (see Figure 7.2b) whereas, for a receding contact line, the contact line speed increases with decreasing dynamic contact angle until the speed approaches a limit known as the maximum speed of dewetting (see Figure 7.2a).

As U_c is increased, the range of contact line speeds, for which the contact angle is equal to the relevant static angle, increases. Therefore, if U_c is sufficiently large then the

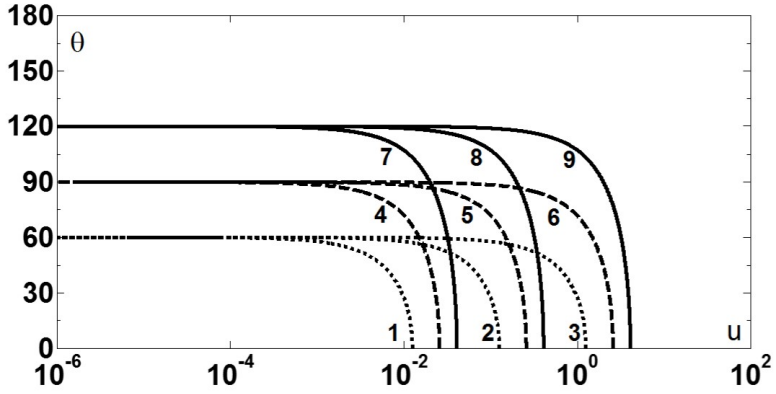

(a) The receding contact line where $\theta_r = \theta_s$

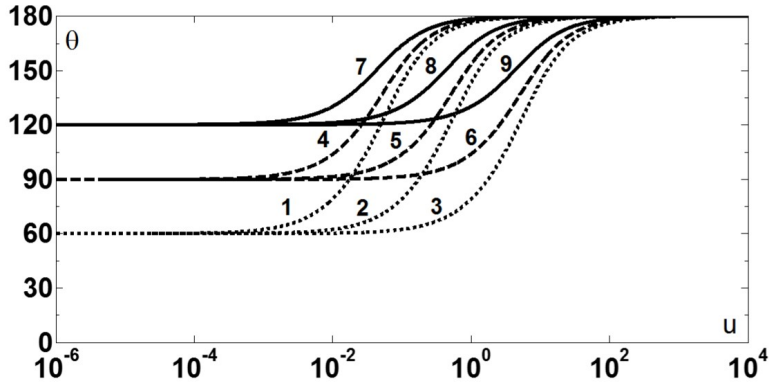

(b) The advancing contact line where $\theta_a = \theta_s$ with the absolute value of the contact line speed u since, in the problem, $u < 0$ when the contact line advances.

Figure 7.2: Dynamic contact angle θ versus dimensionless contact line speed u for different values of U_c and θ_s, where $\theta_s = \theta_r$, when the contact line recedes, and $\theta_s = \theta_a$, when the contact line advances. For $\theta_s = \frac{\pi}{3}$ and $U_c = 0.1$, (line 1), 1 (2), 10 (3), $\theta_s = \frac{\pi}{2}$ and $U_c = 0.1$ (4), 1 (5), 10 (6) and $\theta_s = \frac{2\pi}{3}$ and $U_c = 0.1$, (7), 1 (8), 10 (9).

dynamic contact angle will be equal to θ_r, when the contact line recedes, and θ_a, when the contact line advances. This will be referred to as the 'constant contact angle regime'.

7.4 Amendments to the Numerical Platform

In order to simulate the formation of a bubble whose contact line is free to move, the numerical platform described in Chapter 4 and validated in Chapter 5 must be amended.

The continuity residual (4.38) and the z component of the momentum residual (4.35b) remain unchanged whilst, since the contact line is no longer pinned, the kinematic residual (4.36) is given entirely by its free surface contribution,

$$R_I^K = \left(R_I^K\right)_{A_1} \qquad I = 1, ..., N_1. \tag{7.4}$$

However, as stated above, if the contact line becomes pinned to the rim of the orifice, the original equation (4.36) must be applied instead of (7.4).

The r component of the momentum residual (4.35a) must account for the implementation of the Navier-slip condition rather than the no-slip condition. From (4.24b) and the Navier-slip boundary condition (7.1b), the solid surface contribution to the momentum residuals is given by

$$\begin{aligned}\left(R_I^{M,\alpha}\right)_{A_2} &= Oh^2 \int_{A_2} \phi_{1,I}\mathbf{e}_\alpha \cdot \mathbf{P} \cdot \mathbf{e}_z \, dA_2 \\ &= Oh^2\beta \int_{A_2} \phi_{1,I}\mathbf{e}_\alpha \cdot \mathbf{u} \cdot (\mathbf{I} - \mathbf{e}_z\mathbf{e}_z) \, dA_2\end{aligned} \tag{7.5}$$

which can be evaluated using the techniques shown in Chapter 4.

Therefore the r component to the momentum residual is now given by

$$R_I^{M,r} = \begin{cases} \left(R_I^{M,r}\right)_{A_3} & \text{for } I \in X_3 \backslash (X_2 \cup X_4) \\ \left(R_I^{M,r}\right)_{A_4} & \text{for } I \in X_4 \backslash X_5 \\ \left(R_I^{M,r}\right)_{V} & \text{for } I \in X \backslash (X_1 \cup X_2 \cup X_3 \cup X_4 \cup X_5) \\ \left(R_I^{M,r}\right)_{V} + \left(R_I^{M,r}\right)_{A_1} & \text{for } I \in X_1 \backslash (X_2 \cup X_5) \\ \left(R_I^{M,r}\right)_{V} + \left(R_I^{M,r}\right)_{A_2} & \text{for } I \in X_2 \backslash X_1 \\ \left(R_I^{M,r}\right)_{V} + \left(R_I^{M,r}\right)_{A_1} + \left(R_I^{M,r}\right)_{A_2} + \left(R_I^{M,r}\right)_{L} & \text{for } I \in X_1 \cap X_2. \end{cases} \tag{7.6}$$

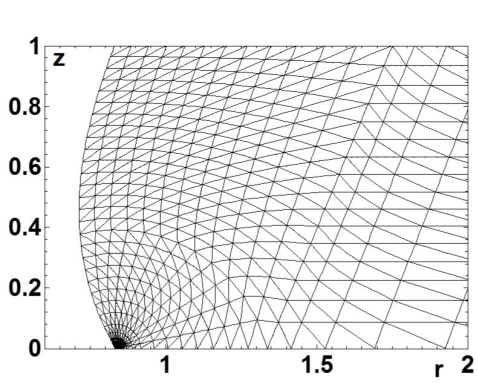

(a) The pinch-off region of the computational mesh.

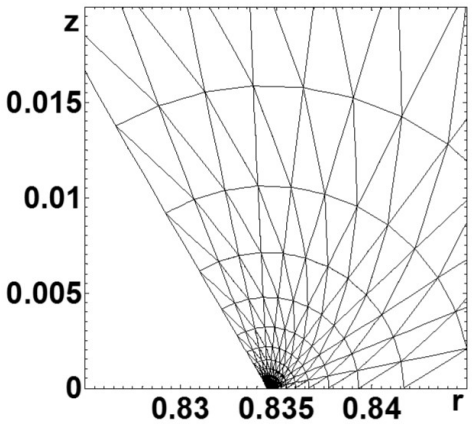

(b) The computational mesh adjacent to the contact line.

Figure 7.3: The refinement of the mesh near adjacent to the contact line.

Finally, (7.2) is added to the system of equations as it is written with the dynamic contact angle θ becoming the required additional unknown for the system.

7.5 Mesh Independence

An important consideration of any numerical platform when simulating a flow that involves a moving contact line is to ensure that the slip region adjacent to the contact line has been fully resolved (Sprittles & Shikhmurzaev, 2012c). An advantage of the finite element method is that the computational mesh can be refined near the contact line in order to capture the small dimensionless length scale given by $1/\beta$ (see Figure 7.3b).

To verify that the results produced in this chapter were independent of the mesh, i.e. the contact line region was sufficiently resolved, to avoid mistaking numerical artifacts for physical effects, for the first time for the bubble formation phenomenon with a moving contact line, a test case is carried out for several values of the slip coefficient β and mesh refinement. The refinement of the mesh is measured by length of the first element along

the solid surface adjacent to the contact line, this length will be referred to as l_{min}. The smallest value which was computationally achievable was $l_{min} = 5 \times 10^{-6}$.

The test case considered will be the formation of a bubble in water ($Oh = 2.24 \times 10^{-3}$) with a gas flow rate $Q = 10^{-3}$ and initial base radius $r_i = 0.1$. The characteristic contact line speed is $U_c = 10^5$ so that the behaviour of the dynamic contact angle belongs to the constant contact angle regime where the angle relaxes almost instantly to its equilibrium value $\theta_i = \theta_r = \theta_a = 2\pi/3$. The slip coefficients to be examined are $\beta = 10^4$, 10^5, 10^6 and 10^7, where, dimensionally, if $L = 1$ mm, these correspond to a dimensional slip length in the range $\ell = 0.1 - 100$ nm. In order to confirm that the simulations are indeed mesh independent, the volume of the bubble formed V_d, the formation time t_d and the radius of the contact line at pinch-off r_d are considered.

Another concern is the accuracy of the computed contact angle as to whether it is equal to the weakly imposed angle the free surface makes with the solid surface at the contact line, θ. This angle, referred to as θ_c, can be calculated from the tangent vector to the free surface at the contact line, $\mathbf{t} = (-n_z, n_r)$, whose components are given by (4.110) and found from the position of the first three nodes along the free surface. The relative error of the contact angle, given by $\frac{|\theta - \theta_c|}{\theta}$, is found at every time step and the maximum relative error, $\Delta\theta$, is presented alongside the results for mesh independence.

Tables 7.1–7.4 give the mesh independence results for $\beta = 10^4$, 10^5, 10^6 and 10^7, respectively, for various $5 \times 10^{-6} \leqslant l_{min} \leqslant 10^{-3}$. For a given β, the relative error of V_d is calculated by $\frac{|V_d - V_d^{min}|}{V_d^{min}}$ where V_d^{min} is V_d for $l_{min} = 5 \times 10^{-6}$. Similar relative errors for t_d and r_d are also found and presented graphically in Figure 7.4.

The raw data in Tables 7.1–7.4 show that even the largest l_{min} considered is fine for an approximate measure (within 1%) of V_d and t_d, however this is not the case for r_d, which is the most sensitive measure of mesh independence. In contrast to V_d and t_d, it is found that r_d depends on a consistent formulation for slip near the contact line. This is

Table 7.1: Mesh independence test for $\beta = 10^4$.

l_{min}	V_d	t_d	r_d	$\Delta\theta$
5×10^{-6}	9.9323	9937.48	0.1454	1.165×10^{-3}
10^{-5}	9.9323	9937.49	0.1455	1.676×10^{-3}
5×10^{-5}	9.9321	9937.23	0.1455	3.852×10^{-3}
10^{-4}	9.9316	9936.81	0.1459	5.289×10^{-3}
5×10^{-4}	9.9331	9938.39	0.1472	1.514×10^{-2}
10^{-3}	9.9346	9940.10	0.1492	2.77×10^{-2}

Table 7.2: Mesh independence test for $\beta = 10^5$.

l_{min}	V_d	t_d	r_d	$\Delta\theta$
5×10^{-6}	9.9351	9940.78	0.1513	4.042×10^{-3}
10^{-5}	9.9353	9940.99	0.1514	5.9×10^{-3}
5×10^{-5}	9.9356	9941.40	0.1528	1.466×10^{-2}
10^{-4}	9.9366	9942.56	0.1547	2.294×10^{-2}
5×10^{-4}	9.9429	9950.85	0.1715	7.447×10^{-2}
10^{-3}	9.9491	9959.04	0.1926	0.1329

Table 7.3: Mesh independence test for $\beta = 10^6$.

l_{min}	V_d	t_d	r_d	$\Delta\theta$
5×10^{-6}	9.9382	9944.82	0.1583	1.501×10^{-2}
10^{-5}	9.9388	9945.32	0.1601	2.287×10^{-2}
5×10^{-5}	9.9444	9952.44	0.1758	7.36×10^{-2}
10^{-4}	9.9514	9961.99	0.1971	0.1259
5×10^{-4}	10.0008	10039.21	0.3493	0.3436
10^{-3}	10.0364	10123.02	0.4996	0.4934

Table 7.4: Mesh independence test for $\beta = 10^7$.

l_{min}	V_d	t_d	r_d	$\Delta\theta$
5×10^{-6}	9.9459	9954.62	0.1808	7.181×10^{-2}
10^{-5}	9.9531	9964.22	0.2012	0.1228
5×10^{-5}	10.0019	10041.20	0.3518	0.339
10^{-4}	10.0375	10124.68	0.5008	0.473
5×10^{-4}	10.0846	10457.17	1.0297	0.8212
10^{-3}	10.0029	10482.55	1.1813	0.8885

to be expected as r_d depends strongly on the dynamics of the contact line. Calculating this value accurately is particularly important for a stream of bubbles where the residual bubble determines the initial conditions for next bubble. As l_{min} decreases, V_d, t_d and r_d all converge to at least three significant figures for $\beta = 10^4$ and 10^5, and to at least two significant figures for $\beta = 10^6$.

The contact angle error $\Delta\theta$ also reduces as l_{min} decreases. For $\beta = 10^4$ and 10^5, $\Delta\theta < 1\%$ for $l_{min} \leqslant 10^{-5}$, whilst when under resolved, as in Table 7.4, large errors in θ can occur. Therefore, to ensure that the contact line region has been sufficiently refined so that the contact angle and the effect of slip can be captured accurately, the greatest slip coefficient for which the results were satisfactorily mesh independent is $\beta = 10^5$. Therefore, for all following simulations, $\beta = 10^5$ and $l_{min} = 5 \times 10^{-6}$. This is reasonable and expected since $l_{min} = 5 \times 10^{-6} < 10^5 = \beta^{-1}$ and agrees with the findings for wetting flows in Sprittles & Shikhmurzaev (2012c). Dimensionally, this corresponds to $\ell \approx 10$ nm, which is well within the range of experimentally measured values (Lauga *et al.*, 2007).

7.6 Results

In Chapter 6, each simulation could be characterised in terms of the three parameters (r_o, Oh, Q). With the additional parameters incorporated into the model due to the moving contact line, simulations are now chracterised by $(r_i, Oh, Q, \theta_r, \theta_a, \theta_i, U_c)$. A simulation runs until either the minimum neck radius $r_{min} = r_{tol}$ or the radius of the contact line $r_c = r_{tol}$ where $r_{tol} = 2 \times 10^{-2}$, if $L = 1$ mm, r_{tol} corresponds to 20 μ m. Once again the formation time t_d is the time of the final solution, whilst the volume V_d of the bubble that is formed is either the volume of the bubble above the point on the free surface which represents the minimum neck radius in the case of $r_{min} = r_{tol}$, or if $r_c = r_{tol}$, V_d will be the total volume of the bubble.

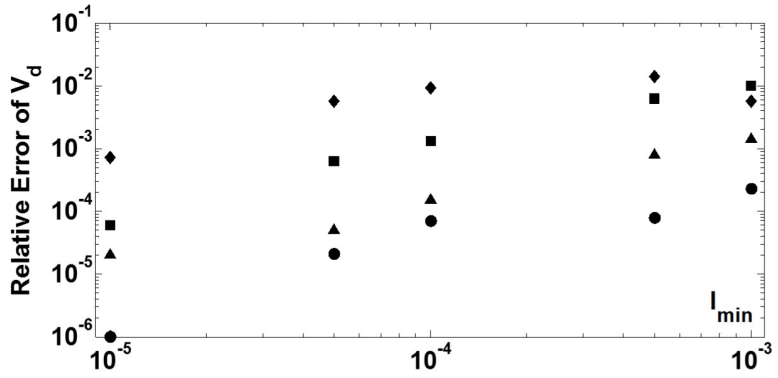

(a) The relative error of V_d against l_{min} for several β.

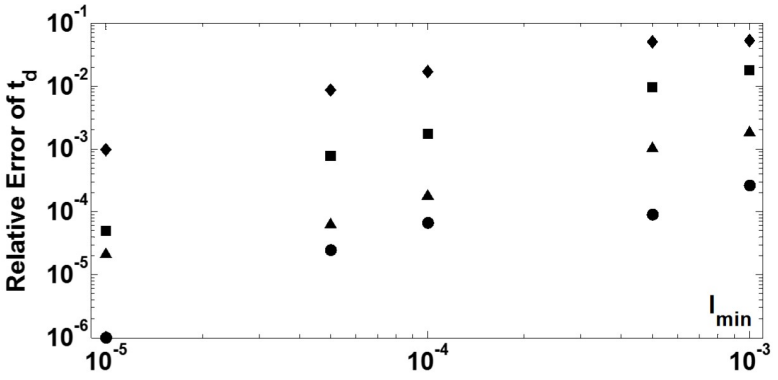

(b) The relative error of t_d against l_{min} for several β.

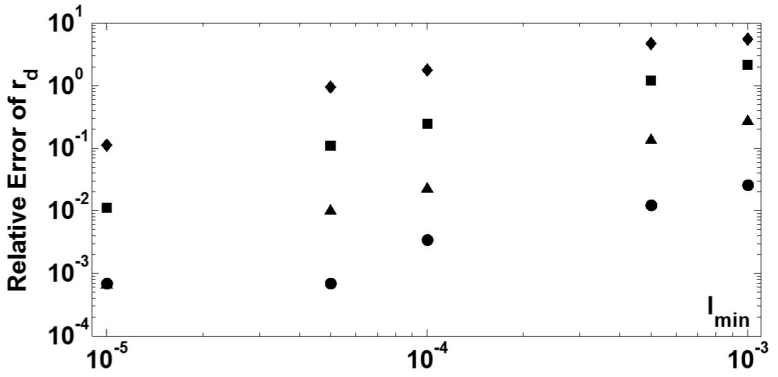

(c) The relative error of r_d against l_{min} for several β.

Figure 7.4: The relative error of V_d, t_d and r_d against l_{min} for $\beta = 10^4$ ($\circ$), 10^5 ($\triangle$), 10^6 ($\square$) and 10^7 ($\diamond$).

The first case to consider is the formation of a bubble in the constant contact angle regime with an infinitesimally small orifice.

7.6.1 Constant Contact Angle Regime

The characteristic contact line speed is set sufficiently high, $U_c = 10^5$, so that as the contact line recedes, the dynamic contact angle θ will remain equal to the static receding contact angle θ_r, and as the contact line advances, the contact angle takes the value of the static advancing contact angle θ_a. In this constant contact angle regime, it is assumed that the initial angle $\theta_i = \theta_r$ and there is no contact angle hysteresis so $\theta_a = \theta_r$. The initial base radius is $r_i = 0.1$.

Figure 7.5a shows that as the static receding angle θ_r is increased, the radius of the contact line r_c attains a greater maximum value as the contact line recedes further. This also increases the formation time of the bubble and in turn increases the volume of the bubble formed as seen in Figure 7.5b and Figure 7.11. Clearly changes in wettability strongly influence the bubble formation process.

Figure 7.5a also confirms that, in this constant contact angle regime, the dynamic contact angle θ remains equal to θ_r. This can also be observed in the free surface shapes at pinch-off (see Figure 7.5c). For smaller values of θ_r, the bubble pinches off at the base as $r_c = r_{tol}$, whilst at larger values, the bubble pinches at the neck where $r_{min} = r_{tol}$. At the base of the bubble at pinch-off, when $r_c = r_d$, r_d increases with larger θ_r and where a bubble pinches at the neck, the height of the point of minimum neck radius increases. Whether a residual bubble remains after the bubble has pinched off could have a strong influence on the growth of subsequent bubbles as it makes a clear site for future bubble growth.

These differences in where the bubble pinches off can be seen in the evolution of the free surface for the cases of $\theta_r = \pi/3$ and $2\pi/3$ (see Figure 7.6). For the case of a hydrophilic surface, $\theta_r = \pi/3$, the bubble pinches at the base (see Figure 7.6a), whilst in the case of a hydrophobic surface, $\theta_r = 2\pi/3$, the bubble pinches at the neck (see Figure 7.6b). In both figures, line 1 is the initial free surface shape, line 3 is the bubble at maximum r_c and line

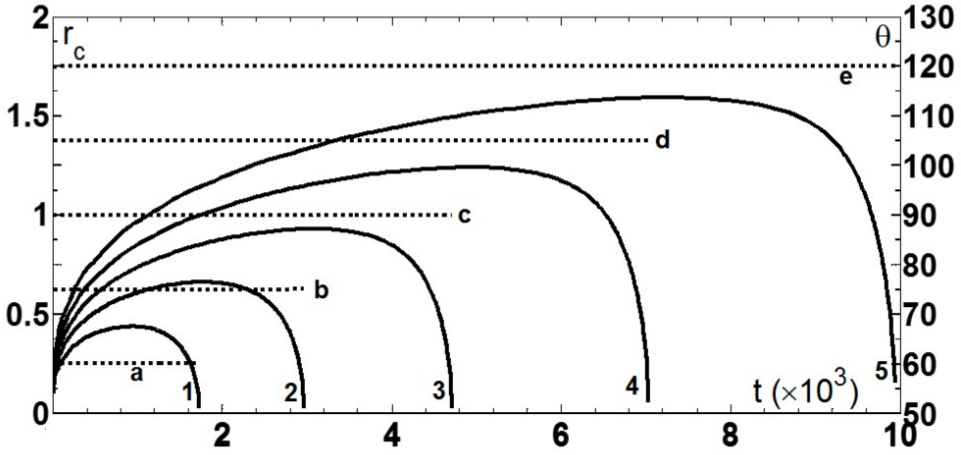

(a) The evolution of the contact line $r_c(t)$ (solid lines) and the dynamic contact angle $\theta(t)$ (dashed lines).

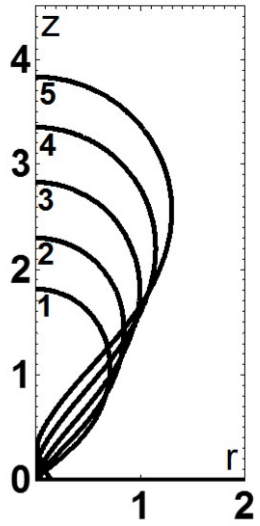

(b) The free surface at pinch-off.

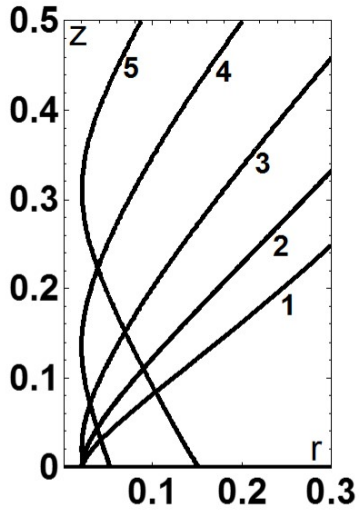

(c) A close up of the contact line region at pinch-off.

Figure 7.5: The global and contact line dynamics for different static receding contact angles $\theta_r = \pi/3$ (lines 1 and a), $\theta_r = 5\pi/12$ (2 and b), $\theta_r = \pi/2$ (3 and c), $\theta_r = 7\pi/12$ (4 and d) and $\theta_r = 2\pi/3$ (5 and e) where $Oh = 2.24 \times 10^{-3}$, $r_i = 0.1$, $U_c = 10^5$ and $Q = 10^{-3}$.

2 is equally spaced in time between these. For $\theta_r = \pi/3$, line 5 is the bubble at pinch-off and line 4 is the bubble at a time equally spaced between lines 3 and 5. For $\theta_r = 2\pi/3$, line 6 is the bubble at pinch-off and line 4 is the bubble at a time equally spaced between

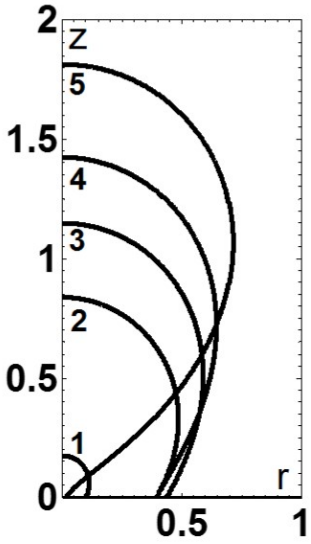

(a) The hydrophilic case, $\theta_r = \pi/3$, for $t = 0$ (line 1), 4.68×10^2 (2), 9.35×10^2 (3), 1.332×10^3 (4) and 1.729×10^3 (5).

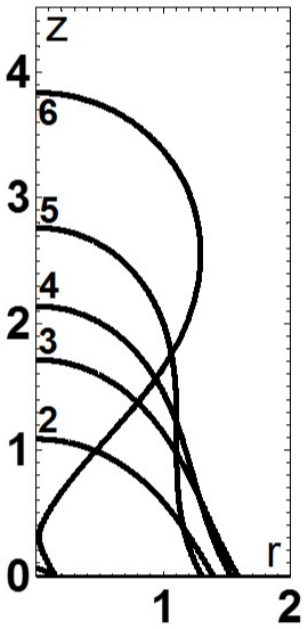

(b) The hydrophobic case, $\theta_r = 2\pi/3$, for $t = 0$ (line 1), 3.583×10^3 (2), 7.165×10^3 (3), 8.551×10^3 (4), 9.935×10^3 (5) and 9.937×10^3 (6).

Figure 7.6: The evolution of the free surface for a hydrophilic and hydrophobic solid surface where $Oh = 2.24 \times 10^{-3}$, $r_i = 0.1$, $U_c = 10^5$ and $Q = 10^{-3}$.

lines 3 and 6 whilst line 5 is the shape of the bubble when the neck first forms. In both cases, the period of time for which the contact line advances is much shorter than the period of time for which it recedes. In the case of when the bubble pinches off at the neck, the pinch-off process takes place very quickly relative to the formation time of the bubble (see curves 5 and 6 on Figure 7.6b).

For the range of volumetric gas flow rates Q considered, the flow rate has a negligible influence on the maximum radius of the contact line, as shown by Figure 7.7a for $\theta_r = \pi/3$ and Figure 7.7b for $\theta_r = 2\pi/3$. The lines 1–3 are indistinguishable on Figure 7.7a. Therefore, in the range of Q considered, the most important parameter in determining the maximum radius of the contact line is the static receding angle θ_r.

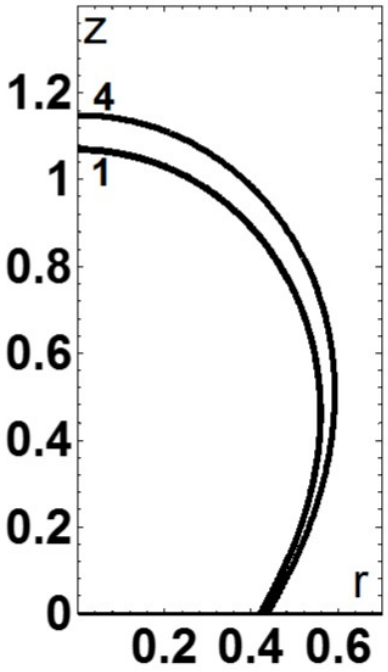

(a) The case of $\theta_r = \pi/3$ where $Q = 10^{-6}$ (line 1, $t = 7.761 \times 10^5$), $Q = 10^{-5}$ (2, $t = 7.761 \times 10^4$), $Q = 10^{-4}$ (3, $t = 7.8 \times 10^3$), $Q = 10^{-3}$ (4, $t = 9.23 \times 10^2$).

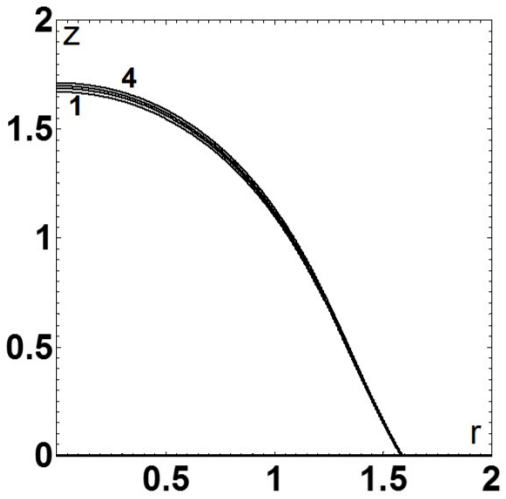

(b) The case of $\theta_r = 2\pi/3$ where $Q = 10^{-6}$ (line 1, $t = 6.925 \times 10^6$), $Q = 10^{-5}$ (2, $t = 6.997 \times 10^5$), $Q = 10^{-4}$ (3, $t = 7.049 \times 10^4$), $Q = 10^{-3}$ (4, $t = 7.165 \times 10^3$).

Figure 7.7: The free surface profile with maximum contact line radius for various flow rates $10^{-6} \leqslant Q \leqslant 10^{-3}$ where $Oh = 2.24 \times 10^{-3}$, $r_i = 0.1$, and $U_c = 10^5$.

However, Figure 7.8 shows that the flow rate Q does influence the volume of the bubble formed at pinch-off, V_d. Although lines 1 and 2 are indistinguishable for both $\theta_r = \pi/3$ (see Figure 7.8a) and $\theta_r = 2\pi/3$ (see Figure 7.8b), line 4 clearly deviates. Therefore once the flow rate is sufficiently large, V_d increases with Q. This suggests that once again there may be two regimes of bubble formation, where at low flow rates, bubble formation is in the static regime where Q had a negligible influence on V_d, whilst at greater flow rates V_d increases with Q. The influence of the flow rate Q on V_d is also shown by Figure 7.11.

For the full range of Q considered, the bubble always pinches off at the base for

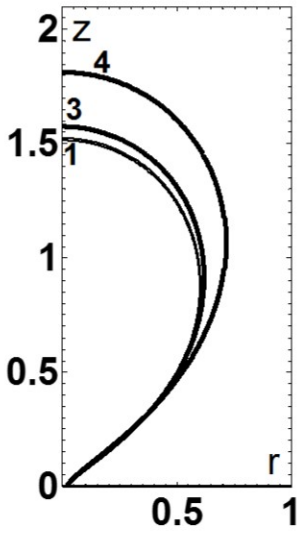

(a) The case of $\theta_r = \pi/3$ where $Q = 10^{-6}$ (line 1, $t_d = 1.025 \times 10^6$), $Q = 10^{-5}$ (2, $t_d = 1.049 \times 10^5$), $Q = 10^{-4}$ (3, $t_d = 1.138 \times 10^4$), $Q = 10^{-3}$ (4, $t_d = 1.729 \times 10^3$).

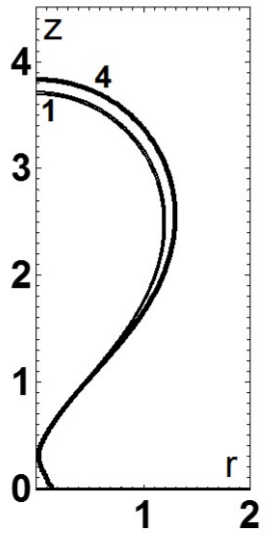

(b) The case of $\theta_r = 2\pi/3$ where $Q = 10^{-6}$ (line 1, $t_d = 8.01 \times 10^6$), $Q = 10^{-5}$ (2, $t_d = 8.053 \times 10^5$), $Q = 10^{-4}$ (3, $t_d = 8.317 \times 10^4$), $Q = 10^{-3}$ (4, $t_d = 9.937 \times 10^3$).

Figure 7.8: The final free surface profiles for a various flow rates $10^{-6} \leqslant Q \leqslant 10^{-3}$ where $Oh = 2.24 \times 10^{-3}$, $r_i = 0.1$, and $U_c = 10^5$.

$\theta_r = \pi/3$ and at the neck for $\theta_r = 2\pi/3$. As Q is increased, r_d deceases for $\theta_r = 2\pi/3$.

Figure 7.9 shows that as the Ohnesorge number Oh is increased, the formation time of the bubble decreases. In the case of a hydrophilic surface, the maximum radius of the contact line decreases with increasing Oh (see Figure 7.9a), whilst, in the case of a hydrophobic surface, the influence of Oh on the maximum radius of the contact line is negligible (see Figure 7.9b).

In the case of $Oh = 2.24 \times 10^{-3}$, for the full range of Q considered, when $\theta_r = \pi/3$, the bubble always pinches off at its base (see Figure 7.8a), and when $\theta_r = 2\pi/3$, the bubble always pinches off at the neck (see Figure 7.8b). However as Oh is increased, Figure 7.9a shows that r_d increases for both $\theta_r = \pi/3$ and $2\pi/3$. Therefore, for $\theta_r = \pi/3$, increasing Oh leads to the bubble pinching off at the neck rather than the base.

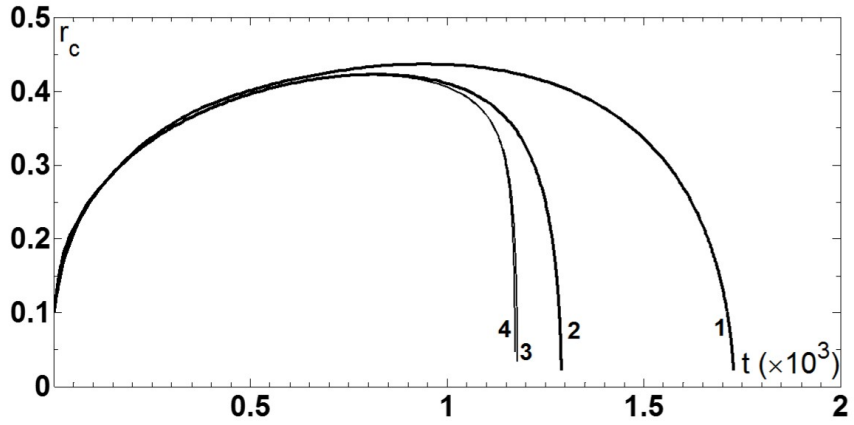

(a) The case of $\theta_r = \pi/3$.

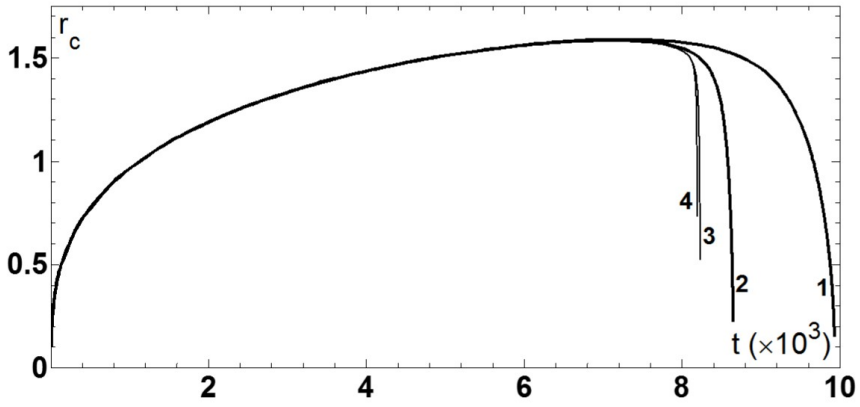

(b) The case of $\theta_r = 2\pi/3$.

Figure 7.9: The influence of Ohnesorge number on the evolution of the contact line where $r_i = 0.1$, $U_c = 10^5$ and $Q = 10^{-3}$. The case of $Oh = 2.24 \times 10^{-3}$ is given by line 1, $Oh = 10^{-2}$ (2), $Oh = 10^{-1}$, (3) and $Oh = 10$ (4).

Figures 7.10b and 7.10d confirm that as the Ohnesorge number Oh increases so does r_d. The increase in Oh also leads to a decrease in V_d as can be seen from the final bubble shapes in Figures 7.10a and 7.10c.

The influence of the Ohnesorge number Oh, volumetric gas flow rate Q and static receding contact angle θ_r on the bubble volume V_d in the constant contact angle regime where $\theta_a = \theta_i = \theta_r$ and $r_i = 0.1$ is shown in Figure 7.11. Similar to the formation of a bubble whose contact line is pinned to the rim of the orifice (see Chapter 6), Figure 7.11

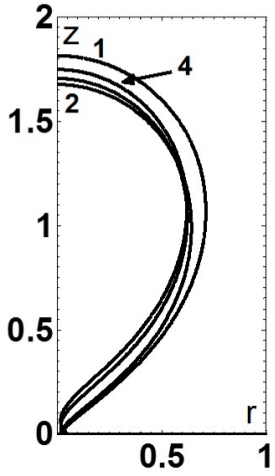

(a) The free surface at pinch-off for $\theta_r = \pi/3$.

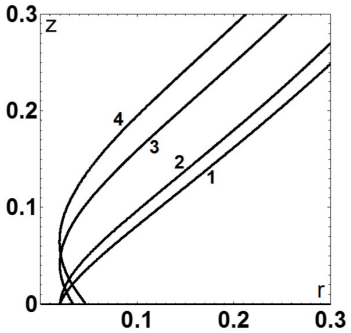

(b) A close up of the contact line region for $\theta_r = \pi/3$.

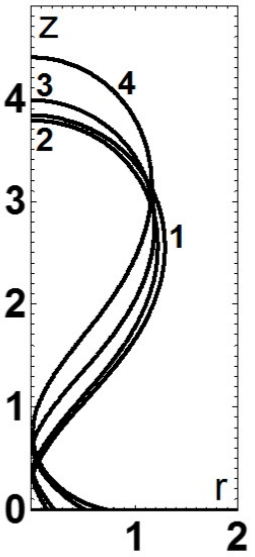

(c) The free surface at pinch-off for $\theta_r = 2\pi/3$.

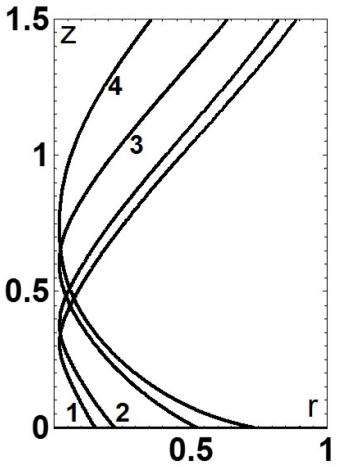

(d) A close up of the contact line region for $\theta_r = 2\pi/3$.

Figure 7.10: The influence of Ohnesorge number on the final free surface where $Q = 10^{-3}$, $r_i = 0.1$ and $U_c = 10^5$ The case of $Oh = 2.24 \times 10^{-3}$ is given by line 1, $Oh = 10^{-2}$ (2), $Oh = 10^{-1}$, (3) and $Oh = 10$ (4).

shows that the two regimes of bubble formation, static and dynamic, are also observed when the contact line is free to move. At a given static receding contact angle θ_r, in the

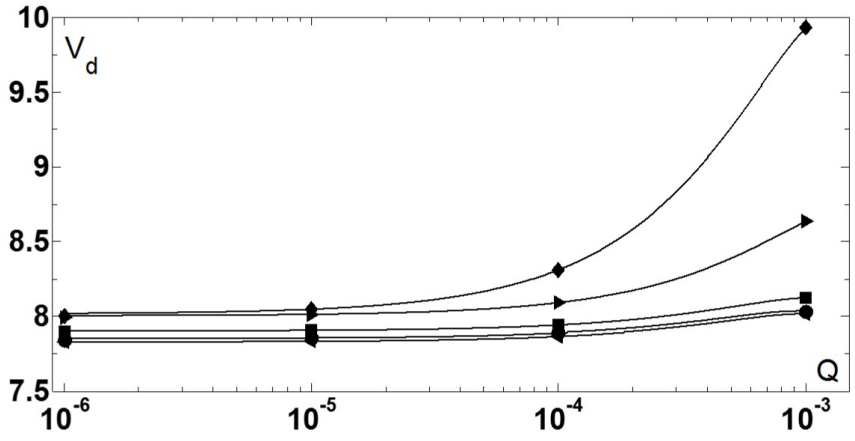

(a) The case of $\theta_r = 2\pi/3$.

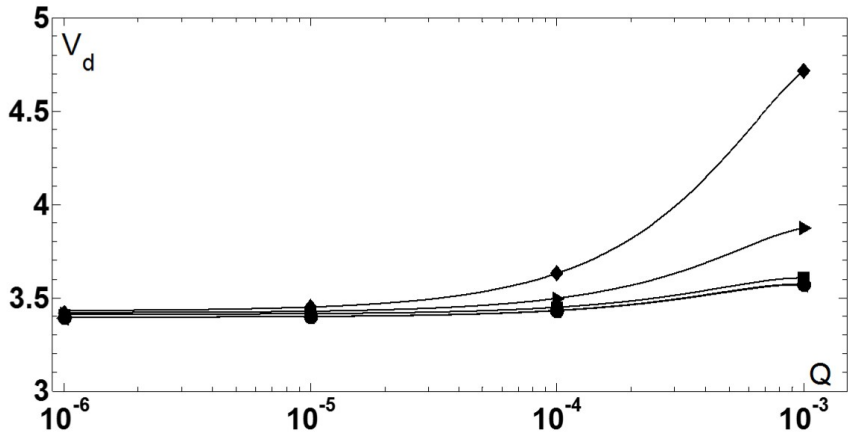

(b) The case of $\theta_r = \pi/2$.

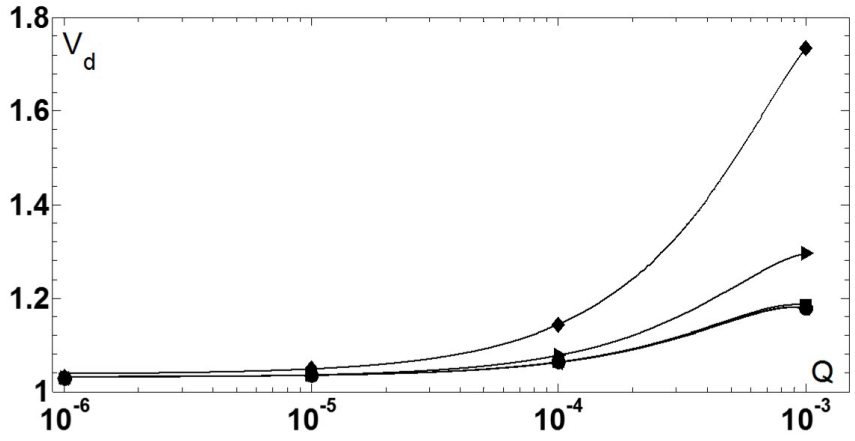

(c) The case of $\theta_r = \pi/3$.

Figure 7.11: The influence of the flow rate Q on the bubble volume for various Ohnesorge numbers Oh and static contact angles θ_r, where $r_i = 0.1$ and $U_c = 10^5$. The various Ohnesorge numbers are represented by ($\diamond$) $Oh = 2.24 \times 10^{-3}$, ($\triangleright$) $Oh = 10^{-2}$, ($\square$) $Oh = 10^{-1}$, ($\circ$) $Oh = 1$ and ($\triangleleft$) $Oh = 10$. Curves of best fit were obtained using cubic splines.

static regime at low flow rates, the volume of the detachment bubble V_d is independent of Ohnesorge number Oh and flow rate Q. However as the flow rate is increased, bubble formation enters the dynamic regime and V_d increases with increasing Q and decreasing Oh. The volume V_d also increases with static receding contact angle θ_r.

7.6.2 Constant Contact Angle Regime with Contact Angle Hysteresis

A static advancing contact angle θ_a, that differs from the static receding contact angle θ_r, can now be introduced in order to mimic the behaviour exhibited by contact angle hysteresis.

Figures 7.12 & 7.13 show that in this constant contact angle regime, the contact line recedes with the static receding contact angle $\theta_r = \pi/3$. As the contact line becomes pinned due to contact angle hysteresis, the contact angle increases due to the larger bubble volume. Then, as the contact line advances, the contact angle takes the value of the given static advancing contact angle θ_a. The formation time t_d increases with θ_a.

For $Oh = 2.24 \times 10^{-3}$, Figure 7.12b shows that in the range of θ_a considered, the bubble still pinches off at its base, as can also be seen in Figure 7.14a. In the case of $Oh = 10$, Figure 7.13b shows that r_d increases with θ_a. This behaviour is also shown in Figure 7.14b. Figure 7.14 also shows that as θ_a increases, the volume of the bubble V_d formed increases.

7.6.3 Comparison with Experiments

Chen *et al.* (2013b) carried out experiments on the formation of a bubble from an orifice of finite size where the contact line was free to move along the solid surface. Air was pumped at dimensional volumetric gas flow rate $\overline{Q}$ through a circular orifice of dimensional radius

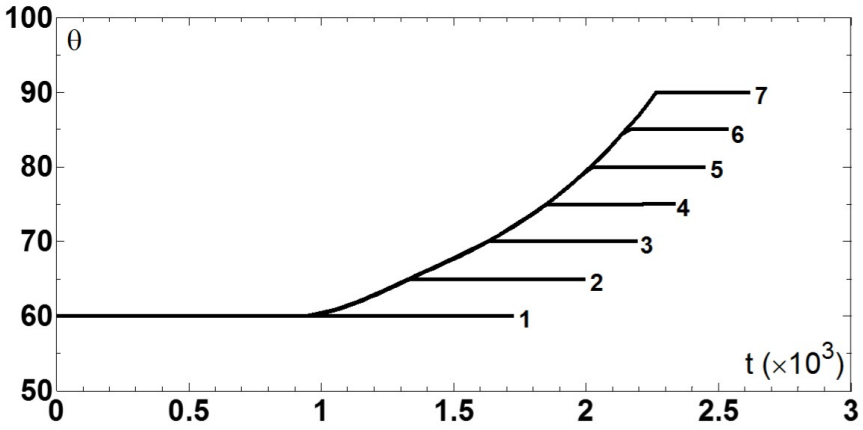

(a) The evolution of the dynamic contact angle θ.

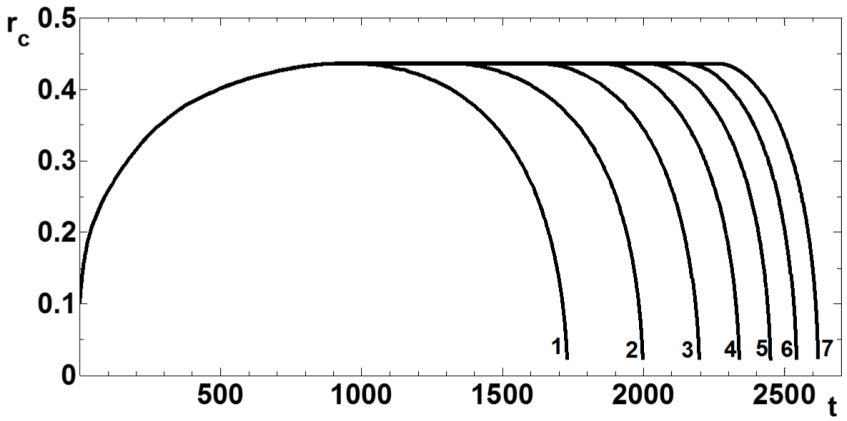

(b) The evolution of the radius of the contact line r_c.

Figure 7.12: The evolution of the dynamic contact angle θ and radius of the contact line r_c for various static advancing contact angles, where $\theta_a = 60°$ is given by line 1, $\theta_a = 65°$ (2), $\theta_a = 70°$ (3), $\theta_a = 75°$ (4), $\theta_a = 80°$ (5), $\theta_a = 85°$ (6) and $\theta_a = 90°$ (7). Also, $r_i = 0.1$, $U_c = 10^5$, $Q = 10^{-3}$, $Oh = 2.24 \times 10^{-3}$ and $\theta_r = \pi/3$.

$\overline{r}_o$ in a solid surface submerged in water. Therefore, for the experiments considered here, $Oh = 2.24 \times 10^{-3}$. The temporal evolution of the radius of the contact line, the dynamic contact angle and the free surface shape were reported.

Two of these experiments used the same solid surface and orifice size with only the volumetric gas flow rate differing. Therefore the aim here is to find a set of parameters θ_r, θ_a and U_c that can describe both experiments with θ_i used as a fitting parameter.

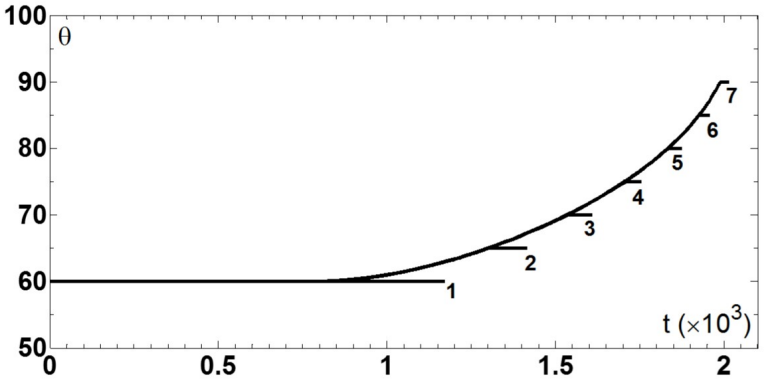

(a) The evolution of the dynamic contact angle θ.

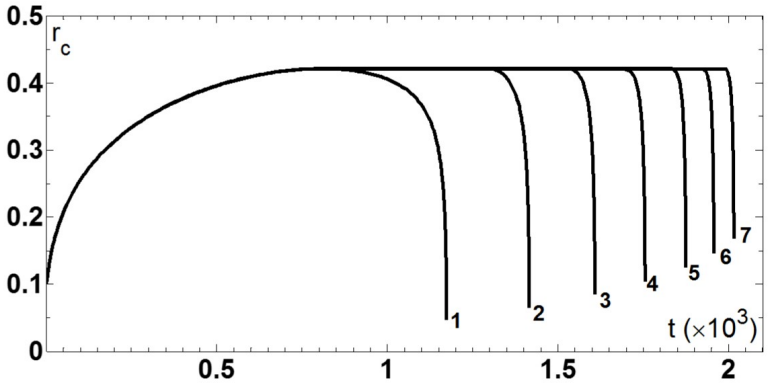

(b) The evolution of the radius of the contact line r_c.

Figure 7.13: The evolution of the dynamic contact angle θ and radius of the contact line r_c for various static advancing contact angles, where $\theta_a = 60°$ is given by line 1, $\theta_a = 65°$ (2), $\theta_a = 70°$ (3), $\theta_a = 75°$ (4), $\theta_a = 80°$ (5), $\theta_a = 85°$ (6) and $\theta_a = 90°$ (7). Also, $r_i = 0.1$, $U_c = 10^5$, $Q = 10^{-3}$, $Oh = 10$ and $\theta_r = \pi/3$.

The dimensional orifice radius is $\overline{r}_o = 1.5$ mm which corresponds to $r_o = 5.49 \times 10^{-1}$. The dimensional flow rate reported in the first experiment, denoted here by 'Experiment A', was $\overline{Q} = 0.53$ cm^{3}s^{-1} which corresponds to $Q = 9.74 \times 10^{-4}$, whilst in the second experiment, 'Experiment B', $\overline{Q} = 6.79$cm^{3}s^{-1} which corresponds to $Q = 1.24 \times 10^{-2}$. The key measure used as a comparison between the simulations and the experiments is the maximum value of the contact line radius r_m.

The constant contact angle regime, where $U_c = 10^5$ and $\theta_i = \theta_r$, is unable to describe

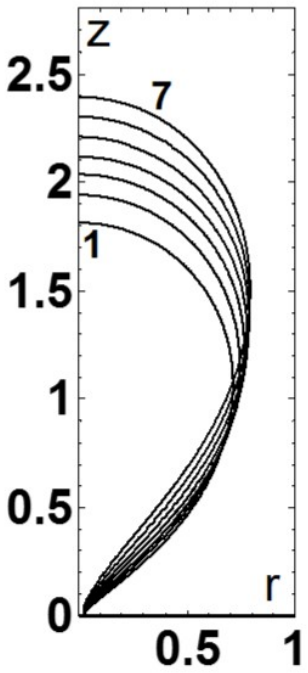

(a) The case of $Oh = 2.24 \times 10^{-3}$.

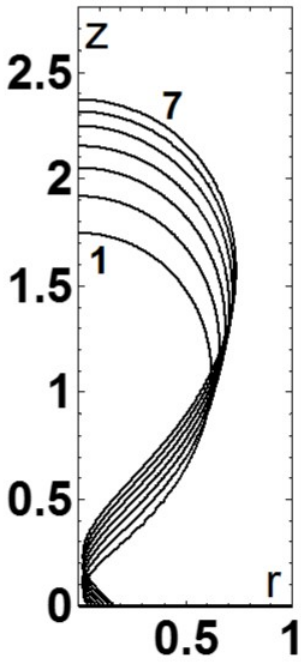

(b) The case of $Oh = 10$

Figure 7.14: The influence of the static advancing contact angle on the final bubble shape where $\theta_a = 60°$ is given by line 1, $\theta_a = 65°$ (2), $\theta_a = 70°$ (3), $\theta_a = 75°$ (4), $\theta_a = 80°$ (5), $\theta_a = 85°$ (6) and $\theta_a = 90°$ (7). Also, $r_i = 0.1$, $U_c = 10^5$, $Q = 10^{-3}$ and $\theta_r = \pi/3$.

the experiments. For large θ_a, Figure 7.15a shows that when $\theta_r = 94°$ (curve 6), the maximum contact line radius matches that observed in Experiment A. However, Figure 7.15b shows that when $\theta_r = 94°$, the contact line recedes much further than required in Experiment B, and it is $\theta_r = 80°$ (curve 3) that matches the maximum contact line radius. Therefore a dynamic contact angle may be required to describe the experiments.

Figure 7.16 shows that by reducing U_c, so that bubble formation is no longer in the constant contact angle regime, the distance the contact line recedes decreases. As established once again in Figure 7.15, increasing the static receding contact angle θ_r, increases the distance that the contact line recedes. Therefore, there may exist a combination of θ_r and U_c which describe both Experiment A and B, i.e. a dynamic contact angle is required.

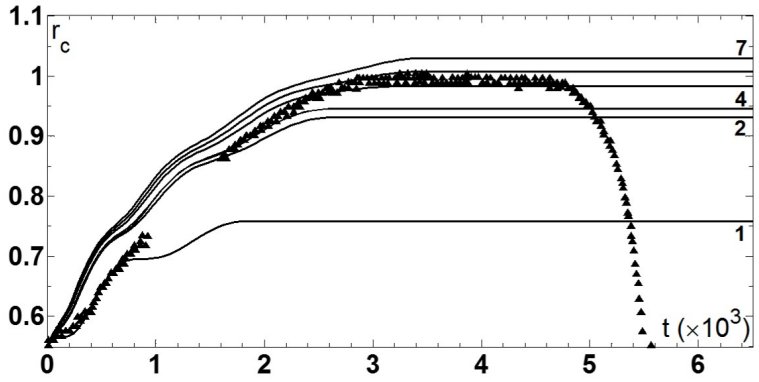

(a) Experiment A where $Q = 9.74 \times 10^{-4}$ and $\theta_r = 80°$ (line 1), 90° (2), 91° (3), 92° (4), 93° (5), 94° (6) and 95° (7).

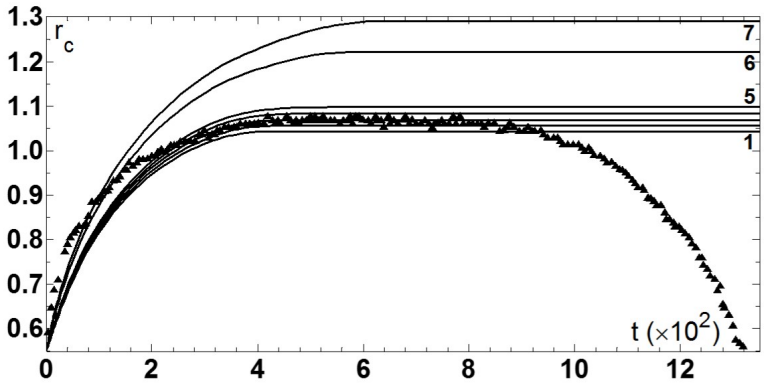

(b) Experiment B where $Q = 1.24 \times 10^{-2}$ and $\theta_r = 78°$ (line 1), 79° (2), 80° (3), 81° (4), 82° (5), 90° (6) and 94° (7).

Figure 7.15: The evolution of the radius of the contact line r_c for various θ_r where $r_o = 0.549$, $U_c = 10^5$, $\theta_i = \theta_r$, $Oh = 2.24 \times 10^{-3}$ and $\theta_a = 180°$. The $\triangle$ symbols represent the data from experiments.

It was found that by choosing $U_c = 10^{-2}$ and $\theta_r = \theta_i = 94°$, the maximum contact line radius observed in both experiments could be reproduced by the simulations. Figure 7.17 shows that increasing the static advancing contact angle results in an increase in formation time t_d. The influence of the initial contact angle θ_i can now be investigated to see whether the entire temporal evolution of the radius of the contact line, rather than just the maximum value, can be more accurately described by the simulations.

For Experiment A, Figure 7.18a shows that the initial contact angle θ_i has a negli-

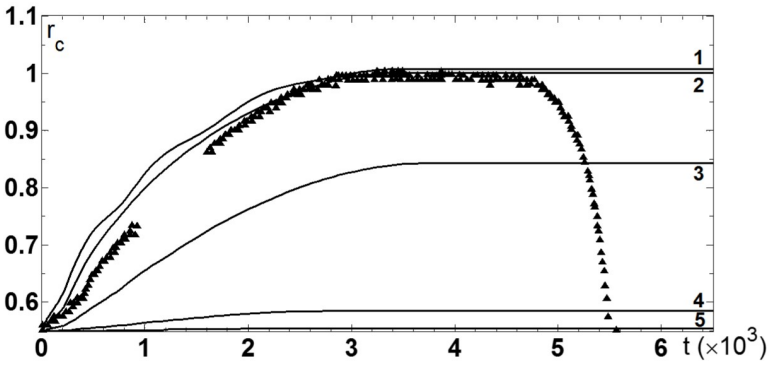

(a) Experiment A where $Q = 9.74 \times 10^{-4}$ and $\theta_r = 94°$.

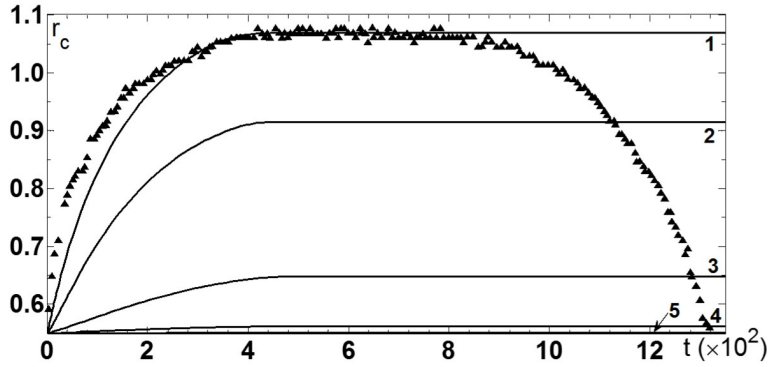

(b) Experiment B where $Q = 1.24 \times 10^{-2}$ and $\theta_r = 80°$.

Figure 7.16: The evolution of the radius of the contact line r_c for various U_c where $U_c = 10^5$ (line 1), 10^{-2} (2), 10^{-3} (3), 10^{-4} (4) and 10^{-5} (5). Also $r_o = 0.549$, $\theta_i = \theta_r$, $Oh = 2.24 \times 10^{-3}$ and $\theta_a = 180°$. The $\triangle$ symbols represent the data from experiments.

gible influence on the maximum radius of the contact line given the values of the other parameters. Increasing θ_i, more accurately describes the evolution of the contact line as it recedes, whilst decreasing θ_i more accurately describes the contact line as it advances. It was also seen that if $\theta_i > 96°$, then the contact line would initially pin to the rim of the orifice. The simulations slightly underestimate the value of the dynamic contact angle measured from the experiment, especially as the contact line advances.

Figure 7.18b shows that a decrease in θ_i leads to the contact line receding further, given the values of the other parameters used to describe Experiment B. This also results in an increase in the formation time t_d. The initial contact angle has a negligible influence on

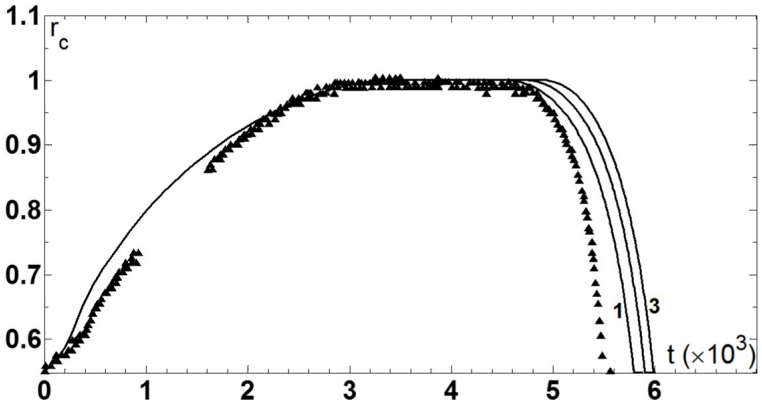

(a) Experiment A where $Q = 9.74 \times 10^{-4}$.

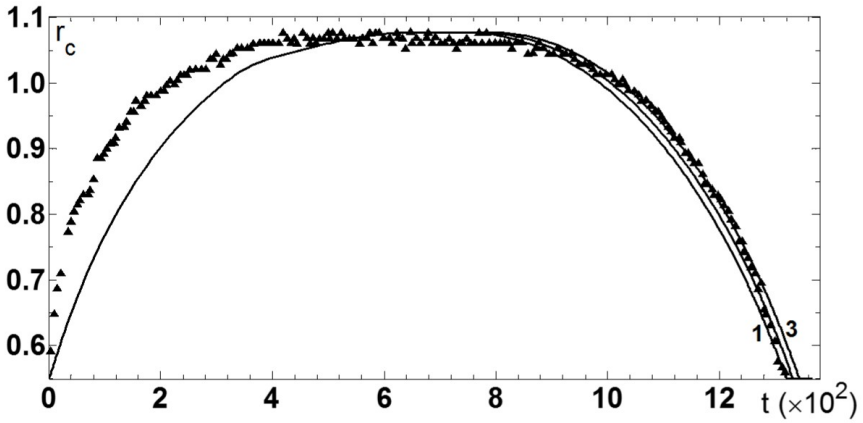

(b) Experiment B where $Q = 1.24 \times 10^{-2}$.

Figure 7.17: The evolution of the radius of the contact line r_c for various θ_a where $\theta_a = 100°$ (line 1), $102°$ (2) and $104°$ (3). Also $r_o = 0.549$, $\theta_i = \theta_r = 94°$, $U_c = 10^{-2}$ and $Oh = 2.24 \times 10^{-3}$. The $\triangle$ symbols represent the data from experiments.

the initial contact line motion as it recedes. The simulations underestimate the dynamic contact angle and the speed of the contact line as it initially recedes. On the other hand, the behaviour of the dynamic contact angle and the contact line as it advances it captured relatively accurately.

The changes in the initial contact angle θ_i considered in Figure 7.18 influence the formation time t_d, however they have a negligible effect on the final free surface shape and volume V_d of the bubble (see Figure 7.19).

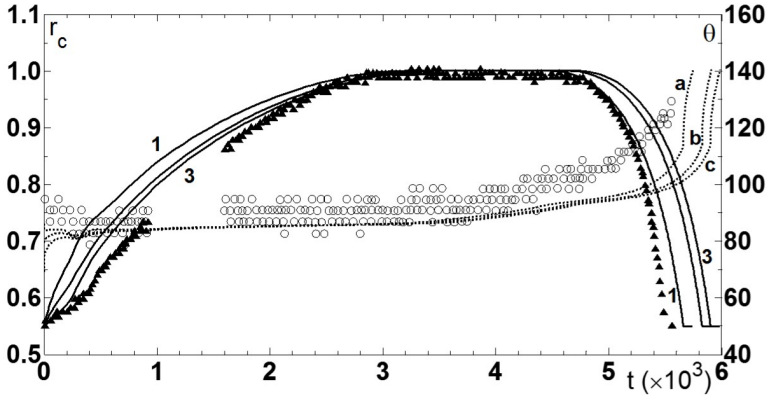

(a) Experiment A where $Q = 9.74 \times 10^{-4}$ and $\theta_i = 74°$ (lines 1 and a), 84° (2 and b) and 94° (3 and c).

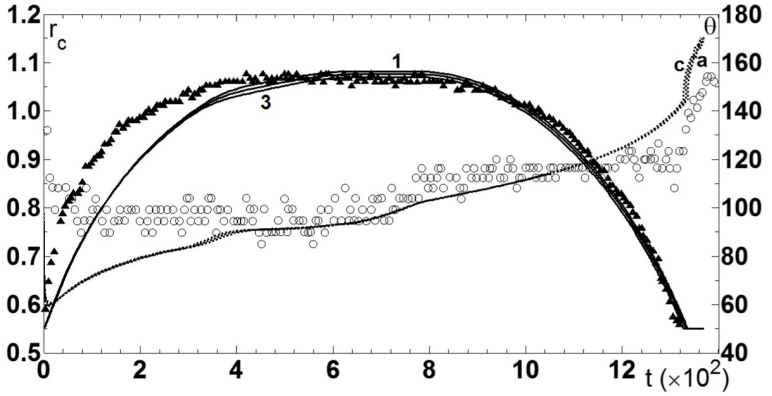

(b) Experiment B where $Q = 1.24 \times 10^{-2}$ and $\theta_i = 90°$ (lines 1 and a), 94° (2 and b) and 98° (3 and c).

Figure 7.18: The evolution of the radius of the contact line r_c (solid lines) and dynamic contact angle θ (dotted lines) for various θ_i. Also $r_o = 0.549$, $\theta_r = 94°$, $\theta_a = 102°$, $U_c = 10^{-2}$ and $Oh = 2.24 \times 10^{-3}$. The experimental data is given by the $\triangle$ symbols for r_c and the $\circ$ symbols for θ.

For Experiment A, the initial contact angle is chosen as $\theta_i = 74°$ (curves 1 and a in Figure 7.18a). The final free surface shape observed in the experiment had a dimensional experimental time of $\bar{t}_e = 218.2$ ms whilst the final simulated free surface profile occurred at the dimensional time $\bar{t} = 214.83$ ms. Therefore by applying $\bar{t} = \bar{t}_e - 3.37 \times 10^{-3}$ s a series of simulated free surface profiles can be compared to those from the experiment. Figure 7.20 shows that there is very good agreement between the experiment and sim-

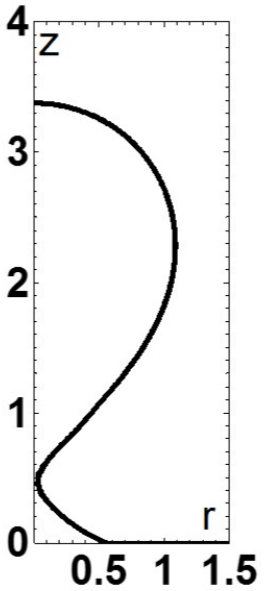

(a) Experiment A where $Q = 9.74 \times 10^{-4}$ and $\theta_i = 74°$, $84°$ and $94°$.

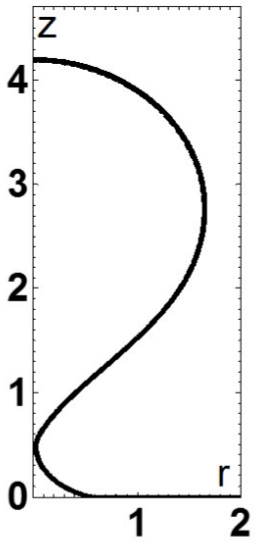

(b) Experiment B where $Q = 1.24 \times 10^{-2}$ and $\theta_i = 90°$, $94°$ and $98°$.

Figure 7.19: The free surface at pinch-off for various θ_i. Also $r_o = 0.549$, $\theta_r = 94°$, $\theta_a = 102°$, $U_c = 10^{-2}$ and $Oh = 2.24 \times 10^{-3}$.

ulation apart from the final stages of bubble formation where the experimental bubble loses axisymmetry. The nine dimensional experimental times are $\bar{t}_e = 8$ ms, 44.2 ms, 79.2 ms, 120.5 ms, 157.5 ms, 183.4 ms, 202.6 ms, 213.8 ms and 218.2 ms whilst the nine dimensional simulation times for the corresponding images are $\bar{t} = 4.63$ ms, 40.83 ms, 76.53 ms, 117.13 ms, 154.13 ms, 180.03 ms, 199.23 ms, 210.43 ms, and 214.83 ms.

For Experiment B, the initial contact angle is chosen as $\theta_i = 94°$ (curves 2 and b in Figure 7.18b). The final free surface shape observed in the experiment had a dimensional experimental time of $\bar{t}_e = 50.5$ ms whilst the final computed free surface profile had a dimensional time of $\bar{t} = 51.11$ ms. Therefore by applying $\bar{t} = \bar{t}_e + 6.1 \times 10^{-4}$ s the corresponding simulated free surface shapes can be found to compare with the experimental ones. Figure 7.21 shows that once again there is quite good agreement between the experiment and the simulation where the five dimensional experimental times were

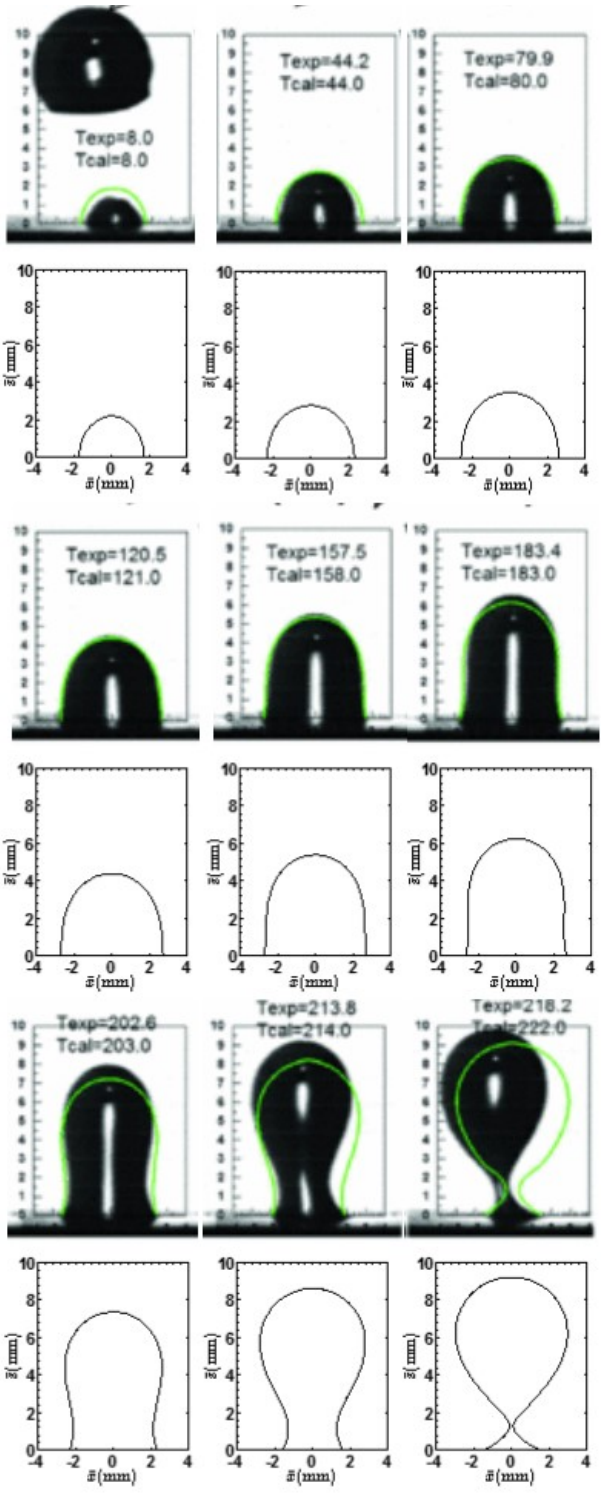

Figure 7.20: A comparison between the evolution of the free surface observed in Experiment A with simulations where $r_o = 0.549$, $\theta_r = 94°$, $\theta_a = 102°$, $\theta_i = 74°$, $U_c = 10^{-2}$ $Q = 9.74 \times 10^{-4}$ and $Oh = 2.24 \times 10^{-3}$. The results of the stick-slip model presented in Chen *et al.* (2009) are superimposed on the experimental images.

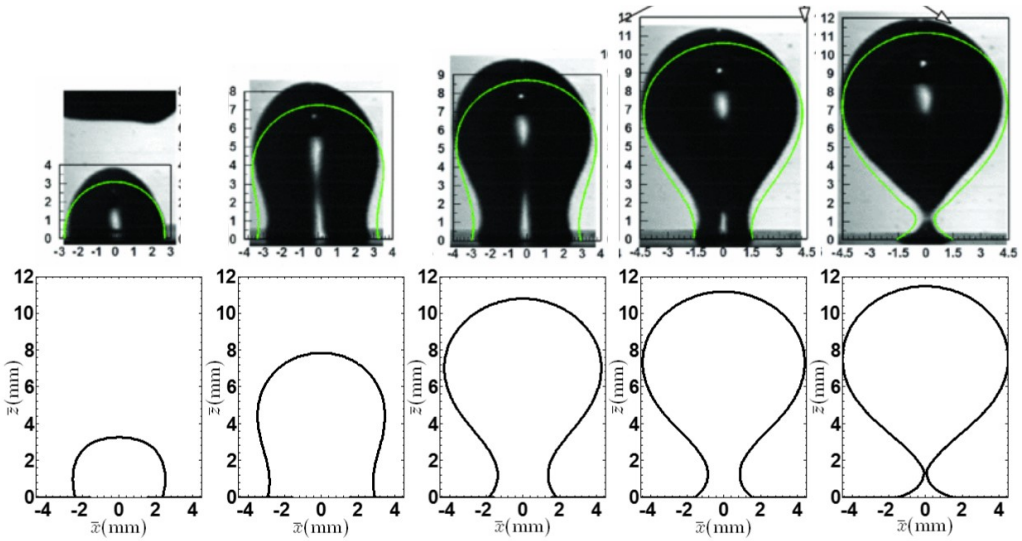

Figure 7.21: A comparison between the evolution of the free surface observed in Experiment B with simulations where $r_o = 0.549$, $\theta_r = 94$, $\theta_a = 102°$, $\theta_i = 94°$, $U_c = 10^{-2}$ $Q = 1.24 \times 10^{-2}$ and $Oh = 2.24 \times 10^{-3}$. The results of the stick-slip model presented in Chen *et al.* (2009) are superimposed on the experimental images.

$\bar{t}_e = 6$ ms, 31 ms, 47 ms, 49 ms, and 50.5 ms, and the five dimensional simulation times were $\bar{t} = 6.61$ ms, 31.61 ms, 47.61 ms, 49.61 ms, and 51.11 ms.

As well as presenting experimental results, Chen *et al.* (2013b) also attempted to describe the experiments using their contact angle model reported in Chen *et al.* (2009). The authors admitted that this so-called stick-slip model "is basically a kind of hypothesis" and has not been "justified by experiments or theories". In contrast to the contact angle model presented in this thesis (7.2), there is no explicit relationship between the dynamic contact angle and the contact line speed.

Even though the only difference between Experiments A and B is the volumetric gas flow rate, Chen *et al.* (2013b) used different pairs of static receding and advancing contact angles to describe the experiments. The static contact angles used to describe Experiment A were 95° and 115° (see Figure 7.22a) whilst 90° and 110° were used for Experiment B (see Figure 7.22b). This is in opposition to the contact angle model here which used

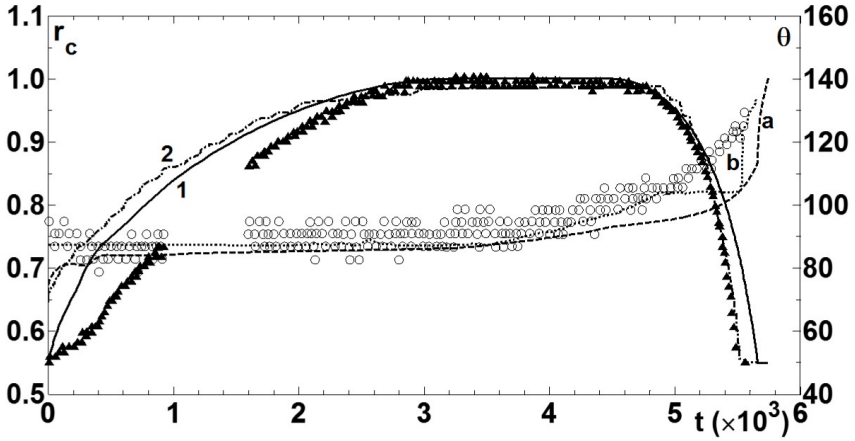

(a) Experiment A where $Q = 9.74 \times 10^{-4}$ and $\theta_i = 74°$.

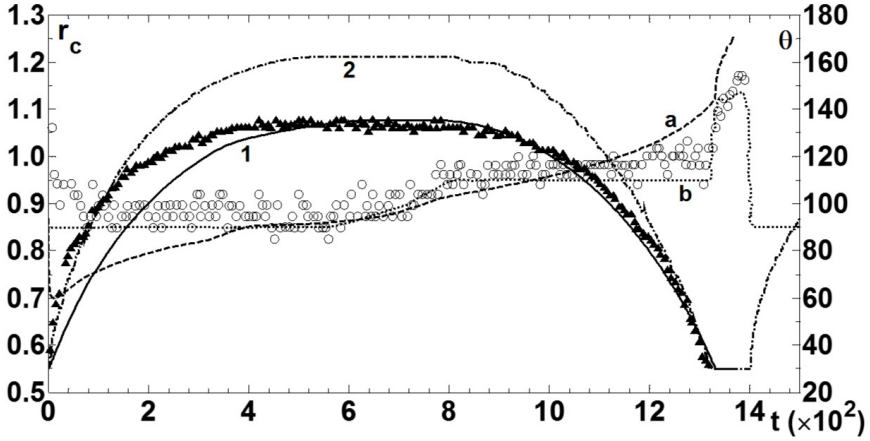

(b) Experiment B where $Q = 1.24 \times 10^{-2}$ and $\theta_i = 94°$.

Figure 7.22: A comparison with the contact angle model described in Chen *et al.* (2009). Lines 1 and a are the evolution of the contact line r_c and dynamic contact angle θ for the finite element simulations where $r_o = 0.549$, $\theta_r = 94°$, $\theta_a = 102°$ and $Oh = 2.24 \times 10^{-3}$. Lines 2 and b are the evolution of r_c and θ for the contact angle model described in Chen *et al.* (2009). The experimental data is given by the $\triangle$ symbols for r_c and the $\circ$ symbols for θ.

$\theta_r = 94°$ and $\theta_r = 102°$ for both experiments, which should be expected.

For Experiment A, Figure 7.22a shows that both contact angle models describe the maximum contact line radius accurately. The stick-slip model describes the advancing stage more accurately but the initial contact line radius does not match that of the

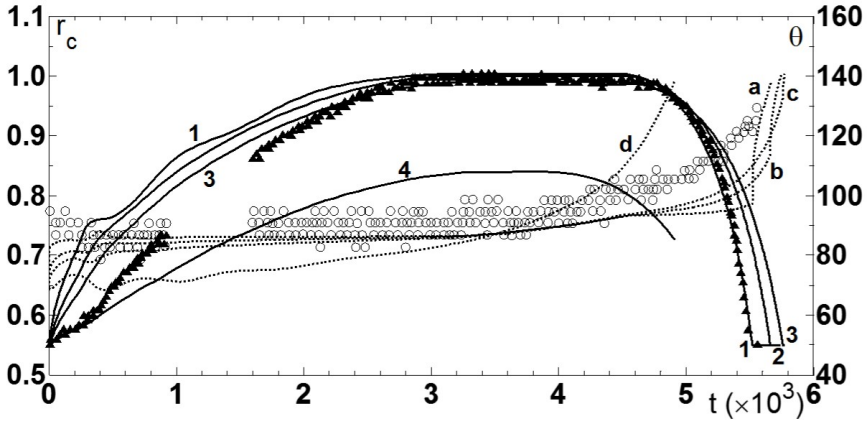

(a) Experiment A where $Q = 9.74 \times 10^{-4}$ and $\theta_i = 74°$.

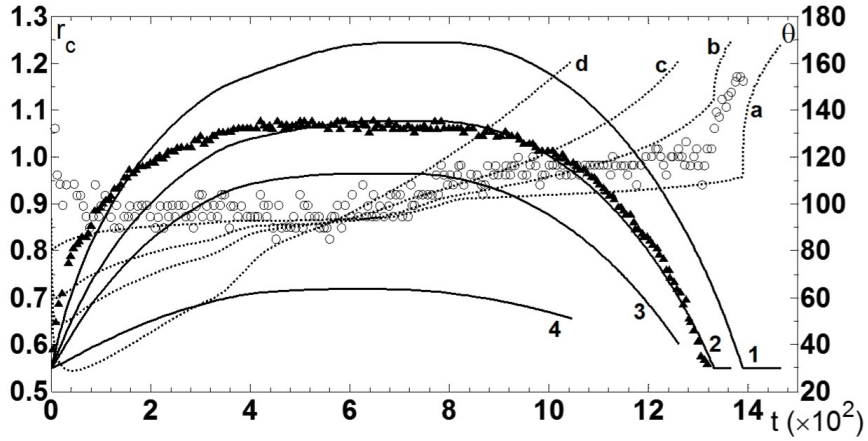

(b) Experiment B where $Q = 1.24 \times 10^{-2}$ and $\theta_i = 94°$.

Figure 7.23: The evolution of the radius of the contact line r_c (solid lines) and dynamic contact angle θ (dotted lines) for various U_c where $U_c = 5 \times 10^{-2}$ (lines 1 and a), 10^{-2} (2 and b), 5×10^{-3} (3 and c) and 10^{-3} (4 and d). Also $r_o = 0.549$, $\theta_r = 94°$, $\theta_a = 102°$ and $Oh = 2.24 \times 10^{-3}$. The experimental data is given by the $\triangle$ symbols for r_c and the $\circ$ symbols for θ.

experiment, unlike the simulations presented here. Figure 7.20 shows that the free surface shapes described by the stick-slip model and the present model are very similar.

For Experiment B, Figure 7.22b shows that the model described here is much more accurate in describing the maximum contact line radius since the stick-slip model overshoots this by some margin. The current model is also more accurate in describing both

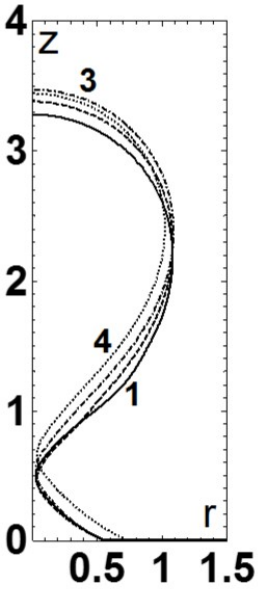

(a) Experiment A where $Q = 9.74 \times 10^{-4}$ and $\theta_i = 74°$.

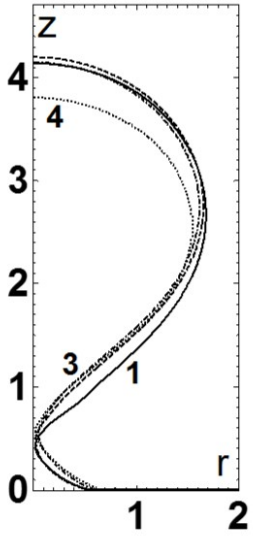

(b) Experiment B where $Q = 1.24 \times 10^{-2}$ and $\theta_i = 94°$.

Figure 7.24: The free surface at pinch-off for various U_c where $U_c = 5 \times 10^{-2}$ (solid line 1), 10^{-2} (dashed line 2), 5×10^{-3} (dot-dashed line 3) and 10^{-3} (dotted line 4). Also $r_o = 0.549$, $\theta_r = 94°$, $\theta_a = 102°$ and $Oh = 2.24 \times 10^{-3}$.

the receding and advancing phases of the contact line. Figure 7.21 shows that the current model is also better in describing the evolution of the free surface. This can be shown by the difference in height between the simulations from the current model and the stick-slip model.

At first glance, Figures 7.22a and 7.22b show that the stick-slip model presented is more successful in tracking the evolution of the dynamic contact angle. However, Chen *et al.* (2013b) did not restrict themselves to using the same static receding and advancing contact angles for both experiments, as the current model does, which would be expected. Therefore matching the experimentally observed evolution of the dynamic contact angle would be an unfair test of the accuracy of the current model and the stick-slip model.

Figure 7.23 shows once again that by decreasing U_c, the distance the contact line

recedes decreases whilst Figure 7.24 shows that this results in a smaller bubble being formed.

7.7 Summary

In this chapter the formation of a bubble from an orifice whose contact line is free to move was investigated. The numerical platform described in Chapter 4 was extended to incorporate amended boundary conditions which ensured the resolution of the moving contact line problem. The influence of wettability on the bubble formation process was investigated and simulations were compared with experiments. In the next chapter, the formation of a single and compound liquid drops are considered.

Chapter 8

Generation of Compound Microdrops

The following research into the generation of a compound microdrop from an annular nozzle was undertaken as part of a six month research grant from the EPSRC Centre for Innovative Manufacturing in Additive Manufacturing at the University of Nottingham. They are interested in the development and optimisation of the materials and systems required for the next generation of multi-material additive manufacturing applications. The aim of the study was to determine theoretically whether or not a compound micro-droplet could be generated using the technique of coaxial jetting without the use of flow focusing.

The generation of single drops by pumping a liquid through a nozzle, at low volumetric flow rates (dripping regime) or high volumetric flow rates (jetting regime), and the associated break-up of the liquid phase, has been well studied both theoretically and experimentally for the case of drop formation in air (Basaran, 2002; Eggers, 1997; Chen *et al.*, 2002; Notz *et al.*, 2001; Xu & Basaran, 2007; Wilkes *et al.*, 1999; Dong *et al.*, 2006; Zhang & Basaran, 1995; Zhang, 1999; Henderson *et al.*, 1997; Fawehinmi *et al.*, 2005;

Ambravaneswaran *et al.*, 2004) or in a quiescent/co-flowing/flow-focusing liquid (Suryo & Basaran, 2006; Zhang & Stone, 1997; Stone, 1994; Doshi *et al.*, 2003; Cramer *et al.*, 2004; Utada *et al.*, 2007; Anna *et al.*, 2003; Lee *et al.*, 2009; Hua *et al.*, 2007; Chen *et al.*, 2013a; Lister & Stone, 1998; Leppinen & Lister, 2003).

By introducing a third fluid into the flow-focusing process, compound drops in an ambient liquid, also known as a double emulsion, can be produced (Vu *et al.*, 2013; Zhou *et al.*, 2006; Lee *et al.*, 2007; Utada *et al.*, 2005; Okushima *et al.*, 2004). The production of even higher order droplets by utilising co-flow and flow focusing microfluidic devices to form emulsions is also well established (Shah *et al.*, 2008), however, whilst the stability of compound threads has received much attention (Craster *et al.*, 2005; Herrada *et al.*, 2010; Chauhan *et al.*, 2000; Suryo *et al.*, 2006; Radev & Tchavdarov, 1988), the controlled formation of a compound droplet by coaxial jetting in air, without the use of flow focusing, on the characteristic dimensions associated with inkjet printing remains an open question.

8.1 Problem Formulation

Consider two quiescent, immiscible, incompressible, viscous Newtonian fluids being pumped through an annular nozzle with an outer radius r_1 and inner radius r_2 in the direction of gravity where, once again, the fluid flow is assumed to be axisymmetric about the vertical axis (see Fig. 8.1). The 'carrier' or outer liquid with a constant density ρ_1 and dynamic viscosity μ_1 is pumped through the outer nozzle at a constant volumetric flow rate Q_1 whilst the 'core' or inner liquid with a constant density ρ_2 and dynamic viscosity μ_2 is pumped through the inner nozzle at a constant volumetric flow rate Q_2. The drop is surrounded by an inviscid and dynamically-passive gas whose pressure p_g is assumed to be a constant. The respective surface tensions of the liquid-gas and liquid-liquid interfaces are σ_1 and σ_2.

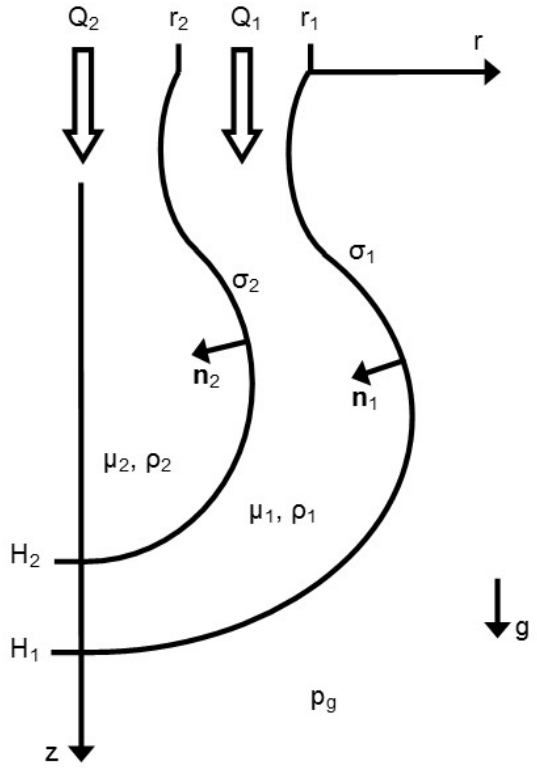

Figure 8.1: A sketch of the flow domain in the (r, z)-plane.

The velocity and pressure fields may be written as $\mathbf{u}_1(r, z, t) = u_1(r, z, t)\mathbf{e}_r + w_1(r, z, t)\mathbf{e}_z$ and $p_1(r, z, t)$ for the carrier fluid, and $\mathbf{u}_2(r, z, t) = u_2(r, z, t)\mathbf{e}_r + w_2(r, z, t)\mathbf{e}_z$ and $p_2(r, z, t)$ for the inner fluid. The unit normal vector to the liquid-gas interface that points into the outer liquid phase is denoted by $\mathbf{n}_1$ whilst the unit normal vector to the liquid-liquid interface that points into the inner liquid phase is denoted by $\mathbf{n}_2$.

The dimensional Navier-Stokes equations are given by (3.1) with $\mathbf{u} = \mathbf{u}_1$, $p = p_1$, $\rho = \rho_1$ and $\mu = \mu_1$ for the outer liquid phase and $\mathbf{u} = \mathbf{u}_2$, $p = p_2$, $\rho = \rho_2$ and $\mu = \mu_2$ for the inner liquid phase. In both liquid phases $\mathbf{g} = g\mathbf{e}_z$ whilst the stress tensor for the outer and inner liquids are denoted by $\mathbf{P}_1$ and $\mathbf{P}_2$, respectively.

On the liquid-gas interface, the dimensional combined stress condition is given by substituting $\mathbf{P} = \mathbf{P}_1$, $\sigma = \sigma_1$ and $\mathbf{n} = \mathbf{n}_1$ into (3.5), whilst on the liquid-liquid interface,

the combined stress condition is given by substituting $\mathbf{P} = \mathbf{P}_2$, $\mathbf{P}_g = \mathbf{P}_1$, $\sigma = \sigma_2$ and $\mathbf{n} = \mathbf{n}_2$ into (3.5).

The following scales are defined for length r_1, velocity U, time r_1/U, pressure σ_1/r_1 and flow rate Ur_1^2. The following ratios are also defined for nozzle radius $\widehat{r} = r_2/r_1$, flow rate $\widehat{Q} = Q_2/Q_1$, density $\widehat{\rho} = \rho_2/\rho_1$, dynamic viscosity $\widehat{\mu} = \mu_2/\mu_1$ and surface tension $\widehat{\sigma} = \sigma_2/\sigma_1$. All quantities are now dimensionless unless stated.

The incompressible flow in the respective outer and inner bulk fluids is governed by the dimensionless Navier-Stokes equations,

$$\nabla \cdot \mathbf{u}_1 = 0, \qquad Re\left[\frac{\partial \mathbf{u}_1}{\partial t} + (\mathbf{u}_1 \cdot \nabla)\,\mathbf{u}_1\right] = \nabla \cdot \mathbf{P}_1 + \frac{Bo}{Ca}\mathbf{e}_z, \tag{8.1a}$$

$$\nabla \cdot \mathbf{u}_2 = 0, \qquad \widehat{\rho}Re\left[\frac{\partial \mathbf{u}_2}{\partial t} + (\mathbf{u}_2 \cdot \nabla)\,\mathbf{u}_2\right] = \nabla \cdot \mathbf{P}_2 + \widehat{\rho}\frac{Bo}{Ca}\mathbf{e}_z, \tag{8.1b}$$

where $\mathbf{P}_1 = -\frac{p_1}{Ca}\mathbf{I} + \nabla\mathbf{u}_1 + (\nabla\mathbf{u}_1)^T$ and $\mathbf{P}_2 = -\frac{p_2}{Ca}\mathbf{I} + \widehat{\mu}\left[\nabla\mathbf{u}_2 + (\nabla\mathbf{u}_2)^T\right]$ are the respective stress tensors of the outer and inner fluids. The Reynolds, capillary and Bond numbers are given by $Re = \rho_1 r_1 U/\mu_1$, $Ca = \mu_1 U/\sigma_1$ and $Bo = \rho_1 g r_1^2/\sigma_1$, respectively.

A kinematic boundary condition (3.19) is required on both free surfaces. Therefore on the liquid-gas and liquid-liquid interfaces,

$$\frac{\partial f_1}{\partial t} + \mathbf{u}_1 \cdot \nabla f_1 = 0, \tag{8.2a}$$

$$\frac{\partial f_2}{\partial t} + \mathbf{u}_2 \cdot \nabla f_2 = 0, \tag{8.2b}$$

respectively, where $f_1(r, z, t) = 0$ and $f_2(r, z, t) = 0$ denote the a-priori unknown liquid–gas and liquid-liquid interfaces.

The dimensionless combined stress condition on the liquid-gas interface is then

$$\frac{p_g}{Ca}\mathbf{n}_1 + \mathbf{n}_1 \cdot \mathbf{P}_1 = \frac{1}{Ca}\mathbf{n}_1 \nabla \cdot \mathbf{n}_1, \tag{8.3}$$

with the respective normal and tangential projections given by

$$\frac{p_g}{Ca} + \mathbf{n}_1 \cdot \mathbf{P}_1 \cdot \mathbf{n}_1 = \frac{1}{Ca} \nabla \cdot \mathbf{n}_1, \tag{8.4a}$$

$$\mathbf{n}_1 \cdot \mathbf{P}_1 \cdot (\mathbf{I} - \mathbf{n}_1 \mathbf{n}_1) = \mathbf{0}. \tag{8.4b}$$

On the liquid-liquid interface, the dimensionless combined stress condition is

$$\mathbf{n}_2 \cdot (\mathbf{P}_2 - \mathbf{P}_1) = \frac{\widehat{\sigma}}{Ca} \mathbf{n}_2 \nabla \cdot \mathbf{n}_2, \tag{8.5}$$

with the respective normal and tangential projections,

$$\mathbf{n}_2 \cdot (\mathbf{P}_2 - \mathbf{P}_1) \cdot \mathbf{n}_2 = \frac{\widehat{\sigma}}{Ca} \nabla \cdot \mathbf{n}_2, \tag{8.6a}$$

$$\mathbf{n}_2 \cdot (\mathbf{P}_2 - \mathbf{P}_1) \cdot (\mathbf{I} - \mathbf{n}_2 \mathbf{n}_2) = \mathbf{0}. \tag{8.6b}$$

An additional condition that is required for the liquid-liquid interface is the continuity of velocity across it,

$$\mathbf{u}_1 = \mathbf{u}_2. \tag{8.7}$$

At the axis of symmetry adjacent to the respective outer and inner liquid phases, the conditions of axial symmetry and smoothness of the velocity field are applied,

$$u_1 = 0, \qquad \frac{\partial w_1}{\partial r} = 0, \tag{8.8a}$$

$$u_2 = 0, \qquad \frac{\partial w_2}{\partial r} = 0. \tag{8.8b}$$

It is assumed that the fluid flow through each nozzle exit has fully developed into a Poiseuille flow and so the velocity at the exits of the respective outer and inner nozzles

are,

$$u_1 = 0, \qquad w_1 = \frac{2Q}{\pi\,(1-\widehat{r}^2)}\frac{(1-\widehat{r}^2)\ln r + (r^2-1)\ln\widehat{r}}{\widehat{r}^2 - 1 - (\widehat{r}^2+1)\ln\widehat{r}}, \qquad \widehat{r} \leqslant r \leqslant 1, \tag{8.9a}$$

$$u_2 = 0, \qquad w_2 = \frac{2\widehat{Q}Q}{\pi\widehat{r}^2}\left(1 - \frac{r^2}{\widehat{r}^2}\right), \qquad 0 \leqslant r \leqslant \widehat{r}, \tag{8.9b}$$

where Q is the dimensionless volumetric flow rate through the outer nozzle.

The normal stress boundary conditions, (8.4a) on the liquid-gas interface and (8.6a) on the liquid-liquid interface, are themselves differential equations determining the shape of the corresponding free surfaces and as such require their own boundary conditions. First of all, where the interfaces meet the axis of symmetry, at the apexes $(0, H_1)$ and $(0, H_2)$, respectively, the free surface is smooth,

$$\nabla f_1 \cdot \mathbf{e}_r = 0, \qquad \nabla f_2 \cdot \mathbf{e}_r = 0, \tag{8.10}$$

and secondly, the liquid-gas and liquid-liquid interfaces remain pinned to the outer and inner wall of the annular nozzle, respectively, for all time,

$$f_1(1, 0, t) = 0, \qquad f_2(\widehat{r}, 0, t) = 0. \tag{8.11}$$

Finally, for this initial-value problem, the initial velocity field and the initial shape of both free surfaces must be prescribed. It is assumed that both liquid phases are initially at rest,

$$u_1 = u_2 = w_1 = w_2 = 0, \tag{8.12}$$

and the respective liquid-gas and liquid-liquid interfaces are initially hemispherical,

$$r^2 + z^2 = 1, \qquad 0 \leqslant r \leqslant 1, \qquad 0 \leqslant z \leqslant 1, \tag{8.13a}$$

$$r^2 + z^2 = \widehat{r}^2, \qquad 0 \leqslant r \leqslant \widehat{r}, \qquad 0 \leqslant z \leqslant \widehat{r}. \tag{8.13b}$$

This set of dimensionless equations (8.1)–(8.13) is characterised by the nine dimensionless parameters; $\widehat{r}$, Q, $\widehat{Q}$, Re, Ca, Bo, $\widehat{\rho}$, $\widehat{\mu}$ and $\widehat{\sigma}$.

8.2 Amendments to the Numerical Platform

The numerical platform described in Chapter 4 can be amended once again to solve the set of dimensional equations (8.1)–(8.13). Only brief details are given, however, the incorporation of a second moving boundary, the liquid-liquid interface, and a second bulk phase is extremely technically challenging.

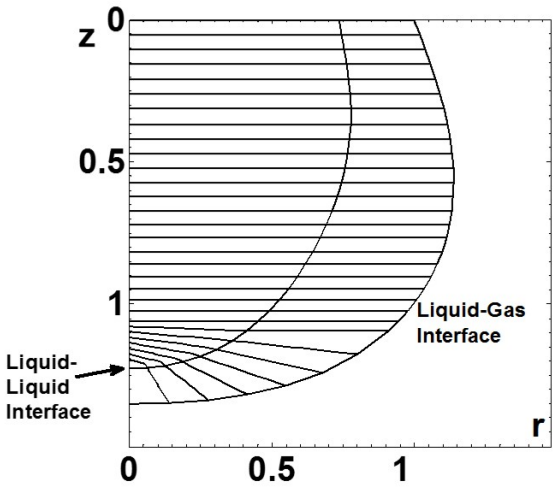

(a) The arrangement of the spines in the mesh.

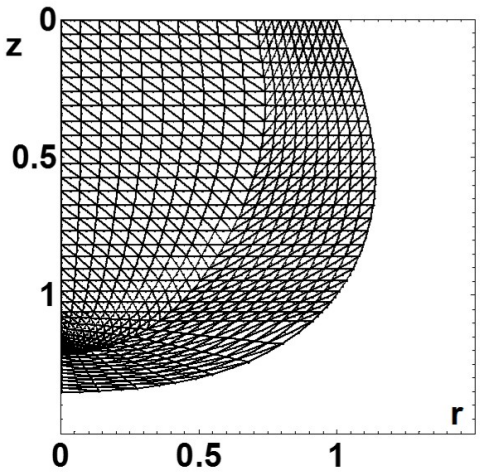

(b) The arrangement of the elements in the mesh.

Figure 8.2: The design of the computational mesh for the simulation of a compound droplet.

The design of the computational mesh is once again based on the 'method of spines' described in Section 4.2, however this time there are two moving boundaries to track explicitly. Figure 8.2a shows how the spines are arranged throughout the mesh. Each spine runs from the axis of symmetry to the liquid-liquid interface and then onto the liquid-gas interface. Therefore, if there are N_1 nodes distributed along the liquid-gas interface, there are also N_1 nodes distributed along the liquid-liquid interface. The design of the mesh is simpler than that used for the formation of a bubble as, rather than having to include spines based on a bipolar-coordinate system, here the majority of spines are positioned horizontally. Spines near the apex of the inner liquid phase then run radially in order to capture the shape of both moving boundaries.

For each node distributed along the liquid-gas and liquid-liquid interface, its position is once again determined by two free surface unknowns. The first free surface unknown ζ is simply the distance of each node along its corresponding spine from the axis of symmetry. Then for a given spine, the second free surface node χ, is the same for the node on the liquid-gas interface and liquid-liquid interface. Where a spine is horizontal, χ is the height of the spine, and where a spine is at an angle, χ is the angle the spine makes with the horizontal.

The nodes distributed along the liquid-liquid interface must be treated differently from those on the liquid-gas interface. Due to the capillary pressure of the liquid-liquid interface, the value of the outer pressure field as a node on the liquid-liquid interface is approached from the outer liquid phase is different from that of the inner pressure field as the same node is approached from the inner liquid phase. Therefore, in order to ensure the incompressibility of both the inner and outer liquid phases, at each node on the liquid-liquid interface the value of both the r and z components of the inner and outer velocity fields must be determined, and when a node is also a pressure node, the value of inner and outer pressure field must be found.

The total number of nodes in the computational domain $N = N_i + N_o + N_1$, where N_i and N_o are the number of nodes in the inner and outer liquid phases, including those distributed along the axis of symmetry, mouth of orifices and liquid-gas interface but excluding those distributed along the liquid-liquid interface. Of the $N_o + N_1$ nodes at which the outer velocity field must be found, at $N_{p,o}$ of these nodes the outer pressure field must be determined. Similarly, of the $N_i + N_1$ nodes at which the inner velocity field must be found, at $N_{p,i}$ of these nodes the inner pressure field must be determined. Therefore the unknowns that need to be found at each time step are:

- Both components of the outer velocity field, $u_{1,J}(r_J, z_J, t)$ and $w_{1,J}(r_J, z_J, t)$, where $J = 1, ..., N_o + N_1$
- Both components of the inner velocity field, $u_{2,J}(r_J, z_J, t)$ and $w_{2,J}(r_J, z_J, t)$, where $J = 1, ..., N_i + N_1$
- The outer pressure field, $p_{1,J}(r_J^{(p)}, z_J^{(p)}, t)$, where $J = 1, ..., N_{p,o}$, at every pressure node in the outer liquid phase including those on the liquid-liquid interface
- The inner pressure field, $p_{2,J}(r_J^{(p)}, z_J^{(p)}, t)$, where $J = 1, ..., N_{p,i}$, at every pressure node in the inner liquid phase including those on the liquid-liquid interface
- The free surface unknown, $\zeta_{1,J}$ where $J = 1, ..., N_1$ at every node distributed along the liquid-gas interface
- The free surface unknown, $\zeta_{2,J}$ where $J = 1, ..., N_1$ at every node distributed along the liquid-liquid interface
- The free surface unknown, χ_J where $J = 1, ..., N_1$ for every spine in the computational domain

Therefore there are $N_T = 2(N_o + N_i) + 5N_1 + N_{p,o} + N_{p,i}$ unknowns in total. These are determined by the r and z components of the momentum residual for the outer liquid

phase ($N_o + N_1$ equations), the r and z components of the momentum residual for the inner liquid phase ($N_i + N_1$ equations), the continuity residual for the outer liquid phase ($N_{p,o}$ equations), the continuity residual for the inner liquid phase ($N_{p,i}$ equations), the kinematic residual on the liquid-gas interface (N_1 equations), the kinematic residual on the liquid-liquid interface (N_1 equations) and the mesh residual that determines how nodes are distributed along either the liquid-liquid interface or the liquid-gas interface (N_1 equations).

Unlike the formation of a gas bubble, the value of the pressure field does not need to be arbitrarily prescribed at a point in the flow domain. The 'level' of the pressure field is instead determined by the gas pressure p_g, and for all simulations, $p_g = 0$ is used as the reference pressure.

8.3 Formation of a Single Drop

Before the generation of a compound microdrop is simulated, a test case of the formation of a single drop is considered. The problem formulation for the compound drop can describe the formation of a single drop by setting $\widehat{r} = 0$, choosing $U = 2Q_1/\pi r_1^2$ as the velocity scale and therefore applying $w = 1 - r^2$ at the mouth of the orifice. The problem is then characterised by the three dimensionless parameters (Re, Ca, Bo).

Zhang & Basaran (1995) carried out experiments on the formation of a single drop from a nozzle and recorded the evolution of the free surface. For the case considered here, a water drop ($\rho = 996$ kg m^{-3}, $\mu = 10^{-3}$ mPa s, $\sigma = 73$ mN m^{-1}) forms out of a nozzle of dimensional radius $r_1 = 1.6 \times 10^{-3}$ m with a dimensional volumetric flow rate of $Q_1 = 1.67 \times 10^{-8}$ m^3 s^{-1}. The values of the dimensionless parameters are then given by $Re = 6.62$, $Ca = 5.69 \times 10^{-5}$ and $Bo = 0.343$.

Figure 8.3 shows the comparison of the experiment with the simulations produced by

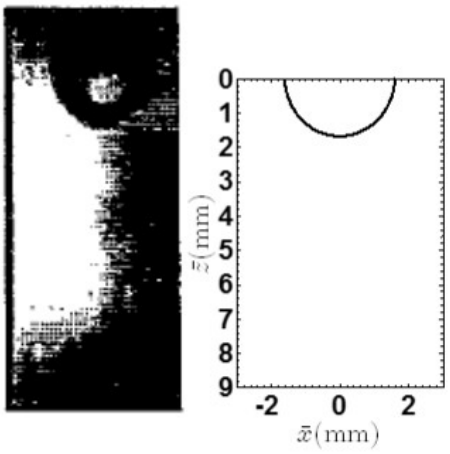

(a) $\bar{t}_e = 0.05$ s and $\bar{t} = 0.015$ s.

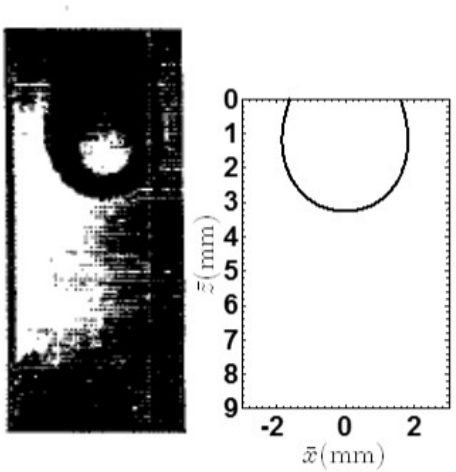

(b) $\bar{t}_e = 1.09$ s and $\bar{t} = 1.055$ s.

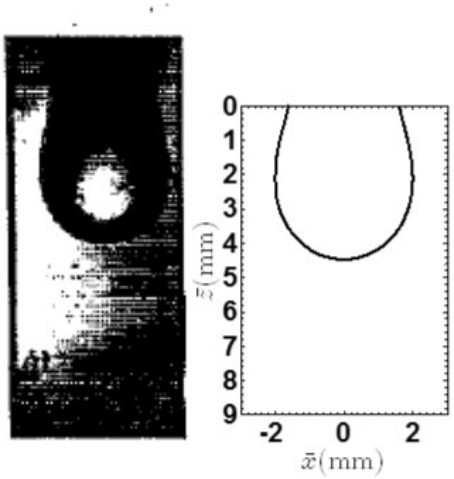

(c) $\bar{t}_e = 2.092$ s and $\bar{t} = 2.057$ s.

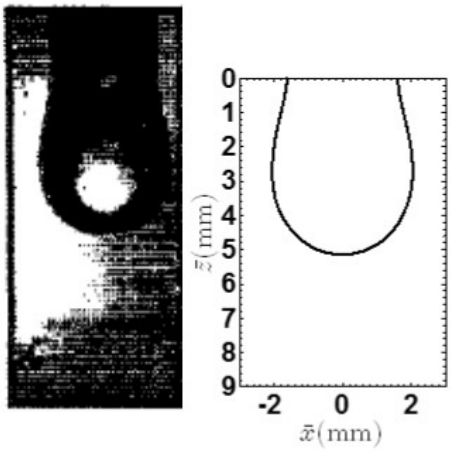

(d) $\bar{t}_e = 2.59$ s and $\bar{t} = 2.555$ s.

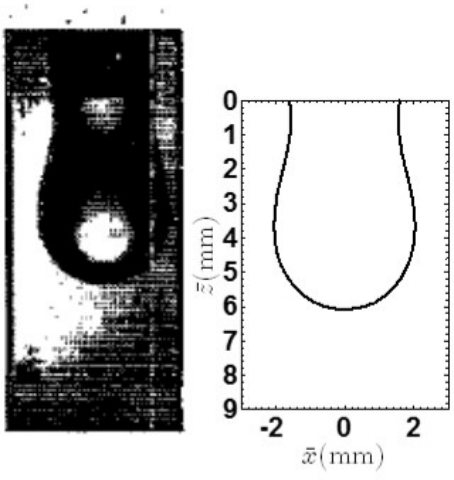

(e) $\bar{t}_e = 2.99$ s and $\bar{t} = 2.955$ s.

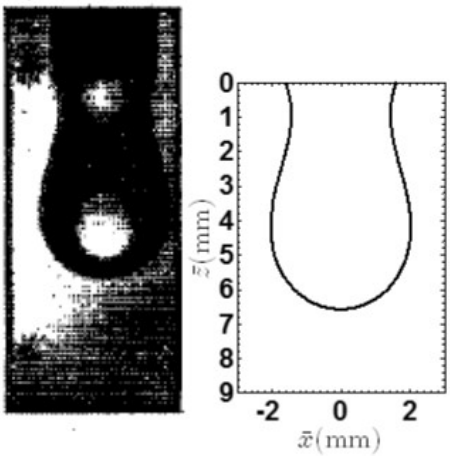

(f) $\bar{t}_e = 3.04$ s and $\bar{t} = 3.005$ s.

Figure 8.3: continued.

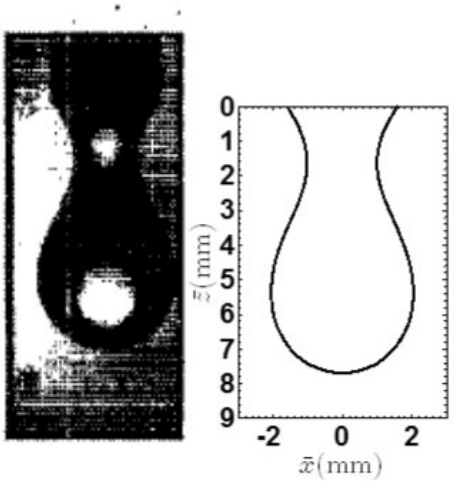

(g) $\bar{t}_e = 3.075$ s and $\bar{t} = 3.04$ s.

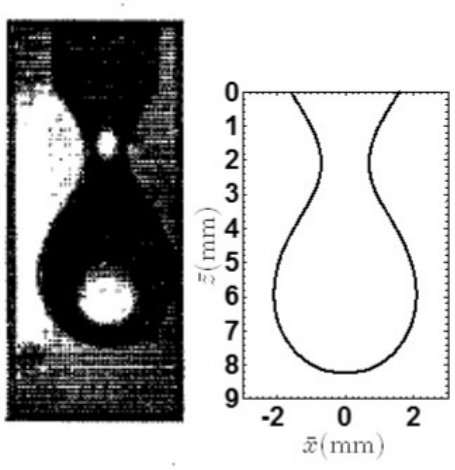

(h) $\bar{t}_e = 3.083$ s and $\bar{t} = 3.048$ s.

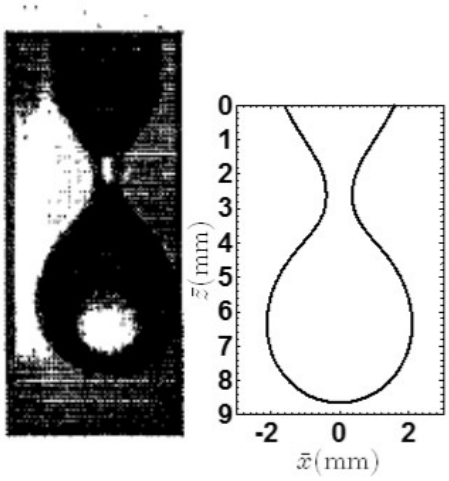

(i) $\bar{t}_e = 3.087$ s and $\bar{t} = 3.052$ s.

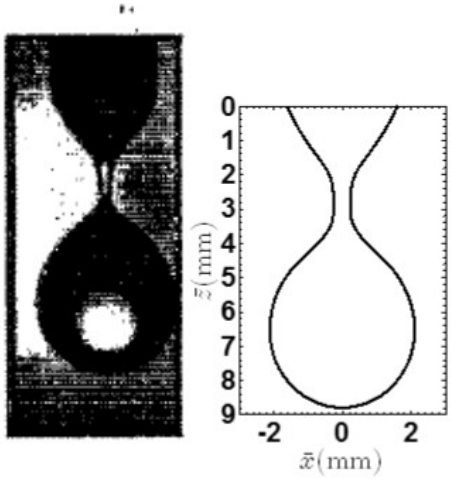

(j) $\bar{t}_e = 3.089$ s and $\bar{t} = 3.054$ s.

Figure 8.3: A comparison between experimental images from Zhang & Basaran (1995) and computational free surface profiles for the formation of a single drop. The dimensional case of a water drop forming at a flow rate of $Q_1 = 1.67 \times 10^{-8}$ m^3 s^{-1} through a nozzle of orifice radius $r_1 = 1.6 \times 10^{-3}$ m corresponds to the dimensionless case of $(Re, Ca, Bo) = (6.62, 5.69 \times 10^{-5}, 0.343)$. The dimensional experimental $\bar{t}_e$ and simulation $\bar{t}$ times are given with each subfigure.

the numerical platform at various time steps during the evolution of the drop. The images from the computations best matched those from the experiments when $\bar{t} = \bar{t}_e - 0.035$ where $\bar{t}$ is the dimensional simulation time and $\bar{t}_e$ is the dimensional experimental time reported in Zhang & Basaran (1995).

There is good agreement between the experimental images and the free surface profiles computed by the numerical platform. The drop begins as a hemisphere (see Figure 8.3a) and grows spherically as the force of capillarity dominates the initial growth (see Figure 8.3b). As the volume of the drop increases, the gravitational force becomes more important and the drop lengthens away from the nozzle (see Figure 8.3e). A neck then appears (see Figure 8.3f) before inertia takes over from the capillarity force and the drop pinches rapidly (see Figure 8.3j). Once again the topological change associated with the break up of the fluid volume cannot be handled.

Figure 8.4 shows the evolution of the computational mesh. The nodes along the free surface are distributed in such a way as to refine regions of greatest free surface curvature so that the pinch-off process can be captured with additional precision.

Subsequent simulations of single drop formation were carried out for greater dimensional flow rates and higher viscosities. At greater flow rates, drop formation leaves the dripping regime shown in Figure 8.3 and enters the jetting regime where the apex of the drop travels much further from the nozzle. As the viscosity of the liquid was increased, the drops that form were less spherical and had longer necks. These findings are consistent with experiments found in the literature (Zhang & Basaran, 1995; Ambravaneswaran *et al.*, 2004; Wilkes *et al.*, 1999).

The formation of a compound microdrop can now be considered.

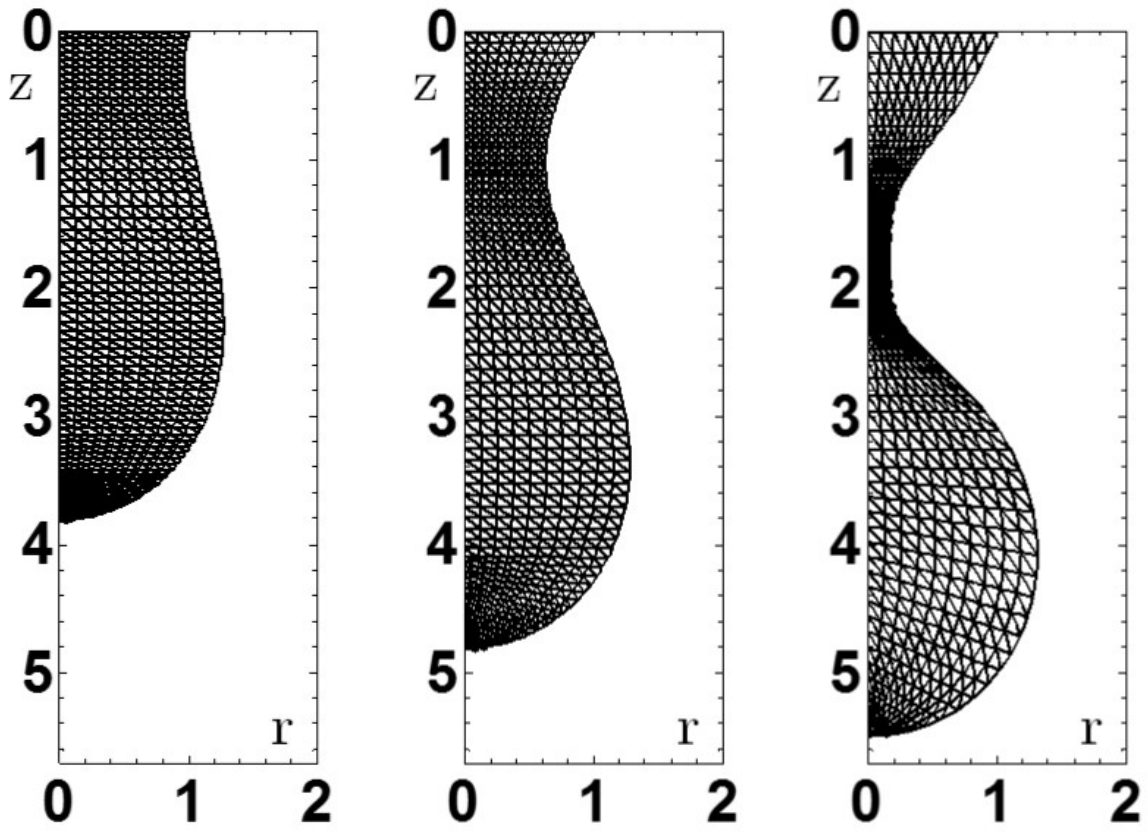

(a) $\bar{t}_e = 2.99$ s and $\bar{t} = 2.955$ s.

(b) $\bar{t}_e = 3.075$ s and $\bar{t} = 3.04$ s.

(c) $\bar{t}_e = 3.089$ s and $\bar{t} = 3.054$ s.

Figure 8.4: The evolution of the computational mesh for the formation of a single drop.

8.4 Parameter Regime of Interest

The set of dimensionless equations (8.1)–(8.13) is characterised by the nine dimensionless parameters; $\widehat{r}$, Q, $\widehat{Q}$, Re, Ca, Bo, $\widehat{\rho}$, $\widehat{\mu}$ and $\widehat{\sigma}$. By making a series of modelling assumptions it is possible to reduce the number of parameters.

The velocity scale U for the compound drop problem has not been specified. The regime of interest is where the forces of inertia and capillarity are of similar magnitude and so it is assumed that the Weber number $We = Re\,Ca$ is unity. Therefore $Ca = 1/Re$ and $Re = \sqrt{\rho_1 \sigma_1 r_1}/\mu_1$ as $U = \sqrt{\sigma_1}/\sqrt{\rho_1 r_1}$. In addition, the dimensional outer radius of

the annular nozzle r_1 will be on the scale of tens or hundreds of microns, and since this is the length scale of the problem, the Bond number will be very small. Therefore, it is assumed that $Bo = 0$. The parameter space has been reduced to seven dimensions,

$$\left(\widehat{r}, Q, \widehat{Q}, Re, \widehat{\rho}, \widehat{\mu}, \widehat{\sigma}\right). \tag{8.14}$$

Some physically relevant vales for each parameter can now be estimated in order to attempt to find a relevant base case. It is assumed that the surface areas of the outer and inner nozzles are equal and so $\widehat{r} = 1/\sqrt{2}$. By setting the outer nozzle radius $r_1 = 100$ μ m, using the material properties of water, $\rho_1 = 998$ kg m^{-3}, $\mu_1 = 1$ mPa s, and $\sigma_1 = 73$ mN m^{-1}, and assuming the liquid leaves the nozzle at around 2 m s^{-1}, then $Q = 3$ and $Re = 100$. By presuming that the outer and inner liquids had similar densities and viscosities, $\widehat{\rho} = \widehat{\mu} = 1$, then there are just two remaining dimensionless parameters, $\widehat{Q}$ and $\widehat{\sigma}$. However, it is not clear what values these should take.

8.5 Results

After many simulations and refining the parameter values, the choice of $\widehat{Q} = 1/2$ and $\widehat{\sigma} = 3/4$ produced the compound microdrop shown in Figure 8.5. The process of generating a compound drop is clearly much more complex than a single drop.

After both free surfaces start as hemispheres (see Figure 8.5a), the outer fluid begins to travel further away from the nozzle than the inner fluid due to the greater fluid flow rate through the outer nozzle (see Figure 8.5b). The shape of the liquid-gas interface downstream of the nozzle remains quite spherical as the inner fluid nearly protrudes through the outer fluid (see Figure 8.5e). The liquid-gas interface then almost pinches to the liquid-liquid interface (see Figure 8.5f) before the inner liquid comes close to protruding through the other liquid once again (see Figure 8.5g). Finally, the liquid-liquid interface

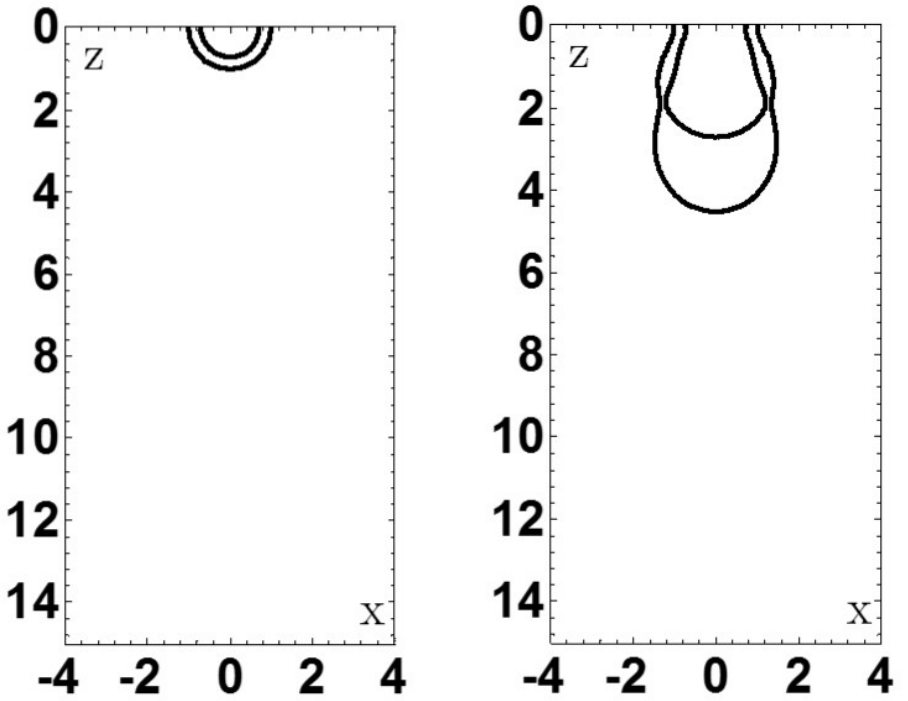

(a) $t = 0$.

(b) $t = 5$.

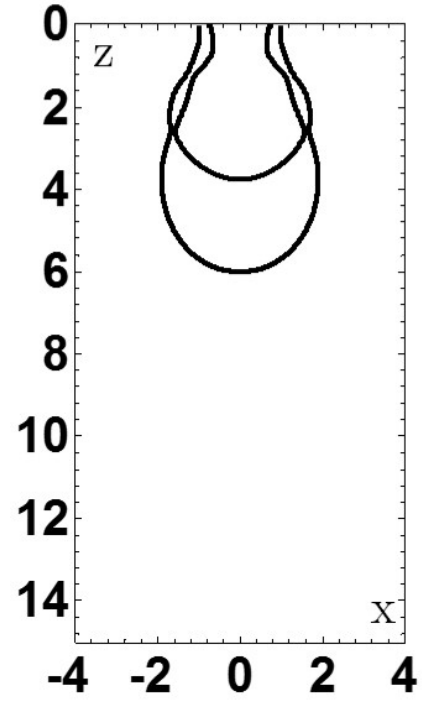

(c) $t = 10$.

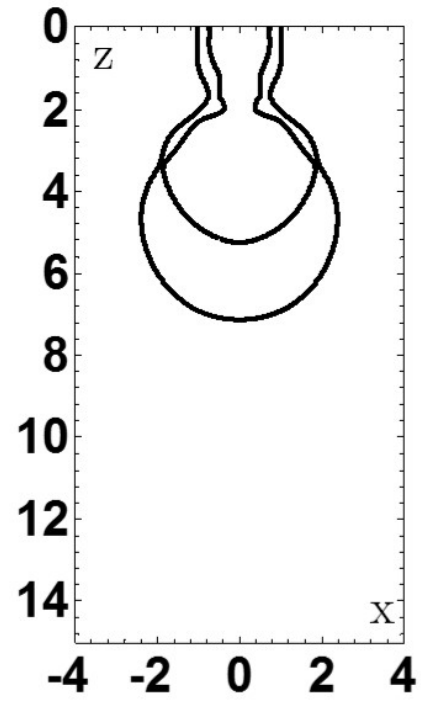

(d) $t = 15$.

Figure 8.5: continued.

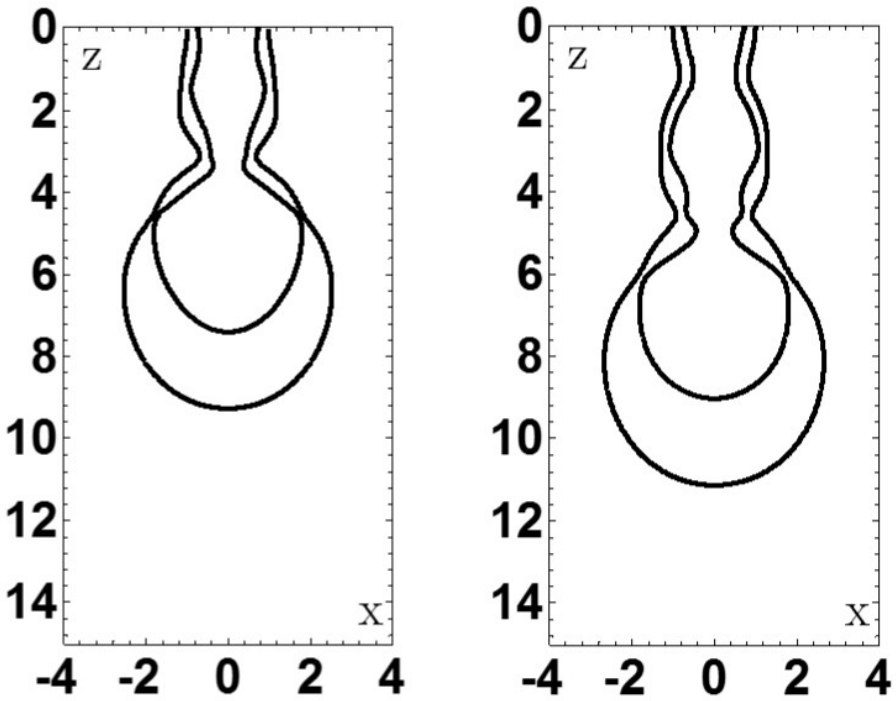

(e) $t = 20$.

(f) $t = 25$.

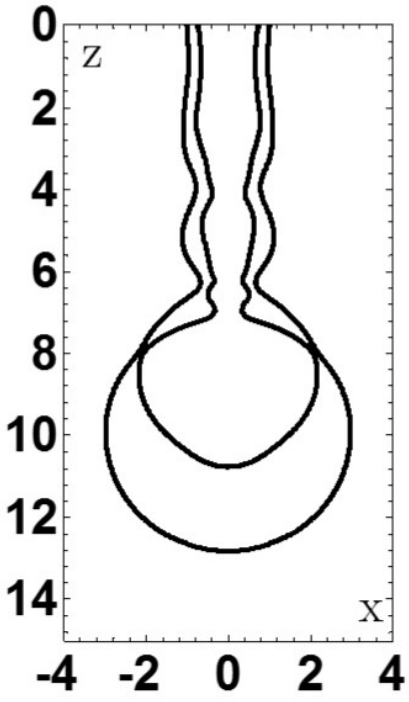

(g) $t = 30$.

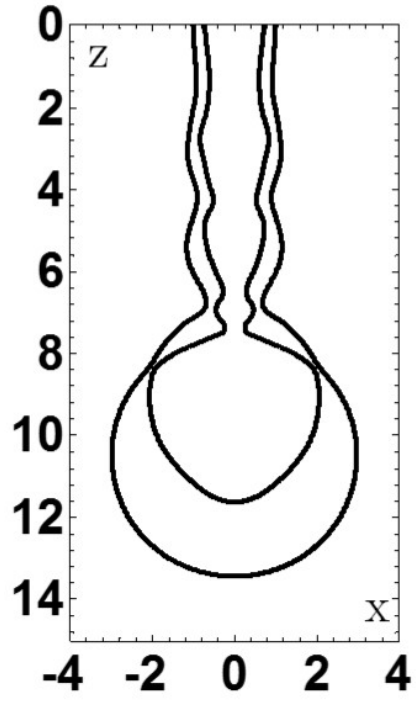

(h) $t = 31$.

Figure 8.5: continued.

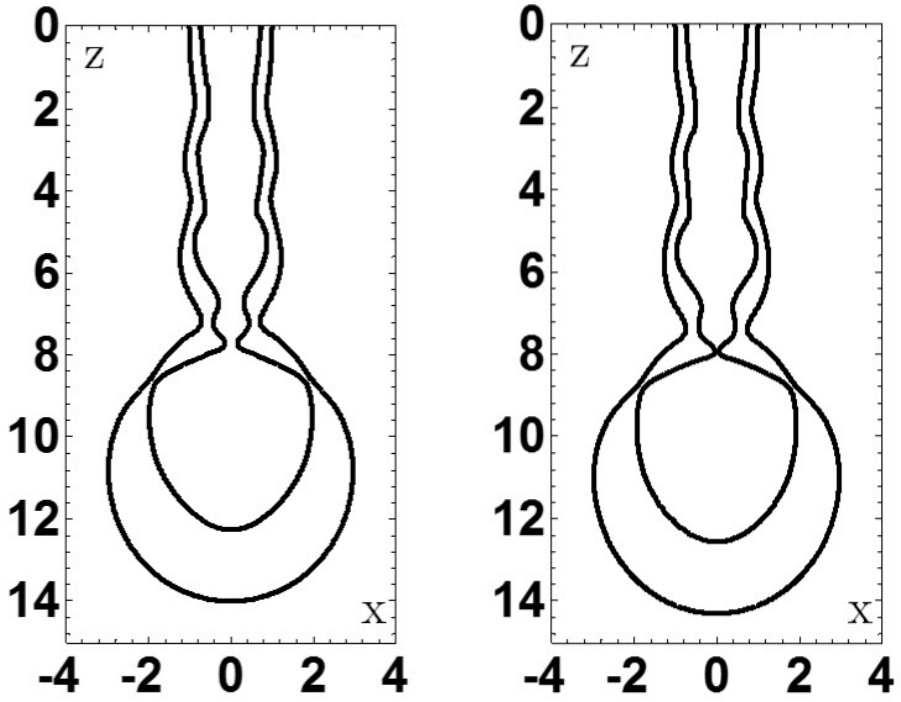

(i) $t = 32$. (j) $t = 32.6$.

Figure 8.5: The formation of a compound drop for the base case $\left(\widehat{r}, Q, \widehat{Q}, Re, \widehat{\rho}, \widehat{\mu}, \widehat{\sigma}\right) = \left(\frac{1}{\sqrt{2}}, 3, \frac{1}{2}, 100, 1, 1, \frac{3}{4}\right)$.

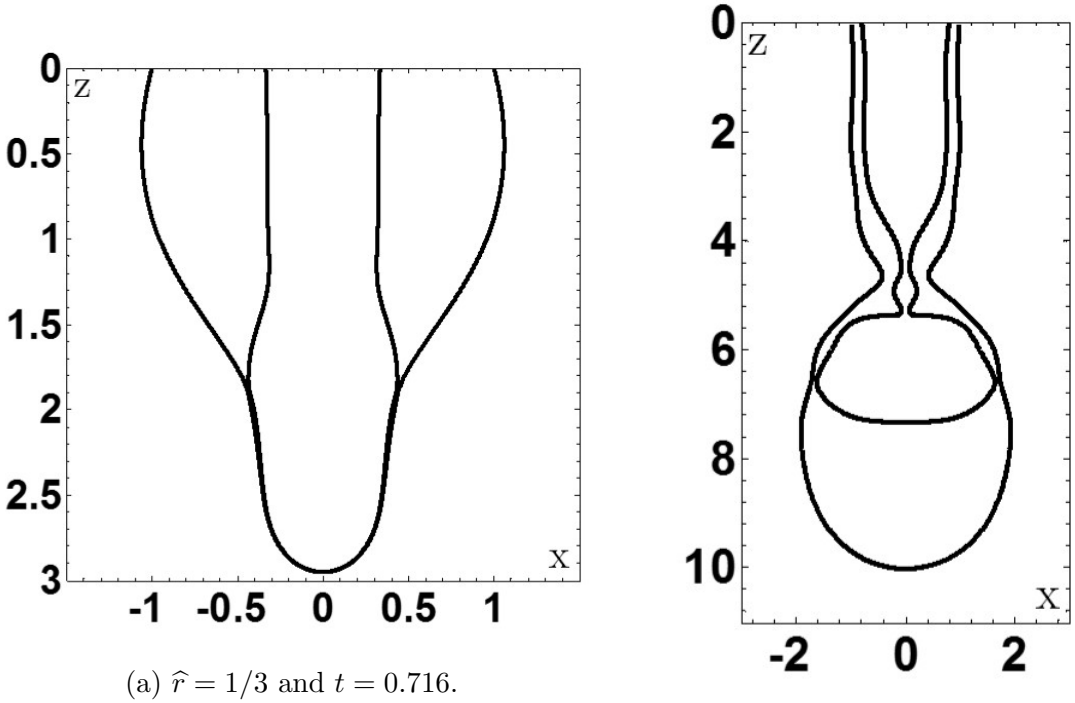

(a) $\widehat{r} = 1/3$ and $t = 0.716$.

(b) $\widehat{r} = 4/5$ and $t = 11.86$.

Figure 8.6: The influence of $\widehat{r}$ where $\widehat{r} = 1/\sqrt{2}$ in the base case.

pinches thus forming a core droplet downstream, whilst the liquid-gas interface looks like it is about to pinch into the liquid-liquid interface upstream of this (see Figure 8.5j).

Once again, the formation of a fluid volume could only be simulated up to the point in time at which a topological change is approached. However, the potential for the generation of a compound microdrop using a co-axial jetting technique has been demonstrated. The parameters $\left(\widehat{r}, Q, \widehat{Q}, Re, \widehat{\rho}, \widehat{\mu}, \widehat{\sigma}\right) = \left(\frac{1}{\sqrt{2}}, 3, \frac{1}{2}, 100, 1, 1, \frac{3}{4}\right)$ will now be referred to as the 'base case' as the influence of each parameter on the generation process can now be investigated separately.

Figure 8.6a shows that by decreasing $\widehat{r}$ from $1/\sqrt{2}$ to $1/3$, the inner liquid phase protrudes through the outer liquid phase and liquid-liquid interface catches up to the liquid-gas interface. The outer liquid would fail to encapsulate the inner liquid. By

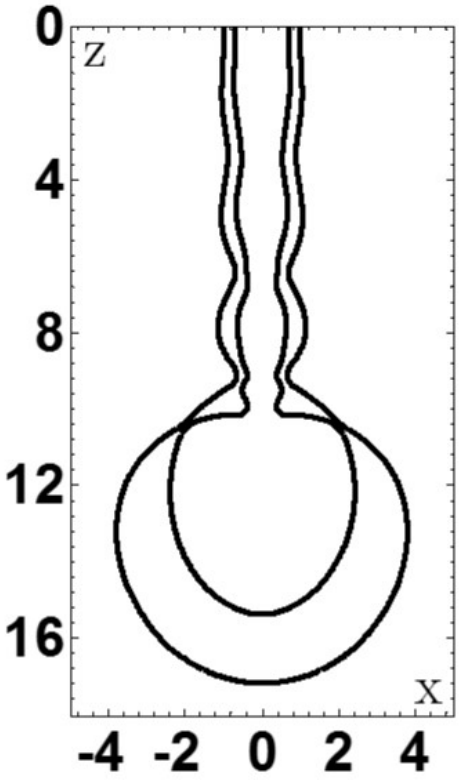

(a) $Q = 2.75$ and $t = 62.3$.

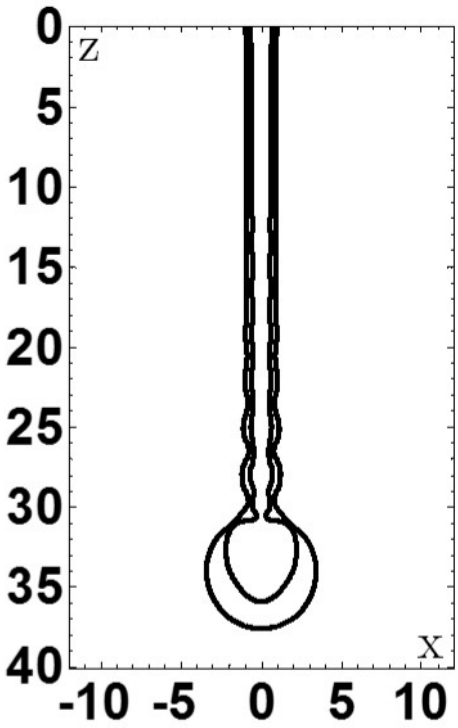

(b) $Q = 3.25$ and $t = 55$.

Figure 8.7: The influence of Q where $Q = 3$ in the base case.

decreasing $\widehat{r}$, the flux through the inner nozzle increases and this causes the inner liquid to travel with a greater velocity. On the other hand, by increasing $\widehat{r}$ from $1/\sqrt{2}$ to $4/5$, Figure 8.6b shows that once again a compound drop is formed by the liquid-liquid interface pinching off. However due to the reduced flux through the inner nozzle, the inner liquid has travelled a shorter distance from the nozzle than was observed in the base case and so the compound drop was formed in a shorter time.

By decreasing the outer flow rate Q from 3 to 2.75, Figure 8.7a shows that the liquid-liquid interface meets the liquid-gas interface just before the liquid-liquid interface pinches itself. Due to the decrease in Q, the time taken to reach this pinching has nearly doubled from the base case. Figure 8.7b shows that by increasing Q from 3 to 3.25 the compound

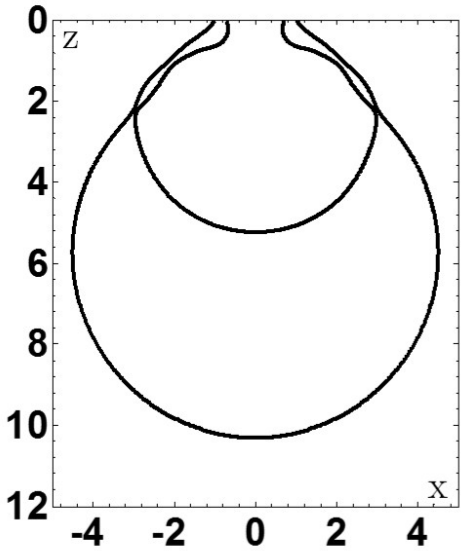

(a) $\widehat{Q} = 1/4$ and $t = 110$.

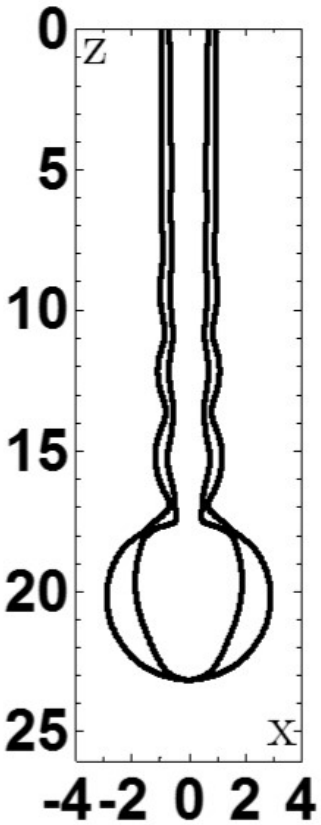

(b) $\widehat{Q} = 3/4$ and $t = 30.2$.

Figure 8.8: The influence of $\widehat{Q}$ where $\widehat{Q} = 1/2$ in the base case.

jet travels much further downstream than the base case before the liquid-gas interface pinches into the liquid-liquid interface. The longer jet caused by only a slight increase in Q results in a greater formation time.

Figure 8.8a shows that by decreasing $\widehat{Q}$ from 1/2 to 1/4, the inner liquid stays close to the nozzle whilst the volume of the outer liquid increases at a greater rate. Due to the much greater size of the outer liquid phase relative to the inner liquid phase, the numerical platform was unable to continue the simulation past this point due to issues with the mesh design. By increasing $\widehat{Q}$ from 1/2 to 3/4, the compound jet travels further downstream from the nozzle due to the increase in flux through the inner nozzle. The

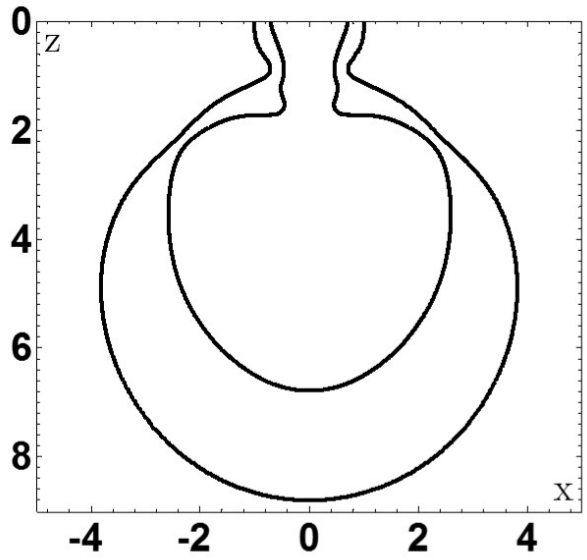

Figure 8.9: The influence of decreasing Re to 50 from 100 in the base case. Also $t = 52.9$.

liquid-liquid interface then looks to protrude through the liquid-gas interface.

Figure 8.9 shows that by decreasing the Reynolds number Re from 100 to 50, the liquid-liquid interface comes close to being horizontal. This suggests that the inner liquid phase may overturn. However, since the spines run horizontally in this region of the flow domain, the simulation can not continue any further.

Figure 8.10a shows that decreasing $\widehat{\rho}$ from 1 to 3/4 leads to the inner liquid phase growing spherically from the inner nozzle as the capillarity of the liquid-liquid interface becomes dominant over the inertia of the inner liquid. The simulation ends as the liquid-gas interface meets the liquid-liquid interface close to the nozzle. By increasing $\widehat{\rho}$ from 1 to 5/4, Figure 8.10b shows that the increased inertia in the inner liquid allows the drop to travel further away from the nozzle. The liquid-gas interface pinches into the liquid-liquid interface.

By decreasing $\widehat{\mu}$ from 1 to 1/2, Figure 8.11a shows that the compound jet travels further downstream from the nozzle before the liquid-gas interface pinches into the liquid-

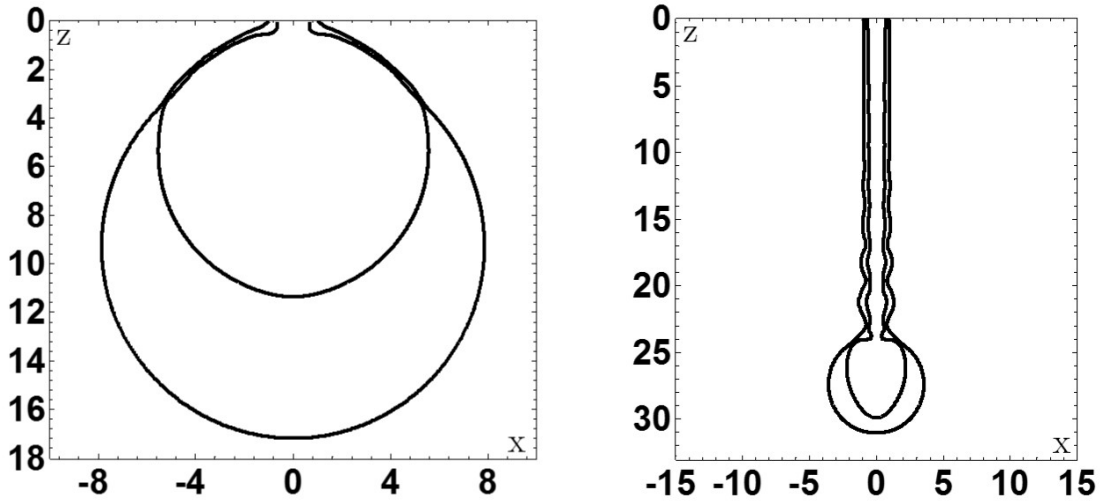

(a) $\widehat{\rho} = 3/4$ and $t = 470$.

(b) $\widehat{\rho} = 5/4$ and $t = 60.8$.

Figure 8.10: The influence of $\widehat{\rho}$ where $\widehat{\rho} = 1$ in the base case.

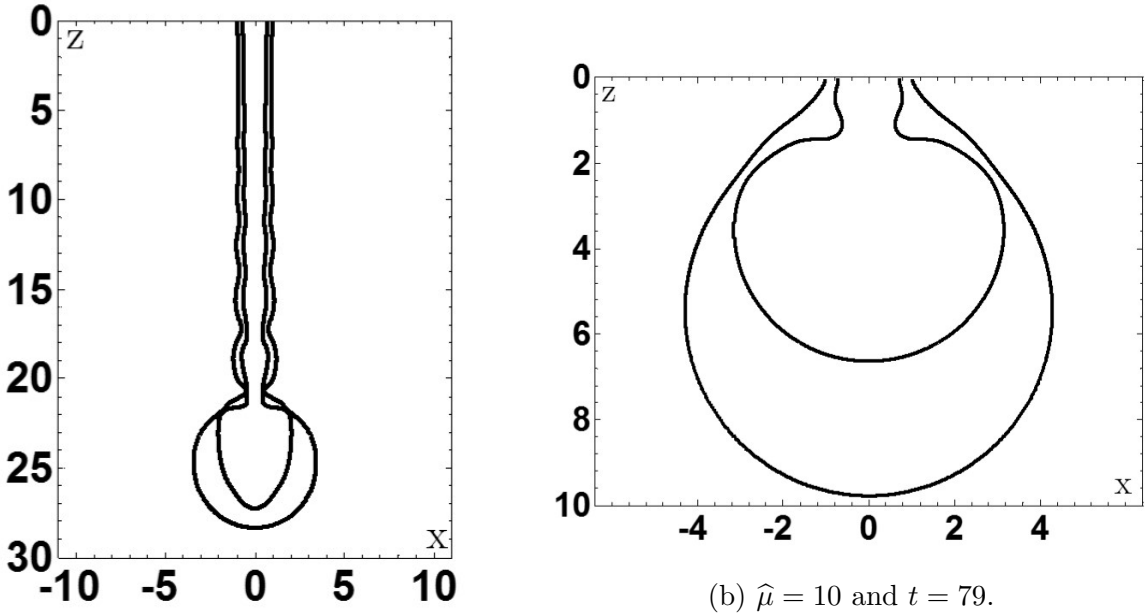

(a) $\widehat{\mu} = 1/2$ and $t = 54.9$.

(b) $\widehat{\mu} = 10$ and $t = 79$.

Figure 8.11: The influence of $\widehat{\mu}$ where $\widehat{\mu} = 1$ in the base case.

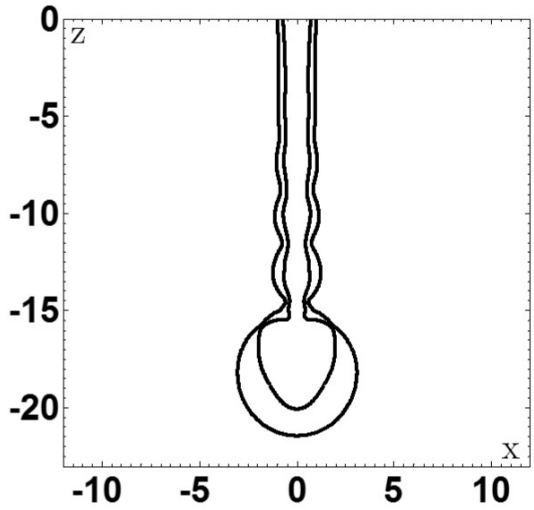

(a) $\widehat{\sigma} = 1/2$ and $t = 39.1$.

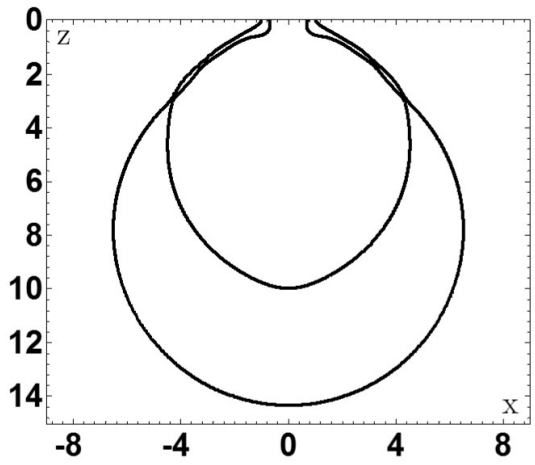

(b) $\widehat{\sigma} = 4/5$ and $t = 447$.

Figure 8.12: The influence of $\widehat{\sigma}$ where $\widehat{\sigma} = 3/4$ in the base case.

liquid interface. Figure 8.11b shows that increasing $\widehat{\mu}$ from 1 to 10 causes the liquid-liquid interface to once again become horizontal and so the simulation ends.

Finally, decreasing $\widehat{\sigma}$ from 3/4 to 1/2 allows the inertia of the inner liquid to dominate the capillarity of the liquid-liquid interface and so the compound jet travels further from the nozzle before the liquid-gas interface pinches into the liquid-liquid interface (see Figure 8.12a). In contrast, Figure 8.12b shows that by increasing $\widehat{\sigma}$ from 3/4 to 4/5 causes the inner liquid phase to grow spherically before the liquid-gas interface meets the liquid-liquid interface close to the nozzle.

These results show just how sensitive the process is to slight changes in the parameter values and reinforces the merits of a computational approach over that of experiments. Further computational modelling is required in order to identify the regimes where the compound drops can be reliably produced to a given specification, for example, the core droplet and carrier fluid each being of a required volume.

8.6 Summary

In this chapter, the formation of single and compound drops was considered. The numerical platform was tested against experiments of single drop formation before the generation of a compound microdroplet by the technique known as coaxial jetting was shown to be feasible. The sensitivity of the process to changes in the dimensionless parameters was then investigated.

Chapter 9

Conclusions and Further Work

The research presented in this thesis was motivated by the necessity to understand the dynamics of the formation of gas bubbles and liquid drops, processes that are found in a wide range of industries, and to accurately predict the evolution of such fluid flows. Since the time and length scales inherent in the generation of these single phase and compound fluid volumes are small, a theoretical approach has certain advantages over an experimental one. Due to the complexity of the mathematical model presented in Chapter 3, a numerical platform based on the finite element method was developed to undertake this task.

The first problem considered was the formation of a gas bubble from an orifice in a submerged solid surface where the three phase solid-liquid-gas contact line remains pinned to the rim of the orifice for all time due to the high wettability of the solid surface. As shown, the code accurately reproduced results from experiments and a full investigation of the influence of the dimensionless parameters, that characterise this process, on the bubble volume and formation time was presented. These results were then used to evaluate various scaling laws found in the literature. The key findings were as follows:

- The existence of the two regimes of bubble formation, the low gas flow rate (or static)

and high gas flow rate (or dynamic) regimes, was confirmed. In the static regime, the flow rate and Ohnesorge number has no effect on the volume of bubbles formed and the initial growth of bubbles in this regime can be modelled as a quasi-static process using the Young-Laplace equation. In the dynamic regime, the eventual bubble volume is proportional to the flow rate and inversely proportional to the Ohnesorge number and the formation time approaches a constant.

- The scaling laws proposed in the published literature fail to accurately predict the volume of bubbles produced for the range of flow rates considered here.

- At sufficiently high flow rates and Ohnesorge number, the liquid phase can enter the mouth of the orifice in the final stages of the pinch-off process.

- The longitudinal curvature of the neck of the bubble, in the final stages of pinch-off, increases with decreasing Ohnesorge number.

The influence of the wettability of the solid surface on the bubble formation process was then investigated as the contact line was free to move along the surface. The 'constant contact angle regime' was first considered whereby the contact line was dynamic but the contact angle remained static. The key findings were as follows,

- For crude measurements of bubble volume V_d and formation time t_d, resolving the slip length is not a major issue. However, if the local dynamics associated with the moving contact line are of interest then it is imperative that this small length scale is resolved in order to obtain solutions independent of the computational mesh.

- By decreasing the wettability of the substrate, the contact line recedes further and the bubble formed is larger.

- In the case of an infinitesimally small orifice, if the wettability of the substrate is sufficiently large, the bubble will pinch-off at its base, leaving no residual bubble on

the substrate, whilst for smaller wettabilities the bubble pinches off at the neck.

- For a given static contact angle, the two regimes of bubble formation identified in the case of a pinned contact line also exist.
- With contact angle hysteresis, the larger the static advancing contact angle, the longer the contact line remains pinned having receded and therefore the larger the volume of the bubble formed.
- Increasing the Ohnesorge number leads to a decrease in formation time and also increases radius of the contact line at pinch-off.
- Simulations of a moving contact line with a static contact angle were unable to reproduce the contact line motion observed in experiments.

By introducing a dynamic contact angle with the dynamic contact line,

- Experiments could be better described then using contact angle models seen elsewhere.
- The maximum contact line radius could be controlled.

This shows that the dynamics of the contact angle must be taken into account when modelling such fluid flows as it is unreliable to assume that the contact angle attains the value of the static angle for all time.

The numerical platform was then used to investigate the formation of single and compound droplets. Since the formation of single drops has been well studied, the work concentrated on the formation of compound drops on the length scales associated with ink-jet printing. This complex phenomenon, with the introduction of a second liquid phase and a second free surface, was handled in a consistent manner by the code. The findings of this work were:

- It is possible to generate a compound drop using the technique of co-axial jetting on the scales associated with ink-jet printing without the use of flow focusing.
- The formation of a compound drop was extremely sensitive to small changes in the values of the dimensionless parameters. This could cause the inner jet to protrude through the outer jet or the outer jet could fail to encapsulate the inner jet. This emphasises the importance of the role of computational models in guiding experimental research.

In the case of bubble formation, the numerical platform could be extended to incorporate a viscous gas or to generate a bubble with a constant gas pressure rather than a constant volumetric flow rate. The latter of these could be used to simulate the evolution of a vapour bubble on a wall where the evaporation is such that the vapour pressure remains constant. The formation of a bubble in micro-gravity, with elevated system pressure or with a co-flowing liquid phase could also be considered.

In the case a moving contact line, the formation of a thin liquid film deposited on the solid surface behind a receding contact line could be introduced. This residual film will affect the dynamics of the receding contact line and also the advancing contact line as the contact line re-wets the solid surface.

Further extensions of the numerical platform could involve the introduction of heat transfer and its interplay with the contact line dynamics.

In the case of drop formation, extensions to the numerical platform could involve the introduction of a non-uniform flow rate, such as a flow rate generated by time dependent pressure pulses. Surfactants could also be added to the model. One problem with the code is that it could not simulate the overturning of the liquid drop, where the free surface approaches the horizontal, as the spines in the computational mesh become tangential to the free surface. An unstructured meshing technique could resolve this problem.

Perhaps the major drawback of the numerical platform was the inability to simulate

the topological change associated with the break-up of a fluid body. The effect of a preceding bubble in a chain on the next bubble could be investigated as could the cases of compound drop formation which 'failed', such as the inner fluid protruding through the outer fluid or when the outer fluid fails to encapsulate the inner fluid. Currently, this problem is outstanding and requires further research.

The research into the formation of a bubble with a pinned contact line is summarised in Simmons *et al.* (2015) whilst the work on bubble formation with a moving contact line is contained in a forthcoming publication.

Appendix A

Rescaling the Results

In order to convert the results into the dimensionless system used in some works on bubble dynamics, recall that $\overline{r}_o = Lr_o$ and $\overline{Q} = L^2UQ$ are the respective dimensional orifice radius and volumetric gas flow rate. In some works $\overline{r}_o$ and $\overline{Q}/\overline{r}_o^2$ are used as the length and velocity scales rather than those used here of $L = \sqrt{\sigma/\rho g}$ and $U = \sigma/\mu$, respectively.

Rescaling in this manner leads to a different group of dimensionless parameters, which will be denoted with hats. Rather than (r_o, Oh, Q), there is $\left(\widehat{Bo}, \widehat{Oh}, \widehat{We}\right)$ or $\left(\widehat{Bo}, \widehat{Oh}, \widehat{Ca}\right)$, where $\widehat{Bo} = \rho g\overline{r}_o^2/\sigma$, $\widehat{Oh} = \mu/\sqrt{\rho\overline{r}_o\sigma}$, $\widehat{We} = \rho\overline{Q}^2/\sigma\overline{r}_o^3$ and $\widehat{Ca} = \mu\overline{Q}/\overline{r}_o^2\sigma$, are the rescaled Bond, Ohnesorge, Weber and capillary numbers. The rescaled dimensionless formation time and volume are denoted by $\widehat{t_d}$ and $\widehat{V_d}$. Then, to convert the parameters used here into the rescaled parameters, we have,

$$
\begin{aligned}
\widehat{Bo} &= r_o^2, \\
\widehat{Oh} &= Oh/\sqrt{r_o}, \\
\widehat{We} &= Q^2/Oh^2 r_o^3, \\
\widehat{Ca} &= Q/r_o^2, \\
\widehat{t_d} &= Q t_d/r_o^3, \\
\widehat{V_d} &= V_d/r_o^3,
\end{aligned}
$$

and the inverse is,

$$
\begin{aligned}
r_o &= \sqrt{\widehat{Bo}}, \\
Oh &= \widehat{Oh}\ \widehat{Bo}^{\frac{1}{4}}, \\
Q &= \widehat{Bo}\ \widehat{Oh}\sqrt{\widehat{We}} = \widehat{Bo}\widehat{Ca}, \\
t_d &= \sqrt{\widehat{Bo}}\ \widehat{t_d}/\widehat{Oh}\sqrt{\widehat{We}} = \sqrt{\widehat{Bo}}\ \widehat{t_d}/\widehat{Ca}, \\
V_d &= \widehat{Bo}^{\frac{3}{2}}\widehat{V_d}.
\end{aligned}
$$

Appendix B

A Simple Bipolar Coordinate System

The design of the spines in the pinch-off region of the computational mesh incorporated in the numerical platform requires the use of a bipolar coordinate system (χ, ζ). Consider the simplest bipolar coordinate system in the (x, y)-plane with foci at $(-x_f, 0)$ and $(x_f, 0)$. The corresponding bipolar coordinates for a point in the (x, y)-plane are given by

$$\chi = \operatorname{arctanh}\left(\frac{2xx_f}{x_f^2 + x^2 + y^2}\right), \tag{B.1a}$$

$$\zeta = \arctan\left(\frac{2yx_f}{x_f^2 - x^2 - y^2}\right), \tag{B.1b}$$

where $0 < \chi < \infty$ if $x > 0$, $-\infty < \chi < 0$ if $x < 0$ and $0 \leqslant \zeta < 2\pi$. The inverse of this transformation is given by

$$x = x_f \frac{\sinh\chi}{\cosh\chi + \cos\zeta}, \tag{B.2a}$$

$$y = x_f \frac{\sin\zeta}{\cosh\chi + \cos\zeta}. \tag{B.2b}$$

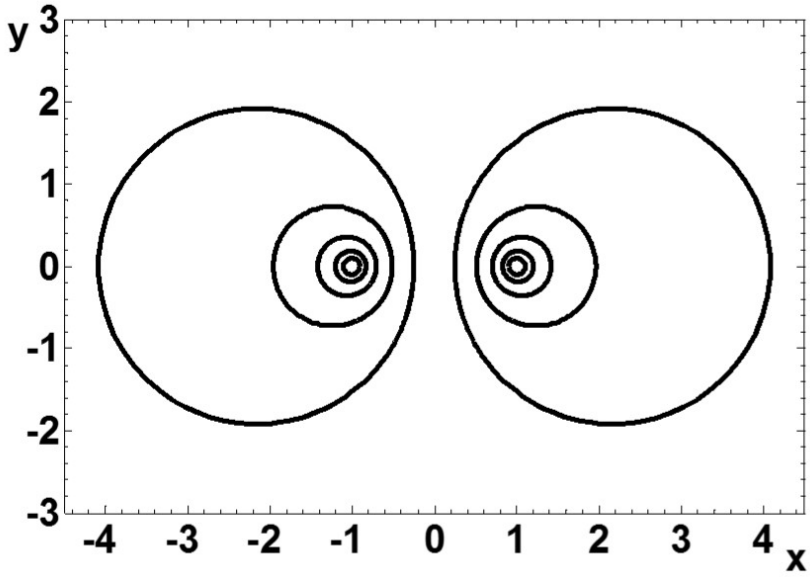

Figure B.1: Circles produced in a Cartesian coordinate system (x, y) from various values of χ where $x_f = 1$.

Figure B.1 shows how each value of χ describes a circle in the (x, y)-plane given by

$$\left(x - \frac{x_f}{\tanh\chi}\right)^2 + y^2 = \left(\frac{x_f}{\sinh\chi}\right)^2. \tag{B.3}$$

In the (r, z)-plane on which the computational mesh is constructed, in order to match the bipolar spines in the pinch-off region of the mesh with the straight spines in the detachment region, the bipolar spines should straighten as $z = \chi_S$ is approached. The circles in Figure B.1 are transformed to those shown in Figure B.2 using the transformation,

$$r = \frac{\chi_S y}{x_f} + r_c, \tag{B.4a}$$

$$z = \frac{\chi_S x}{x_f} + \chi_S. \tag{B.4b}$$

When $\chi < 0$, the focus is at the contact line $(r_c, 0)$ and the spines straighten as $z = \chi_S$

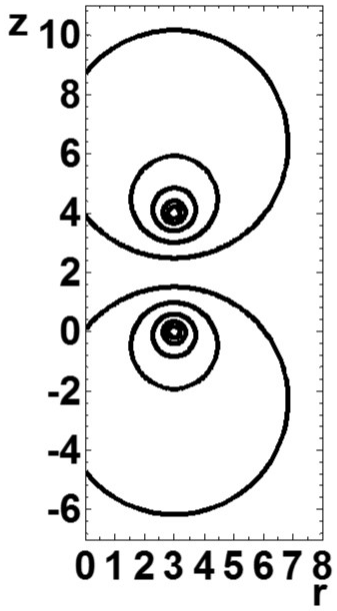

Figure B.2: Circles produced in the (r, z)-plane from various values of χ where $r_c = 3$ and $\chi_S = 2$.

is approached. The circles in Figure B.2 are therefore given by,

$$(r - r_c)^2 + \left(z - \chi_S - \frac{\chi_S}{\tanh\chi}\right)^2 = \left(\frac{\chi_S}{\sinh\chi}\right)^2, \tag{B.5}$$

where

$$\chi = \operatorname{arctanh}\left(\frac{2(z-\chi_S)\chi_S}{\chi_S^2 + (z-\chi_S)^2 + (r-r_c)^2}\right), \tag{B.6a}$$

$$\zeta = \arctan\left(\frac{2(r-r_c)\chi_S}{\chi_S^2 - (z-\chi_S)^2 - (r-r_c)^2}\right), \tag{B.6b}$$

and

$$r = r_c + \frac{\chi_S \sin\zeta}{\cosh\chi + \cos\zeta}, \tag{B.7a}$$

$$z = \chi_S + \frac{\chi_S \sinh\chi}{\cosh\chi + \cos\zeta}. \tag{B.7b}$$

Appendix C

Evaluated Element Matrices in Master Element

In this section the coefficients of the system of algebraic equations identified in Section 4.10 are mapped to the master element in the (ξ, η)-plane. The coefficients that involve volume integrals, the mass matrix (4.71) and the matrices for the body force (4.72), inertial terms (4.73), viscous terms (4.74) and continuity terms (4.69), are rewritten as

$$M_{ij} = \int_{\xi=-1}^{\xi=1} \int_{\eta=-1}^{\eta=-\xi} \phi_i \phi_j r^e \det J_e d\eta d\xi, \tag{C.1}$$

$$G_i = \int_{\xi=-1}^{\xi=1} \int_{\eta=-1}^{\eta=-\xi} \phi_i r^e \det J_e d\eta d\xi, \tag{C.2}$$

$$a^{(1)}_{ijk} = \int_{\xi=-1}^{\xi=1} \int_{\eta=-1}^{\eta=-\xi} \phi_i T^{(1)}_j \phi_k r^e d\eta d\xi, \tag{C.3}$$

$$a^{(2)}_{ijk} = -\int_{\xi=-1}^{\xi=1} \int_{\eta=-1}^{\eta=-\xi} \phi_i T^{(2)}_j \phi_k r^e d\eta d\xi, \tag{C.4}$$

$$V_{ij}^{(11)} = \int_{\xi=-1}^{\xi=1} \int_{\eta=-1}^{\eta=-\xi} \left[\frac{r^e}{\det J_e} \left(2T_i^{(1)} T_j^{(1)} + T_i^{(2)} T_j^{(2)} \right) + 2\phi_i \phi_j \frac{\det J_e}{r^e} \right] d\eta d\xi, \tag{C.5}$$

$$V_{ij}^{(12)} = - \int_{\xi=-1}^{\xi=1} \int_{\eta=-1}^{\eta=-\xi} T_i^{(2)} T_j^{(1)} \frac{r^e}{\det J_e} d\eta d\xi, \tag{C.6}$$

$$V_{ij}^{(22)} = \int_{\xi=-1}^{\xi=1} \int_{\eta=-1}^{\eta=-\xi} \left(T_i^{(1)} T_j^{(1)} + 2T_i^{(2)} T_j^{(2)} \right) \frac{r^e}{\det J_e} d\eta d\xi, \tag{C.7}$$

$$C_{ij}^{(1)} = \int_{\xi=-1}^{\xi=1} \int_{\eta=-1}^{\eta=-\xi} \psi_i \left(T_j^{(1)} r^e + \phi_j \det J_e \right) d\eta d\xi, \tag{C.8}$$

$$C_{ij}^{(2)} = - \int_{\xi=-1}^{\xi=1} \int_{\eta=-1}^{\eta=-\xi} \psi_i T_j^{(2)} r^e d\eta d\xi, \tag{C.9}$$

respectively. The coefficients that involve integration over the free surface, the matrices for the free surface stress terms (4.64) and the kinematic terms (4.76), are given by

$$F_i^{(11)} = \int_{\eta=-1}^{\eta=1} \left(\frac{r_1^e \frac{d\phi_{1,i}}{d\eta} \frac{dr_1^e}{d\eta}}{\sqrt{\left(\frac{dr_1^e}{d\eta} \right)^2 + \left(\frac{dz_1^e}{d\eta} \right)^2}} + \phi_{1,i} \sqrt{\left(\frac{dr_1^e}{d\eta} \right)^2 + \left(\frac{dz_1^e}{d\eta} \right)^2} \right) d\eta, \tag{C.10}$$

$$F_i^{(21)} = \int_{\eta=-1}^{\eta=1} \frac{r_1^e \frac{d\phi_{1,I}}{d\eta} \frac{dz_1^e}{d\eta}}{\sqrt{\left(\frac{dr_1^e}{d\eta} \right)^2 + \left(\frac{dz_1^e}{d\eta} \right)^2}} d\eta, \tag{C.11}$$

$$F_i^{(12)} = - \int_{\eta=-1}^{\eta=1} \phi_{1,i} \frac{dz_1^e}{d\eta} r_1^e \, d\eta, \tag{C.12}$$

$$F_i^{(22)} = \int_{\eta=-1}^{\eta=1} \phi_{1,i} \frac{dr_1^e}{d\eta} r_1^e d\eta, \tag{C.13}$$

$$K_{ij}^{(1)} = \int_{\eta=-1}^{\eta=1} \phi_{1,i}\phi_{1,j}\frac{dz_1^e}{d\eta}r_1^e d\eta, \tag{C.14}$$

$$K_{ij}^{(2)} = -\int_{\eta=-1}^{\eta=1} \phi_{1,i}\phi_{1,j}\frac{dr_1^e}{d\eta}r_1^e d\eta, \tag{C.15}$$

respectively. Finally the coefficients that involve integration over the side boundary, the side boundary matrices (4.78), are given by

$$B_{ij}^{(11)} = \int_{\eta=-1}^{\eta=1} \phi_{1,i}\phi_{1,j}Rz_1^e\left|\frac{dz_1^e}{d\eta}\right| d\eta, \tag{C.16}$$

$$B_{ij}^{(12)} = -\int_{\eta=-1}^{\eta=1} \phi_{1,i}\phi_{1,j}R^2\left|\frac{dz_1^e}{d\eta}\right| d\eta, \tag{C.17}$$

$$B_{ij}^{(111)} = \int_{\eta=-1}^{\eta=1} \phi_{1,i}R^2\left(z_1^e\frac{d\phi_{1,i}}{d\eta} - 2\phi_{1,j}\left|\frac{dz_1^e}{d\eta}\right|\right) d\eta, \tag{C.18}$$

$$B_{ij}^{(112)} = \int_{\eta=-1}^{\eta=1} \phi_{1,i}Rz_1^e\left(z_1^e\frac{d\phi_{1,j}}{d\eta} - 2\phi_{1,j}\left|\frac{dz_1^e}{d\eta}\right|\right) d\eta, \tag{C.19}$$

$$B_{ij}^{(121)} = -\int_{\eta=-1}^{\eta=1} \phi_{1,i}T_j^{(1)}\frac{R^3}{\det J_e}\left|\frac{dz_1^e}{d\eta}\right| d\eta, \tag{C.20}$$

$$B_{ij}^{(122)} = -\int_{\eta=-1}^{\eta=1} \phi_{1,i}T_j^{(1)}\frac{R^2z_1^e}{\det J_e}\left|\frac{dz_1^e}{d\eta}\right| d\eta, \tag{C.21}$$

whilst the coefficients that involve integration over the top boundary, the top boundary matrices (4.80), are given by

$$B_{ij}^{(21)} = -\int_{\eta=-1}^{\eta=1} \phi_{1,i}\phi_{1,j} r_1^e Z \left|\frac{dr_1^e}{d\eta}\right| d\eta, \tag{C.22}$$

$$B_{ij}^{(22)} = \int_{\eta=-1}^{\eta=1} \phi_{1,i}\phi_{1,j} \left(r_1^e\right)^2 \left|\frac{dr_1^e}{d\eta}\right| d\eta, \tag{C.23}$$

$$B_{ij}^{(211)} = \int_{\eta=-1}^{\eta=1} \phi_{1,i} \left(r_1^e\right)^2 \left(2\phi_{1,j} \left|\frac{dr_1^e}{d\eta}\right| + r_1^e \frac{d\phi_{1,j}}{d\eta}\right) d\eta, \tag{C.24}$$

$$B_{ij}^{(212)} = \int_{\eta=-1}^{\eta=1} \phi_{1,i} r_1^e Z \left(2\phi_{1,j} \left|\frac{dr_1^e}{d\eta}\right| + r_1^e \frac{d\phi_{1,j}}{d\eta}\right) d\eta, \tag{C.25}$$

$$B_{ij}^{(221)} = -\int_{\eta=-1}^{\eta=1} \phi_{1,i} T_j^{(2)} \frac{\left(r_1^e\right)^2 Z}{\det J_e} \left|\frac{dr_1^e}{d\eta}\right| d\eta, \tag{C.26}$$

$$B_{ij}^{(222)} = -\int_{\eta=-1}^{\eta=1} \phi_{1,i} T_j^{(2)} \frac{Z^2 r_1^e}{\det J_e} \left|\frac{dr_1^e}{d\eta}\right| d\eta. \tag{C.27}$$

Appendix D

Scaling Law for Bubble Volumes in High Gas Flow Rate Regime

The scaling law for bubble volume is assumed to take the form,

$$V_d = \frac{Q^{6/5+c\ f(Oh)}}{f(Oh)}, \quad f(Oh) = \frac{a\ Oh^{6/5}}{b\ Oh^{6/5}+1}. \tag{D.1}$$

Then, applying $V_d \to V_0$ as $Oh \to 0$, and $V_d \to V_\infty$ as $Oh \to \infty$, gives,

$$a = 1/A_1, \quad b = A_2/A_1, \quad c = -9\ A_2/20,$$

where V_0 and A_1 are given by (6.4) and V_∞ and A_2 are given by (6.5).

For each Ohnesorge number investigated in this work, Figure D.1 shows that as the flow rate Q increases, the results from the simulations tend towards those predicted by the scaling law (D.1) as $Q \to \infty$, but do not give an accurate representation for moderate Q.

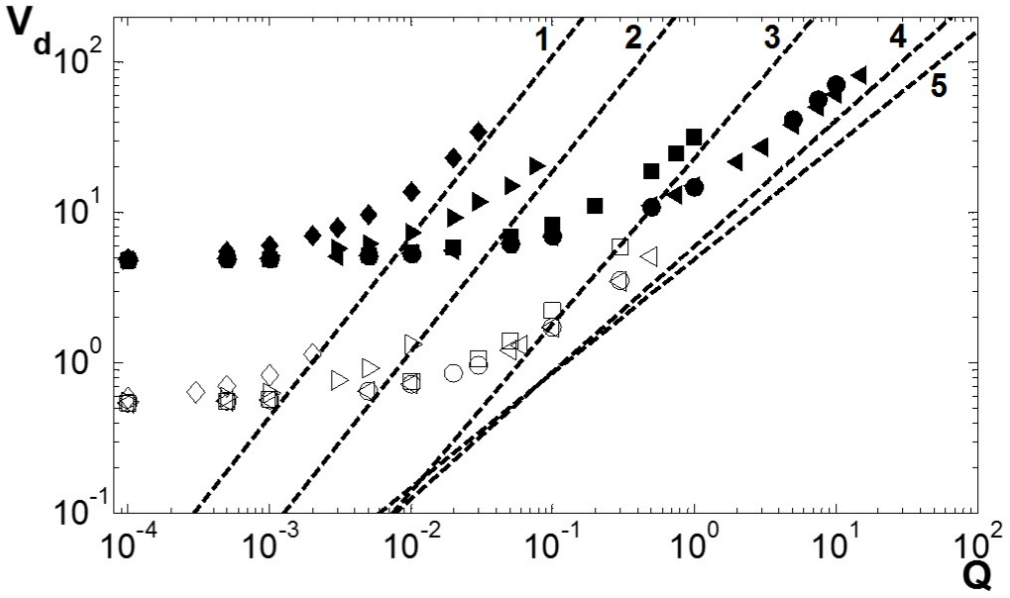

Figure D.1: Comparing the scaling law given by equation (D.1) for V_d in the high gas flow rate regime, depicted by the dashed lines, against the results presented in Figure 6.4b for $Oh = 2.24 \times 10^{-3}$ (line 1), $Oh = 10^{-2}$ (2), $Oh = 10^{-1}$, (3), $Oh = 1$, (4) and $Oh = 10$ (5).

Bibliography

Albadawi, A., Donoghue, D. B., Robinson, A. J., Murray, D. B., & Delauré, Y. M. C. 2013. On the analysis of bubble growth and detachment at low capillary and Bond numbers using volume of fluid and level set methods. *Chemical Engineering Science*, **90**, 77–91.

Ambravaneswaran, B., Subramani, H. J., Phillips, S. D., & Basaran, O. A. 2004. Dripping-jetting transitions in a dripping faucet. *Physical Review Letters*, **93**(3), 034501.

Anna, S. L., Bontoux, N., & Stone, H. A. 2003. Formation of dispersions using flow focusing in microchannels. *Applied Physics Letters*, **82**(3), 364–366.

Aris, R. 2012. *Vectors, tensors and the basic equations of fluid mechanics*. Courier Corporation.

Aziz, A. K. 1972. *The mathematical foundations of the finite element method with applications to partial differential equations*. Academic Press, New York.

Badam, V. K., Buwa, V., & Durst, F. 2007. Experimental investigations of regimes of bubble formation on submerged orifices under constant flow condition. *The Canadian Journal of Chemical Engineering*, **85**, 257–267.

Basaran, O. A. 2002. Small-scale free surface flows with breakup: Drop formation and emerging applications. *AIChE Journal*, **48**(9), 1842–1848.

Blake, T. D. 2006. The physics of moving wetting lines. *Journal of Colloid and Interface Science*, **299**, 1–13.

Blake, T. D., Clarke, A., & Ruschak, K. J. 1994. Hydrodynamic assist of dynamic wetting. *AIChE Journal*, **40**, 229–242.

Blake, T. D., Bracke, M., & Shikhmurzaev, Y. D. 1999. Experimental evidence of nonlocal hydrodynamic influence on the dynamic contact angle. *Physics of Fluids*, **11**, 1995–2007.

Bolaños Jiménez, R., Sevilla, A., Martínez-Bazán, C., & Gordillo, J. M. 2008. Axisymmetric bubble collapse in a quiescent liquid pool. II. Experimental study. *Physics of Fluids*, **20**(11), 112104.

Bolaños Jiménez, R., Sevilla, A., Martínez-Bazán, C., van der Meer, D., & Gordillo, J. M. 2009. The effect of liquid viscosity on bubble pinch-off. *Physics of Fluids*, **21**(7), 072103.

Burton, J. C., Waldrep, R., & Taborek, P. 2005. Scaling and instabilities in bubble pinch-off. *Physical Review Letters*, **94**(18), 184502.

Buwa, V. V., Gerlach, D., Durst, F., & Schlücker, E. 2007. Numerical simulations of bubble formation on submerged orifices: Period-1 and period-2 bubbling regimes. *Chemical Engineering Science*, **62**, 7119–7132.

Buyevich, Y. A., & Webbon, B. W. 1996. Bubble formation at a submerged office in reduced gravity. *Chemical Engineering Science*, **51**(21), 4843–4857.

Byakova, A. V., Gnyloskurenko, S. V., Nakamura, T., & Raychenko, O. I. 2003. Influence of wetting conditions on bubble formation at orifice in an inviscid liquid - Mechanism of bubble evolution. *Colloids and Surfaces A: Physicochemical and Engineering Aspects*, **229**, 19–32.

Cairncross, R. A., Schunk, P. R., Baer, T. A., Rao, R. R., & Sackinger, P. A. 2000. A finite element method for free surface flows of incompressible fluids in three dimensions. Part I. Boundary fitted mesh motion. *International Journal for Numerical Methods in Fluids*, **33**(3), 375–403.

Calvert, P. 2001. Inkjet printing for materials and devices. *Chemistry of Materials*, **13**(10), 3299–3305.

Chakraborty, I., Ray, B., Biswas, G., Durst, F., Sharma, A., & Ghoshdastidar, P. S. 2009. Computational investigation on bubble detachment from submerged orifice in quiescent liquid under normal and reduced gravity. *Physics of Fluids*, **21**, 062103.

Chakraborty, I., Biswas, G., & Ghoshdastidar, P. S. 2011. Bubble generation in quiescent and co-flowing liquids. *International Journal of Heat and Mass Transfer*, **54**, 4673–4688.

Chauhan, A., Maldarelli, C., Papageorgiou, D. T., & Rumschitzki, D. S. 2000. Temporal instability of compound threads and jets. *Journal of Fluid Mechanics*, **420**, 1–25.

Chen, A. U., Notz, P. K., & Basaran, O. A. 2002. Computational and experimental analysis of pinch-off and scaling. *Physical Review Letters*, **88**(17), 174501.

Chen, Y., Mertz, R., & Kulenovic, R. 2009. Numerical simulation of bubble formation on orifice plates with a moving contact line. *International Journal of Multiphase Flow*, **35**(1), 66–77.

Chen, Y., Wu, L., & Zhang, C. 2013a. Emulsion droplet formation in coflowing liquid streams. *Physical Review E*, **87**(1), 013002.

Chen, Y., Liu, S., Kulenovic, R., & Mertz, R. 2013b. Experimental study on macroscopic contact line behaviors during bubble formation on submerged orifice and comparison with numerical simulations. *Physics of Fluids*, **25**(9), 092105.

Christodoulou, K. N., & Scriven, L. E. 1992. Discretization of free surface flows and other moving boundary problems. *Journal of Computational Physics*, **99**(1), 39–55.

Clift, R., Grace, J. R., & Weber, M. E. 1978. *Bubbles, drops, and particles*. Academic Press, London.

Corchero, G., Medina, A., & Higuera, F. J. 2006. Effect of wetting conditions and flow rate on bubble formation at orifices submerged in water. *Colloids and Surfaces A: Physicochemical and Engineering Aspects*, **290**, 41–49.

Cowper, G. R. 1973. Gaussian quadrature formulas for triangles. *International Journal for Numerical Methods in Engineering*, **7**(3), 405–408.

Cramer, C., Fischer, P., & Windhab, E. J. 2004. Drop formation in a co-flowing ambient fluid. *Chemical Engineering Science*, **59**(15), 3045–3058.

Craster, R. V., Matar, O. K., & Papageorgiou, D. T. 2005. On compound liquid threads with large viscosity contrasts. *Journal of Fluid Mechanics*, **533**, 95–124.

Das, A. K., Das, P. K., & Saha, P. 2011. Formation of bubbles at submerged orifices - Experimental investigation and theoretical prediction. *Experimental Thermal and Fluid Science*, **35**, 618–627.

Davidson, J. F., & Schüler, B. O. G. 1960a. Bubble formation at an orifice in a viscous liquid. *Transactions of the Institution of Chemical Engineers*, **38**, 144–154.

Davidson, J. F., & Schüler, B. O. G. 1960b. Bubble formation at an orifice in an inviscid liquid. *Transactions of the Institution of Chemical Engineers*, **38**, 335–342.

De Gennes, P.-G. 1985. Wetting: statics and dynamics. *Reviews of Modern Physics*, **57**(3), 827.

De Gennes, P.-G., Brochard-Wyart, F., & Quéré, D. 2004. *Capillarity and wetting phenomena: drops, bubbles, pearls, waves*. Springer Science & Business Media.

Di Bari, S., & Robinson, A. J. 2013. Experimental study of gas injected bubble growth from submerged orifices. *Experimental Thermal and Fluid Science*, **44**, 124–137.

Dimitrov, D., Schreve, K., & De Beer, N. 2006. Advances in three dimensional printing-state of the art and future perspectives. *Journal for New Generation Sciences*, **4**(1), 136–149.

Dong, H., Carr, W. W., & Morris, J. F. 2006. An experimental study of drop-on-demand drop formation. *Physics of Fluids*, **18**(7), 072102.

Doshi, P., Cohen, I., Zhang, W. W., Siegel, M., Howell, P., Basaran, O. A., & Nagel, S. R. 2003. Persistence of memory in drop breakup: The breakdown of universality. *Science*, **302**(5648), 1185–1188.

Dussan V, E. B. 1976. The moving contact line: The slip boundary condition. *Journal of Fluid of Mechanics*, **77**, 665–684.

Dussan V, E. B. 1979. On the spreading of liquids on solid surfaces: Static and dynamic contact lines. *Annual Review of Fluid Mechanics*, **11**, 371–400.

Eggers, J. 1997. Nonlinear dynamics and breakup of free-surface flows. *Reviews of Modern Physics*, **69**(3), 865–929.

Eggers, J., & Villermaux, E. 2008. Physics of liquid jets. *Reports on Progress in Physics*, **71**(3), 036601.

Eggers, J., Lister, J. R., & Stone, H. A. 1999. Coalescence of liquid drops. *Journal of Fluid Mechanics*, **401**, 293–310.

Eggers, J., Fontelos, M. A., Leppinen, D., & Snoeijer, J. H. 2007. Theory of the collapsing axisymmetric cavity. *Physical Review Letters*, **98**(9), 094502.

Eral, H. B., & Oh, J. M. 2013. Contact angle hysteresis: A review of fundamentals and applications. *Colloid and Polymer Science*, **291**(2), 247–260.

Fawehinmi, O. B., Gaskell, P. H., Jimack, P. K., Kapur, N., & Thompson, H. M. 2005. A combined experimental and computational fluid dynamics analysis of the dynamics of drop formation. *Proceedings of the Institution of Mechanical Engineers, Part C: Journal of Mechanical Engineering Science*, **219**(9), 933–947.

Fontelos, M. A., Snoeijer, J. H., & Eggers, J. 2011. The spatial structure of bubble pinch-off. *SIAM Journal on Applied Mathematics*, **71**(5), 1696–1716.

Fordham, S. 1948. On the calculation of surface tension from measurements of pendant drops. *Proceedings of the Royal Society of London. Series A. Mathematical, Physical & Engineering Sciences*, **194**, 1–16.

Fritz, W. 1935. Maximum volume of vapor bubbles. *Physik Zeitschr*, **36**(11), 379–384.

Fukai, J., Zhao, Z., Poulikakos, D., Megaridis, C. M., & Miyatake, O. 1993. Modeling of the deformation of a liquid droplet impinging upon a flat surface. *Physics of Fluids A*, **5**(11), 2588–2599.

Gaddis, E. S., & Vogelpohl, A. 1986. Bubble formation in quiescent liquids under constant flow conditions. *Chemical Engineering Science*, **41**(1), 97–105.

Gekle, S., Snoeijer, J. H., Lohse, D., & van der Meer, D. 2009. Approach to universality in axisymmetric bubble pinch-off. *Physical Review E*, **80**(3), 036305.

Gerlach, D., Biswas, G., Durst, F., & Kolobaric, V. 2005. Quasi-static bubble formation on submerged orifices. *International Journal of Heat and Mass Transfer*, **48**, 425–438.

Gerlach, D., Alleborn, N., Buwa, V., & Durst, F. 2007. Numerical simulation of periodic bubble formation at a submerged orifice with constant gas flow rate. *Chemical Engineering Science*, **62**, 2109–2125.

Gibson, I., Rosen, D. W., & Stucker, B. 2010. *Additive manufacturing technologies*. Springer.

Gnyloskurenko, S. V., Byakova, A. V., Raychenko, O. I., & Nakamura, T. 2003. Influence of wetting conditions on bubble formation at orifice in an inviscid liquid. Transformation of bubble shape and size. *Colloids and Surfaces A: Physicochemical and Engineering Aspects*, **218**, 73–87.

Gordillo, J. M. 2008. Axisymmetric bubble collapse in a quiescent liquid pool. I. Theory and numerical simulations. *Physics of Fluids*, **20**(11), 112103.

Gordillo, J. M., & Pérez-Saborid, M. 2006. Axisymmetric breakup of bubbles at high Reynolds numbers. *Journal of Fluid Mechanics*, **562**, 303–312.

Gordillo, J. M., Sevilla, A., Rodríguez-Rodríguez, J., & Martínez-Bazán, C. 2005. Axisymmetric bubble pinch-off at high Reynolds numbers. *Physical Review Letters*, **95**(19), 194501.

Gresho, P. M., & Sani, R. L. 1998. *Incompressible flow and the finite element method: Volume Two. Isothermal laminar flow*. John Wiley & Sons, New York.

Gupta, K. K., & Meek, J. L. 1996. A brief history of the beginning of the finite element method. *International Journal for Numerical Methods in Engineering*, **39**(22), 3761–3774.

Henderson, D. M., Pritchard, W. G., & Smolka, L. B. 1997. On the pinch-off of a pendant drop of viscous fluid. *Physics of Fluids*, **9**(11), 3188–3200.

Herrada, M. A., Montanero, J. M., Ferrera, C., & Gañán-Calvo, A. M. 2010. Analysis of the dripping–jetting transition in compound capillary jets. *Journal of Fluid Mechanics*, **649**, 523–536.

Higuera, F. J. 2005. Injection and coalescence of bubbles in a very viscous liquid. *Journal of Fluid Mechanics*, **530**, 369–378.

Higuera, F. J., & Medina, A. 2006. Injection and coalescence of bubbles in a quiescent inviscid liquid. *European Journal of Mechanics B/Fluids*, **25**, 164–171.

Hocking, L. M. 1990. Spreading and instability of a viscous fluid sheet. *Journal of Fluid Mechanics*, **211**, 373–392.

Hoffman, R. L. 1975. A study of the advancing interface. I. Interface shape in liquid-gas systems. *Journal of Colloid and Interface Science*, **50**(2), 228–241.

Hooper, A. P. 1986. A study of bubble formation at a submerged orifice using the boundary element method. *Chemical Engineering Science*, **41**(7), 1879–1890.

Hopkinson, N., Hague, R., & Dickens, P. 2006. *Rapid manufacturing: An industrial revolution for the digital age*. John Wiley & Sons.

Hopper, R. W. 1990. Plane Stokes flow driven by capillarity on a free surface. *Journal of Fluid Mechanics*, **213**, 349–375.

Hua, J., Zhang, B., & Lou, J. 2007. Numerical simulation of microdroplet formation in coflowing immiscible liquids. *AIChE Journal*, **53**(10), 2534–2548.

Huh, C., & Scriven, L. E. 1971. Hydrodynamic model of steady movement of a solid/liquid/fluid contact line. *Journal of Colloid and Interface Science*, **35**, 85–101.

Hysing, S, Turek, S., Kuzmin, D., Parolini, N., Burman, E., Ganesan, S., & Tobiska, L. 2009. Quantitative benchmark computations of two-dimensional bubble dynamics. *International Journal for Numerical Methods in Fluids*, **60**(11), 1259–1288.

Jamialahmadi, M., Zehtaban, M. R., Müller-Steinhagen, H., Sarrafi, A., & Smith, J. M. 2001. Study of bubble formation under constant flow conditions. *Chemical Engineering Research and Design*, **79**, 523–532.

Jimack, P. K., & Wathen, A. J. 1991. Temporal derivatives in the finite-element method on continuously deforming grids. *SIAM Journal on Numerical Analysis*, **28**(4), 990–1003.

Khurana, A. K., & Kumar, R. 1969. Studies in bubble formation - III. *Chemical Engineering Science*, **24**(11), 1711–1723.

Kistler, S. F. 1993. Hydrodynamics of wetting. *Pages 311–429 of:* Berg, J. C. (ed), *Wettability*. Marcel Dekker.

Kistler, S. F., & Scriven, L. E. 1983. Coating flows. *Pages 243–299 of:* Pearson, J. R. A., & Richardson, S. M. (eds), *Computational analysis of polymer processing*. Springer.

Kulkarni, A. A., & Joshi, J. B. 2005. Bubble formation and bubble rise velocity in gas-liquid systems: A review. *Industrial & Engineering Chemistry Research*, **44**, 5873–5931.

Kumar, R., & Kuloor, N. R. 1970. The formation of bubbles and drops. *Advances in Chemical Engineering*, **8**, 255–368.

La Nauze, R. D., & Harris, I. J. 1972. On a model for the formation of gas bubbles at a single submerged orifice under constant pressure conditions. *Chemical Engineering Science*, **27**(11), 2102–2105.

Lauga, E., Brenner, M., & Stone, H. A. 2007. Microfluidics: The no-slip boundary condition. *Springer Handbook of Experimental Fluid Mechanics*, 1219–1240.

Lee, S., & Tien, W. 2009. Growth and detachment of carbon dioxide bubbles on a horizontal porous surface with a uniform mass injection. *International Journal of Heat and Mass Transfer*, **52**, 3000–3008.

Lee, S., & Yang, C. 2012. On the transition stage of bubble formation on the orifice of a submerged vertical nozzle. *The Canadian Journal of Chemical Engineering*, **90**, 612–620.

Lee, S. Y., Snider, C., Park, K., & Robinson, J. P. 2007. Compound jet instability in a microchannel for mononuclear compound drop formation. *Journal of Micromechanics and Microengineering*, **17**(8), 1558.

Lee, W., Walker, L. M., & Anna, S. L. 2009. Role of geometry and fluid properties in droplet and thread formation processes in planar flow focusing. *Physics of Fluids*, **21**(3), 032103.

Leppinen, D., & Lister, J. R. 2003. Capillary pinch-off in inviscid fluids. *Physics of Fluids*, **15**(2), 568–578.

Lesage, F. J., & Marois, F. 2013. Experimental and numerical analysis of quasi-static bubble size and shape characteristics at detachment. *International Journal of Heat and Mass Transfer*, **64**, 53–69.

Lesage, F. J., Cotton, J. S., & Robinson, A. J. 2013. Analysis of quasi-static vapour bubble shape during growth and departure. *Physics of Fluids*, **25**(6), 067103.

Lin, J. N., Banerji, S. K., & Yasuda, H. 1994. Role of interfacial-tension in the formation and the detachment of air bubbles. 1. A single hole on a horizontal plane immersed in water. *Langmuir*, **10**(3), 936–942.

Lister, J. R., & Stone, H. A. 1998. Capillary breakup of a viscous thread surrounded by another viscous fluid. *Physics of Fluids*, **10**(11), 2758–2764.

Longuet-Higgins, M. S., Kerman, B. R., & Lunde, K. 1991. The release of air bubbles from an underwater nozzle. *Journal of Fluid Mechanics*, **230**, 365–390.

Lukyanov, A. V., & Shikhmurzaev, Y. D. 2007. Effect of flow field and geometry on the dynamic contact angle. *Physical Review E*, **75**(5), 051604.

Ma, D., Liu, M., Xu, Y., & Tang, C. 2012. Two-dimensional volume of fluid simulation studies on single bubble formation and dynamics in bubble columns. *Chemical Engineering Science*, **72**, 61–77.

Marmur, A., & Rubin, E. 1973. Equilibrium shapes and quasi-static formation of bubbles at submerged orifice. *Chemical Engineering Science*, **28**, 1455–1464.

Marmur, A., & Rubin, E. 1976. A theoretical model for bubble formation at an orifice submerged in an inviscid liquid. *Chemical Engineering Science*, **31**(6), 453–463.

McCann, D. J., & Prince, R. G. H. 1969. Bubble formation and weeping at a submerged orifice. *Chemical Engineering Science*, **24**(5), 801–814.

McCann, D. J., & Prince, R. G. H. 1971. Regimes of bubbling at a submerged orifice. *Chemical Engineering Science*, **26**(10), 1505–1512.

Moffatt, H. K. 1964. Viscous and resistive eddies near a sharp corner. *Journal of Fluid Mechanics*, **18**(1), 1–18.

Nakano, M. 2000. Places of emulsions in drug delivery. *Advanced drug delivery reviews*, **45**(1), 1–4.

Navier, C. L. M. H. 1823. Mémoire sur les lois du mouvement des fluides. *Mémoires de lAcadémie Royale des Sciences de lInstitut de France*, **6**, 389–440.

Notz, P. K., Chen, A. U., & Basaran, O. A. 2001. Satellite drops: Unexpected dynamics and change of scaling during pinch-off. *Physics of Fluids*, **13**(3), 549–552.

Oğuz, H. N., & Prosperetti, A. 1993. Dynamics of bubble growth and detachment from a needle. *Journal of Fluid Mechanics*, **257**, 111–145.

Ohta, M., Kikuchi, D., Yoshida, Y., & Sussman, M. 2011. Robust numerical analysis of the dynamic bubble formation process in a viscous liquid. *International Journal of Multiphase Flow*, **37**, 1059–1071.

Okushima, S., Nisisako, T., Torii, T., & Higuchi, T. 2004. Controlled production of monodisperse double emulsions by two-step droplet breakup in microfluidic devices. *Langmuir*, **20**(23), 9905–9908.

Pinczewski, W. V. 1981. The formation and growth of bubbles at a submerged orifice. *Chemical Engineering Science*, **36**, 405–411.

Plesset, M. S., & Prosperetti, A. 1977. Bubble dynamics and cavitation. *Annual Review of Fluid Mechanics*, **9**(1), 145–185.

Ponter, A. B., & Surati, A. I. 1997. Bubble emissions from submerged orifices–A critical review. *Chemical Engineering & Technology*, **20**(2), 85–89.

Quan, S., & Hua, J. 2008. Numerical studies of bubble necking in viscous liquids. *Physical Review E*, **77**(6), 066303.

Radev, S., & Tchavdarov, B. 1988. Linear capillary instability of compound jets. *International Journal of Multiphase Flow*, **14**(1), 67–79.

Ramakrishnan, S., Kumar, R., & Kuloor, N. R. 1969. Studies in bubble formation - I Bubble formation under constant flow conditions. *Chemical Engineering Science*, **24**(4), 731–747.

Rayleigh, Lord. 1892. XVI. On the instability of a cylinder of viscous liquid under capillary force. *The London, Edinburgh, and Dublin Philosophical Magazine and Journal of Science*, **34**(207), 145–154.

Reddy, J. N. 1993. *An introduction to the finite element method*. McGraw-Hill New York.

Rohsenow, W. M. 1971. Boiling. *Annual Review of Fluid Mechanics*, **3**(1), 211–236.

Ruschak, K. J. 1985. Coating flows. *Annual Review of Fluid Mechanics*, **17**(1), 65–89.

Satyanarayan, A., Kumar, R., & Kuloor, N. R. 1969. Studies in bubble formation - II Bubble formation under constant pressure conditions. *Chemical Engineering Science*, **24**, 749–761.

Seveno, D., Vaillant, A., Rioboo, R., Adão, H., Conti, J., & DeConinck, J. 2009. Dynamics of Wetting Revisited. *Langmuir*, **25**, 13034–13044.

Shah, R. K., Shum, H. C., Rowat, A. C., Lee, D., Agresti, J. J., Utada, A. S., Chu, L., Kim, J., Fernandez-Nieves, A., Martinez, C. J., & Weitz, D. A. 2008. Designer emulsions using microfluidics. *Materials Today*, **11**(4), 18–27.

Shikhmurzaev, Y. D. 1993. The moving contact line on a smooth solid surface. *International Journal of Multiphase Flow*, **19**(4), 589–610.

Shikhmurzaev, Y. D. 2006. Singularities at the moving contact line. Mathematical, physical and computational aspects. *Physica D*, **217**, 121–133.

Shikhmurzaev, Y. D. 2007. *Capillary Flows with Forming Interfaces*. Chapman & Hall/CRC, Boca Raton.

Simmons, J. A., Sprittles, J. E., & Shikhmurzaev, Y. D. 2015. The formation of a bubble from an orifice. *European Journal of Mechanics - B/Fluids*, **53**, 24–36.

Sprittles, J. E., & Shikhmurzaev, Y. D. 2012a. Coalescence of liquid drops: Different models versus experiment. *Physics of Fluids*, **24**(12), 122105.

Sprittles, J. E., & Shikhmurzaev, Y. D. 2012b. The dynamics of liquid drops and their interaction with solids of varying wettabilities. *Physics of Fluids*, **24**, 082001.

Sprittles, J. E., & Shikhmurzaev, Y. D. 2012c. Finite element framework for describing dynamic wetting phenomena. *International Journal for Numerical Methods in Fluids*, **68**, 1257–1298.

Sprittles, J. E., & Shikhmurzaev, Y. D. 2013. Finite element simulation of dynamic wetting flows as an interface formation process. *Journal of Computational Physics*, **233**, 34–65.

Sprittles, J. E., & Shikhmurzaev, Y. D. 2014. A parametric study of the coalescence of liquid drops in a viscous gas. *Journal of Fluid Mechanics*, **753**, 279–306.

Starov, V. M., Velarde, M. G., & Radke, C. J. 2007. *Wetting and spreading dynamics*. CRC press.

Stone, H. A. 1994. Dynamics of drop deformation and breakup in viscous fluids. *Annual Review of Fluid Mechanics*, **26**(1), 65–102.

Stone, H. A., Stroock, A. D., & Ajdari, A. 2004. Engineering flows in small devices: Microfluidics toward a lab-on-a-chip. *Annual Review of Fluid Mechanics*, **36**, 381–411.

Suryo, R., & Basaran, O. A. 2006. Tip streaming from a liquid drop forming from a tube in a co-flowing outer fluid. *Physics of Fluids*, **18**(8), 082102.

Suryo, R., Doshi, P., & Basaran, O. A. 2006. Nonlinear dynamics and breakup of compound jets. *Physics of Fluids*, **18**(8), 082107.

Tan, R. B. H., & Harris, I. J. 1986. A model for non-spherical bubble-growth at a single orifice. *Chemical Engineering Science*, **41**(12), 3175–3182.

Terasaka, K., & Tsuge, H. 1990. Bubble formation at a single orifice in highly viscous liquids. *Journal of Chemical Engineering of Japan*, **23**(2), 160–165.

Terasaka, K., & Tsuge, H. 1993. Bubble formation under constant-flow conditions. *Chemical Engineering Science*, **48**(19), 3417–3422.

Thoroddsen, S. T., Takehara, K., & Etoh, T. G. 2005. The coalescence speed of a pendent and a sessile drop. *Journal of Fluid Mechanics*, **527**, 85–114.

Thoroddsen, S. T., Etoh, T. G., & Takehara, K. 2007. Experiments on bubble pinch-off. *Physics of Fluids*, **19**, 042101.

Utada, A. S., Lorenceau, E., Link, D. R., Kaplan, P. D., Stone, H. A., & Weitz, D. A. 2005. Monodisperse double emulsions generated from a microcapillary device. *Science*, **308**(5721), 537–541.

Utada, A. S., Fernandez-Nieves, A., Stone, H. A., & Weitz, D. A. 2007. Dripping to jetting transitions in coflowing liquid streams. *Physical Review Letters*, **99**(9), 094502.

Vafaei, S., & Wen, D. 2010. Bubble formation on a submerged micronozzle. *Journal of Colloid and Interface Science*, **343**, 291–297.

Vafaei, S., Borca-Tasciuc, T., & Wen, D. 2010. Theoretical and experimental investigation of quasi-steady-state bubble growth on top of submerged stainless steel nozzles. *Colloids and Surfaces A: Physicochemical and Engineering Aspects*, **369**, 11–19.

Vafaei, S., Angeli, P., & Wen, D. 2011. Bubble growth rate from stainless steel substrate and needle nozzles. *Colloids and Surfaces A: Physicochemical and Engineering Aspects*, **384**, 240–247.

Velarde, M. G. 2011. *Discussion and Debate: Wetting and Spreading Science - quo vadis?* The European Physical Journal Special Topics.

Vu, T. V., Homma, S., Tryggvason, G., Wells, J. C., & Takakura, H. 2013. Computations of breakup modes in laminar compound liquid jets in a coflowing fluid. *International Journal of Multiphase Flow*, **49**, 58–69.

Weinstein, S. J., & Ruschak, K. J. 2004. Coating flows. *Annual Review of Fluid Mechanics*, **36**, 29–53.

Wilkes, E. D., Phillips, S. D., & Basaran, O. A. 1999. Computational and experimental analysis of dynamics of drop formation. *Physics of Fluids*, **11**(12), 3577–3598.

Wilson, M. C. T., Summers, J. L., Gaskell, P. H., & Shikhmurzaev, Y. D. 2001. Moving contact-line models and the effect of hydrodynamic assist of dynamic wetting. *Pages 345–352 of: IUTAM Symposium on Free Surface Flows*. Springer.

Wilson, M. C. T., Summers, J. L., Shikhmurzaev, Y. D., Clarke, A., & Blake, T. D. 2006. Nonlocal hydrodynamic influence on the dynamic contact angle: Slip models versus experiment. *Physical Review E*, **73**(4), 041606.

Wong, H., Rumschitzki, D., & Maldarelli, C. 1998. Theory and experiment on the low-Reynolds-number expansion and contraction of a bubble pinned at a submerged tube tip. *Journal of Fluid Mechanics*, **356**, 93–124.

Wraith, A. E. 1971. Two stage bubble growth at a submerged plate orifice. *Chemical Engineering Science*, **26**, 1659–1671.

Xiao, Z., & Tan, R. B. H. 2005. An improved model for bubble formation using the boundary-integral method. *Chemical Engineering Science*, **60**, 179–186.

Xu, Q., & Basaran, O. A. 2007. Computational analysis of drop-on-demand drop formation. *Physics of Fluids*, **19**(10), 102111.

Yang, G. Q., Du, B., & Fan, L. S. 2007. Bubble formation and dynamics in gas-liquid-solid fluidization - A review. *Chemical Engineering Science*, **62**, 2–27.

Young, T. 1805. An essay on the cohesion of fluids. *Philosophical Transactions of the Royal Society (London)*, **95**, 65–87.

Zhang, D. F., & Stone, H. A. 1997. Drop formation in viscous flows at a vertical capillary tube. *Physics of Fluids*, **9**(8), 2234–2242.

Zhang, J., Li, E., & Thoroddsen, S. T. 2014. A co-flow-focusing monodisperse microbubble generator. *Journal of Micromechanics and Microengineering*, **24**(3), 035008.

Zhang, L., & Shoji, M. 2001. Aperiodic bubble formation from a submerged orifice. *Chemical Engineering Science*, **56**, 5371–5381.

Zhang, X. 1999. Dynamics of growth and breakup of viscous pendant drops into air. *Journal of Colloid and Interface Science*, **212**(1), 107–122.

Zhang, X., & Basaran, O. A. 1995. An experimental study of dynamics of drop formation. *Physics of Fluids*, **7**(6), 1184–1203.

Zhou, C., Yue, P., & Feng, J. J. 2006. Formation of simple and compound drops in microfluidic devices. *Physics of Fluids*, **18**(9), 092105.